SELF-ORGANIZATION PATHWAYS IN ACTIVE FILAMENT BUNDLES

Moritz Striebel

München 2023

SELF-ORGANIZATION PATHWAYS IN ACTIVE FILAMENT BUNDLES

Dissertation

submitted to the
Faculty of Physics at the
Ludwig–Maximilians–Universität München
for the degree of

Doctor rerum naturalium

by

Moritz Striebel

born in Backnang, Germany

Munich, 20th September 2023

First referee: Prof. Dr. Erwin Frey
Second referee: Prof. Dr. Benedikt Sabaß
Day of the oral examination: 09.11.2023

ZUSAMMENFASSUNG

Lebende Zellen sind auf den aktiven Umbau von Zytoskelettstrukturen angewiesen. Dieser Umbau wird durch die Wechselwirkung von Filamenten mit einer Vielzahl von verschiedenen assoziierten Proteinen vermittelt, am wichtigsten sind hierbei Motorproteine. Motorproteine funktionieren, indem sie chemische Energie nutzen, um Kraft und Bewegung zu erzeugen. Filament-Motor-Mischungen sind daher ein exemplarisches Beispiel für Nichtgleichgewichts Physik. Die Umwandlung von chemischer Energie ermöglicht es Filament-Motor-Mischungen sich räumliche und zeitlich zu Organisieren. Die Frage wie die Wechselwirkungen zwischen Motorproteinen und Filamenten, welche auf der Längenskala von Nanometern stattfinden, zu räumlicher Organisation auf der Längenskala von bis zu hunderten von Mikrometern führen kann, steht im Mittelpunkt dieser Arbeit. Um diese Frage zu untersuchen, habe ich zwei representative Wechselwirkungen zwischen Motorproteinen und Zytoskelettfilamenten untersucht: Erstens Längenregulierung von Filamenten durch Motorproteine in Kapitel 2 und zweitens die motorinduzierte Kräfte zwischen Filamenten im Kapitel 3.

Im Kapitel Collective filament length regulation in filament-motor mixtures untersuchen wir ein minimales biophysikalisches Modell zur Regulierung der Filamentlänge durch Motorenproteine in einer Mischung von Kinesin-8-Motoren und Mikrotubuli. Dabei berücksichtigen wir explizit die diffuse Umverteilung von zytosolischem Tubulin und Kinesin-8. Wir leiten eine hydrodynamische Beschreibung des Modells auf der Grundlage von Zeit- und Längenskalenseperationsargumenten her. Diese theoretische Beschreibung wird von umfangreichen Computersimulationen begleitet, welche unsere theoretische Beschreibung untermauern. Bemerkenswerterweise stellen wir fest, dass das Filament-Motor-Gemisch trotz der Tatsache, dass die Filamente nur indirekt über einen gemeinsamen Ressourcenpool miteinander interagieren, in der Lage ist, sich in Strukturen zu organisieren die meherere Filamentlängen überspannen und eine Ordnung der Filament Ausrichtung aufweißen, die jener von Filamentastern ähnelt. In dem nachfolgenden Abschnitt formalisieren wir unseren theoretischen Ansatz und führen eine Momenten- und Gradientenentwicklung durch, um unsere hydrodynamische Theorie herzuleiten. Unter Verwendung von agenten basierten Simulationen untersuchen wir die Langzeitdynamik des Systems auf einer phänomenologischen Ebene und finden spontane Symmetriebrechungen in der räumlichen Orientierung der Filamente, als auch Wellenlösungen, Koaleszenz und Coarsening der entstehenden Filamentstrukturen.

Im Kapitel Collective filament motion in active filament bundles untersuchen wir die emergente kollektive Dynamik in Filamentbündeln, die durch Motorproteine vernetzt sind, welche mechanische Kräfte auf die Filamente ausüben. Ausgehend von einem mikroskopischen Modell und basierend auf einem Argument der Trennung von Zeitskalen leiten wir eine effektive Filament-Filament-Wechselwirkung ab. Basierend auf dieser effektiven Filament-Filament-Wechselwirkung untersuchen wir das kollektive Zusammenspiel zwischen den von den Motoren erzeugten Kräften und der Dynamik des Filamentbündels. Im ersten Abschnitt untersuchen wir ein Bündel von Filamenten, welche durch eine Vielzahl von verschiedenen Motoren vernetzt sind, und fragen, welche Mechanismen die Tendenz des Filamentbündel, sich zusammenzuziehen oder auszudehnen, kontrollieren. Auf der Grundlage eines generischen Modells für motorische Vernetzer leiten wir einen Formalismus zur Quantifizierung der aktiven Spannung in einem Bündel vernetzter Filamente ab. Mit Hilfe dieses generischen Modells untersuchen wir ein System, das aus Filamenten, passiven Vernetzern und Motorproteinen besteht, welche sich am Ende von Filamenten ansammeln können.

In diesem System identifizieren wir drei externe Kontrollparameter, die die Tendenz der Filamentbündel, sich zusammenzuziehen oder auszudehnen, regulieren: Erstens, die Gesamtzahl der Motoren im System. Zweitens, die Gesamtzahl der passiven Vernetzer und drittens die Filamentlänge. Wir validieren unsere theoretischen Vorhersagen und untersuchen die entstehende Langzeitdynamik des Filamentbündels mit Hilfe von agentenbasierten Simulationen. Unsere Vorhersagen sind im Einklang mit neusten *in vitro* Experimenten. In den folgenden Abschnitten haben wir die Frage behandelt, wie motorische Vernetzer die Filamentgleitgeschwindigkeit in einem Bündel vernetzter Filamenten kontrollieren. Auf der Skala eines einzelnen Filamentpaares scheint die motorisch erzeugte Filamentbewegung von der relativen Orientierung der Filamente abzuhängen. *In vivo* und *in vitro* Beobachtungen an der mitotischen Spindel zeigen jedoch, dass die Geschwindigkeit von Filamenten unabhängig von der lokalen Anzahl der Interaktionspartner mit gleicher oder entgegengesetzter Orientierungen ist. Motiviert durch diesen scheinbaren Widerspruch setzten wir uns das Ziel zu verstehen, welche Prozesse die Filamentgeschwindigkeit in aktiven nematischen Netzwerken regulieren: Wir haben einen Mechanismus für die kollektive Filamentbewegung identifiziert: Aufgrund der starken Vernetzung im Filamentbündel kann lokal erzeugte Kraft über eine charakteristische Längenskala durch das Netzwerk propagiert werden. Diese Längenskala wird durch den Antagonismus zwischen dem Widerstand gegenüber der umgebenden Flüssigkeit und den aktiven motorischen Kräften, die auf das Filament einwirken, bestimmt. Anschließend haben wir mit Hilfe von Computersimulationen untersucht, wie der identifizierte Mechanismus von der Konnektivität des Filamentnetzwerks abhängt.

Zusammengefasst haben wir untersucht, wie die Wechselwirkungen zwischen Motorproteinen und Filamenten, die auf der Nanometerskala stattfinden, die emergente kollektive Dynamik von Filament-Motor-Gemischen auf der Mikrometerskala beeinflusst. Wir haben gezeigt, dass die aktive Depolymerisation von Filamenten in Kombination mit Massenerhaltung nicht nur die Größe der emergenten Filamentstrukturen kontrolliert, sondern auch einen Weg zur Selbstorganisation von Filamentstrukturen bietet. In Bündeln von Filamenten, die durch Motorproteine vernetzt sind, welche mechanische Kräfte auf die Filamente ausüben können, haben wir gezeigt, wie die aktive Spannung und die Filamentgeschwindigkeit von den kinetischen und mechanischen Eigenschaften der motorischen Vernetzer abhängt. Unsere Arbeit zeigt, warum einige motorische Vernetzer zu einer Kontraktion des Filamentnetzwerks führen, während andere ein sich ausdehnendes Filament-Motor-Gemisch erzeugen.

In der lebenden Zelle sind motorvermittelte Filamentlängenregulation und motorvermittelte mechanische Wechselwirkungen zwischen Filamenten keine isolierten Prozesse - sie finden gleichzeitig statt. Es wird eine spannende Forschungsfrage sein, die kollektive Dynamik von Filamentmotormischungen zu verstehen, in welchen sowohl motorvermittelte mechanische Filament-Filament-Wechselwirkung als auch Längenregulation stattfinden.

SUMMARY

Living cells rely on the active remodeling of cytoskeletal structures. This remodeling is mediated by the interaction of filaments with a variety of different associated proteins, most importantly motor proteins. Motor proteins operate by using chemical energy to generate force and movement. Thus, filament-motor-mixtures are a paradigmatic example of out-of-equilibrium physics. The transduction of chemical energy enables filament-motor-mixtures to obtain spatial and temporal organization. How interactions between motor proteins and cytoskeletal filaments, which happen on the nanometer scale, can give rise to spatial organization on the scale of up to hundreds of micrometers is the main focus of this thesis. To approach this question, I studied two typical interactions between motor proteins and cytoskeletal filaments: First, motor-mediated length regulation of filaments in chapter 2, and second, motor-mediated force generation in chapter 3.

In the chapter Collective filament length regulation in filament-motor mixtures, we study a minimal biophysical model for motor-mediated filament length regulation in an ensemble of kinesin-8 motors and microtubules. Importantly, we account explicitly for the diffusive redistribution of cytosolic tubulin and kinesin-8 motors. We derive a hydrodynamic description of the model on the basis of time and length scale separation arguments. Our theoretic description is accompanied by large-scale computer simulations. Strikingly, we find that, even though filaments interact only indirectly via a shared pool of resources, the filament-motor-mixture is capable of self-organizing into structures that span multiple filament lengths and show aster-like orientational order. In the subsequent section, we formalize our theoretical approach and perform a moment and gradient expansion to derive our hydrodynamic theory. Using agent-based simulations, we study the long-term dynamics of the system on a phenomenological level and find spontaneous symmetry breaking in the orientational order, traveling wave solutions, coalescence and coarsening of the emerging filament structures.

In the chapter Collective filament motion in active filament bundles, we investigate emergent collective dynamics in filament bundles cross-linked by motor proteins that exert mechanical forces on the filaments. Starting from a microscopic model and based on a time-scale separation argument, we derive a coarse-grained filament-filament interaction. Based on this filament-filament interaction, we study the collective interplay between motor-generated forces and filament bundle dynamics. In the first section, we study a bundle of filaments that are cross-linked by a set of motors and ask which mechanisms control the filament bundles' propensity to contract or expand. Based on a generic model for motor cross-linkers, we derive a formalism to quantify the active tension in a bundle of cross-linked filaments. Using this generic model, we study a system composed of filaments, passive bundling agents, and cross-linking motors that can dwell at the filament tip. In this system, we identify three external control parameters that regulate the filament bundles' propensity to contract or expand: First, the total number of motors in the system. Second, the total number of bundling agents, and third, the filament length. We validate our theoretical predictions and study the emergent long-term dynamics of the filament bundle using agent-based simulations. Our predictions are in accordance with recent *in vitro* experiments. In the following sections, we addressed the question of how motor cross-linkers control the filament sliding speed in a bundle of cross-linked filaments. On the microscopic scale, motor-generated filament motion seems to be inherently linked to the relative orientation of cross-linked filaments. However, *in vivo* and *in vitro* observations in the mitotic spindle demonstrated that the speed of filament sliding is independent

of the local number of interaction partners with equal and opposite orientations. Motivated by this apparent contradiction, we sought to understand which processes regulate collective filament sliding in active nematic networks. We identified a mechanism for collective filament sliding: Owing to the cross-linking in the filament network, the locally generated force can be propagated through the network over a characteristic length scale. This length scale is set by the antagonism between dissipation to the surrounding fluid and active motor-driven forces imposed on the filament. We then proceeded to study how the identified mechanism depends on the connectivity of the filament network with the help of large-scale computer simulations.

Taken together, we have studied how interactions of motor proteins and filaments, which take place on the nanometer scale, affect the emergent collective dynamics of filament-motor-mixtures on the scale of micrometers. We have shown that the active, motor-mediated depolymerization of filaments, in combination with mass conservation, does not only control the size of emergent filament structures but provides a self-organization pathway on its own. In bundles of filaments cross-linked by motor proteins capable of exerting mechanical force, we have shown how the active tension and the sliding speed of filaments depend on the kinetic and mechanical properties of the cross-linking motor proteins. Thereby, our work clarifies why some motor cross-linkers cause filament network contraction while others promote extensile tension in filament-motor mixtures.

In the living cell, motor-mediated filament length regulation and motor-mediated mechanical interactions between filaments are no isolated processes – they take place simultaneously. It will be an interesting avenue for future research to understand the collective dynamics of filament-motor-mixtures where both motor-mediated mechanical filament-filament interactions and length regulation are present.

List of Publications

Published

2. M. Striebel, F. Brauns, and E. Frey, "Length Regulation Drives Self-Organization in Filament-Motor Mixtures", Physical Review Letters **129**, 238102 (2022)

1. M. Striebel, I. R. Graf, and E. Frey, "A Mechanistic View of Collective Filament Motion in Active Nematic Networks", Biophysical Journal **118**, 313–324 (2020)

In preperation

2. M. Striebel and E. Frey, "Bridging scales in filamentous active matter", Manuscript in preparation, 2023

1. M. Striebel, A. Sciortino, I. Maryshev, A. R. Bausch, and E. Frey, "Connectivity tunes filament velocity in filament-motor mixtures", Manuscript in preparation, 2023

CONTENTS

PREFACE

Living cells demonstrate an astonishing diversity of capabilities and functions. This includes cell division, cell motility, exerting force and resisting deformation, and transporting intracellular cargo [5–7]. An essential component enabling the cell to exhibit those stunning properties is the cytoskeleton. Biopolymer filaments such as actin and microtubules, molecular motors, and associated proteins are the main building blocks of this structure [7–9]. For cytoskeletal filament assemblies to perform their tasks, they must have a high degree of spatial and temporal organization that spans multiple time and length scales [10–14]. Those time and length scales range from the transport of individual proteins on single filaments that exist only for seconds to the formation of cytoskeletal filament structures that exist for up to hours, contain thousands of filaments, and exhibit specific spatial organization. This leads to the question: *How can the orchestrated interplay of many small, short-living components emerge in large-scale spatial and temporal organization without a conductor?* Essential for the self-organization of cytoskeletal filament structures is the ability of molecular motors to transduce chemical energy [8, 15]. The ability to convert chemical energy into mechanical work makes filament-motor mixtures an exemplary system for nonequilibrium physics and enables them to obtain spatial and temporal organization. Unlike equilibrium systems, for non-equilibrium systems, no general concepts bridge the properties of a single component to the collective properties of the system [16]. In the absence of a general theoretical framework, a complementary approach is to study individual exemplary systems with different microscopic dynamics in the hope that insights gained from those systems might reveal general principles.

Arguably the most prominent example of cytoskeletal self-organization is the mitotic spindle, a complex structure necessary to accurately segregate chromosomes during cell division [17–19]. In the 1950s, the spindle was discovered to consist of fibers [20] later identified as microtubules. To segregate chromosomes, it was proposed that those fibers exert force on the chromosomes by (de)polymerization kinetics [21]. This interpretation was challenged by the discovery of short interconnections between microtubules, which were referred to as cross-bridges [22]. This discovery has led to the idea of a sliding filament mechanism for chromosome segregation [23]. The relative importance of polymerization kinetics and filament sliding has long been under debate, with the prevailing view being that both processes are essential for proper spindle functionality [19]. But how do those processes emerge from the interplay of individual proteins, the elementary building blocks of the cell? A constantly expanding set of experimental methods has led to the identification of approximately 200 proteins thought to be essential for proper spindle functionality [24]. Yet a mechanistic understanding of how these proteins self-organize to generate force and shape the spindle is still missing [17].

The overwhelming number of proteins and the complexity of the cytoskeletal organelle assembly have led to the development of reconstituted systems composed of purified components. Those systems allow the study of individual proteins under well-controlled conditions and more accurate measurement techniques. The range of reconstituted systems spans from single filament experiments to collections of thousands of filaments mixed with several purified proteins, leading to a new research area on its own. Single filament experiments are used to assess mechanical properties of individual microtubules and actin fibers [25–30] as well as their interplay with specific associated proteins [31–36]. Thereby it is possible to gain insight into how filament polymerization kinetics and filament cross-bridging are regulated. In contrast, large-scale reconstituted systems investigate the

emergent collective dynamics of filament-motor mixtures [37–40]. The hope is that insights gained from those "minimal" systems allow us to draw conclusions about fundamental mechanisms driving self-organization of cytoskeletal filament structures *in vivo*.

To gain insight into the physical principles that determine the dynamics of single filaments, theorists have developed kinetic models accounting for filament-protein interactions [41–47]. These models are accompanied by hydrodynamic theories, which are built on symmetry arguments those theories are used to describe the collective dynamics of filament-motor mixtures. While these theories have been proven to be a powerful tool to understand the large-scale dynamics on a phenomenological level [48–52] they come at a price and contain phenomenological parameters that are difficult to relate to microscopic interactions of the constituents.

A key challenge for theorists in the field is to bridge the gap between insights from single filament experiments to the collective dynamics of filament-motor mixtures. Successfully doing so would allow for a more accurate design of reconstituted cytoskeletal materials and, hopefully, for more precise manipulation of *in vivo* filament structures. The difficulty in deriving such theories is that they have to span multiple time and length scales. The small scale constitutes the (reaction-)dynamics of proteins with individual filaments, which happens on the time scale of milliseconds and on the typical length scale of protein size (nanometers). The large scale is set by the lifetime of cytoskeletal filament assemblies and the spatial organization of reconstituted filament systems (up to millimeter scale). A theory accounting for the dynamics on all those scales is elusive or, if not, most certainly not particularly insightful due to its complexity. More promising are approaches that rely on time and/ or length scale separation. *The overarching goal of this thesis is to start from well-established single filament experiments and apply those approximation techniques to derive consequences at the collective level.* Specifically, we will discuss systems composed of microtubules and motor proteins that play a role in the two hallmark processes of spindle assembly – filament (de)polymerization and filament sliding.

CHAPTER ABSTRACTS

Each chapter starts with a short introduction to the biological context of the studied model, followed by a minimal example that highlights the mathematical modeling approaches used in the subsequent sections. A more comprehensive review of the biological background is given in chapter 1. The individual sections of the chapters are self-contained, i.e., each section can be read on its own, and no knowledge of prior chapters or sections is needed.

1. INTRODUCTION

The introduction of this thesis gives a short introduction to the biology of cytoskeletal filament motor mixtures from a physicist's perspective. Where do cytoskeletal filament assemblies play a role in the cell? What are the major constituents they are built of, and which properties do they have? Those are the guiding questions of the introductory chapter. The focus here is on the biological aspects and not on the mathematical modeling approaches. An introduction from a modeling perspective is given at the beginning of each chapter. The introduction given here is by no means complete. Where possible, I refer to review articles I found helpful, though this might be a matter of personal taste.

2. COLLECTIVE LENGTH REGULATION IN FILAMENT MOTOR MIXTURES

LENGTH REGULATION DRIVES SELF-ORGANIZATION IN FILAMENT-MOTOR MIXTURES:

Length regulation of filaments plays a crucial role in many cellular contexts. For example, it has been observed that the pole-to-pole length and the mass of the spindle apparatus depend crucially on the length of the individual microtubules [53–55]. At different cell stages, biology exploits this dependence by regulating microtubule length and, thereby, the spindle length via the interaction with different microtubule-associated proteins (MAPs) [53, 56, 57].

Previous studies focus on the question of how individual MAPs regulate the length of individual filaments by affecting their rates of polymerization kinetics [42–44, 58–63]. Alternatively, a globally accessible pole of constituents was assumed [64–68]. However, there is increasing experimental evidence that the local availability of MAPs and (or) tubulin plays an essential role in the self-organization and maintenance of large-scale microtubule structure [53, 57, 69–73].

In the first project on length regulation in filament motor mixtures, we ask the question of how the interplay of a specific microtubule-binding protein, kinesin-8, and microtubules in combination with spatial redistribution of resources (kinesin-8 and tubulin) through cytosolic diffusion can lead to self-organization in large scale filament-motor mixtures. We find that the interplay of motor-catalyzed depolymerization in combination with local resource availability is sufficient to self-organize the filament motor mixtures into structures with aster-like orientational order, that span multiple filament lengths.

Project contributions: Fridjof Baruns and I contributed equally to this work. Fridjof Brauns, Erwin Frey, and I conceptualized the study. Fridjof Brauns and I performed the analytic analysis. I performed numerical analysis, data analysis, and data visualization. Erwin Frey supervised the research.

FILAMENT BUNDLE FORMATION AND POLARITY SORTING THROUGH LENGTH REGULATION:

Focusing on the core concepts established in the project *Length regulation drives self-organization in filament-motor mixtures*, we study a minimal one-dimensional model of the system. We systematically derive a hydrodynamic description by coarse-graining the microscopic dynamics. Thereby, we were able to get to the bottom of how length regulation drives polarity sorting in the emerging filament structures. We then turn to agent-based simulations to study the long-term dynamics of the model on a phenomenological level. We find spontaneous symmetry breaking in the orientational order, moving filament structures, coarsening of filament structures, and coalescence of filament structures, all in the absence of mechanical interactions between filaments.

Project contributions: Fridjof Brauns, Erwin Frey, and I conceptualized the study. I performed the analytic analysis in discussion with Fridjof Brauns. I performed numerical analysis, data analysis, and data visualization. Erwin Frey supervised the research.

3. COLLECTIVE FILAMENT MOTION IN ACTIVE NEMATIC NETWORKS

BRIDGING SCALES IN FILAMENTOUS ACTIVE MATTER

Assemblies of cytoskeletal filaments and associated proteins form diverse, dynamic structures that play essential roles in many intracellular processes. An important ability to perform their task is to generate force. Often, this force is generated by an extending or contracting network of cross-linked filaments. Examples are the mitotic spindle, which extends to segregate chromosomes during cell division, or the actin cortex, which contracts to drive changes in cell shape during tissue morphogenesis.

In *in vitro* filament-motor mixtures, the extensile or contractile nature of filament networks yields a broad range of behavior, including local and global network contraction with the subsequent formation of asters or foams as well as Euler-type buckling instabilities and turbulent-like behavior [38, 40, 74–79].

Previous studies have focused on the question of how the different behaviors of contractile and extensile filament networks yield self-organization on the macroscopic scale of the filament network. These studies use phenomenological hydrodynamic theories built on symmetry arguments. In those theories, the contractile or extensile nature of the filament network is reflected in an apolar active stress [50, 80–86]. However, how this stress emerges from the microscopic interplay between motor proteins and microtubules is less well understood.

In this Section, we use a complementary approach and study a minimal but generic theoretical model for bundles of filaments cross-linked by motor proteins or passive cross-linkers. Starting from a general microscopic model for motor cross-linkers, we derive a framework to evaluate the contribution of a motor cross-linker to the bundles propensity to expand or contract. Thereby, we bridge the gap between the microscopic dynamics of individual motor cross-linkers interacting with filaments and the mesoscopic scale of a filament bundle.

We use our theoretical framework to study filament-motor mixtures composed of motors that can cross-link and walk on neighboring filaments and crowding agents that bundle filaments together. In addition, we allow motor cross-linkers to dwell at the filament end they are walking towards. This set of constituents resembles a minimal model for a broad range of experimental systems [38, 40, 75–79, 87–93]. We identify three mechanisms that control the propensity of the filament bundle to contract or extent. First, contractile tension is caused by filament-filament interactions between filaments with equal orientation, mediated by end-dwelling motors. Second, internal friction is needed for motors to generate an extensile stress, and the extensile stress can be increased by increasing the friction between filaments. This yields the counterintuitive prediction that holding individual filaments in the network together increases the materials' propensity to expand. Using

our theoretical framework, we summarize those requirements in a set of mesoscopic control parameters. By specifying a microscopic model, we relate the set of mesoscopic control parameters to three externally controllable parameters: First, the number of motors per filament. Second, the number of passive cross-linkers in the filament, and last, the filament length. Our theory predicts that the filament bundle is extensile at high concentrations of passive cross-linkers and for long filaments. In contrast, high concentrations of motors and short filaments promote contractile stress in the filament bundle. All those predictions are in line with recent *in vitro* experiments [75, 77–79, 91–93].

To verify our theoretic predictions and to study the long-term dynamics, including steady-state filament structures, we use agent-based simulations. The emergent long-term dynamics are reminiscent of *in vitro* observations of filament-motor mixtures composed of similar constituents [38, 40, 77, 87, 94].

Project contributions: I conceptualized the study and performed the analytic analysis, numerical analysis, data analysis, and data visualization. Erwin Frey supervised the research. I thank Henrik Weyer and Martin Lenz for stimulating discussions.

A MECHANISTIC VIEW OF COLLECTIVE FILAMENT MOTION IN ACTIVE NEMATIC NETWORKS:

The cytoskeleton plays an essential role in many cellular processes ranging from force generation to chromosome segregation. The interplay between filaments and molecular motors is essential to establish those tasks. A variety of proteins and molecular motors are capable of cross-linking neighboring filaments. Thereby, they arrange filaments into large networks. A specific type of molecular motor, kinesin-5, has been shown to be able to cross-link two microtubules and simultaneously move toward the plus end of both microtubules it cross-links. Thereby, kinesin-5 is capable of sliding neighboring filaments. This filament motion depends on the relative orientation of the cross-linked filaments. If the cross-linked filaments are oriented in opposite directions (anti-parallel) the filaments are slid apart at approximately twice the motor velocity [95]. In contrast, filaments oriented in the same direction (parallel) do not move relative to each other. On the level of individual filaments, this type of filament-filament interaction suggests that the filament velocity depends on the local network environment, more specifically, the local number of parallel and anti-parallel interaction partners expressed in the local network polarity. However, this intuition is in conflict with experimental findings for metaphase spindles in Xenopus egg extract [96–98]. There, it was observed that microtubules move at velocities, which are independent of the local network polarity.

To get to the bottom of these observations, we study a minimal conceptual model for motor-induced filament sliding. Thereby, we were able to derive a continuum theory that relates the filament velocity to the network polarity. We show that the filament velocity depends in a non-local way on the network polarity. Due to the entire network being interconnected, locally generated force is propagated through the network over a characteristic length. We show that this characteristic length is set by the strength of motor forces imposed on a filament and dissipation to the surrounding fluid. In the limit of low dissipation or large motor forces, we recover the experimental findings that the filament velocity is independent of the local network environment.

Project contributions: Isabella R. Graf and I contributed equally to this work. Isabella R. Graf, Erwin Frey, and I conceptualized the study. Isabella R. Graf and I performed the analytic analysis. I performed numerical analysis, data analysis, and data visualization. Erwin Frey supervised the research. The publication is also part of Isabella Graf's thesis.

CONNECTIVITY TUNES FILAMENT VELOCITY IN FILAMENT-MOTOR MIXTURES

Building on the insights gained in the project *A mechanistic view of collective filament motion in active nematic networks*, we ask the question of how the degree of network connectivity affects the network's ability to propagate force and, thereby affect the filament sliding velocities. To this end, we use an *in-vitro* reconstituted system composed of stabilized microtubules, molecular motors, and passive cross-linkers. We find that an increase in the passive cross-linker concentration leads to a non-monotonous change in the mean filament velocity. Surprisingly, we find that an increase in passive cross-linkers can lead to an increase in filament velocities. This is counterintuitive since passive cross-linkers impose friction on adjacent filaments. We build an agent-based model that reproduces our key experimental observations. Based on this model, we relate the mean filament velocity to the network architecture and, ultimately, to the connectivity in the filament network. Using large-scale numerical simulations, we identify previously reported physical properties of sparse and highly cross-linked networks at low and high cross-linker concentrations, respectively. Specifically, we show that the mean filament velocities become insensitive to the local network environment (polarity) as the passive cross-linker concentration is increased, a feature which was predicted for highly cross-linked filament networks [2, 99]. Based on a minimal model, we derive a semi-analytical theory that can encompass both sparse and highly cross-linked regimes and predict the mean filament velocity as a function of the active motor and passive cross-linker concentration. Last, we compare our analytic results to measurements from the agent-based simulation.

Project contributions: Alfredo Sciortino, Erwin Frey and I conceptualized the study. Alfredo Sciortino designed and performed the experiments. I performed the formal analysis and the numerical simulations in discussion with Ivan Maryshev. I visualized the data. Alfredo Sciortino, Erwin Frey, and I wrote the manuscript. Andreas Bausch and Erwin Frey supervised the research. The experimental results are part of Alfredo Sciortino's thesis.

1

INTRODUCTION

1.1. SELF-ORGANIZATION OF FILAMENT MOTOR MIXTURES *in vivo* AND *in vitro*

The incredible variety of tasks performed by cytoskeletal filament assemblies makes it necessary that their size and shape vary enormously, even within a single organism and cell type. Here we will introduce some prominent examples of large-scale self-organization of biological and reconstituted filament motor mixtures. Those filament assemblies self-organize into a diverse range of structures ranging over multiple length scales and persist over multiple time scales.

The actin cortex plays a key role for the cell mechanics [100]. It has a typical thickness of 50 – 400 nm and is localized at the cell membrane [101–103]. Probably its most important function is to generate force [100, 104] making it an essential element that determines cell mechanics [102, 105]. It consists of actin filaments, the molecular motor myosin II, which can cross-link, pull and organize actin filaments [35, 106] and a variety of associated proteins that regulate the assembly, disassembly, and nucleation dynamics [35].

The spindle apparatus: is responsible for chromosome segregation during cell division [19]. The importance and robustness of this task become apparent when we consider the number of cells in the human body, which is estimated to be on the order of $\sim 10^{13}$ cells which are generated by cell division [107]. Errors in the process of chromosome segregation and cell division can lead to aneuploidy and can become a first step towards cancer [17]. Up to date, a comprehensive understanding of how the ~ 200 proteins involved in spindle assembly cooperate to achieve this stunning task is missing [17, 24]. This is because a variety of challenges complicates the study of the spindle: First, it is a highly dynamic structure, and microtubules in the spindle turn over every ~ 30 s [19]. Second, the number of microtubules (up to $\sim 10^5$) and the number of associated proteins involved in spindle assembly ~ 200 make it an incredibly complex structure. Last despite being built of the same constituents the spindle apparatus can vary significantly in length, mass, and shape even within a single organism [54, 69, 70, 73].

Microtubule asters are radial arrays of microtubules that span out from the centrosome. During different phases of the cell cycle, they differ significantly in size. While mitotic asters are comparably small, interphase asters span the entire cell. Aster microtubules perform multiple tasks, this includes the transport of organelles [108, 109], they are involved in the positioning of the cleavage furrow, the mitotic spindle, and the nucleus [110–113]. Large asters in interphase are built out of a branching array of dynamic microtubules which have a length of ~ 16 µm and live time of ~ 1 min [114–116], though the microtubule aster can span hundreds of micrometers. In addition to showing complex self-organization dynamics on their own, pairs of asters interact to define the cleavage

plane. At the midplane, where a pair of asters meets, they form an overlap of anti-parallel microtubules, which in turn recruits upstream regulatory factors [112]. Thereby the aster pair defines the cleavage plane. The complex physics of aster growth, interaction, and positioning is still an ongoing field of research [117].

Active filament gels The complexity and the overwhelming number of proteins involved in cytoskeletal filament assemblies have motivated biophysicists to develop minimal *in vitro* systems composed of a well-controlled set of proteins which are made from cytoskeletal components. Those systems allow for a more systematic "bottom-up" approach to studying active filament systems. In the context of the dynamics of collective filaments, two systems have emerged as paradigmatic experimental systems of active matter. First A. Baush and colleagues mixed actin filaments which are propelled by immobilized myosin motors in the planar geometry of a standard motility assay [37]. In this experimental setup, they were able to demonstrate the collective self-organization of stabilized actin filaments into clusters, interconnected bands, and swirls. This system is appealing as the stability of the collective dynamics can be experimentally accessed by varying the filament density. A second exemplary active matter system composed of stabilized microtubules of fixed length and engineered kinesin motors was first introduced by the Dogic lab [38]. Compared to the actomyosin assay, the observed patterns were much more complex. Since then, this system has been used to study active materials, e.g., in vesicles [118] and ridged confinements [78, 119, 120] or systems where activity has been controlled via optical response [77, 121]. Moreover, there is an increasing list of experiments that mix different motors and cross-linkers types [40, 79, 88, 91] and studies investigating active filament-motor mixtures of non-stabilized microtubules which change their length [75, 88]. The incredible variety of possible dynamics which emerges from the simple interaction of motors and stabilized microtubules in collective dynamics is still not understood and is a rapidly evolving research area.

Xenopus egg extract: Xenopus egg extract [122, 123] is a cell free system used in many experiments. It contains all essential building blocks present in the cell while lacking a cell membrane that complicates high-resolution imaging and physical and chemical perturbations. Xenopus egg extract has been shown to be remarkably functional. As an example, it was shown to be able to undergo multiple cell cycles [124], can self-organize into the bipolar spindle even in the absence of centrosomes [125], and is even able to spontaneously self-organize into cell-like compartments after being homogenized [126]. As such it can be seen as a model system bridging the gap between reconstituted systems and *in vivo* systems.

1.2. CYTOSKELETAL FILAMENTS

In this section, we will give a brief summary of cytoskeletal filaments and their (bio)physical properties. I ignore intermediate filaments as they play no role in this thesis. For more comprehensive reviews, please refer to [127] for microtubules and [35] for actin filaments.

1.2.1. MICROTUBULES

Microtubules are built out of the protein tubulin, more precisely α and $\beta-$tubulin, which form $\alpha/\beta-$heterodimers. These heterodimers assemble into linear structures called protofilaments with $\alpha-$tubulin at the head (plus-end) and $\beta-$tubulin at the tail (minus-end); see Fig. 1.1. This organization gives the protofilament a polarity. This means they have a direction throughout their lattice. The vast majority of microtubules are built out of thirteen protofilaments [133–135] which form a hollow tube making them relatively rigid objects; see Fig. 1.1. The persistence length (~

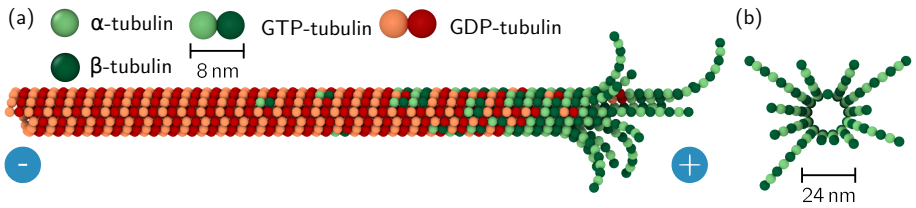

Figure 1.1: Sketch of a microtubule. (a) The majority of microtubules are built out of thirteen protofilaments, which are themselves assembled from α/β tubulin heterodimers. Newly added tubulin is in the GTP-state and undergoes random hydrolyzes (GTP-tubulin → GDP-tubulin) once incorporated into the microtubule lattice. (b) Top view of a microtubule tip. Note the textbook picture of growing protofilaments being uncurled is challenged by recent experiments [127–132].

0.1 mm – 5 mm) of microtubules is approximately a thousand times their typical length [25, 30]. From a modeling perspective, this often allows to treat microtubules as rigid rods.

The microtubule exchanges its building blocks with the surrounding cytosol at both ends through (de)polymerization kinetics. However, the dynamics at the plus end is considerably faster. Both *in vitro* and *in vivo* the microtubule undergoes stochastic changes between phases of growth and shrinkage at the plus end, a process termed dynamic instability [136]. This process is taking place for isolated microtubules assembled from purified tubulin. However, it appears to be tightly regulated by a whole machinery of associated proteins *in vivo* [36, 137]. Despite being studied for several decades, the mechanistic origin of dynamic instability is still under debate [128]. Increasing evidence is building up that two key features are involved: First, as the microtubule is polymerized a cap of GTP-tubulin is formed [138, 139]. Incorporation into the microtubule lattice triggers hydrolyses into GDP-tubulin [140]. GDP-tubulin is thought to have different mechanical properties, which weaken the stability of the microtubule lattice [128, 141]. The stochastic switch from growth to shrinkage is thought to be related to the loss of this GTP-cap. The second feature which seems to play an essential role is the "raggedness" of the microtubule tip, which increases over the course of time in the growing phase [127–129, 131, 142]. While the process of dynamic instability as such is not well understood, it is even less clear how it is regulated by associated proteins.

To circumvent complications arising from the fast (de)polymerization dynamics of microtubules often stabilized microtubules are used in reconstituted systems. One common way to stabilize microtubules is to assemble them from the (very) slowly hydrolyzable GTP-tubulin analog GMPCPP. A major advantage of GMPCPP stabilized microtubules is that they are thought to be a model system for the GTP-cap of non-stabilized microtubules. For example, proteins that affect the catastrophe rate (switch from growth to shrinkage) of unstabilized microtubules have often been shown to be able to depolymerize GMCPP-stabilized microtubules [58, 59, 143]. Moreover, stabilized microtubules are extensively used to study self-organization principles in mixtures of proteins capable of exerting force on filaments and microtubules [38, 40, 92, 99, 119, 144].

1.2.2. ACTIN

Actin filaments have many similarities with microtubules. They are polar and change their length at both ends through (de)polymerization of their elementary building blocks; F-actin. However, instead of assembling into straight protofilaments, F-actin arranges into a double helix shape. Those double helices are significantly thinner than microtubules. Due to their structural difference, actin filaments are more flexible having a typical persistence length of ~ 17 µm [25]. As for microtubules, there is a variety of actin-binding proteins which contribute to the (de)polymerization dynamics of actin filaments and cross-link them. When assembled into a network actin filaments can exert both strong contracting and pushing forces. While the former emerges from an interplay with bipolar

filaments of myosin II [35, 104] the latter has been related to the (de)polymerization dynamics of actin filaments [35, 104].

As we have seen, actin filaments and microtubules share several similarities from a coarse-grained perspective. In this work, we will therefore sometimes use the word filament interchangeably for both filament types when the underlying (minimal) model can be applied to both actin and microtubules.

1.3. MICROTUBULE BINDING PROTEINS

While actin and microtubules show complex (de)polymerization dynamics when assembled from purified components their dynamics appear to be highly regulated throughout the cell cycle [32, 33, 36, 137]. This regulation arises from the interplay with a large number of associated proteins that regulate filament dynamics. To the best of my knowledge, there is no comprehensive review of the interplay of all the various associated proteins with the corresponding filaments. This is due to their large number and diverse functionality. Here we will review only some key players involved in the self-organization of cytoskeletal filament assemblies. In particular, we will focus on proteins involved in filament length regulation and filament transport - processes relevant to this work. That being said there are many more processes regulated by associated proteins e.g., filament nucleation, end-clustering, or severing. More comprehensive reviews can be found in [32, 33, 36, 137].

Molecular motors and microtubule-associated proteins (MAPs) are two types of proteins that interact with and regulate microtubules. Molecular motors have in common that they use ATP hydrolyses to generate force and movement along the microtubule (or actin filament), which is commonly referred to as motor activity. MAPs, in contrast, are a family of proteins that interact with microtubules to regulate their stability, (de)polymerization dynamics, and functionality but do not have motor activity themselves. Though they can break detailed balance due to specific binding kinetics at the filament ends [45, 145]. Sometimes they pair up with molecular motors to perform their tasks.

1.3.1. MOLECULAR MOTORS

One class of proteins involved in many, if not all, self-organization processes of cytoskeletal filaments are so-called molecular motors. There is evidence that molecular motors, together with actin and tubulin, were at the origin of eukaryotic life 2.2 Billion years ago [146, 147]. All motor proteins have in common that they operate by using the energy released from ATP-hydrolysis [147], and few use GTP-hydrolysis [148]. By locally converting chemical energy, they can generate force and movement, which drives filament-motor mixtures out of equilibrium. There are three types of molecular motors. Kinesin and dynein, which interact with microtubules, and myosin which interacts with actin filaments. Their major role is to transport cargo, crosslink, and slide filaments, and to regulate filament tip dynamics. Figure 1.2 (a) shows the typical structural organization of a dimeric kinesin motor such as conventional kinesin-1. It consists of two heads (motor domain), which are structurally similar to those of dynein. The motor domain is connected to a cargo binding domain through the coild-colied stalk. The two motor heads bind to distinct sides of the microtubule (see Fig. 1.2 (b)). Through ATP hydrolysis, kinesins regulate the head affinity to the microtubule binding site, and the subsequent motor binding site detaches. Upon attachment of the loose head the motor moves directionally on the microtubule in a step-like fashion [149, 150]; see Fig. 1.2 (b). While differing in details, this step-like motion is common to both dynein and kinesin motors. Kinesin motors usually move towards the microtubule plus end. However, some kinesin superfamily members move in the opposite direction and some perform diffusive motion. Dynein moves to the minus end. Between different subfamilies of kinesins, the motor heads show the strongest similarities while the tails are more divergent [34]. As a result, the kinetic parameters of different kinesin subfamilies differ significantly. Among all kinesin motors velocity and processivity differ significantly. For ex-

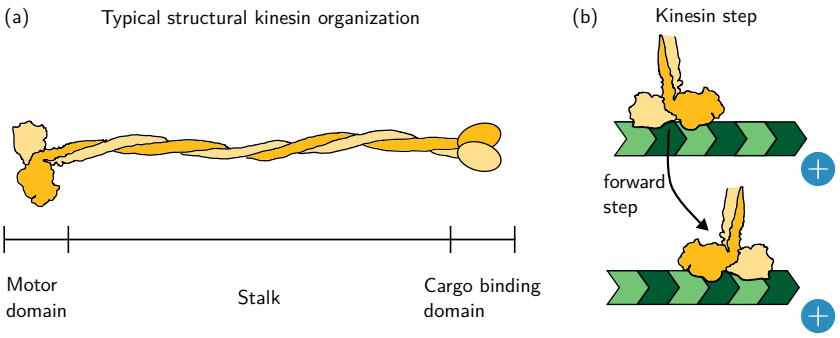

Figure 1.2: Sketch of kinesin motor. (a) Typical structural organization of a dimeric kinesin motor. It consist of a motor domain with two motor heads, which are connected to a cargo binding site through the coiled-coiled stalk. (b) Step-like directional movement of a kinesin motor on a microtubule protofilament. The two motor heads bind to distinct sites in the microtubule protofilament (α-tubulin light green and β-tubulin dark green). The illustration is schematic; the actual step can be split into several "substeps". See e.g. [34] for a detailed review.

ample kinesin-1 is fast ($0.9\,\mu m s^{-1}$) but has low processivity (run length before detaching $l_{run} \sim 1\,\mu m$) [151] and kinesin-8 is slow ($0.05\,\mu m s^{-1}$) in comparison and processive ($l_{run} \sim 10\,\mu m$) [152]. Others, such as members of the Kinesin-5 subfamily, can form tetramers with motor domains on both ends [34]. This enables them to crosslink and walk on two microtubules, ultimately resulting in filament sliding [95] (see Chapter 3 for further details). Throughout this thesis, we focus mainly on systems containing molecular motors from the kinesin family.

1.3.2. MICROTUBULE ASSOCIATED PROTEINS

Microtubule associated proteins can be loosely grouped by their activity class. Essential activities of MAPs are regulation of microtubule dynamics, regulation of microtubule number, linking microtubules to other cellular structures, and microtubule cross-linking. In the following, we will give a brief overview of those types of microtubule MAP interactions.

A large class of MAPs is involved in the regulation of microtubule dynamics. On a macroscopic level, microtubule dynamics can be described by four parameters: growth velocity, shrinkage velocity, and transition rates between growth and shrinkage (catastrophe and rescue rates). *In vivo* all of those rates are controlled by MAPs. Listing all of them goes beyond the scope of this introduction. A somewhat comprehensive review on the topic can be found in [153]. Some important MAPs controlling microtubule length are XMAP215 (growth), tau (shrinkage), MCAK (catastrophe), and CLASPs (rescue) [153]. What complicates the matter is that most of those proteins take dual roles when it comes to regulating the microtubule dynamics. As an example, XMAP215 does not only impact microtubule growth but was also shown to increase shrinkage [154]. Not only that it also cooperates with other MAPs, which changes the impact on microtubule dynamics again; in combination with the end tracking protein EB1, XMAP215 further increases growth velocity, but at the same time, the catastrophe frequency [155]. How the zoo of different MAPs cooperates to regulate microtubule dynamics remains a riddle up to date. Recently some progress has been made by systematically controlling the rates of microtubule dynamics at both ends (minus and plus end of the microtubule) by combining different MAPs [67].

An important class of length-regulating MAPs are so-called plus-end tracking proteins (plus end proteins). Members of this class of proteins are characterized by their ability to locate and track the microtubule plus end [32, 153]. Most plus-end proteins undergo an energy-consuming reaction when bound to the microtubule plus-end. Thus they drive the system out of thermal equilibrium even if their motion along the microtubule (e.g., the diffusive motion of XMAP215) does not require

ATPase activity [145].

MAPs control the number of microtubules through different types of activities. The most important one is microtubule nucleation. There are two major microtubule nucleation pathways. First, via microtubule organizing centers (MOCs) such as the centrosome [17, 156, 157]. Second microtubule branching, i.e., nucleation of microtubules from existing microtubules [17, 158–161]. Both pathways require interaction with MAPs. Important MAPs which are involved in the nucleation process are γ−tubulin, TPX2, and augmin [158, 160–163]. In addition, there are MAPs that play roles in polymerization kinetics and microtubule nucleation [164]. Microtubule severing is an additional pathway to control the number of microtubules which is also regulated by MAPs [165].

The third class of MAPs includes proteins that anchor microtubules to other cellular structures to promote cell organization [32, 36]. Many of those proteins are also plus-end tracking proteins [32]. One of their important tasks is, e.g., the anchoring of microtubules to the kinetochores.

Lastly, cross-linkers, such as proteins of the MAP65/Ase1/PCR1 family, bundle microtubules together to form a network [166]. Somewhat surprisingly, most microtubule stabilizers also show microtubule bundling activity [36].

Taken together, the zoo of different MAPs is overwhelming by its sheer number of proteins and functions. In addition, they do not appear isolated, e.g., most processes stated here are present in the mitotic spindle; see Fig. 1.3.

From a physicist's perspective, it makes sense to think about if the microtubule MAP interaction breaks detailed balance and, if yes, at which step. Besides of directed motion of molecular motors, there are other possibilities for how MAPs can break detailed balance to drive the microtubule ensemble out of equilibrium. One example is, e.g., the diffusion and capture mechanism proposed to localize proteins such as XMAP215 at the microtubule plus end [45, 145] and microtubule nucleation has been shown to depend on the nucleotide exchange of RAN-GTP [167, 168].

1.4. FILAMENT-PROTEIN INTERACTIONS

To highlight the diversity of filament-protein interactions, we would like to take the mitotic spindle as an exemplary example. The activity of microtubule-protein interactions is essential for the self-organization of the mitotic spindle. Using a full genome RNA interference (RNAi) allowed us to identify ~ 200 proteins essential for proper spindle assembly [24]. Their interaction with microtubules can be grouped into different classes; see Fig. 1.3. This includes proteins that control the number of spindle microtubules via nucleation [158, 169–171] and severing [172, 173]. Proteins which regulated the stability of microtubules [67, 143, 155, 174] and control their growth [57, 174] and shrinkage velocity.

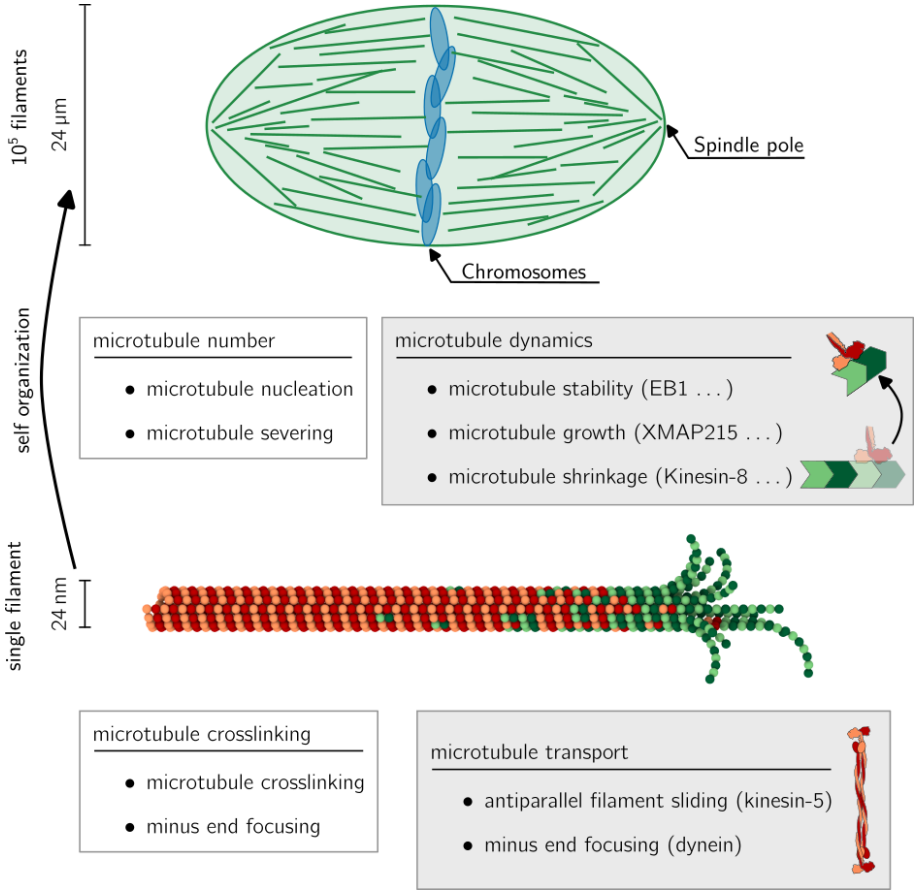

Figure 1.3: Protein-mediated regulation of spindle microtubules that lead to the self-organization of the mitotic spindle. The mitotic spindle is composed of ~ 10^5 filaments and 200 different associated protein types which have been found to be essential for proper spindle assembly and functionality [17, 19]. The interactions of those proteins with microtubules can be broadly grouped into four different classes. (1) Proteins that regulate the number of spindle microtubules through nucleation or severing. Examples are TPX2 (nucleation) [158, 161, 171] or active katanin (severing) [165]. Up and down regulation of those proteins plays an essential role in spindle scaling [53–56, 73]. (2) There exists a large number of proteins that regulate microtubule dynamics by influencing their growth and shrinkage velocity as well as catastrophe and rescue rate. Prominent examples are XMAP215 (up to 5-fold increase of growth velocity [60, 155]), members of the Kinesin-8 and Kinesin-13 family (regulation of catastrophe rate and shrinkage velocity [58, 59, 143, 175, 176]) and e.g. CLASP is involved in the regulation of rescues. See, e.g., [32, 33, 36, 137] for reviews on the topic. (3) Proteins cross-link microtubules along their lattice to form a network (e.g., PCR1) or are involved in focusing microtubule minus ends (e.g., NUMA). How all those proteins act together at the nanometer scale to self-organize into the mitotic spindle, which is a thousand times larger, is a question that is far from being answered. Filament-protein interactions studied in this work are highlighted in gray.

Molecular motors which arrange their spatial organization [14, 19, 34, 177] and cross-linking proteins which tethered microtubules to each other to form a network [178]. Listing all these proteins and their functionality goes way beyond the scope of this work; please refer to [17, 34, 36, 179] for a state-of-the-art review. While RNAi of individual MAPs or molecular motors allows us to identify their importance for spindle assembly by linking them to a whole phenotype of abnormal and dysfunctional spindles [24] it remains unclear why the knock-out of individual proteins leads to specific functional perturbations of the spindle. Moreover, there is increasing evidence that some

proteins do not have a single role in microtubule regulation but are involved in multiple processes. XMAP215, for example, is essential to regulate microtubule growth [60] but has also been shown to be involved in microtubule nucleation [164]. It is, therefore, often not even clear which loss in microtubule regulation causes the disruption in spindle self-organization.

In addition, sometimes, double inhibitions restore the spindle functionality. For example, the inhibition of kinesin-5, which is involved in microtubule transport, does lead to the formation of monopolar spindles [180–182] and the inhibition of dynein leads to unfocused spindles [183, 184]. However, double inhibition of kinesin-5 and dynein rescues spindle bipolarity [183, 184].

From a physicist's perspective, with the current knowledge, it remains illusive to understand how a large number of proteins act together with microtubules at the nanometer scale to assemble the mitotic spindle, which is three orders of magnitude larger and contains on the order of $\sim 10^5$ microtubules. An alternative approach is to focus on individual processes, such as regulation of microtubule dynamics or microtubule transport, and ask how they are reflected at a collective level. Thereby, we hope to understand key mechanisms that can drive self-organization in filament-motor mixtures. In this thesis, we are going to consider two mechanisms: First filament length regulation and second filament cross-linking and sliding; see Fig. 1.3. In the following, we will review key aspects of filament-protein interactions on a single filament level relevant to the work presented in this thesis.

1.4.1. FILAMENT LENGTH REGULATION

Microtubule dynamics change significantly throughout the cell cycle. For example, the kinetic parameters of interphase microtubules differ significantly from metaphase microtubules [174]. The change in microtubule dynamics often goes hand in hand with the up or down regulation of MAPs or molecular motors. In this section, we will review some key principles used by those proteins to regulate microtubule dynamics.

Irrespective if those proteins regulate microtubule growth, shrinkage, or catastrophe, they have in common that they have to reach the microtubule plus end (or minus end). To achieve this goal, those proteins use different strategies. This includes preferred attachment to the microtubule tip [32], directed motion along the microtubule [32, 58, 175], "hitchhiking" of molecular motors [32] or diffusion along the microtubule lattice [32, 59, 60]; see Fig. 1.4. Once the plus end is reached, they

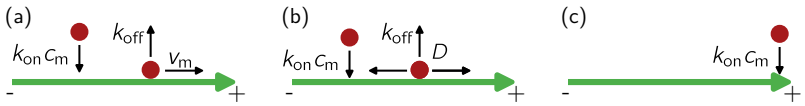

Figure 1.4: (a)-(c) Different interactions between MAPs/ molecular motors and filaments. All of them have in common that they attach to the filament from the cytosol and detach from the microtubule. But there are proteins that bind preferably to the filament tip (c). (a) Most molecular motors move directional towards the filament plus or minus end. (b) Others perform one-dimensional diffusion along the filament.

catalyze a corresponding reaction to control microtubule dynamics.

In this work, we focus on proteins that move directional towards the plus end. A representative member of this class of proteins is the molecular motor kinesin-8. *In vivo* it has been reported that kinesin-8 plays an essential role, e.g., spindle length regulation, proper positioning, and orientation of the spindle and chromosome segregation [185–189]; for a review see [152]. A significant contribution of kinesin-8 to these tasks is its ability to regulate microtubule length [152].

The capability of kinesin-8 to regulate microtubule length has been studied *in vitro* using single-molecule microscopy assays [58, 175]. In these studies, it has been shown that kinesin-8 moves unidirectional towards the filament plus end and barely detaches before reaching the plus end (run

length before detaching ~ 12µm). Upon reaching the microtubule plus end it catalyzed filament shrinkage of both GMPCPP and taxol stabilized microtubules [58]. Interestingly it has been found that the depolarization rate is length dependent, with longer filaments depolymerizing faster than short ones [58, 175]. This is facilitated by the directed motion and persistence of Kinesin-8 motors [42, 62, 175]. As Kinesin-8 driven length regulation will be an essential part of this thesis an introduction from a modeling perspective will be given in Chapter 3.

1.4.2. FILAMENT TRANSPORT

In the cell, microtubules move in order to form a specific spatial and orientational organization. This motion is generated by motor proteins that expend chemical energy to generate force [190, 191]. The directional movement of the motor proteins then helps to self-organize the microtubule network into a specific structure. There are different mechanisms of motor-based microtubule transport present in the cell. On a coarse level, we can classify them into microtubule transport along other structures, such as the cell cortex and sliding of microtubules along other microtubules [14]. Here we are interested in the relative sliding of microtubules, i.e., microtubule transport along other microtubules.

Both dynein and some members of the kinesin family are involved relative sliding of microtubules; see Fig. 1.5. In the following, we will discuss some of their key differences. Dynein has one motor

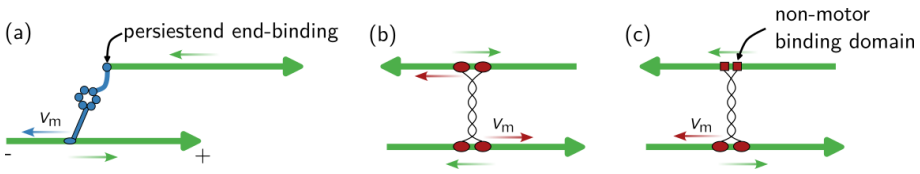

Figure 1.5: (a)-(c) Filaments (green) cross-linked by a motor protein. Filament direction is indicated in (a). Different types of motor proteins induce relative filament sliding. The direction of motion of the motors is indicated by arrows in the color of the motor and the resulting filament motion by green arrows. (a) Dynein motors (blue) move towards the microtubule minus-end, where they accumulate. Due to end dwelling dynein slides adjacent filaments irrespective of their relative orientation. (b) Kinesin-5 forms tetramers which have two motor domains. Thereby it can bind to and move on two neighboring filaments. Kinesin-5 shows no strong microtubule end accumulation. This yields distinct behavior for filaments oriented in the same (parallel) and opposite directions (anit-parallel). Anti-parallel filaments slide apart at $2v_m$, and parallel filaments do not move relative to each other. (c) Kinesin-1 and Kinesin-14 have only one motor domain and utilize a non-motor microtubule-binding domain to cross-link adjacent filaments and drive microtubule sliding. Here we depict Kinesin-14, which moves in the direction of microtubule minus ends.

domain that moves directional towards the minus end of microtubules where it accumulates [179, 192]. Together with dynactin, dynein forms the complex DDB, which is persistent (low detachment rate) [193]. *In vitro* it was observed that accumulations of dynein (more precisely DDB) at the minus end of a filament are able to generate a pulling force towards the minus end of an adjacent filament; see Fig. 1.5 (a) [193]. The minus end accumulation of dynein has been shown to drive robust filament sliding independent of the initial orientation of the filaments [193] and promotes minus end clustering; see Fig. 1.5 (a). In an ensemble of many filaments and dynein motors, this leads to the formation of microtubule asters, [193] and was shown to yield bulk contraction in millimeter-scale microtubule networks [194, 195]. In the spindle, dynein is essential for the proper formation of spindle poles [19].

In contrast to dynein, (most) kinesins move towards the plus end of microtubules. There are different kinesin motors involved in microtubule transport. One particularly important member is

Kinesin-5, which has two motor domains. This gives Kinesin-5 the ability to simultaneously bind to two microtubules and move on them [95]. The speed, v_m, at which the motor domains move towards the microtubule plus end was shown to depend on the load applied to the motor [191, 196]. In contrast to dynein, kinesin-5 shows no strong microtubule end accumulation. This yields distinct behavior for parallel and anti-parallel microtubules. If the microtubules cross-linked by a molecular motor are oriented in opposite directions (anti-parallel), the motor motion results in the sliding of the filaments in opposite directions; see Fig. 1.5 (b). In contrast, if the microtubules are oriented in the same direction, the filaments do not move relative to each other [95].

Other members from the kinesin superfamily, which are also involved in microtubule transport, are Kinesin-1 and Kinesin-14. In contrast to kinesin 5, both kinesin-1 and 14 have only one motor domain. They utilize a non-motor microtubule-binding domain to drive microtubule sliding; see Fig. 1.5 (c). In contrast to kinesin-5 and kinesin-1, kinesin-14 is a minus-end directed motor, therefore driving filament sliding in the direction of their plus ends [197].

Motor-mediated filament sliding will be an essential part of this thesis. An introduction from a modeling perspective will be therefore given in Chapter 3.

2

COLLECTIVE FILAMENT LENGTH REGULATION IN FILAMENT-MOTOR MIXTURES

2.1. BIOLOGICAL BACKGROUND

Microtubules are not static. In the living cell, they exhibit an ongoing cycle of growth, shortening, and regrowth - termed dynamic instability [136]. In different cell stages, the typical length of microtubules differs significantly, even within a single cell type and organism. As an example, microtubules found in Xenoupus interphase asters have an estimated mean length of $16\,\mu m - 20\,\mu m$ [116, 198] while microtubules in the metaphase spindle of Xenoupus have a mean length of $\sim 7\,\mu m$ [184]. Moreover, it has been shown that the spindle length scales with microtubule length [53]. To achieve this diverse behavior, microtubule dynamics is tightly regulated by a whole machinery of microtubule associated proteins (MAPs) [36]. The change in microtubule dynamics throughout the cell cycle and cell stages is tied to the up or down regulation of those proteins [56, 57, 69, 70, 73].

However, the measured kinetic parameters for growth, shrinkage, and the switching rates between the periods of growth and shrinkage do not only differ between cell stages and different phases of the cell cycle but also within the same organism, phase, and stage. As an example the measured growth rate of microtubules in interphase Xenopus egg extract ranges from $7\,\mu m\,min^{-1}$ to $30\,\mu m\,min^{-1}$ [116, 198–200]. How to explain this variety in measured rates is an open question puzzling the scientific community.

Recent experiments show increasing evidence that the local density of microtubules feedback's on their kinetic parameters. This could explain the previously scattered measurement data of e.g. growth rates as those measurements were not spatially resolved. New measurements show that the growth velocity [201], depolymerization velocity [200], and catastrophe frequency [202] of microtubules are functions of the local density of microtubules. One possible explanation of this observation would be that steric interactions between filaments impact their length regulation dynamics. Alternatively, a high local density of microtubules could deplete the local pool of available MAPs. By depleting the cytosolic pool of available MAPs the kinetic rates could be determined by local resource competition between filaments.

In this chapter, we will focus on the question of how the local availability of MAPs and/ or tubulin in combination with their spatial redistribution via cytosolic diffusion affects collective filament length regulation. How MAPs interact with microtubules that undergo dynamic instability is poorly understood [36, 137], making an explicit modeling approach illusive. We, therefore, focus on a minimal model of GMPCPP stabilized microtubules and molecular motors, which are capable of depolymerizing them. Specifically, we focus on resource-limited length regulation of stabilized microtubules by the kinesin-8 homolog Kip3 from *Saccharomyces cerevisiae*. The advantage of this system

is that it is well characterized and most kinetic rates are known from single filament experiments [58, 175]. In the following, I will present a minimal model to address the Kinesin-8 catalyzed microtubule depolymerization, first in the absence of resource limitation and later including resource limitation. Ideas presented here will be reused through the rest of this chapter.

2.1.1. MODELING APPROACH

To understand the length-dependent filament depolymerization of kinsin-8 motors we neglect possible correlations between neighboring protofilaments. This approximation allows us to model the microtubule by a single protofilament, i.e., an effectively one-dimensional structure of length ℓ; see Fig. 2.1. Cytosolic motors can bind along the protofilament at rate k_{on} (measured per volume concentration, per length, per time) and detach from the filament at the rate k_{off}. Kinesin-8 motors move directional along the arc length $s \in (0, \ell)$ of the protofilament with constant velocity v_{m} towards the plus-end, where they catalyze depolymerization at rate δ; see Fig. 2.1 (b). The length change of the filament is governed by

$$\partial_t l(t) = -v_{\mathrm{s}}(t) \tag{2.1}$$

where v_{s} denotes the shrinkage velocity of the filament. If we neglect spontaneous depolymerization, which has been shown to be slow for GMPCPP stabilized microtubules [60, 203], the shrinkage velocity is given by

$$v_{\mathrm{s}}(t) = a\delta\, m^{+}(t)\,. \tag{2.2}$$

Here $m^{+}(t)$ denotes the density of kinesin-8 motors at the plus end and a the length of a tubulin unit ($\sim 8\,\mathrm{nm}$). If we assume the motor dynamics to be fast as compared to the length change dynamics we can assume the motor dynamics on the filament to be in quasi steady state. Denoting the total number of motors bound to the filament by, M, and the cytosolic motor concentration by, c_{m}, we can derive the shrinkage velocity from a simple flux balance argument. The on-flux, j_{on}, of motors onto the filament is given by attachment events of motors $j_{\mathrm{on}} = k_{\mathrm{on}} c_{\mathrm{M}} l$. The off-flux, j_{off}, is given by detachment of motors $k_{\mathrm{off}} M$ *and* depolymerization events v_{s}/a, therefore $j_{\mathrm{off}} = k_{\mathrm{off}} M + v_{\mathrm{s}}/a$. In steady state the on-flux of motors has to be balanced by the off-flux, thereby we find the depolymerization velocity of filaments:

$$v_{\mathrm{s}} = a(k_{\mathrm{on}} c_{\mathrm{M}} l - k_{\mathrm{off}} M) \tag{2.3}$$

To obtain the filament bound motor number M we have to solve for the steady state motor density $m(s)$ on the filament. The governing equation is given by a combination of directed transport of motors to the plus end and Langmuir kinetics, where the motors attach from the cytosol at the rate $k_{\mathrm{on}} c_{\mathrm{m}}$ and detach at the rate k_{off}

$$0 = -v_{\mathrm{m}} \partial_s m(s) - k_{\mathrm{off}} m(s) + k_{\mathrm{on}} c_{\mathrm{M}}\,, \tag{2.4}$$

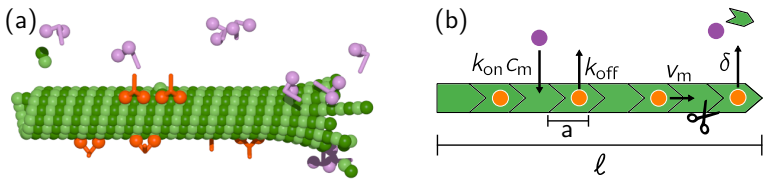

Figure 2.1: (a) Illustration of a microtubule interacting with molecular motors. Motors can be either cytosolic (purple) or filament bound (orange). (b) Schematic representation of the illustration in (a). The filament consists of discrete units of length a, has a total length ℓ, and has a direction (from minus to plus). Cytosolic motors attach to the filament at rate $k_{\mathrm{on}} c_{\mathrm{m}}$. Filament bound motors detach at rate k_{off} and move unidirectionally towards the filament plus end at a constant speed v_{m}. Motors at the filament plus end depolymerize the filament by one unit of length a.

Note here we neglected any stochastic and collective (e.g. steric exclusion) effects of the motor dynamics. Together with the boundary condition $m(0) = 0$ we find the steady state solution for the motor density profile

$$m(s) = \frac{k_{\text{on}} c_{\text{M}}}{v_{\text{m}}} l_{\text{run}} \left(1 - \mathrm{e}^{-s/l_{\text{run}}}\right) . \tag{2.5}$$

Here we introduced the typical run length of a motor before detaching from the microtubule $l_{\text{run}} = v_{\text{m}}/k_{\text{off}}$. Eq. 2.5 results in the so called antenna profile $m(s) \approx \frac{k_{\text{on}} c_{\text{M}}}{v_{\text{m}}} s$ for long run length $l_{\text{run}} \gg \ell$. Upon integration, we obtain the total number of bound motors M. Substitution into Eq. 2.3 yields the shrinkage velocity which is given by

$$v_{\text{s}} = a k_{\text{on}} c_{\text{M}} l_{\text{run}} \left(1 - \mathrm{e}^{-\ell/l_{\text{run}}}\right) = a k_{\text{on}} c_{\text{M}} \begin{cases} \ell & \ell \ll \ell_{\text{run}} \\ l_{\text{run}} & \ell \gg l_{\text{run}} . \end{cases} \tag{2.6}$$

The two limiting cases can intuitively be understood by the following argument: If the filament length is significantly smaller than the typical run length of kinesin-8 motors ($\ell \ll l_{\text{run}}$) almost all motors that attach to the filament reach the plus end. The contribution of detachment events to the off-flux j_{off} is then negligible $k_{\text{off}} M \approx 0$ and the shrinkage velocity equals the on-flux in quasi steady state; cf. Eq. 2.3. In contrast, if the filament is significantly longer than the typical run length ($l \gg l_{\text{run}}$) only motors that attach within the distance l_{run} from the filament plus end reach the tip and contribute to a shrinkage event. Motors that attach further apart detach before reaching the plus end. This prediction was experimentally tested by reducing the kinesin-8 run length. The theoretical result for the shrinkage velocity is in good agreement with the experiments by Varga et al. in a regime where the antenna profile is valid [175]. However, it should be noted that the minimal model presented here is not sufficient to account for the full dynamics observed by Varga et al. This is because the experiments were performed under conditions where motor crowding effects on the microtubule play an essential role in the depolymerization dynamics. A comprehensive theory taking motor crowding into account can be found in [44, 62] and is in good agreement with the full range of experimental observations.

In the remainder of this chapter, we will consider a model that considers a limited number of resources per microtubule. This is we consider a microtubule in a fixed volume V_0, that contains a total concentration, ρ_{T}, of tubulin dimers and, ρ_{M}, of motors. The microtubule, therefore, has access to a limited number of tubulin dimers, $\rho_{\text{T}} V_0$, and a limited number of motors $\rho_{\text{M}} V_0$. This imposes the additional constraint of mass conservation both on motors and tubulin dimers, which read

$$\begin{aligned} \rho_{\text{T}} V_0 &= c_{\text{T}} V_0 + \ell/a \\ \rho_{\text{M}} V_0 &= c_{\text{M}} V_0 + M . \end{aligned}$$

As we will see in the following this will have a major impact on the length regulation dynamics. In particular, if many filaments share a common pool of resources they can deplete.

In contrast to the experiment by Varga et al. motor crowding is not expected to play a significant role if limited resources and high microtubule densities are considered. This can be understood by a simple rule of thumb calculation: Varga et al. explicitly engineered their experimental setup to minimize sequestering effects of Kinesin-8 by the microtubules. This was done by using only a low density of microtubules with a volume $V_0 > 5 \times 10^5\,\mu\text{m}^3$ per microtubule (2 – 5 microtubules per $80\,\mu\text{m} \times 80\,\mu\text{m} \times 400\,\mu\text{m}$). At 1 nM Kinesin-8 this corresponds to $\sim 10^5$ motors per filament. A microtubule of length $l = 7\,\mu\text{m}$ has approximately $\sim 10^4$ tubulin heterodimers available as binding sites for Kinesin-8 motors. Comparing those numbers, 10^5 motors per microtubule, and 10^4 binding sites, make crowding effects on the microtubule possible (depending on the attachment and detachment rate).

In contrast *in vivo* the volume per microtubule can be estimated to be significantly lower. Its precise value depends on species and cell type. However, even if we take a large cell of diameter $\sim 200\,\mu m$ (e.g. early stage X.lavis cells) and $\sim 10^5$ microtubules present in the cell (as estimated for Xenopus spindles) we find a volume $V_0 \sim 10\,\mu m^3$ per microtubule. At 1 nM Kinesin-8 this leads to ~ 6 Kinesin-8 motors per microtubule. Compared to the $\sim 10^4$ binding sites of a microtubule (of length $l = 7\,\mu m$) crowding effects appear to be quite unlikely, even at high motor concentrations. Therefore, as long as the volume per microtubule is small enough and/or motor concentrations are low enough we can rely on the minimal model presented here which neglects interactions between motors. However, its validity should always be tested numerically taking steric interactions of motors into account.

2.2. LENGTH REGULATION DRIVES SELF-ORGANIZATION IN FILAMENT-MOTOR MIXTURES

2.2.1. SIGNIFICANCE

Cytoskeletal structures play essential roles in many cellular processes, including intracellular transport, cell division, and cell motility. The formation and regulation of these structures involve many types of proteins that associate with the cytoskeletal filaments to regulate their nucleation and polymerization, crosslink them, and exert mechanical forces on them. Past studies on the collective organization of many filaments have focused on the mechanical interactions between filaments and force-generating (cross-linking) motors. In contrast, studies on length regulation have exclusively focused on single filaments and have not addressed any collective effects.

Here, we study collective length regulation in a conceptual model for a filament-motor mixture. Importantly, we explicitly account for the diffusive redistribution of cytosolic tubulin units and depolymerizing motors. We derive a hydrodynamic description of the collective dynamics of tubulin, motors, and filaments. Employing a linear stability analysis, we discover a long wavelength spatial instability that is driven by diffusive redistribution of tubulin mass. These analytical investigations are complemented by agent-based simulations that account for the spatial extent of the filaments. These simulations show that the long wavelength instability leads to the formation of filament clusters with aster-like orientational order.

The instability mechanism we discover is operational in a large parameter regime, including physiological parameters. Indeed, our minimal model provides a possible mechanism underlying the striking microtubule self-organization in homogenized cell extracts observed in recent experiments [126]

2.2.2. PUBLICATION

This section is based on the publication

Length Regulation Drives Self-Organization in Filament-Motor Mixtures

by
M. Striebel[1,*], **F. Brauns**[1,*] **and E. Frey**[1,2]
[1] Arnold Sommerfeld Center for Theoretical Physics and Center for NanoScience, Department of Physics, Ludwig-Maximilians-Universität München, Theresienstrasse 37, D-80333 Munich, Germany
[2] Max Planck School Matter to Life, Hofgartenstraße 8, D-80539 Munich, Germany

Physical Review Letters **129**, 238102 (2022)

DOI: 10.1103/PhysRevLett.129.238102
Also available on arXiv: arXiv:2109.05091

Supplemental material: The supplemental material can be found in Sec. 2.5. Associated movies online

Author contributions: Fridjof Baruns and I contributed equally to this work. Fridjof Brauns, Erwin Frey and I conceptualized the study. Fridjof Brauns and I performed the analytic analysis. I performed numerical analysis, data analysis, and data visualization. Fridjof Brauns, Erwin Frey and I wrote the manuscript. Erwin Frey supervised the research.

Length Regulation Drives Self-Organization in Filament-Motor Mixtures

Abstract

Cytoskeletal networks form complex intracellular structures. Here we investigate a minimal model for filament-motor mixtures in which motors act as depolymerases and thereby regulate filament length. Combining agent-based simulations and hydrodynamic equations, we show that resource-limited length regulation drives the formation of filament clusters despite the absence of mechanical interactions between filaments. Even though the orientation of the individual remains fixed, collective filament orientation emerges in the clusters, aligned orthogonal to their interfaces.

The microtubule cytoskeleton plays an important role in numerous cellular functions such as intracellular transport and cell division [9, 204]. These complex processes are based on the active remodelling of the cytoskeletal structure [191], which is mediated by the interaction of microtubules with a variety of microtubule associated proteins (MAPs) [17, 34, 190]. In addition to generating forces between microtubules [177], MAPs play an important role in regulating the length of individual microtubules by affecting the rates of their polymerisation kinetics from tubulin subunits [31, 59, 60, 175]. How forces affect the large-scale self-organization of microtubules has been studied in detail both theoretically and experimentally [48, 74, 99, 177, 194, 205, 206]. In contrast, the role of length regulation has only been investigated in the context of individual filaments [42–44, 58–63], or of a globally accessible pool of constituents (tubulin and MAPs) [64, 65, 67, 116]. However, recently the focus of interest is shifting to their role in many filament systems, as there is increasing experimental evidence that this regulatory function, in combination with the local availability of MAPs and tubulin, plays an essential role in the self-organization, scaling and maintenance of microtubule structures [53, 57, 69–73]. It remains an important open question how the interplay and spatial redistribution of these resources through cytosolic diffusion and transport along microtubules affects the self-organization of the microtubule cytoskeleton [200–202, 207].

Here, we approach this question by studying the collective motor-filament dynamics with limited resources of tubulin units and molecular motors. These cytosolic resources are spatially redistributed by diffusion while filament-bound motors additionally move uni-directionally towards the filament plus-end where they act as depolymerases (Fig. 2.2). We show that the interplay of motor-catalyzed depolymerization and local resource availability leads to self-organization of the filament assembly into aster-like patterns. Those patterns show co-localisation of microtubule plus ends and polarity sorting at the interfaces of emerging filament clusters.

Model. — We propose an agent-based model that builds on current in vitro experiments and theoretical studies addressing the resource-limited length regulation of a single stabilized microtubule by the kinesin-8 homologue Kip3 from *Saccharomyces cerevisiae* [63]. Specifically, we study filament dynamics containing a finite number of tubulin units (N_T), molecular motors (N_M), and filaments (N_F); see Fig. 2.2(b). Each individual filament $i \in 1,\ldots,N_F$ is represented by a directed rigid rod with fixed minus-end position $\mathbf{b}_i$ and fixed orientation $\theta_i \in [0,2\pi)$, which are drawn randomly from uniform distributions. We have checked that diffusive motion of filaments does not affect the mechanism described here (see Supplementary Material Sec. IV and Movies 3-5) [208]. The lengths $l_i(t)$ of the individual filaments are dynamic variables that change by polymerization kinetics at the plus end. When filaments shrink to zero length, they are assumed to regrow form the same minus-end position and with the same orientation; filament shrinkage to zero length, though, rarely occurs. In the cytosol, both motors and tubulin units diffuse freely with diffusion constants D_M and D_T, respectively. Cytosolic motors can bind with rate k_on to any point that is within the binding radius r_M along a filament; for details see Supplemental Material Sec. SII [208]. Filament-bound motors

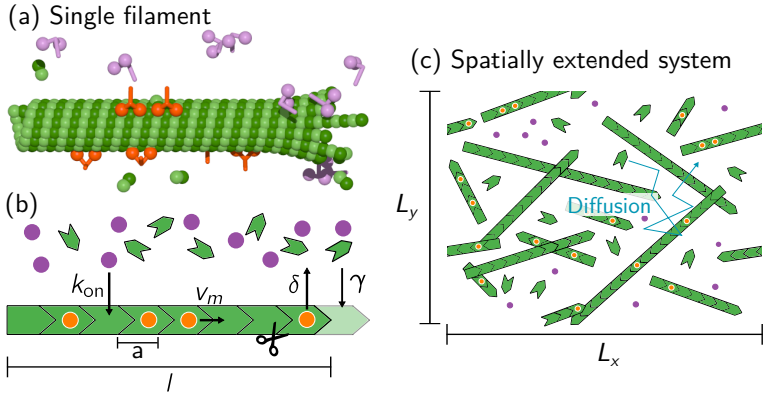

Figure 2.2: Agent-based model. (a) Illustration of a filament interacting with a finite amount of tubulin (green) and motor proteins. Motors can be either cytosolic (purple) or filament-bound (orange). (b) Model representation of a single protofilament. (c) Illustration of a filament-motor mixture in a box geometry with periodic boundary conditions.

move towards the filament plus-end at speed v_m, where they catalyse filament depolymerization at rate δ [see Fig. 2.2(b)]. Upon depolymerization, the filament length is reduced by one tubulin unit (of length a) and both the plus-end-bound motor and the associated tubulin unit are released into the cytosol As we consider stabilized microtubules no rapid depolymerization events upon microtubule catastrophes are considered here. Cytosolic tubulin within a distance r_T of a filament plus-end, binds to it at the rate γ, increasing filament length by a [Fig. 2.2(d)]. We implicitly assume fast tubulin nucleotide exchange by allowing for immediate reattachment of tubulin. Finite nucleotide exchange does not qualitatively change the results (see Supplementary Material Sec. V) [208].

Single-filament dynamics. — Consider a cytosolic volume V_0, containing a single filament and a finite number of tubulin units $\rho_T V_0$ and motor proteins $\rho_M V_0$. For now, we assume for simplicity that the cytosolic concentrations c_M and c_T are spatially uniform; this assumption is relaxed when we discuss a spatially extended system with many filaments. The length change of the filament is determined by the antagonism between polymerization and depolymerization kinetics $\partial_t l(t) = v_g - v_s$ with the growth and shrinkage velocity given by $v_g = a\, c_T\, \gamma$ and $v_s = a\, m^+(t)\, \delta$, respectively, where $m^+(t)$ denotes the density of motors bound to the plus end [44, 62].

For biologically relevant parameter ranges, the motor dynamics are fast compared to filament growth and shrinkage [63, 175]. This separation of time scales implies that for a given filament length, the motor density can be assumed to be in a quasi-steady state, where the total attachment flux of motors onto the filament, $j_{on} = k_{on}\, \tilde{c}_M\, l$, and the off-flux due to depolymerization events at the plus end, $j_{off} = \tilde{v}_s / a$, are in balance; quasi-steady states are indicated by a tilde. Thus, the depolymerization velocity $\tilde{v}_s = a\, k_{on}\, l\, \tilde{c}_M$ is determined by the cytosolic density $\tilde{c}_M$, which in turn is related to the filament-bound motor number $\tilde{M}$ via mass conservation $\rho_M V_0 = \tilde{c}_M V_0 + \tilde{M}$. In steady state, the filament-bound motor density exhibits an antenna profile $\tilde{m}(s) = \frac{k_{on}\tilde{c}_M}{v_m}\, s$ [1], which is inferred from the transport equation $\partial_t m(s,t) = -v_m \partial_s m(s,t) + k_{on} c_M(t)$ [209, 210], implying $\tilde{M} = \frac{k_{on}\tilde{c}_M}{2 v_m}\, l^2$. Combining the expression for the number of bound motors $\tilde{M}$ with mass conservation allows to express the shrinkage velocity in terms of the filament length and the total motor concentration ρ_M

$$\tilde{v}_s(l, \rho_M) = a\, k_{on}\, l\, \tilde{c}_M = a\, k_{on}\, l\, \frac{\rho_M}{1 + l^2/l_c^2}\,, \tag{2.7}$$

[1] Note the occupation density of motors at the filament plus-end is not equivalent to $\tilde{m}(l)$. The filament-bound motor density exhibits a boundary layer such that $v_m \tilde{m}(l) = a m^+ \delta$ [209],[210]

where we have defined the characteristic length scale $l_c := \sqrt{2\nu_m V_0/k_{on}}$. For filament lengths $l < l_c$, the shrinkage velocity increases with the filament length, as would be expected with unlimited motor resources and has been observed experimentally [58, 175]. At $l = l_c$ the number of cytosolic motors $c_M V_0$ equals the number of filament-bound motors $\tilde{M} = \frac{k_{on}\tilde{c}_M}{2\nu_m} l^2$. Increasing the filament length beyond l_c leads to a depletion of the cytosolic motor pool and thereby a decreased on-flux $k_{on}\tilde{c}_M l$. According to the flux balance condition, this reduces the off-flux $\tilde{v}_s/a$ and thus the shrinkage velocity, so that $\tilde{v}_s \sim 1/l$ for $l \gg l_c$ [see Fig. 2.3(a)].

The growth velocity v_g can be written in terms of filament length l and total tubulin density ρ_T using tubulin mass conservation ($\rho_T V_0 = c_T V_0 + l/a$) as $v_g(l, \rho_T) = \gamma(\rho_T a - l/V_0)$. At steady state the filament growth and shrinkage velocity are balanced, $v_g(l, \rho_T) = \tilde{v}_s(l, \rho_M)$, which determines the steady state length $l^*(\rho_T, \rho_M)$ [Fig. 2.3(a)] [2].

Self-organization in a spatially extended system. — How does the length regulation of individual filaments play out in a spatially extended system where resources are shared by cytosolic diffusion between many filaments? In the limiting case where the cytosolic concentration is slowly varying on the scale of the (typical) filament length, the filaments can be treated as point-like objects carrying a tubulin mass proportional to their length $l(\mathbf{x}, t)$. The single filament dynamics can then immediately be generalized to a local length regulation dynamics

$$\partial_t l(\mathbf{x}, t) = a\gamma c_T(\mathbf{x}, t) - \tilde{v}_s(\mathbf{x}, t)\,, \tag{2.8}$$

with the local shrinkage speed given in terms of the local quasi-steady state approximation for the cytosolic motor density, $\tilde{v}_s(\mathbf{x}, t) = a k_{on} l(\mathbf{x}, t)\tilde{c}_M[l(\mathbf{x}, t), \rho_M(\mathbf{x}, t)]$ (cf. Eq. 2.7). The dynamics of the cytosolic tubulin concentration is governed by a reaction-diffusion equation

$$\partial_t c_T(\mathbf{x}, t) = D_T \nabla^2 c_T(\mathbf{x}, t) - \frac{\gamma c_T(\mathbf{x}, t) - \tilde{v}_s(\mathbf{x}, t)/a}{V_0}\,, \tag{2.9}$$

where the local polymerization kinetics induces sinks and sources of cytosolic tubulin; here $V_0 = V/N_F$ denotes the cytosolic volume associated with a single filament. The total motor density is redistributed by cytosolic diffusion

$$\partial_t \rho_M(\mathbf{x}, t) = D_M \nabla^2 \tilde{c}_M[l(\mathbf{x}, t), \rho_M(\mathbf{x}, t)]\,, \tag{2.10}$$

where we again used the local quasi-steady state approximation for the cytosolic motor density $\tilde{c}_M(\mathbf{x}, t)$. Taken together, Eqs. (2.8)–(2.10) form a closed set governing the system's dynamics in the long-wavelength limit.

[2] Depending on the functional form of the shrinkage velocity $\tilde{v}_s(l)$ the dynamics is either monostable with a single steady state length or bistable; see Supplemental Material Sec. SIV for details [208].

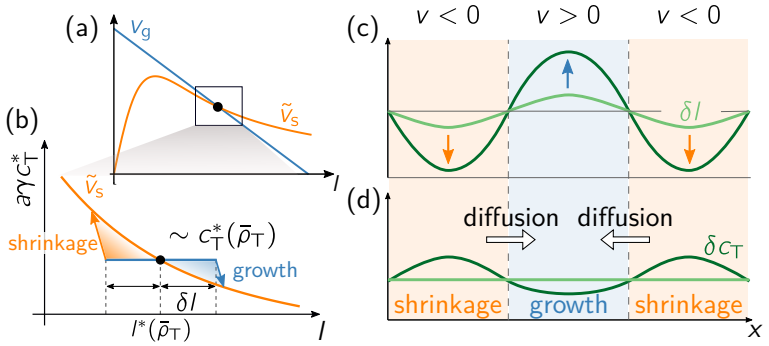

Figure 2.3: (a) Shrinkage velocity $\tilde{v}_s$ and growth velocity v_g as a function of the filament length l with the steady state length l^* determined by the intersection point(s) of v_g and $\tilde{v}_s$. (b)-(d) Graphical analysis of the lateral instability.

The stability of a spatially uniform state $(l^*, c_T^*, \bar{\rho}_M)$ against spatial perturbations can be studied using a linear stability analysis (see Supplemental Material Sec. SIV for details [208]). Figure 2.4 shows a typical dispersion relation $\sigma(q)$ for the eigenvalue with the largest real part and the ensuing stability diagram as a function of $\bar{\rho}_M$ and $\bar{\rho}_T$. For $\bar{\rho}_T > \bar{\rho}_T^{crit}(\bar{\rho}_M)$ there is a band of unstable Fourier modes $q \in (0, q_{max})$ extending to long wavelengths ($q \to 0$). It is instructive to first consider the particular limit of well-mixed cytosolic tubulin. Then, the marginal mode q_{max} reduces to $q_{max}^2 = -\rho_M \partial_l \tilde{v}_s|_{l^*}/(D_M \tilde{c}_M)$. This implies that there is an instability against spatial perturbations (lateral instability) only if $\partial_l \tilde{v}_s|_{l^*} < 0$. Moreover, the band of unstable modes narrows with increasing D_M, showing that cytosolic motor diffusion attenuates the lateral instability. Relaxing the assumption of well-mixed cytosolic tubulin, i.e., explicitly accounting for tubulin diffusion, yields the critical ratio of diffusion constants $D_T^{crit}/D_M \approx \gamma/(a k_{on} V_0 \bar{\rho}_M)$ in the limit $l^* \gg l_c$. For physiological parameters, we find that the there is a lateral instability if the average number of motors per filament satisfies $\bar{\rho}_M^{crit} V_0 > 0.57\, D_M/D_T$. This condition is well met for biologically relevant motor concentrations as $D_M/D_T \sim 1/6$ (see Supplemental Material Sec. SI [208]).

The feedback mechanism underlying the lateral instability can be explained in terms of a mass-redistribution instability [211–213]. To simplify the argument, we set $D_M = 0$ for the moment so that the total motor density remains invariant under the dynamics and therefore spatially uniform $\rho_M = \bar{\rho}_M$, cf. Eq. (2.10). Consider now a small perturbation $\delta l(\mathbf{x})$ added to the homogeneous state l^*, while keeping the cytosolic tubulin concentration $c_T(\mathbf{x}) = c_T^*$ initially constant [Fig. 2.3(b,c)]. Since then $v_g = a\gamma c_T$ initially remains uniform, the effect of $\delta l(\mathbf{x})$ on the net growth velocity $v = v_g - \tilde{v}_s$ depends on the slope of the shrinkage velocity at l^*. For $\partial_l \tilde{v}_s|_{l^*} < 0$, filaments grow (shrink) when they are long (short). This leads to an decrease (increase) of the cytosolic tubulin concentration [arrows in Fig. 2.3(b,c)] creating gradients in the cytosolic tubulin concentration that drive diffusive transport of tubulin mass towards regions of increased filament length. Since this tubulin mass redistribution leads to an increase of v_g in regions where $\delta l > 0$, it promotes further filament growth there, i.e., the initial spatial perturbation $\delta l(\mathbf{x})$ is amplified [Fig. 2.3(b)]. In contrast, if the regulatory kinetics is such that the shrinkage velocity increases with filament length ($\partial_l \tilde{v}_s|_{l^*} > 0$), the effect is opposite. Cytosolic tubulin diffusion then redistributes the tubulin mass to regions with shorter filaments, counteracting the original disruption. Taken together, one finds the condition $\partial_l \tilde{v}_s|_{l^*} < 0$ for a spatial instability that is driven by free tubulin diffusion, in accordance with the result of the linear stability analysis.

The above reasoning also explains why cytosolic diffusion of motor proteins mitigates the lateral instability. Regions with short filaments contain fewer binding sites for motors and thus the cytosolic motor concentration is high there. The opposite holds for regions with long filaments. This creates gradients, and thereby diffusive fluxes, of motors towards regions of long filaments. The

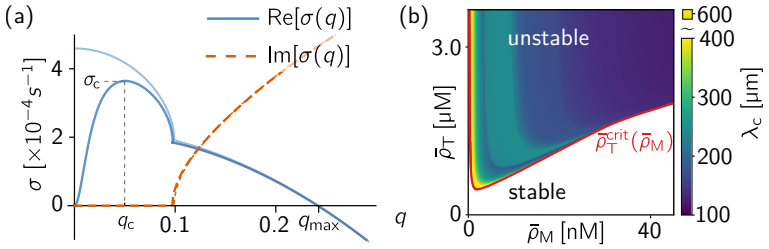

Figure 2.4: (a) Leading eigenvalue in the dispersion relation $\sigma(q)$ for $\bar{\rho}_M = 50\,\text{nM}$, $\bar{\rho}_T = 2.75\,\mu\text{M}$, $D_M = 0.5\,\mu\text{m}^2\text{s}^{-1}$ and $D_T = 6\,\mu\text{m}^2\text{s}^{-1}$; other parameters are specified in the Supplemental Material Sec. SI [208]. The dispersion relation in the limit of well-mixed cytosolic tubulin is shown in light blue. (b) Stability diagram and wavelength of the fastest growing mode q_c in the $(\bar{\rho}_M, \bar{\rho}_T)$-parameter space. The boundary of the laterally stable parameter regime, $\bar{\rho}_T^{crit}(\bar{\rho}_M)$, is shown in red.

resulting diffusive influx of motors increases the rate of filament depolymerization there and thus counteracts the instability driven by tubulin diffusion.

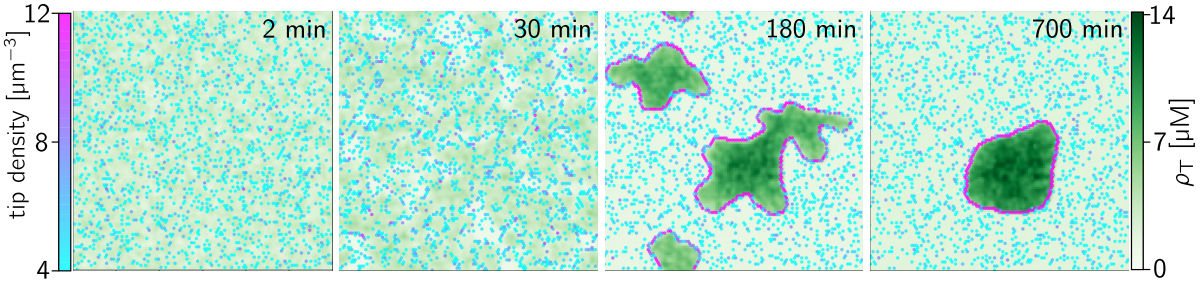

Figure 2.5: Snapshots of the total tubulin density $\rho_T(\mathbf{x}, t)$ and the tip density. Parameters are as in Fig. 2.4(a); $L_x = L_y = 150\,\mu m$.

Agent-based simulations. — To study the spatio-temporal dynamics above the critical tubulin concentration $\bar{\rho}_T^{crit}(\bar{\rho}_M)$ we perform agent-based simulations. While Eqs. (2.8)–(2.10) capture well the initial dynamics at the long-wavelength instability, they fail to give the correct dynamics once gradients begin to emerge at the small length scales (see Supplemental Material Sec. SIV [208]). What this continuum theory lacks are effects due the spatial extent of the filaments which includes motor binding along the length of filaments as well as motion of each filament plus-end due to polymerization kinetics.

Figure 2.5 shows a time sequence obtained from the simulations (see also Movie 1). First, regions with short (depletion zones) and long (clusters) filaments are formed, which corresponds to the initial dynamics described by the mass redistribution instability (Fig. 2.5, $t = 30\,min$). Moreover, filament plus-ends start to accumulate at the interface between these zones. As the dynamics progresses, the depletion zones grow in size and the interfaces sharpen (Fig. 2.5, $t = 60\,min$). At this time point, the filament-length distributions match on a qualitative level with experimental measurements [63] (see Supplemental Material Sec. SIII [208]). Subsequently, the high density regions segregate into individual large scale filament clusters, which are characterized by sharp boundaries and strong co-localization of filament plus-ends at their periphery (Fig. 2.5, $t = 180\,min$). This co-localization is caused by the movement of the filaments' plus-end due to polymerization dynamics that is directed to zones where the net growth rate changes sign, namely cluster interfaces. In the long run, the large filament clusters grow at the expense of the smaller ones, until eventually only a single cluster remains, which then develops into an aster-like structure (Fig. 2.5, $t = 700\,min$).

Inside the clusters, the filaments exhibit net polar order that is aligned along tubulin-density gradients, i.e., orthogonal to the cluster boundaries. This is because the plus ends localized there belong predominantly to filaments whose minus end lies within the cluster's interior, implying an orientation orthogonal to the boundary on average (see Fig. 2.6 and Movie 2).

To quantify this effect, we monitor the density gradient $\nabla\rho_T$, the local net polarity $\mathbf{p}$, and the angle θ enclosed between these vectors. Figure 2.6(d) shows the time evolution of the histogram $\mathscr{P}(\theta)$ of the angle θ weighted by the product of the magnitudes of $\nabla\rho_T$ and $\mathbf{p}$ to highlight the alignment of filaments near the cluster boundaries. The initially uniform distribution $\mathscr{P}(\theta)$ evolves quickly into a peaked distribution centered around zero—indicating the onset of polar order—and subsequently sharpens slowly; see also snapshots in insets of Fig. 2.6(a). The onset of this polar order occurs simultaneously with the mass-redistribution instability, as can be seen from the comparison of the spatial averages $\langle \mathbf{p} \cdot \nabla\rho_T \rangle$ and $\langle |\nabla\rho_T|^2 \rangle$, which are coarse-grained measures of filament orientation and density gradients, respectively; Fig. 2.6(e).

The polar order leads to advective flow of filament-bound motors out of clusters, which is balanced against diffusive influx caused by gradients in cytosolic motor concentration [see Fig. 2.6(c)]. Fast binding of motors inside clusters together with advective motor transport leads to the depletion

of motors in the cluster interior and the formation of sharp gradients in cytosolic motor concentration. Those gradients help to maintain the filament plus-end localization at the interfaces: Plus ends that protrude beyond the interface are subjected to an increased on-flux of motors, causing the filaments to shrink back. Conversely, plus-ends within the cluster are subjected to a reduced motor on-flux, causing them to grow towards the interface. Finally, the sharp cytosolic gradient leads to a shrinkage velocity $\tilde{v}_s$ that is independent of filament length because motor attachment occurs only in a narrow band at the interface. This is a collective effect and in contrast to the length regulation of a single filament, which is strongly length-dependent [cf. Eq. (2.7)]. The size regulation of clusters and a quantitative analysis of the final, aster-like, stationary state will be presented in a forthcoming publication [214].

Discussion. — Commonly, the spatial self-organization of cytoskeletal filaments is attributed to motor proteins that reorient and move filaments by mechanical forces, such as dynein or kinesin-5 [2, 99, 177, 193]. Here, we have shown that microtubule length regulation (through kinesin-8) in combination with resource limitation can lead to aster-like spatial patterns. The underlying instability is driven by diffusive redistribution of cytosolic tubulin mass. While we studied a minimal model for stabilized microtubules in an in vitro setting here, we expect that this instability mechanism could also operate in living cells or cell extracts. It has been estimated that up to 60% of the available tubulin heterodimers are used up during the formation of the mitotic spindle [215, 216]. Moreover, length-dependent polymerization kinetics has been observed for non-stabilized microtubules [143]. Those observations — resource limitation and a length-dependent feedback mechanism — are the general requirements for the mass-redistribution instability discussed here. In general we, we expect that the mechanism described here can play a role when tubulin as well as MAPs are limited. The pattern-forming instability we have discovered is also a potential candidate to explain the emergent self-organization observed in cell extracts [126]. Notably, this self-organization is heralded by spatial patterns that emerge in the tubulin density, which have compa-

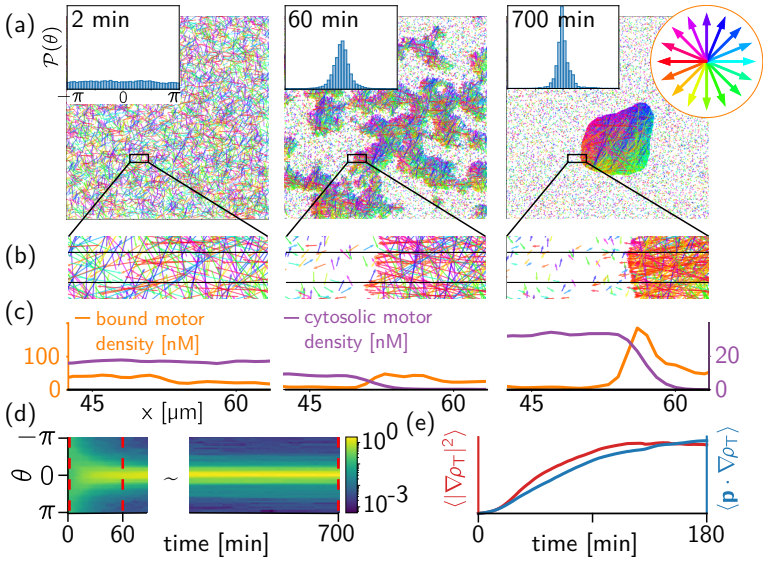

Figure 2.6: (a) Snapshots of filament arrangement in Fig. 2.5. Filaments are color coded according to their orientation (color wheel); insets show the weighted distribution $\mathscr{P}(\theta)$. (b) Zoom into a structure interface. (c) Filament-bound (orange) and cytosolic (purple) motor concentration averaged along the vertical direction for the area enclosed by the black windows in (b). (d) Kymograph of $\mathscr{P}(\theta)$ with the (logarithmic) color scale showing the normalized (by area) frequency of the measured angles; the dashed, red lines correspond to the insets in (a). (e) Time trace of $\langle \mathbf{p}\cdot\nabla\rho_T\rangle$ and $\langle|\nabla\rho_T|^2\rangle$ (ordinate in a.u.).

rable morphology and wavelength (~ 100 μm) as those we observe in our simulations (cf. Fig. 2.5). We also expect that our theory for resource-limited filament length regulation can be used to investigate heterogeneous growth dynamics in systems where spatial heterogeneities in filament length and/or density are imposed, e.g. by experimental design [201] or by upstream gradients [168, 217]. From a broader perspective, the conceptual model investigated here is in itself an interesting active matter system exhibiting self-organized patterns, polarity sorting, and coarsening. Such collective filament organization is usually attributed to the mechanical interaction of filaments [75, 194, 218–220]. Investigating how mechanical interaction and length regulation work together will be an important starting point for further research.

2.3. FILAMENT BUNDLE FORMATION AND POLARITY SORTING TROUGH LENGTH REGULATION

2.3.1. SIGNIFICANCE

This section is an extension of the work presented in Sec. 2.2. We will repeat some of the previous arguments but not all to reduce redundancy.

Here we study a minimal one-dimensional version of the model discussed in Sec. 2.2. In particular, we aim to go beyond the point-like filament approximation used in Sec. 2.2 and take the spatial extent of filaments into account. Based on a systematically coarse-grained hydrodynamic field theory, we seek to understand length-regulated polarity sorting of filaments. Moreover, we include filament diffusion, which has been neglected previously. Upon including filament diffusion, the emerging long-term dynamics shows additional interesting emergent phenomena like coalescence of filament bundles, symmetry breaking of bundle polarity, and traveling wave solutions of filament bundles. All are driven by length regulation, in the absence of mechanical interactions of filaments. I did not explore those phenomena to the last detail. Here, I discuss the long-term dynamics on a rather phenomenological level. From my perspective, the exciting aspect is that polarity sorting, coarsening, and coalescence of microtubule structures are all observed experimentally. However, all of those effects are usually attributed to mechanical interactions between filaments. While this is possibly true in most biological cases, the scientific community widely overlooks the pathway to aster formation, coarsening, and coalescence discussed here.

2.3.2. RESULTS

BIOPHYSICAL MODEL

We propose an agent-based model that builds on our previous studies addressing the resource-limited length regulation of microtubules by the kinesin-8 homolog Kip3 from *Saccharomyces cerevisiae* in a two-dimensional confined volume [1]. In order to study the essential (bio-)physical processes in the system, we further restrict our analysis to a quasi-one-dimensional slab geometry of extend L with periodic boundary conditions, containing a finite number of tubulin units (N_T), molecular motors (N_M) and filaments (N_Mt). Each individual filament $i = 1,\dots,N_\mathrm{Mt}$ is either left ($-$) or right ($+$) oriented (see Fig. 2.7(d)). The length $l_i(t)$ of the individual filaments are dynamic variables and change by polymerization kinetics at the plus-end. We account for fluctuations in the system by an effective length dependent filament diffusion coefficient $D_\mathrm{Mt}(l)$. When filaments shrink to zero length, they are assumed to regrow from the same nucleator with the same orientation; filament shrinkage to zero length, though, rarely occurs. In the cytosol, both motors and tubulin units diffuse freely with diffusion constants D_M and D_T, respectively. Cytosolic motors can bind with rate k_on to any point that is within the binding radius r_M along a filament. Filament-bound motors move towards the filament plus-end at speed v_m, where they catalyze filament depolymerization at rate δ [see Fig. 2.7(b)]. Upon depolymerization, the filament length is reduced by one tubulin unit (of length a), and both the plus-end-bound motor and the associated tubulin unit are released into the cytosol. As we consider stabilized microtubules, no rapid depolymerization events upon microtubule catastrophes are considered here. Cytosolic tubulin within a distance r_T of a filament plus-end binds to it at the rate γ, increasing filament length by a [Fig. 2.7(b)]. For an assessment of the model parameters, see Supplementary Sec. 2.5.

RESULTS

SINGLE FILAMENT DYNAMICS

Let us first consider the minimal setting of a single filament in a small cytosolic volume V_0 with a finite number of tubulin units $\rho_\mathrm{T}V_0$ and motors $\rho_\mathrm{M}V_0$. For now, we assume for simplicity that the cytosolic concentrations c_M and c_T are spatially uniform. This assumption will be relaxed later when

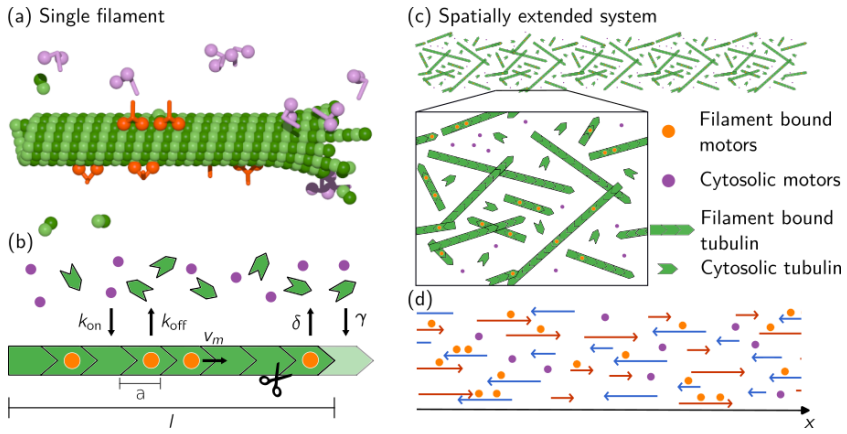

Figure 2.7: (a) Cartoon of a filament interacting with a finite amount of resources. Tubulin is shown in green, filament-bound motors in orange, and free motors in purple. (b) Model representation of the illustration shown above. Motors attach from the cytosol at rate k_{on}. filament-bound motors move towards the filament plus-end at speed v_{m} and detach at rate k_{off}. Motors bound to the filament plus-end catalyze depolymerization at rate δ (c) Two-dimensional representation of a filament arrangement in a finite volume V. (d) Schematic representation of the minimal one-dimensional model system. Filaments can be either left (blue) or right (red) oriented.

we study spatially extended systems and explicitly account for cytosolic gradients on the scale of the filament length.

The length change of a single filament is determined by the antagonism between polymerization and depolymerization kinetics (Fig. 2.7(b))

$$\partial_t l = v_{\mathrm{g}} - v_{\mathrm{s}} \,. \tag{2.11}$$

The polymerisation (growth) velocity v_{g} is given by the available cytosolic tubulin concentration c_{T} and the polymarization rate γ,

$$v_{\mathrm{g}} = a\gamma\, c_{\mathrm{T}} \,. \tag{2.12}$$

The depolymerization (shrinkage) of the filament is driven by motors bound to the filament tip, where they act as depolymerases and catalyze shrinkage at a rate δ,

$$v_{\mathrm{s}} = a\delta\, m^{+}(t) \,. \tag{2.13}$$

Here m^{+} is the density of motors at the filament tip. For biologically relevant parameters, the motor dynamics is fast compared to the filament dynamics. This separation of timescales allows us to treat the motor dynamics in a quasi-steady state. In the following, we will denote quasi-steady state quantities by a tilde. In steady state, the total attachment flux onto the filament $j_{\mathrm{on}} = k_{\mathrm{on}}\tilde{c}_{\mathrm{M}} l$ has to be balanced by the off flux from the filament by detachment and depolymerization $j_{\mathrm{off}} = k_{\mathrm{off}}\tilde{M} + \tilde{v}_{\mathrm{s}}/a$. Thus the depolymerization velocity is determined by the cytosolic motor density $\tilde{c}_{\mathrm{M}}$ and the filament-bound motor number $\tilde{M}$

$$\tilde{v}_{\mathrm{s}} = a(k_{\mathrm{on}}\tilde{c}_{\mathrm{M}} l - k_{\mathrm{off}}\tilde{M}) \,. \tag{2.14}$$

The filament-bound motor number $\tilde{M}$ and the cytosolic motor number $\tilde{c}_{\mathrm{M}}$ are related through mass-conservation

$$\rho_{\mathrm{M}} V_0 = \tilde{c}_{\mathrm{M}} V_0 + \tilde{M} \tag{2.15}$$

The dynamics of the motors on the filament is a combination of transport with constant velocity v_{m} towards the plus-end and Langmuir kinetics, where the motors attach from the cytosol at the rate

k_{on} and detach at the rate k_{off} [209, 210]

$$\partial_t m(s,t) = -v_m \partial_s m(s,t) + k_{on} c_M(t) - k_{off} m(s,t)\,. \tag{2.16}$$

where s denotes the arc-length along the contour of the filament. Since we are interested in the low density regime, we have neglected effects due to steric exclusions; for the relevance of the latter for length regulation, please refer to [44, 62]. In quasi-steady state, this transport equation is solved by $m(s) = \frac{k_{on}}{k_{off}} \tilde{c}_M (1 - e^{-s/l_{run}})$ with the typical run length $l_{run} = v_m / k_{off}$ of the motor. This implies a total number of filament-bound motors

$$\tilde{M} = \frac{k_{on} \tilde{c}_M}{k_{off}} \left[l - l_{run}(1 - e^{-l/l_{run}}) \right]. \tag{2.17}$$

Equations 2.14, 2.15 and 2.17 allow us to express the shrinkage velocity in terms of the total motor density ρ_M and the filament length

$$\tilde{v}_s(l, \rho_M) = a k_{on} \rho_M \frac{l_{run}(1 - e^{-l/l_{run}})}{1 + 2\frac{l_{run}}{l_c^2}\left[l - l_{run}(1 - e^{-l/l_{run}}) \right]}, \tag{2.18}$$

where we have defined the characteristic length scale

$$l_c = \sqrt{\frac{2 v_m V_0}{k_{on}}}\,. \tag{2.19}$$

An intuitive interpretation of the characteristic length l_c can be obtained in the limit of persistent motors; $l_{run} \to \infty$. In this limit, l_c corresponds to the filament length where the number of filament-bound motors $\tilde{M}$ equals the number of cytosolic motors $\tilde{c}_M V_0$. For small filament length, $l \ll l_c$, the shrinkage velocity increases linear, $\tilde{v}_s \sim l$, as would be expected with unlimited motor resources and has been observed experimentally [58, 175]. In contrast, for large filament length, $l \gg l_c$, the shrinkage velocity behaves as $\tilde{v}_s \sim 1/l$. Together, this gives the characteristic hump shape of $\tilde{v}_s(l)$; see Fig. 2.8 (a). Finally, using tubulin mass-conservation

$$\rho_T V_0 = c_T V_0 + l/a\,, \tag{2.20}$$

we can express the growth velocity (Eq.2.12) in terms of the total tubulin concentration ρ_T and the filament length l

$$v_g(l, \rho_T) = a\gamma \left(\rho_T - \frac{l}{a V_0} \right). \tag{2.21}$$

Combining the expressions for the growth and shrinkage speed, we obtain a closed equation for the filament length $\partial_t l(t) = v_g(l, \rho_T) - \tilde{v}_s(l, \rho_M)$. For given kinetic constants, the control parameters of the filament dynamics are the total densities of tubulin (ρ_T) and of motors (ρ_M). At steady state, the growth and shrinkage velocities balance $v_g(l^*, \rho_T) = \tilde{v}_s(l^*, \rho_M)$, and one obtains the steady-state filament length $l^*(\rho_M, \rho_T)$; see Fig. 2.8 (a),(b). In the parameter plane of total densities, we find a regime of bistability where two stable steady-state filament lengths exist; see Fig. 2.8 (c). This regime is determined by the parameter range where the shrinkage velocity $\tilde{v}_s$ and the growth velocity v_g have three intersection points. This means, the region of bistability is delimited by lines along which the curve $\tilde{v}_s(l^*, \rho_M)$ is tangential to $v_g(l^*, \rho_T)$; $\partial_l \tilde{v}_s(l^*, \rho_M) = -\gamma/(a V_0)$ (see Fig. 2.8 (b),(c)). Such bistability was recently observed experimentally [63].

For a wide (biologically relevant) parameter range, the motor run length l_{run} does not change the results on a qualitative level. We, therefore, restrict our analysis to persistent ($l_{run} \to \infty$) motors in the following. In this limit, the shrinkage velocity $\tilde{v}_s$ reduces to the simpler form

$$\tilde{v}_s(l, \rho_M) = a k_{on} \rho_M l \tilde{c}_M = a k_{on} \rho_M \frac{l}{1 + (l/l_c)^2} \tag{2.22}$$

and the motor density exhibits a simple antenna profile along the microtubule $\tilde{m}(s) = (k_{on} \tilde{c}_M / v_m) s$.

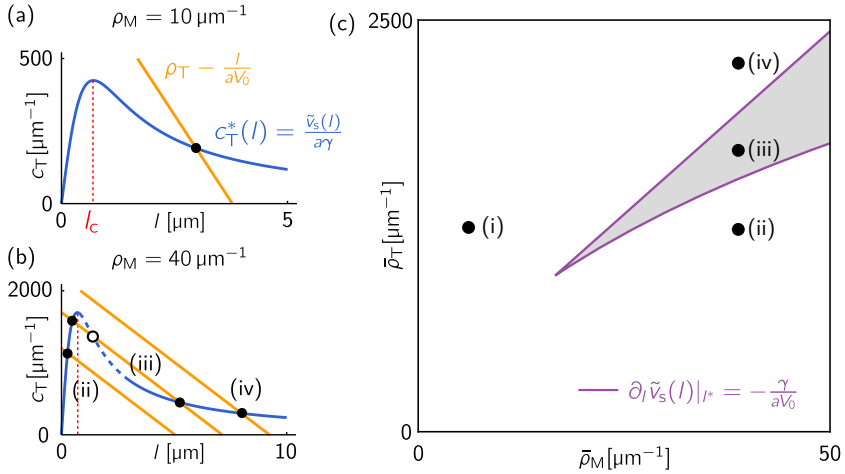

Figure 2.8: (a),(b) Graphical construction of the steady state solution (c_T^*, l^*). Here we used $k_{off} = 0$. steady states are given by the intersection point of the nullcline $a\gamma c_T* = v_s(\rho_M, l^*)$ (blue) and the mass conservation constraint $\rho_T V_0 = l/a + c_T V_0$ (orange). The characteristic length l_c is shown in red. For $k_{off} = 0$, it marks the apex of the nullcline. For low motor concentrations $\rho_M\, \partial_l \tilde{v}_s(l^*, \rho_M) > -\gamma/(aV_0)$ and there exists only one stable fixed point of the reaction dynamics. As the total motor concentration is increased, we find a bistable parameter regime. the region of bistability is delimited by lines along which the curve $\tilde{v}_s(l^*, \rho_M)$ is tangential to $v_g(l^*, \rho_T)$; $\partial_l \tilde{v}_s(l^*, \rho_M) = -\gamma/(aV_0)$. (c) Stability diagram of the length regulation kinetics. Parameters are as given in Sec. 2.5, here we choose $k_{off} = 0$.

COLLECTIVE FILAMENT DYNAMICS IN A SPATIALLY EXTENDED SYSTEM

On the continuum level, the system dynamics is characterized by the cytosolic tubulin concentration $c_T(x,t)$, the cytosolic motor concentration $\tilde{c}_M(x,t)$, and the filament plus-end density $\rho_\pm(x,l,t)$ of left (−) and right (+) pointing filaments of length l at the spatial position x at time t. To simplify notation, we omit the time dependence in the following. The length regulation dynamics of filaments yield an advective flux at speed $v_\pm(x,l) = v_g(x) - \tilde{v}_s(x,l)$ of filament tips both in the spatial and in length domain. Together with length-dependent filament diffusion, the time evolution of filament plus-ends is captured by

$$\begin{aligned}\partial_t \rho_\pm(x,l) = D_{Mt}(l)\partial_x^2 \rho_\pm(x,l) \\ \mp \partial_x[v_\pm(x,l)\rho_\pm(x,l)] - \partial_l[v_\pm(x,l)\rho_\pm(x,l)]\,.\end{aligned} \tag{2.23}$$

If the local net velocity $v_\pm(x)$ is positive, filament tips associated with right (left) oriented filaments are advected to the right (left) and vice versa for negative net velocity. The last term accounts for length changes. Independent of the orientation, a positive/negative net velocity yields filament growth/shrinkage ('advection in the length domain'). Possible nucleation events could be treated as a boundary condition at $l = 0$. Here, however, we will focus on the dynamics in the absence of nucleation and "filament death". To describe the dynamics of the filament-motor mixture, we need to derive expressions for the growth $v_g(x)$ and shrinkage $\tilde{v}_s(x,l)$ velocities for a spatially extended system. The growth velocity can easily be generalized from the single filament dynamics by including the spatial dependence of the cytosolic tubulin concentration; $v_g(x) = a\gamma c_T(x)$. To obtain an expression for the shrinkage velocity, we assume a quasi-steady state for the dynamics of filament-bound motors and use the flux balance condition (cf. Eq. 2.14). However, in a spatially extended system, the attachment of motors appears along the whole contour of the filament. The shrinkage velocity

then becomes

$$\tilde{v}_{\mathrm{s}}^{\pm}(x,l) = a\,k_{\mathrm{on}} \begin{cases} \int_{x-l}^{x} \mathrm{d}x'\,\tilde{c}_{\mathrm{M}}(x') & (+\text{ oriented filaments}) \\ \int_{x}^{x+l} \mathrm{d}x'\,\tilde{c}_{\mathrm{M}}(x') & (-\text{ oriented filaments}) \end{cases}, \tag{2.24}$$

where we assumed persistent motors ($k_{\mathrm{off}} = 0$). For well-mixed cytosolic motors, Eq. 2.24 reduces to Eq. 2.14. As in the case of a single filament, we will express the cytosolic motor concentration in terms of the total motor density

$$\rho_{\mathrm{M}}(x) = \tilde{c}_{\mathrm{M}}(x) + \tilde{\mu}_{+}(x) + \tilde{\mu}_{-}(x)\,. \tag{2.25}$$

Here $\tilde{\mu}_{\pm}(x)$ denote the filament-bound motor density associated with *all* filaments of orientation $\pm$ at position x. The filament-bound motor density of a single filament with the plus-end at position $x \pm (l-s)$ and length l is given by

$$\tilde{m}_{\pm}(x;l,s) = \frac{k_{\mathrm{on}}}{\nu_{\mathrm{m}}} \begin{cases} \int_{x-s}^{x} \mathrm{d}x'\,\tilde{c}_{\mathrm{M}}(x') & (+\text{ oriented}) \\ \int_{x}^{x+s} \mathrm{d}x'\,\tilde{c}_{\mathrm{M}}(x') & (-\text{ oriented}) \end{cases}. \tag{2.26}$$

Note again, the result reduces to the result for a single filament in the limit of well-mixed cytosolic motors. The average filament-bound motor density at position x is then given by

$$\tilde{\mu}_{\pm}(x) = \int_0^{\infty} \mathrm{d}l \int_0^{l} \mathrm{d}s\,\rho_{\pm}(x \pm (l-s), l)\,m_{\pm}(x;l,s)\,. \tag{2.27}$$

Equations (2.25) and (2.27) (in principle) can be solved for the cytosolic quasi steady-state motor concentration $\tilde{c}_{\mathrm{M}}$. To obtain a complete description of the dynamics on a continuum level, we need equations governing the cytosolic redistribution of tubulin and motors. Polymerization kinetics induces sources (filament shrinkage), and sinks (filament growth), and cytosolic tubulin is redistributed via diffusion. In the quasi steady state, the total motor density ρ_{M} is solely redistributed via diffusion. Taken together, this yields

$$\partial_t c_{\mathrm{T}}(x) = D_{\mathrm{T}}\partial_x^2 c_{\mathrm{T}}(x) - \int_0^{\infty} \frac{\mathrm{d}l}{a}\left[v_{+}(x,l)\,\rho_{+}(x,l) + v_{-}(x,l)\,\rho_{-}(x,l)\right], \tag{2.28a}$$

$$\partial_t \rho_{\mathrm{M}}(x) = D_{\mathrm{M}}\partial_x^2 \tilde{c}_{\mathrm{M}}(x)\,. \tag{2.28b}$$

MOMENT EXPANSION AND GRADIENT APPROXIMATION

Eqs. (2.23) and (2.28) constitute a set of integro-differential equations in the x, l domain with an algebraic integral-constraint (Eq. (2.25)). This makes an explicit treatment, even on a numerical level, challenging. The purpose of the continuum description above is that it serves as the basis for a perturbative approach.

We first aim to treat the algebraic integral constraint (Eq. (2.25)). To obtain a feasible expression, we perform a gradient expansion in the cytosolic motor density $\tilde{c}_{\mathrm{M}}$ and the plus-end density $\rho_{\pm}$. The shrinkage velocity then becomes

$$\tilde{v}_{\mathrm{s}}^{\pm}(x,l) = k_{\mathrm{on}} \sum_{k=0}^{\infty} \frac{(\mp 1)^k}{k!}\partial_x^{(k)}\tilde{c}_{\mathrm{M}}(x)\,l^k\,. \tag{2.29}$$

This expression is only guaranteed to be positive if (i) the sum is truncated at 0th order or if (ii) the entire sum is taken into account. Otherwise, the shrinkage velocity will become negative if the cytosolic motor concentration has gradients on the length scale of the local filament length. This means, one either has to truncate the sum at the lowest order or deal with the problem at its entire complexity, or hope that gradients in the cytosolic motor concentrations are not too sharp. To make

progress, we rely on a 0th order gradient expansion. This approximation is valid as long as gradients in the cytosolic motor density are weak and occur on length scales much longer than the typical filament length. Consistently, the filament-bound motor density can be written as

$$\mu_\pm(x) \approx \int_0^\infty \mathrm{d}l\, \frac{k_{\mathrm{on}}}{2v_{\mathrm{m}}} \tilde{c}_{\mathrm{M}}(x) l^2 \rho_\pm(x,l) + \mathcal{O}(|\partial_x \tilde{c}_{\mathrm{M}}|) + \mathcal{O}(|\partial_x \rho_\pm|)\,. \tag{2.30}$$

Next, we perform a moment expansion in the filament length l, which leads to a hierarchy of order parameters,

$$\ell_\pm^{(q)}(x) = \int_0^\infty \mathrm{d}l\, l^q \rho_\pm(x,l)\,. \tag{2.31}$$

The zeroth moment $\ell_\pm^{(0)}(x)$ represents the filament tip density and $\ell_\pm^{(1)}(x)/\ell^{(0)}(x) = \langle l\rangle_\pm$ the mean filament length at position x. Substituting Eq. 2.30 into Eq. 2.25 and using Eq. 2.31 yields

$$\tilde{c}_{\mathrm{M}}(x) \approx \frac{\rho_{\mathrm{M}}(x)}{1 + V_0 \ell^{(2)}(x)/l_{\mathrm{c}}^2}\,, \tag{2.32}$$

where we defined $\ell^{(2)}(x) = \ell_+^{(2)}(x) + \ell_-^{(2)}(x)$. The remaining task is to obtain a set of dynamic equations for the moments $\ell^{(q)}$. To do so, we substitute Eq. 2.31 into Eq. 2.23 and use Eq. 2.29, which yields an infinite set of coupled equations for the moments $\ell_\pm^{(q)}$

$$\begin{aligned}\partial_t \ell_\pm^{(q)} &= \partial_x^2 \int_0^\infty \mathrm{d}l\, l^q D_{\mathrm{Mt}}(l)\rho_\pm(x,l) \\ &\mp a\partial_x\left[\gamma c_{\mathrm{T}} \ell_\pm^{(q)} - k_{\mathrm{on}}\tilde{c}_{\mathrm{M}}\ell_\pm^{(q+1)}\right] + qa\left[c_{\mathrm{T}}\ell_\pm^{(q-1)} - k_{\mathrm{on}}\tilde{c}_{\mathrm{M}}\ell_\pm^{(q)}\right].\end{aligned} \tag{2.33}$$

This is the dynamics of the moments characterized by a diffusion advection reaction equation.

MEAN-FIELD APPROXIMATION

Eq. 2.33 couples the $q-th$ moment to higher moments both through the diffusion term and the advection term. To close the infinite hierarchy of equations, we perform a mean-field approximation of the form

$$\int_0^\infty \mathrm{d}l\, f(l)\rho_\pm(x,l) \approx f(\langle l\rangle_\pm)\ell_\pm^{(0)} = f(\ell_\pm^{(1)}/\ell_\pm^{(0)})\ell_\pm^{(0)}\,, \tag{2.34}$$

for an arbitrary function $f(l)$. This is equivalent to the assumption that the local filament length has zero variance. Thereby we obtain a closed set of equations for the first two moments $\ell^{(0)}$ and $\ell^{(1)}$

$$\partial_t \ell_\pm^{(0)} = \partial_x^2\left[D_{\mathrm{Mt}}(\ell_\pm^{(1)}/\ell_\pm^{(0)})\ell_\pm^{(0)}\right] \mp \partial_x\left(v_\pm \ell_\pm^{(0)}\right), \tag{2.35a}$$

$$\partial_t \ell_\pm^{(1)} = \partial_x^2\left[D_{\mathrm{Mt}}(\ell_\pm^{(1)}/\ell_\pm^{(0)})\ell_\pm^{(1)}\right] \mp \partial_x\left(v_\pm \ell_\pm^{(1)}\right) + v_\pm \ell_\pm^{(0)}\,, \tag{2.35b}$$

with the net polymerization velocity

$$v_\pm = a\left(\gamma c_{\mathrm{T}} - k_{\mathrm{on}}\tilde{c}_{\mathrm{M}}\ell_\pm^{(1)}/\ell_\pm^{(0)}\right) = a\left(\gamma c_{\mathrm{T}} - k_{\mathrm{on}}\tilde{c}_{\mathrm{M}}\langle l\rangle_\pm\right).$$

Equation 2.35a is a diffusion-advection equation for the filament tip-density of left and right-pointing filaments respectively. The first term accounts for the diffusion of filament tips. The second term reflects filament tip advection. Depending on the local net velocity, $v_\pm$, filament tips are advected to the left or right. Equation 2.35b is a diffusion-advection-reaction equation that accounts for the local change in filament-bound tubulin density. As is the case for filament tips, the local filament-bound tubulin density changes through filament diffusion and advection. Moreover, it is changed by incorporation and release of tubulin, which is accounted for by the reaction term $v_\pm \ell_\pm^{(0)}$.

In Sec. 2.2, we used the point-like filament approximation to account for the change in filament-bound tubulin mass at position x. Comparison of Eq. 2.35b to the point like filament approximation used in Sec. 2.2 reveals that there is one additional contribution which we did not account for previously, namely the local change in filament mass caused by advection. This is expected since the advection term describes the local change in filament-bound tubulin mass through polymerization, which can be only present if filaments have a non-zero extent.

Using the mean field approximation (Eq. 2.34) the cytosolic motor concentration $\tilde{c}_\mathrm{M}$ (Eq. 2.32) can be written as a function of $\ell_\pm^{(0)}$ and $\ell_\pm^{(1)}$,

$$\tilde{c}_\mathrm{M}(x) \approx \frac{\rho_\mathrm{M}(x)}{1+\frac{V_0}{l_\mathrm{c}^2}\left(\frac{\ell_+^{(1)2}}{\ell_+^{(0)}}+\frac{\ell_-^{(1)2}}{\ell_-^{(0)}}\right)}. \tag{2.36}$$

In the spatially homogeneous system with an equal number of left and right pointing filaments, Eq. 2.36 reduces to the result for a single filament (cf. Eq. 2.22). Together with the dynamic equations for cytosolic tubulin and motors, expressed in terms of the moments $\ell_\pm^{(0)}$ and $\ell_\pm^{(1)}$, we found a closed set of equations describing the spatio-temporal evolution of the filament motor mixture

$$\partial_t c_\mathrm{T}(x) = D_\mathrm{T}\partial_x^2 c_\mathrm{T}(x) - \frac{1}{a}\left[v_+\ell_+^{(0)} + v_-\ell_-^{(0)}\right], \tag{2.37a}$$

$$\partial_t \rho_\mathrm{M}(x) = D_\mathrm{M}\partial_x^2 \tilde{c}_\mathrm{M}. \tag{2.37b}$$

Note, Eq. 2.37a together with Eq. 2.35b conserves the tubulin mass.

For given kinetic constants, the total motor density $\bar{\rho}_\mathrm{M}$, tubulin density $\bar{\rho}_\mathrm{T}$ and density of left/right pointing filaments $\bar{\ell}_\pm^{(0)}$ are control parameters of the system dynamics. The spatially homogeneous solution to Eq. 2.35 and Eq. 2.37 is given by $(\bar{\ell}_\pm^{(0)}, \ell_\pm^{(1)*}, c_\mathrm{T}^*, \bar{\rho}_\mathrm{M})$ where quantities denoted with an asterisk $(*)$ represent spatially homogeneous solutions determined by the local reaction kinetics.

Before we continue the analysis of the spatio-temporal dynamics, we would like to recapitulate the major approximations made to arrive at a field theoretic description of the system (Eq. 2.35 and Eq. 2.37). First, we made a quasi steady state approximation for the filament-bound motor density. This approximation is expected to work well for biologically relevant parameters and can be checked by numeric simulations taking the motor movement into account; see Sec. 2.5. Second, we made a gradient expansion in the cytosolic motor density and filament tip density, i.e., we neglected gradients on the length scale of the filament. This approximation is expected to work well for the initial dynamics starting the spatially homogeneous steady state (no gradients). However, it might fail once gradients have built up. Last we made a mean-field approximation assuming zero variance in the local filament length. If the reaction kinetics, which sets the spatially homogeneous state, yields a sharply peaked filament length distribution, the mean-field approximation is also expected to work well for the initial dynamics. To verify predictions made based on our field theory, we will rely on agent-based simulations of the full dynamics in the following.

LINEAR STABILITY ANALYSIS

In the following, we will limit the discussion to equal numbers of left and right-oriented filaments in the system $\bar{\ell}_+^{(0)} = \bar{\ell}_-^{(0)}$. Moreover, we have to make a choice for the length dependent filament diffusion coefficient $D_\mathrm{Mt}(l)$, which we choose as

$$D_\mathrm{Mt}(l) = \frac{D_\mathrm{T}}{1+l/l_\mathrm{d}}, \tag{2.38}$$

such that filaments of zero length diffuse with the diffusion constant of cytosolic tubulin. The parameter l_d characterizes how fast the filament diffusivity declines with increasing filament length.

Having a complete field theoretic description of our model, we can study the stability of the spatially homogenous state against spatial perturbations using linear stability analysis. In particular, we can check if the additional advection term in Eq. 2.35b, not present in the point-like filament approximation, affects the linear stability of the system. Comparison to the point-like filament approximation used in Sec. 2.2 reveals that the stability of the spatially homogeneous state is not affected by the advection term. This can be understood on an intuitive level: The net velocity $v_\pm$ is only non-zero if the mass-redistribution instability is present. Otherwise, $v_\pm = 0$, and there is no advective redistribution of filament tips.

In contrast, non-zero filament diffusion can affect the stability of the spatially homogeneous state. If the filament diffusion is fast (l_d is large), the instability can be suppressed. This can be understood in the context of the mass-redistribution instability discussed in Sec. 2.2: The mass-redistribution instability is based on the local imbalance of filament growth and shrinkage; see. Fig. 2.3. Let us first recapitulate the argument for mass-redistribution instability in the absence of filament diffusion. We keep the cytosolic tubulin concentration fixed but add a small perturbation to the local filament-bound tubulin mass $\delta\ell^{(1)}(x)$. If the shrinkage velocity declines as a function of the filament-bound tubulin mass, the perturbation yields spatial regions where the net velocity $v_\pm$ is positive (negative) if the filament-bound tubulin mass is increased (decreased) by $\delta\ell^{(1)}(x)$. Therefore, in regions where filaments are short, this mechanism will yield an increase of cytosolic tubulin due to the net shrinkage of filaments and depletion of cytosolic tubulin in regions where filaments are long. Essential to maintain filament growth (positive feedback) in regions where filament length is increased is the diffusive redistribution of cytosolic tubulin from spatial regions where filaments are short to spatial regions where filaments are long; see Fig. 2.3 (b). Now consider, for simplicity, filaments that diffuse with a length independent diffusion constant D_Mt. If the short and long filaments mix too fast via diffusion the positive feedback mechanism is suppressed and, therefore, the instability; see [213] for a detailed discussion.

Figure 2.9 (a),(b) shows typical stability diagrams in the $(\bar\rho_\mathrm{M}, \bar\rho_\mathrm{T})$ parameter plane for $l_\mathrm{d} = 1\times10^{-2}\,\mu\mathrm{m} \sim a$ and $l_\mathrm{d} = 1\times10^{-1}\,\mu\mathrm{m} \sim a$ in comparison to agent-based simulations (symbols). The onset of the instability appears to be slightly earlier in the agent based-simulation. The qualitative behavior is captured well by our field theory. Above the threshold for lateral instability, we find the formation of filament bundles with local polar order $p(x) = \ell_+^{(1)} - \ell_-^{(1)}$. But the long-term dynamics of the filament bundles depend on l_d as we will discuss in Sec. 2.3.2. Next, we are interested in the dynamics beyond linear stability. We first want to understand the polarity sorting mechanism driven by filament length regulation.

LENGTH REGULATED POLARITY SORTING

In order to investigate the behavior beyond linear stability, we use a twofold approach. First, we perform agent-based simulations of our model, and second, we perform finite element simulations of Eqs. (2.35) and (2.37). Figure 2.10 (a) shows the time evolution of the total tubulin concentration obtained from agent-based simulations of a small system of size $L_x = 250\,\mu\mathrm{m}$ for filaments which do not diffuse ($D_\mathrm{Mt} = 0$). We initialize the system in the leterally unstable parameter regime. Starting from a spatially homogeneous state, the first regions of reduced and increased filament length are formed. This corresponds to the initial dynamics described by the mass-redistribution instability. As the dynamics progresses, the high density regions segregate into large-scale filament bundles. Eventually, the filament motor mixture evolves into a single stable filament bundle, as shown in the latest snapshot ($t = 27.7\,\mathrm{h}$). The final structure has a well-defined orientational order with filament plus-ends centered at the bundle interface; see Fig. 2.10(a).

How can we understand the polarity sorting mechanism driven by length regulation? To answer this question, let us consider the case of zero filament diffusion, $D_\mathrm{Mt} = 0$, first. Above the instability threshold, the mass-redistribution instability will drive the system into regions with net fil-

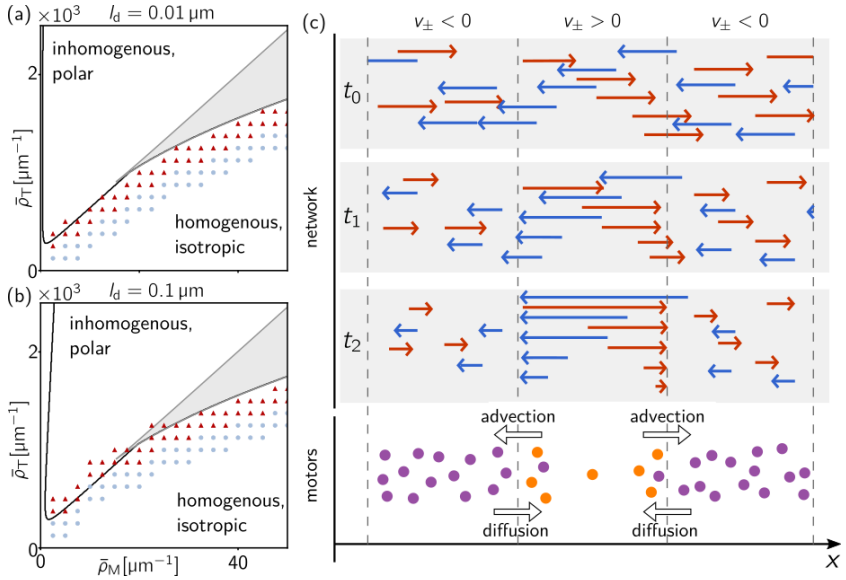

Figure 2.9: (a),(b) Stability diagram obtained from a linear stability analysis of Eq. 2.33 and Eq. 2.37 in comparison to the agent-based simulations (symbols) for different values of l_d. The triangles indicate spatially inhomogeneous and the circles spatially homogeneous patterns. The gray shaded area highlights the parameter regime where the local reaction dynamics is bistable (cf. Fig. 2.8). (c) Schematic illustration of the polarity sorting mechanism in a system without filament diffusion. Starting from an initially homogeneous state (t_0), the mass-redistribution instability drives the filament network into regions with positive/ negative net velocity $v_\pm = v_\mathrm{g} - ak_\mathrm{on}\tilde{c}_\mathrm{M}\langle l\rangle_\pm$. As a result, filaments with opposite orientations will grow/ shrink in opposite directions (t_1). Since the direction of motion of the filament tips reverses at the position where the net velocity $v_\pm$ changes sign, this dynamics yields co-localization of filament tips at interfaces between net filament growth and net filament shrinkage. Thereby, polar filament bundles are formed (t_2). The emerging polar structure, in turn, influences motor dynamics. This, in turn, influences the motor dynamics in the system. Filament depleted regions are associated with high and filament enriched regions with a low cytosolic motor concentration. The resulting concentration gradient generates a diffusive flux of motors into filament bundles. Inside the filament bundle, cytosolic motors bind quickly due to a high density of binding partners (filaments). Due to the network polarity, filament-bound motors are advected back towards the bundle interface, where they are released into the cytosol.

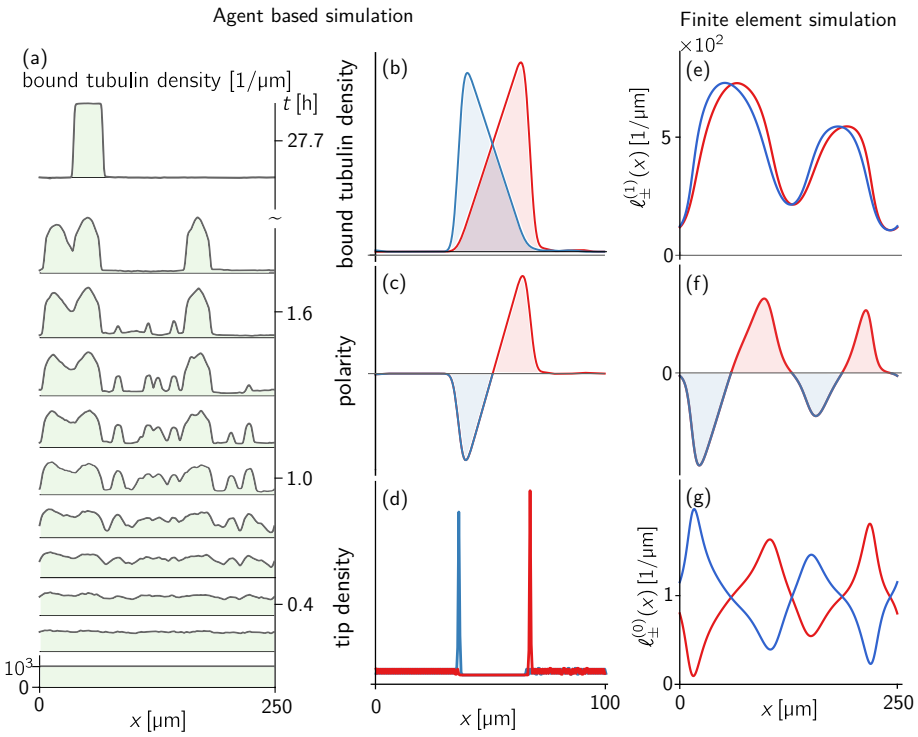

Figure 2.10: (a) Time evolution of the filament-bound tubulin density obtained from agent-based simulations in a small system with lateral extent $L_x = 250\,\mu\text{m}$, total tubulin density $\bar{\rho}_\text{T} = 1200\,\mu\text{m}^{-1}$ and total motor density $\bar{\rho}_\text{M} = 20\,\mu\text{m}^{-1}$ and $D_\text{Mt} = 0$. Time is indicated at the right axes and tubulin density at the left axes. Snapshots are shown every 0.2 h. Starting from a spatially homogeneous state, the mass-redistribution instability leads to a spatial modulation of the filament-bound tubulin density. Depletion zones form in the filament arrangement form regions with reduced tubulin density as the dynamics progress. The newly available cytosolic tubulin is then incorporated into the filament arrangement in regions of long filaments, further increasing the filament-bound tubulin mass there. Eventually, the filament arrangement evolves into a single stable filament bundle, as shown in the latest snapshot ($t = 27.7\,\text{h}$). (b)-(c) Quantification of the emerging filament bundle seen in the last snapshot. The y-axis is in arbitrary units. (b) The filament-bound tubulin density is separated into density profiles of left (blue) and right (red) pointing filaments. As can be seen, the density profiles segregate. (c) The segregation of density profiles implies net polarity (defined as the difference of left and right-oriented bound tubulin density) within the filament bundle. (d) Density profiles of filament tips. Left (right) oriented filament tips accumulate at the left (right) bundle interface. (e)-(f) Bound tubulin density $\ell_\pm^{(1)}/a$, tip density $\ell_\pm^{(0)}$ and unnormalized polarity $p = \ell_+^{(1)} - \ell_-^{(1)}$ obtained by finite element simulations of the PDEs Eqs. (2.35a–b) and Eq. (2.37a–b). Snapshots were taken at $t = 4.2\,\text{h}$. The system was initialized as in (a) with small spatial perturbations in the $\ell_\pm^{(1)}$ fields. Polarity sorting and tip co-localization with interfaces to depletion zones are already nicely visible in the initial phase of pattern formation. Filament tip advection alone is, therefore, sufficient to account for those observations.

ament growth, $v_\pm > 0$, and net filament shrinkage $v_\pm < 0$; see Fig. 2.9 (c), t_0. As a consequence, filament plus-ends will be advected with the net growth velocity, $v_\pm$, in the direction of their orientation. If filament plus-ends are in a spatial region with positive net velocity, right oriented filament plus-ends will move to the right and left oriented filament plus-ends will move to the left and vice versa in regions with net shrinkage; see Fig. 2.9 (c), t_1. This dynamics yields localization of filament plus-ends at the interface between regions of net growth and shrinkage; see Fig. 2.9 (c), t_2. If this intuitive explanation is correct, our zeroth order gradient expansion Eqs. (2.35) and (2.37), which includes tip advection should capture the onset of this dynamics. Fig. 2.9 (e)–(g) shows fields of filament-bound tubulin density $\ell_\pm^{(1)}$, the tip density $\ell_\pm^{(0)}$ and the non-normalised polarity defined as $p(x) = \ell_+^{(1)}(x) - \ell_-^{(1)}(x)$ at the onset of pattern formation. As can be seen, the tip movement alone is sufficient to account for the initial phase of polarity sorting as well as the co-localization of filament tips. However, in order to describe the dynamics of the emerging filament bundles, a perturbative approach, such as the one we have chosen, is not promising, even if higher orders in the gradients are taken into account. This is because the cytosolic motor density will have sharp gradients at the bundle interface (even with non-zero filament diffusion). However, if gradients in the cytosolic motor concentration are taken into account, Eq. 2.29 will become negative at some point, which will lead to nonphysical behavior (negative velocity magnitude). We will therefore stick to our agent-based simulation in the following to investigate the long-term dynamics of our model.

SYMMETRY BREAKING OF ASTER POLARITY, ASTER COALESCENCE, AND ASTER COARSENING

Having a qualitative understanding of how bundle polarity is established, we can ask the question of how finite filament diffusion changes the dynamics. To investigate this behavior, we use our agent-based simulation. We simulate the system for different values of $l_\mathrm{d} = [0.01\,\mu\mathrm{m}, \ldots, 0.11\,\mu\mathrm{m}]$. For the linear stability of the spatially homogeneous state, we find good agreement between our field theory and the agent-based simulation for all chosen values of l_d. However, as we increase l_d, we observe a significant change in the long-term dynamics of the system. At low l_d (filament diffusion decays fast with filament length), we find coarsening of the emerging filament bundles until only one bundle

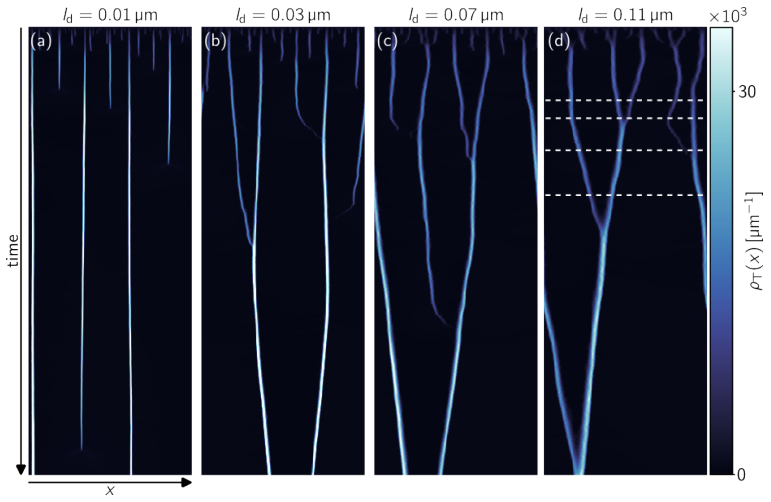

Figure 2.11: (a)-(d) Kymograph of the total tubulin density, $\rho_\mathrm{T}(x)$, for $\bar{\rho}_\mathrm{T} = 1800\,\mu\mathrm{m}^{-1}$ and $\bar{\rho}_\mathrm{M} = 40\,\mu\mathrm{m}^{-1}$. Other parameters are as specified in the supplemental material. Time runs from top to bottom ($t \in [0, 166\,\mathrm{h}]$), space from left to right ($x \in [0, 2000\,\mu\mathrm{m}]$). (a) For low diffusion of filaments, we observe coarsening of the emerging filament bundle. (b)-(d) As the filament diffusion is increased, we observe the movement and coalescence of the emerging filament bundles. White dashed lines in (d) indicate the time points of the snapshots shown in Fig. 2.12.

remains; cf. 2.10 (a) and Fig. 2.11 (a). However, as we increase l_d (filament diffusion decays slower with filament length), we observe filament bundle movement; see Fig. 2.11 (b)-(d). Most of the time, we observe that neighboring filament bundles move toward each other. However, sometimes, they move apart (not shown). Eventually, the filament bundles merge through coalescence, and only one structure remains; see Fig. 2.11 (d).

To get insight into which physical properties drive filament bundle movement and coalescence, we measure the polarity field $p(x)$, the cytosolic motor density $c_M(x)$, and the filament-bound motor density $\mu(x)$ from our agent-based simulations. Remarkably, we find that the symmetry of the polar order of the emerging filament bundles is broken; see Fig. 2.12. Filaments inside the bundles point preferably in one direction. We observe that filament bundles move as opposed to their orientational order; see Fig. 2.12 (a). In the majority of cases, this causes neighboring filament bundles to move towards each other; see Fig. 2.12 (a). However, sometimes the emerging filament bundles move in the same direction; see Fig. 2.13 (c).

How can we understand the movement of filament bundles? If the orientational order of a filament bundle is broken, this impacts the motor dynamics. Motors that attach to filaments at the apolar side (see Fig. 2.13) of the filament bundle will be subject to advective transport towards the polar side of the filament bundle.

This increases the number of filament-bound motors there; see Fig. 2.12 (b), which are released into the cytosol and increase the cytosolic motor concentration at the polar bundle side. Moreover, the cytosolic motor concentration of filaments at the apolar bundle side becomes depleted; see Fig. 2.13. The increase (decrease) of cytosolic motor concentration at the polar (apolar) side of the bundle yields a dysbalance between growth and shrinkage there, with favor towards shrinkage (growth). The shrinkage of filaments at the polar bundle side causes an increasing density of short filaments there. This, in turn, causes a diffusive redistribution of (short) filaments towards the bundle interior, where filament growth is favored (low cytosolic motor concentration); see Fig. 2.13 (a). In contrast, short filaments which diffuse into the region where the cytosolic motor concentration is enriched shrink further; Fig. 2.13 (a). The feedback loop between bundle polarity, advective transport of motors, and gradients in the cytosolic motor density is particularly nicely visible in the rare occasions where bundles move in the same direction; see Fig. 2.13 (b),(c). Taken together, this causes bundle movement opposed to the direction of bundle polarity. From a coarse-grained perspective, one could view the filament bundle as a "mega" filament performing a treadmilling-like motion, where the building blocks (individual filaments) become released at one side and incorporated into the bundle at the other side.

SUMMARY

Here we have studied a minimal conceptual model for motor-mediated polymerization kinetics of filaments (microtubules) based on our previous work [1]. By reducing the model to an effective one-dimensional system, we were able to systematically derive a formalism to describe length regulation in an ensemble of polymerizing filaments in the presence of a motor protein that regulates filament length. The essential steps for deriving a field theoretic description are (i) the quasi steady state approximation for the motor protein dynamics, which allows determining the depolymerization velocity by using a flux-balance argument; cf. Eq. 2.3. (ii) We performed a gradient expansion in the density fields. This is necessary as filaments are spatially extended objects recruiting resources from a spatial domain rather than a point. (iii) Lastly, we performed a moment expansion in terms of the filament length. As the moments in filament length couple to all higher moments, this makes a closure scheme necessary; cf. Eq. 2.33. Here we performed a simple mean field approximation. Comparison to agent-based simulations shows that the derived filed theory captures all essential features of the initial dynamics, including stability of the homogeneous state and demixing of the population of left and right oriented filaments, i.e., polarity sorting. The emerging filament bundles

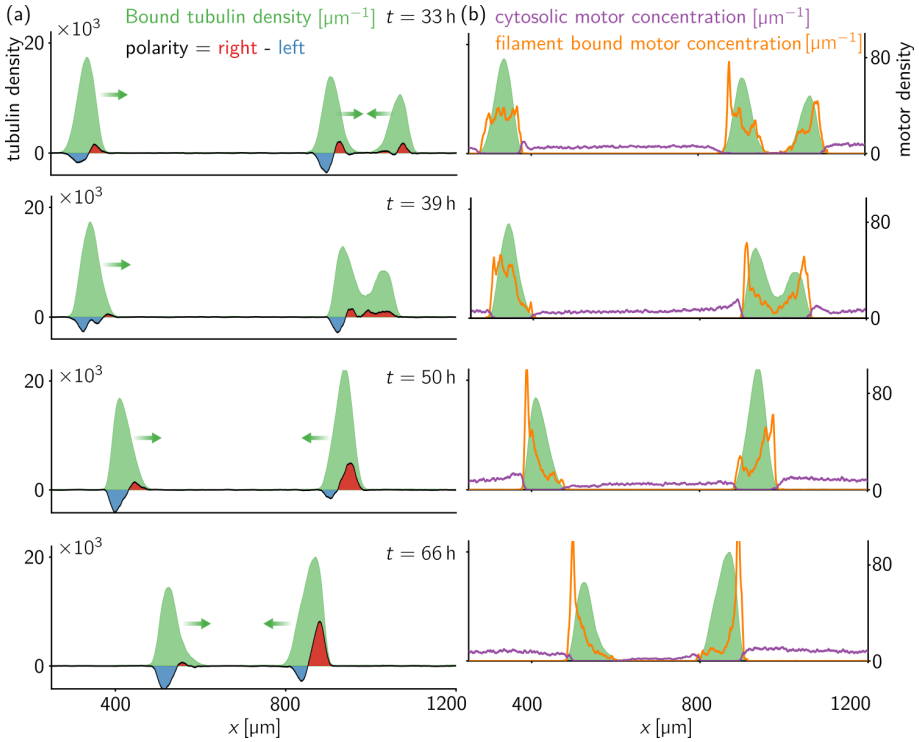

Figure 2.12: (a) Filament-bound tubulin density (green) and polarity (blue, red) obtained from the agent-based simulation for $\bar{\rho}_T = 1800\,\mu m^{-1}$ and $\bar{\rho}_M = 40\,\mu m^{-1}$ and $l_d = 0.11\,\mu m$; cf. Fig. 2.11 (d) dashed lines. Other parameters are as specified in the supplemental material. Only a section of the system $x \in [250\,\mu m, 1200\,\mu m]$ is shown. Regions where the number of left oriented filaments dominates are shown in blue, and regions where right oriented filaments dominate in red. We find that the orientational order (polarity) of filament bundles is broken. Filaments in the bundle point, preferably in one direction. The filament bundles move in opposite direction to its polar order. (b) filament-bound (orange) and cytosolic (purple) motor density. As a result of the polar order of the filament-bound, and the directed motion of motors on the filaments, motors accumulate at the polar side of the bundle, where they get released in the cytosol via depolymerization of filaments. As a result, the cytosolic concentration of motors becomes increased at the polar side of the bundles and decreased at the apolar side. In particular, if two filament bundles with opposed orientational order encapsulate a spatial region, the cytosolic motor concentration in the region between them will be emptied of motors; see (b) $t = 66\,h$

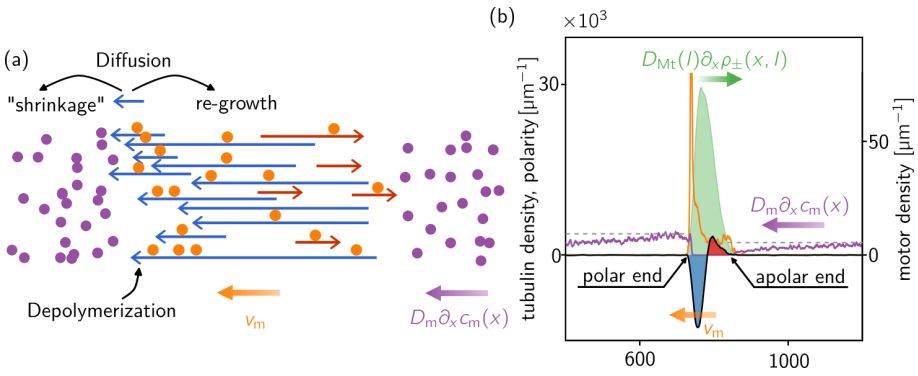

Figure 2.13: (a) Schematic illustration of the mechanism by which filament bundles move. Once the symmetry in the polar order of the filament bundle is broken, cytosolic motors which attach at the apolar bundle side (see (b)) are advected along the filaments towards the polar bundle side, where they depolymerize filaments and are released into the cytosol. This causes an increase (decrease) of cytosolic motor concentration at the polar (apolar) bundle side. This causes a diffusive flux of motors towards the apolar bundle side. Short filaments at the polar bundle side are subject to diffusion. If they diffuse in the bundle interior, they can re-grow. In contrast, if they diffuse into the filament depleted region, they become entirely depolymerized. Taken together, this causes filament bundle movement opposed to the polar order of the bundle. (b) filament-bound tubulin density (green), cytosolic (purple), and filament-bound (orange) motor density in the vicinity of a filament bundle. Dashed gray lines are a guide for the eye to visualize gradients in the cytosolic motor concentration. Note we write the diffusive flux of filaments as $D_{\mathrm{Mt}}(l)\partial_x\rho_\pm(x,l)$ since, at this stage of the dynamics, our mean-field assumption fails and one should not describe the system dynamics by the first two moments only. This is because the local length distribution is not sharply peaked anymore. (c) Snapshot of the density profiles for a rare occasion where neighboring filament bundles move in the same direction. Snapshot was taken at $t = 125\,\mathrm{h}$. Parameters are $\bar{\rho}_{\mathrm{T}} = 1800\,\mu\mathrm{m}^{-1}$, $\bar{\rho}_{\mathrm{M}} = 25\,\mu\mathrm{m}^{-1}$ and $l_{\mathrm{d}} = 0.07\,\mu\mathrm{m}$. Other parameters are as specified in the supplemental material.

are characterized by sharp gradients in the space domain and a large variance in the local filament length. This makes both our gradient expansion and the mean-field approximation questionable in the long run.

We, therefore, turned to agent-based simulations to study the long-term dynamics of the system. We found that the long-term dynamics of the system shows the emergent formation of filament bundles. Those filament bundles show spontaneous symmetry breaking of their orientational order, travelling wave solutions, and coalescence of filament bundles, all driven by length regulation. From my perspective, the exciting aspect is the feedback between emerging orientational order, which controls the collective motor flux in the system, and motor regulation, which in turn impacts the collective dynamics of filaments (movement of filament bundles).

In the context of mechanical filament interactions, the feedback between the orientational order of filaments and spatial motor organization is often considered [Cite] and lately derived from a microscopic model [Cite]. In contrast to these systems in the model studied here, filaments do not interact directly but only via a shared pool of resources. It will be interesting to study systems where both regulatory and mechanical interactions between filaments are present. By doing so, it might be possible to overcome the long timescales at which the dynamics presented here takes place. As an example, contraction into bundles and subsequent polarity sorting could be achieved or accelerated by mechanical motor-filament interactions while the subsequent movement of filament structures could be achieved via regulatory dynamics.

Another significant limitation of the model studied here is that we considered only stabilized microtubules. This was done due to the lack of knowledge of how motor proteins or MAPs impact dynamic instability, in particular if different MAPs and/ or motors act together to regulate microtubule dynamics. However, as long as there is feedback between the density of filament-bound tubulin and the rates controlling microtubule dynamics, combined with resource limitation, we expect that the mechanisms discussed here may play a role. On a speculative level, one could assume that this also accelerates the collective dynamics as the time-limiting processes in our model are the polymerization and depolymerization of individual filaments. Polymerization of microtubules, however, can be accelerated $10-20$ times in the presence of other MAPs, and filament catastrophes provide a pathway to rapid tubulin release. I will briefly discuss some thoughts on the possibility of mass-redistribution instability in an ensemble of dynamic (non stabilized) microtubules in the next section.

2.4. SUMMARY & OUTLOOK

In this chapter, we have studied a minimal model for kinesin-8 driven length regulation in an ensemble of filaments. Importantly we account explicitly for the spatial redistribution of resources (kinesin-8, tubulin, and filaments). Commonly, the self-organization of cytoskeletal filaments is attributed to motor proteins that exert mechanical force on the filaments. Here, in contrast, we have shown that length regulation alone is sufficient to self-organize filament motor mixtures into structures that span multiple filament lengths, and this is despite the fact that the filaments interact only indirectly via a shared pool of resources. The instability underlying this self-organization is driven by the diffusive redistribution of tubulin mass and a shrinkage velocity of filaments that depends on filament length. This length-dependent shrinkage rate is caused by the directed motion and persistence of Kinesin-8 motors.

We studied the long term dynamics of the emergent structures with the help of agent-based computer simulations. Thereby we showed that the emergent filament structures are capable of moving if filament diffusion is included in the model. This motion is driven by an interplay between the advective transport of motor proteins along the filaments and the diffusive redistribution of short filaments. In the long run, this motion can cause coalescence and traveling waves of the filament structures.

We expect that the initial instability discussed here is present in recent *in vitro* experiments that study Kinesin-8 mediated length regulation under the limitation of resources [63]. However, unfortunately in those experiments, the tubulin density was not spatially and temporally resolved. The general requirements for the mass redistribution instability to occur are kinetic rates of filament length regulation that depend on the local filament density and resource limitation. Both requirements have been observed in *Xenopus* egg extract [69, 70, 200–202]. However, filaments there are not stabilized as in our model but undergo stochastic switching between filament growth and shrinkage phases, a process termed dynamic instability [136, 221]. So the question arises as to whether extent the principles discussed in this chapter can be extended to describe the regulatory dynamics in ensembles of non-stabilized microtubules.

As an outlook and potential future project, I would like to share my thoughts on this question: Our knowledge about how different MAPs interact with microtubules that undergo dynamic instability is quite limited. Therefore, from my perspective, it would be really challenging to model explicit MAP-microtubule interactions, as we did in this chapter. However, what is feasible is to postulate a growth velocity, $v_g(\rho)$, shrinkage velocity, $v_s(\rho)$, catastrophe rate (stochastic switch from growth to shrinkage), $k_{cat}(\rho)$, and rescue rate (stochastic switch from shrinkage to growth), $k_{res}(\rho)$, that explicitly depend on the local density of filament-bound tubulin ρ. Since the individual filament is now a stochastic particle whose dynamic is not well characterized by a mean field equation, it does not make sense to apply our framework on a single filament level. However, what one could do is to coarse-grain over a small volume (small compared to the system size) V_0 that contains N filaments. On a mean-field level, we can then approximate the tubulin density in the volume by

$$\rho = \frac{N}{V_0}\frac{\langle l\rangle}{a}\,, \tag{2.39}$$

Here $\langle l\rangle$ is the mean length of filaments in the volume, and a is a factor converting filament length in a number of tubulin units. The probability of a filament in the volume to be in the growing or shrinking phase is given by $p_g(\rho)$ and $p_s(\rho)$ respectively. The probability of being in the growing or shrinking phase is a function of the catastrophe and rescue rate and, therefore, a function of the filament bound tubulin density. Moreover, we write the growth velocity of filaments, $v_g(\rho)$, as a base velocity, $v_{g,0} = a\gamma c_T$, in the absence of MAPs; here c_T denotes the cytosolic tubulin density and a MAP catalyzed contribution, $v_{g,cat}(\rho)$. Taken together, we find the time evolution of the mean filament-bound tubulin mass, ρ, to be governed by

$$\partial_t \rho = \frac{N}{a}\left[p_g(\rho)c_T(a\gamma + v_{g,cat}(\rho)) - p_s(\rho)v_s(\rho)\right]. \tag{2.40}$$

In steady state, $\partial_t \rho = 0$, we can solve for the steady state cytosolic tubulin density c_T^* and obtain

$$a\gamma c_T^*(\rho^*) = \frac{p_s(\rho^*)v_s(\rho^*)}{p_g(\rho^*)[1 + v_{g,cat}(\rho^*)/(a\gamma)]} \equiv f(\rho^*). \tag{2.41}$$

Together with tubulin mass conservation,

$$\rho_T = \rho + c_T \tag{2.42}$$

we have a closed set of equations for the filament-bound tubulin density. Here ρ_T denotes the total tubulin density. Importantly, this set of equations has the same structure as the ones we derived in Sec. Single filament dynamics. Therefore we expect the possibility of a mass redistribution instability if $\partial_\rho^* f(\rho^*) < 0$. It would be an interesting research project to study if the stochastic dynamics of the individual constituents (the filaments) allow a mean-field treatment as outlined here or if stochasticity plays a significant role.

From a broader perspective, it would be interesting to include mechanical interactions between filaments. Even if only steric interactions between filaments are considered, this should have a major impact on the emerging network architecture. This is because the mass redistribution instability discussed in this chapter locally increases the filament density beyond the Onsager ordering threshold. We would therefore expect that the filament network first undergoes phase separation into regions of long and short filaments caused by the mass redistribution instability, and subsequently, if the density is high enough, steric interactions should cause the formation of nematically aligned filament bundles.

2.5. SUPPLEMENTAL MATERIAL

PARAMETER ESTIMATION

Since experimental data are available for many of the parameters in our model [60, 175, 222, 223], we can assign experimentally motivated numerical values to them. In the following we will show how to convert the experimentally measured rates into appropriate rates for our simulation. The experimental and the resulting model parameters are summarized in Tab. 2.1.

A typical microtubule consists of thirteen protofilaments. We simplify our analysis by considering only a single protofilament per microtubule, i.e., we neglect correlations between neighbouring protofilaments of a single microtubule. This is achieved by converting rates and resources to rates and resources per protofilament. Given a height $\tilde{L}_z$ of our simulation environment, the total number of resources per protofilament is given by $N_\mathrm{M} = \bar{\rho}_\mathrm{M} L_x L_y \tilde{L}_z/13$ and $N_\mathrm{T} = \bar{\rho}_\mathrm{T} L_x L_y \tilde{L}_z/13$ for motor proteins and tubulin units respectively. We define $L_z := \tilde{L}_z/13$ as the effective z-extent per protofilament, which corresponds to the effective height of our simulation box. For a given choice of the spatial extents of the simulation box the values for N_T and N_M will be determined from the experimentally given values for the densities $\bar{\rho}_\mathrm{T}$ and $\bar{\rho}_\mathrm{M}$.

The *motor attachment rate* k_on can be determined from the experimentally measured rate constant for motor attachment, which is given in units per concentration, per time, and per length. Varga et al. [175] report a value of $k_\mathrm{on}^\mathrm{exp} = 0.4\,\mathrm{nM}^{-1}\mathrm{s}^{-1}\mu\mathrm{m}^{-1} = 0.66\,\mu\mathrm{m}^3\mathrm{s}^{-1}\mu\mathrm{m}^{-1}$, which was measured over a range of motor concentrations; note that we do not cancel one unit of µm to emphasize that k_on is a rate per volume concentration and per length of the microtubule. The motor on-flux onto a filament of length l at a given motor concentration c_M is than given by $k_\mathrm{on}^\mathrm{exp} c_\mathrm{M} l$. The motor concentration in experiments is measured in nM which is converted into a number densities as $1\,\mathrm{nM} \approx 0.6\,\mathrm{particles}/\mu\mathrm{m}^3$. Since Varga et al. used a TIRF setup, where motors can bind to and walk on approximately 5 protofilaments [224], the attachment rate per protofilament is given by $k_\mathrm{on} = k_\mathrm{on}^\mathrm{exp}/5 \approx 0.13\,\mu\mathrm{m}^3\mathrm{s}^{-1}\mu\mathrm{m}^{-1}$. For our agent-based simulations of the filament-motor mixture, we need to further convert this rate to a per-capita rate for a single motor protein. To this end, we first convert the experimental rate constant per volume concentration into a rate per area concentration by $k_\mathrm{on}^\mathrm{2D} = k_\mathrm{on}^\mathrm{exp}/L_z$. This is converted to a per-capita rate by specifying a reaction radius r_M within which the motors can attach to the filament. Thus, the experimental value for the attachment rate constant per protofilament $k_\mathrm{on}^\mathrm{exp}$ can be converted to a per-capita rate used in the simulations by $k_\mathrm{on}^\mathrm{sim} = k_\mathrm{on}^\mathrm{exp}/(L_z \pi r_\mathrm{M}^2)$.

Given the experimental value for the attachment rate, this scaling relation gives us some freedom in choosing the effective height L_z of the simulation box and the reaction radius r_M. The height of the simulation box has to be chosen such that all concentrations (tubulin, motor and filament concentration) can be assumed to be well mixed in $z-$direction, i.e., $L_z \ll \lambda_\mathrm{c}$, where λ_c is the wavelength of the initial instability (see Sec. 2.5). Moreover L_z has to be chosen large enough such that the number of filaments and particles is high enough to prevent stochastic effects due to number fluctuations. As long as these constrains are fulfilled we are free to choose L_z in a way convenient for our simulations. In particular, this means we choose L_z small to keep the particle numbers sufficiently low for the numerical simulations to be feasible. The reaction radius r_M must be smaller than the average distance covered by a motor in the time interval Δt by diffusion, where Δt is the time increment of the simulation (see Sec. 2.5). Otherwise particles could cover an unphysically large distance in the time interval Δt by successive attachment/ detachment events.

The *spontaneous polymerization rate* γ of microtubules can be obtained similarly to the attachment rate. The polymerization velocity of microtubules has been measured to be $v^\mathrm{exp} = 0.19\,\mu\mathrm{m}\,\mathrm{min}^{-1}\,\mu\mathrm{M}^{-1}$ [60], which corresponds to a polymerization rate constant $\gamma^\mathrm{exp} = v^\mathrm{exp}/a = 0.38\,\mu\mathrm{M}^{-1}\mathrm{s}^{-1} = 6.3 \times 10^{-4}\,\mu\mathrm{m}^3\mathrm{s}^{-1}$. Analogous to the case of the attachment rate constant, the polymerization rate constant depends on the volume concentration of tubulin units. We convert this into a per-capita polymerization rate by $\gamma^\mathrm{sim} = \gamma^\mathrm{exp}/(L_z \pi r_\mathrm{T}^2)$, where r_T denotes the reaction radius of a tubulin unit.

For the simulation results shown in the main text, we choose $r_T = r_M = 0.04\,\mu m$ and $L_z = 0.6\,\mu m$. At average concentrations $\bar{\rho}_T = 2.75\,\mu M$ and $\bar{\rho}_M = 50\,nM$ this results in a total number of $N_T \approx 2.2 \times 10^7$ tubulin units and $N_M \approx 4 \times 10^5$ motor proteins; as well as per-capita binding rates $\gamma^{sim} \approx 0.22\,s^{-1}$ and $k_{on}^{sim} \approx 40\,s^{-1}\mu m^{-1}$ (see Table 2.1).

The diffusion constant of cytosolic tubulin was measured as $D_T = 6\,\mu m^2\,s^{-1}$ [223]. To the best of our knowledge, the cytosolic diffusion constant D_M of Kip3 is not known. Since the molecular mass of Kinesin-8 is about 2–3 times larger than that of tubulin [7], we expect the diffusion constant of Kip3 to be of the order $D_M \sim 1\,\mu m^2\,s^{-1}$. As we discuss in Sec. 2.5 below, the precise value of the motor diffusion is not relevant for the qualitative results of our model. Linear stability analysis predicts that slower motor diffusivities entail a shorter wavelength of the fastest growing mode (see Fig. 2.19). To keep the computational cost of our agent-based simulations reasonable, we choose $D_M = 0.5\,\mu m^2\,s^{-1}$, which allows us to simulate a smaller system and thus keep the number of particles in the simulation volume manageable.

AGENT-BASED SIMULATION

Single-filament simulation: To simulate the motor-mediated length regulation of a single filament, we follow a two-pronged approach: First, we employ the Gillespie algorithm [225] to simulate the full stochastic dynamics of motor proteins using a lattice gas model (TASEP), which has been shown to be a good model system for studying the motion of motor proteins on microtubules. [209, 226–228]. Since this exact simulation approach suffers from performance problems when studying many filaments coupled via a diffusive reservoir, we also implement an approximate simulation scheme in which filament-bound motors move deterministically and steric interactions between motor proteins are neglected. To guarantee its validity, the approximate simulation scheme is compared with the results of the exact Gillespie method in the relevant parameter range.

We develop our approximate simulation schema based on theoretic results of the TASEP-LK model [209, 210]: In the limiting case of low densities, the dynamics of the mean motor proteins on the filament is described by the mean-field equation

$$\partial_t m(s,t) = -v_m \partial_s m(s,t) + k_{on} m(s,t)\,. \tag{2.43}$$

While this result follows strictly from full stochastic dynamics, it can also be obtained from deterministic dynamics where during the time interval Δt the position s_i of the motor proteins is updated as

$$s_i^{n+1} \to s_i^n + v_m \Delta t\,, \tag{2.44}$$

i.e. all motor proteins move ballistically with the same speed v_m. Moreover, for sufficiently high depolymerization rates and low densities, TASEP-LK predicts that the depolymerization rate $\tilde{v}_s$ is given by [63]

$$\tilde{v}_s = v_m\, m(l)[1 - m(l)] = a\, m^+ \delta\,. \tag{2.45}$$

Neglecting effects from particle exclusion, this reduces to $\tilde{v}_s = v_m\, m(l) = a\, m^+ \delta$, i.e., instead of explicitly modeling each depolymerization event, one can simply move the motor forward and if $s_i > l$ depolymerize the filament. Both approximations have the key advantage that they can be performed in parallel in the case of a spatially extended system with many motor proteins. To ensure that several motors do not depolymerize the filament within one iteration step, the time step must be chosen sufficiently small. Throughout all of our simulations we choose $\Delta t = 0.01\,s$. With a motor speed of $v_m = 0.06\,\mu m s^{-1}$, this means that 'double' depolymerization events will only occur if the distance between two consecutive motors is less then $6 \times 10^{-3}\,\mu m$, which is less then the length a of a tubulin unit. Figure 2.14 shows a comparison between the filament length at steady state obtained by a full stochastic simulation and our approximate simulation scheme.

		Experiment	Theory	Simulation	Ref.
Motor parameters					
Motor velocity	v_m	$0.053\,\mu m\,s^{-1}$	$0.06\,\mu m\,s^{-1}$	$0.06\,\mu m\,s^{-1}$	[175]
Cytosolic motor diffusion	D_M	—	$0.5\,\mu m^2 s^{-1}$	$0.5\,\mu m^2 s^{-1}$	—
Attachment rate	k_{on}	$0.13\,\mu m^3 s^{-1}\mu m^{-1}$	$0.12\,\mu m^3 s^{-1}\mu m^{-1}$	$40\,s^{-1}\mu m^{-1}$	[175]
Detachment rate	k_{off}	$5\times10^{-3}\,s^{-1}$	$0\,s^{-1}$	$0\,s^{-1}$	[175]
Depolymerization rate	δ	$2.3\,s^{-1}$	— ($2.3\,s^{-1}$)	— ($2.3\,s^{-1}$)	[175]
Tubulin and filament parameters					
Size of a tubulin dimer	a	8.4 nm	8.4 nm	8.4 nm	[222]
Polymerization rate	γ	$6.3\times10^{-4}\,\mu m^3 s^{-1}$	$1\times10^{-3}\,\mu m^3\,s^{-1}$	$0.33\,s^{-1}$	[60]
Cytosolic tubulin diffusion	D_T	$6\,\mu m^2 s^{-1}$	$6\,\mu m^2 s^{-1}$	$6\,\mu m^2 s^{-1}$	[223]
Volume per filament	V_0	—	$0.5\,\mu m^3$	$0.5\,\mu m^3$	—

Table 2.1: Experimentally measured parameters for the kinesin-8 homolog Kip3 from *Saccharomyces cerevisiae* and parameters chosen in our theoretical discussion. The experimental parameters are meant to provide the correct order of magnitude. The qualitative results of our analysis are not sensitive to the choice of specific parameters (as long as the parameters are in a comparable range). To convert experimental rates into rates required for our simulation we used $r_M = r_T = 0.04\,\mu m$ and $L_z = 0.6\,\mu m$. If not explicitly stated otherwise we used parameters as specified in the column Theory.

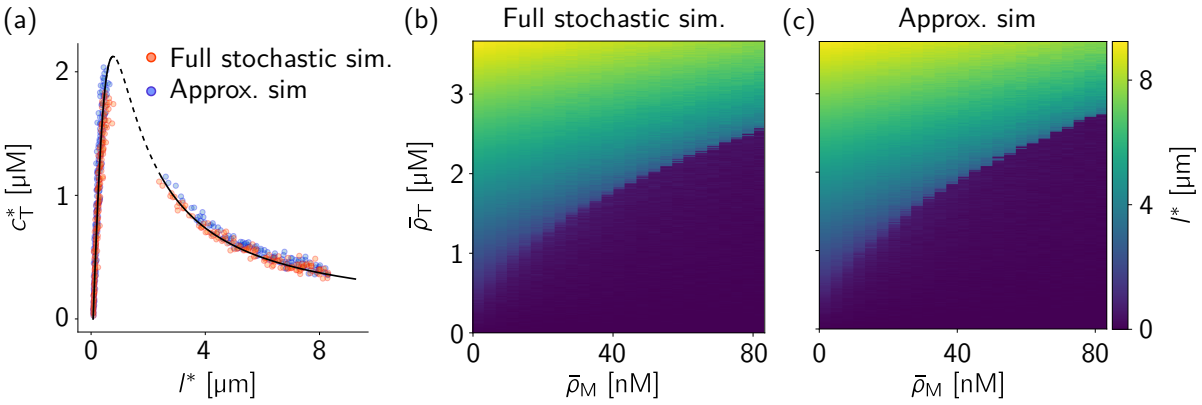

Figure 2.14: Comparison between an exact (Gillespe algorithm) stochastic simulation and our approximate simulation scheme for a single filament. For the relevant parameter range, we find good agreement between the approximate and exact simulation schemes. Filaments were initialized fully polymerized (all tubulin incorporated in the microtubule) for all simulations. Parameters are chosen as specified in Tab. 2.1. (a) Steady-state cytosolic tubulin concentration as a function of the steady-state filament length for $\rho_M = 30\,nM$. The symbols indicate simulation results, the solid black line represents the analytical result; see Eq. (1) in the main text. The dashed line indicates the range of unstable fixed points in the bi-stable parameter range (see Sec. 2.5 and Fig. 2.18 (b) for an explanation). (b)-(c) Filament length l^* in steady state as a function of ρ_M and ρ_T. The results of the exact and approximate simulation schemes agree very well over the entire parameter range.

SPATIALLY EXTENDED SYSTEM

Filament dynamics: A filament in the spatially extended system is characterized by its minus end position $\mathbf{b}_i$, orientation θ_i, and length l_i. The positions and orientations of the minus ends are ini-

tially drawn from a uniform distribution and remain unchanged throughout the simulation. Free tubulin units are inizialized at random positions within the simulation box. The stochastic dynamics of the free tubulin units is implemented as follows: First, we check whether filament plus ends are within the distance r_T of the tubulin unit. For each plus end $(0\dots k)$ within range, a reaction time τ_k is drawn from an exponential distribution; $\tau_k \sim \gamma^{\text{sim}} \exp(\gamma^{\text{sim}} t)$. We choose the smallest reaction time τ_k that fulfills $\tau_k < \Delta t$, where Δt denotes the time increment of the simulation, and perform the respective growth event. If there is no filament plus end in range or if all reaction times are $\tau_k > \Delta t$, we let the tubulin unit perform a free diffusive motion implemented by a Brownian dynamics algorithm [229]. This is the position $\mathbf{x}_i^n = (x_i^n, y_i^n)$ of the tubulin unit is updated as

$$x_i^{n+1} \to x_i^n + A r_i^n \,, \tag{2.46}$$

$$y_i^{n+1} \to x_i^n + A r_i^n \,. \tag{2.47}$$

Here r^n are independent and identically distributed random variables with zero mean and A is an amplitude chosen such that the fluctuation dissipation theorem is satisfied [230]. Importantly, however, it is not necessary for the random numbers to be Gaussian-distributed [229]. Here, we choose uniform random numbers in the interval $(-0.5, 0.5)$ as this has several implementation-specific advantages. Since the variance of uniformly distributed random variables is given by $\langle (r^n)^2 \rangle = 1/12$ this results in $A = \sqrt{24 D_T \Delta t}$. The pseudocode for the stochastic dynamics of cytosolic tubulin units is given in Algorithm 2.

Motor dynamics: The motors can be either filament-bound or free (cytosolic). We perform simulations of the stochastic dynamics of cytosolic motors analogous to that of cytocolic tubulin. First, we determine all potential binding partners, i.e., all filaments $(0\dots k)$ that intersect with a radius r_M around the motor position $\mathbf{x}_i = (x_i, y_i)$ (see Fig. 2.15). Next, the chord length Δl is calculated; for an illustration see Fig. 2.15(b). The per-capita attachment rate for a single motor protein attaching to the filament is then given by $k_{\text{on}}^{\text{sim}} \Delta l$. Similar as for the free tubulin dynamics, the reaction times $\tau_k \sim k_{\text{on}}^{\text{sim}} \Delta l \exp(-k_{\text{on}}^{\text{sim}} \Delta l\, t)$ are drawn from an exponential distribution and the reaction with the smallest reaction time satisfying $\tau_k < \Delta t$ is executed. If a reaction occurs, the motor starts at a random position within the chord length Δl. If no reaction occurs, the motor protein performs free diffusion, which is implemented in the same way as for free tubulin units. The dynamics of filament-bound motors is implemented as discussed above for single filaments.

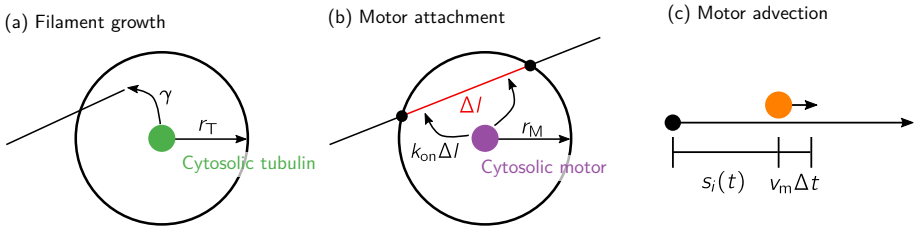

Figure 2.15: (a) Schematic representation for filament growth. If a cytosolic tubulin unit is within a distance r_T of a filament plus end it detaches at rate γ. (b) Analogously, cytosolic motors attach to filaments at the rate $k_{on}\Delta l$ when they are at a distance r_M from the filament. Attachment occurs at a random position on the chord of length Δl. (c) Filament-bound motors move with constant velocity v_m towards the filament plus end.

COMPARISON TO EXPERIMENTAL DATA

We choose the setup of our agent-based model comparable to the experimental system in Rank et al. [63]. The experiments in [63] were performed in a setup where GMP-CPP stabilized microtubules were pre-grown at a concentration of $\bar{\rho}_T = 2\,\mu\text{M}$ in a confined system of $100\,\mu\text{l}$. By varying

the amount of time the microtubules were pre-grown the authors controlled the length distribution of microtubules at the time point of incubation with Kip3. After the initial microtubule growth period the solution was divided into compartments of 25 µl and each compartment was supplemented with a dilution of Kip3 ranging from 0-400 nM. After 60 min of incubation with Kip3 the Kip3-MT interaction was terminated and microfluidic flow channels were constructed to image the microtubules (see Supplemental Material of [63] for details of the experimental setup).

In experiments it is hard to control the precise level of protein concentrations. For example, the concentration of "active" Kip3 could not be determined in [63] since the inactivation of Kip3 during the purification, snap-freezing and thawing process could not be quantified. In addition the authors expect Kip3 to form clusters, which would cause an additional amount of Kip3 that does not participate in the length regulation dynamics in particular for high motor concentrations. In addition to the uncertainties in the protein concentrations, there are measurement inaccuracies because, for example, short microtubules could not be distinguished from tubulin clusters in experiaments. When comparing experiments and agent based simulations we tried to account for this lack of resolution by only taking filament length $l_i > 0.5\,\mu m$ into account. In particular as the protein concentrations that are actively involved in the length regulation process are not known in experiments a quantitative comparison between the experimental data and our agent based simulation is not possible. It is however possible to compare the results on a qualitative level.

In our agent-based simulations we observe a slow initial dynamics consistent with the theoretical result of the linear stability analysis that predicts an initial growth rate of a perturbation which is on the order $\sim \mathcal{O}(10^{-4}s^{-1})$. Once the initial perturbation has grown nonlinear effects start playing a role and the dynamics speeds up significantly. Our agent based simulations show that the system has not yet reached its steady state after one hour of incubation with Kip3, it is rather in the initial phase

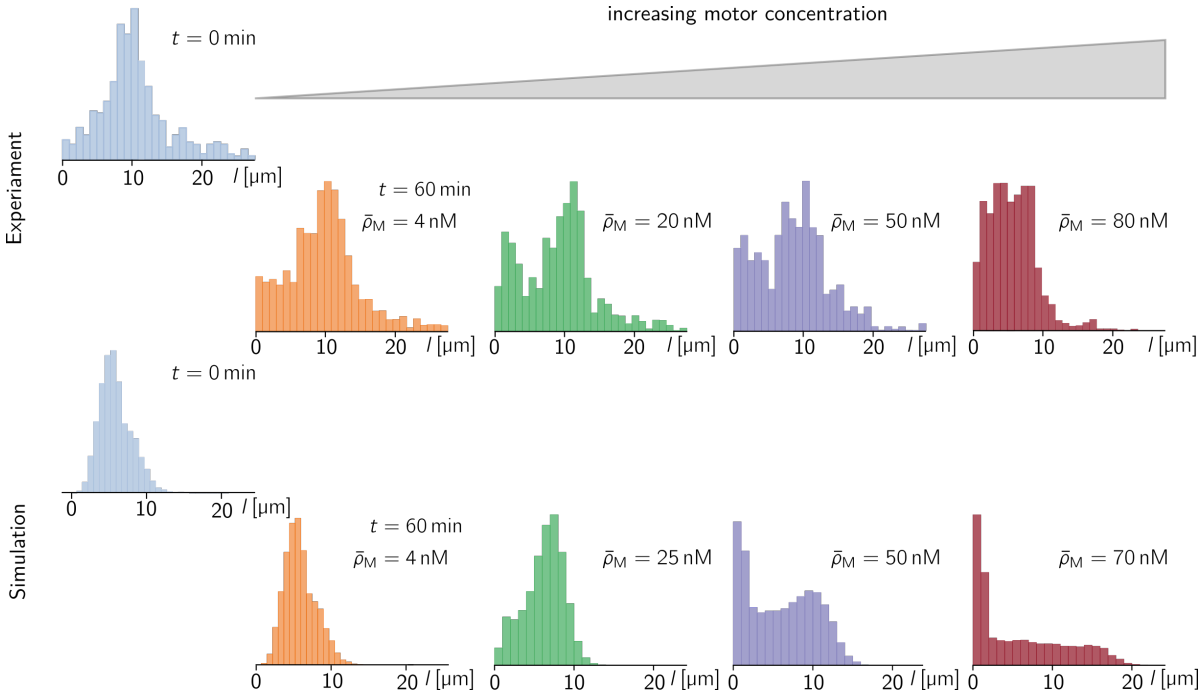

Figure 2.16: Measured filament length distributions after one hour of incubation at various concentrations of Kip3 indicated in the graph. The upper panel shows experimental data taken from [63] and the lower panel shows results obtained from our agent-based simulations. Note that the distributions only show lengths above 0 5µm because smaller lengths could not be distinguished from tubulin clusters in the experiments. The simulation parameters can be found in Tab. 2.1.

of pattern formation (cf. Fig. 4 in the main text). The measured length distribution after 60 min of incubation with Kip3 therefor strongly depend on the initial condition (initial length distribution). In [63] the authors found that for narrow initial length distribution the filament length distributions did not change significantly from the initial length distribution after 60 min of incubation with Kip3 (cf. Fig. S20 in [63]). Those observations are consistent with our theory and observations from the agent based simulation as the initial dynamics is slow (in particular for low motor concentrations) as stated above. For broader initial length distributions the authors observed different behaviour at different concentrations of Kip3 (see upper panel in Fig. 2.16). At low motor concentrations no significant change in the length distribution was observed. At intermediate concentrations the measured length distribution was bi-modal and at high motor concentrations the microtubule length distribution was broad (~ uniform). Those observations are consistent with measurements from our agent-based simulation (see lower panel in Fig. 2.16). Note the volume per microtubule V_0 was estimated to be $1.66\,\mu m^3$ in [63]. Here however we used $V_0 = 0.5\,\mu m^3$ resulting in less resources per filament and therefor shorter microtubules (this was done for the shake of computational feasibility). We used slightly higher tubulin concentrations ($\rho_T \sim 2.5\,\mu M$) in the agent based simulation to obtain similar length distributions. Moreover we find a comparable evolution of the measured microtubule length distribution; see Fig. 2.17.

Our agent-based simulations shows that the microtubule length distribution for narrow initial distributions and low motor concentrations also becomes broad but at significantly later times ($t \gg 60\,\text{min}$). Moreover our simulations suggest that the bi-modal distribution observed in experiments for intermediate motor concentrations is just a transient phenomenon. At later times we observe (in the agent-based simulation) that the length distributions for both intermediate and low motor concentrations becomes more reminiscent of what is observed for high motor concentrations (as long as the concentrations are chosen in a range where patterns form see Fig. 2.18(d)).

We are recognizing that the experimental data available are not sufficient to fully validate our model. A first experimental approach to validate our model would be to repeat the experiments described in [63] and to measure the length distributions over a longer period of time to verify the predictions by our agent based simulations, namely that the length distributions at all motor concentrations were pattern formation is observed become similar. To make further progress in understanding spatiotemporal dynamics, experiments that spatially and temporally resolve tubulin density would be desirable. In particular it would be interesting to systematically sweep the total motor and tubulin concentration in such an experimental system. In this way, the stability diagram Fig. 3(b) could be reproduced experimentally to obtain a quantitative comparison between the predictions of our theory and experiments. For such an experiment, an analysis analogous to that in

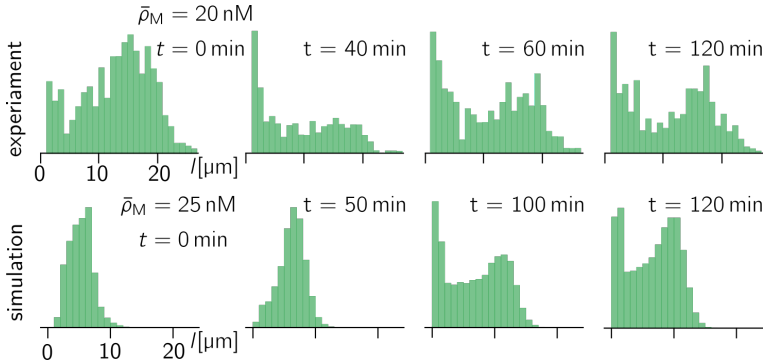

Figure 2.17: Measured filament length distribution at fixed Kip3 concentrations at different time points. The upper panel shows experimental data taken from [63] and the lower panel shows results obtained from our agent-based simulations. Simulation parameters are as specified in Tab. 2.1.

section 2.5 could be made to obtain the wave length and the growth rate of the initial instability. In this way, it would be possible to verify that the qualitative dependencies of these variables on the total motor and tubulin concentration are correctly predicted by our theory.

POINT-LIKE FILAMENT APPROXIMATION

In this section, we provide a detailed analysis of the dynamics in the point-like filament approximation. For the reader's convenience, we repeat the equations that govern the dynamics in this approximation

$$\partial_t l(\mathbf{x},t) = a\gamma c_\mathrm{T}(\mathbf{x},t) - \tilde{v}_\mathrm{s}(\mathbf{x},t)\,, \tag{2.48a}$$

$$\partial_t c_\mathrm{T}(\mathbf{x},t) = D_\mathrm{T}\partial_\mathbf{x}^2 c_\mathrm{T}(\mathbf{x},t) - \left[\gamma c_\mathrm{T}(\mathbf{x},t) - \tilde{v}_\mathrm{s}(\mathbf{x},t)/a\right] V_0^{-1}\,, \tag{2.48b}$$

$$\partial_t \rho_\mathrm{M}(\mathbf{x},t) = D_\mathrm{M}\partial_\mathbf{x}^2 \tilde{c}_\mathrm{M}(\mathbf{x},t)\,, \tag{2.48c}$$

with

$$\tilde{c}_\mathrm{M}(l,\rho_\mathrm{M}) = \frac{\rho_\mathrm{M}}{1+(l/l_\mathrm{c})^2}\,, \tag{2.48d}$$

$$\tilde{v}_\mathrm{s}(l,\rho_\mathrm{M}) = a k_\mathrm{on} l \tilde{c}_\mathrm{M}(l,\rho_\mathrm{M})\,, \tag{2.48e}$$

where $l_\mathrm{c}^2 = 2v_\mathrm{m}V_0/k_\mathrm{on}$. These dynamics conserve the total numbers of tubulin units and motors

$$N_\mathrm{T} = \bar{\rho}_\mathrm{T} L_x L_y = \int_0^{L_x}\mathrm{d}x \int_0^{L_y}\mathrm{d}y \left[c_\mathrm{T}(\mathbf{x},t) + \frac{l(\mathbf{x},t)}{aV_0}\right], \tag{2.49}$$

$$N_\mathrm{T} = \bar{\rho}_\mathrm{M} L_x L_y = \int_0^{L_x}\mathrm{d}x \int_0^{L_y}\mathrm{d}y\, \rho_\mathrm{M}(\mathbf{x},t). \tag{2.50}$$

The corresponding average densities $\bar{\rho}_\mathrm{T}$ and $\bar{\rho}_\mathrm{M}$ will be the main control parameters of interest in the following. We will also discuss the role of the diffusion constants D_T and D_M.

We will first consider the homogeneous steady states, which are fixed points of the single-filament dynamics. In particular, our analysis will show that these fixed points can be read off from a graphical construction in the l–c_T phase plane and that there is a regime of bistability. Next, we will perform a linear stability analysis of the homogeneous steady states against spatial perturbations and discuss various limiting regimes and the role of the diffusion constants D_T and D_M. Finally, we will present numerical simulations of the equations that govern the dynamics in the point-like filament approximation. These simulations capture the patterns that initially emerge from the instability predicted from linear analysis. However, sharp gradients, on scales shorter than the filament lengths, rapidly emerge such that the underlying assumption of point-like filaments is violated.

HOMOGENEOUS STEADY STATES

The homogeneous steady states are given by the fixed points of the polymerization kinetics determined by the local balance of polymerization and depolymerization and conservation of the total density of tubulin

$$a\gamma c_\mathrm{T}^* = \tilde{v}_\mathrm{s}(l^*,\bar{\rho}_\mathrm{M})\,, \tag{2.51a}$$

$$c_\mathrm{T}^* + \frac{l^*}{aV_0} = \bar{\rho}_\mathrm{T}\,. \tag{2.51b}$$

In the l–c_T plane, the solutions to these equations are given by the intersections between the *nullcline* $c_\mathrm{T} = \tilde{v}_\mathrm{s}(l,\bar{\rho}_\mathrm{M})/(a\gamma)$ and the *reactive phase space* $c_\mathrm{T} = \bar{\rho}_\mathrm{T} - l/(aV_0)$; see Fig. 2.18(a,b). This graphical construction allows us to gain insight into the behaviour of the homogeneous steady states as a function of parameters. As long as the slope of the nullcline is larger than $-1/(aV_0)$ for all l, there is

only a single fixed point [Fig. 2.18(a)]. If there is a section where the nullcline slope is more negative than $-1/(aV_0)$, i.e., $\partial_l \tilde{v}_s < -\gamma/V_0$, the reactive phase space can intersect the nullcline three times [Fig. 2.18(b), case (iii)], giving three homogeneous steady states. The bistable region is delimited by saddle-node (also called fold or limit point) bifurcations where the reactive phase space is tangential to the nullcline, i.e. where the nullcline slope is $\partial_l \tilde{v}_s = -\gamma/V_0$.

To determine the stability against these steady states against spatially homogeneous perturbations, we linearize Eq. (2.48a) under the mass conservation constraint $c_T + l/(aV_0) = \bar{\rho}_T$ which yields $\partial_t \delta l = \sigma_{poly} \delta l$, with $\sigma_{poly} = \gamma/V_0 + \partial_l$. Thus, the steady state that lies on the nullcline section with $\partial_l \tilde{v}_s < -\gamma/V_0$ is unstable against spatially homogeneous perturbations (empty disk) while the other two are stable (filled disks).

The locations of these limit point bifurcations can be estimated by simple approximations, which highlight the role of the various parameters for the location of the bistable regime in the $\bar{\rho}_M$–$\bar{\rho}_T$ diagram. Near the apex of the nullcline at $l = l_c$ [marked by a red, dashed line in Fig. 2.18(a,b)], its curvature is large such the slope $\partial_l \tilde{v}_s$ reaches $-\gamma/V_0$ near the apex. Substituting $l^* = l_c$ into the total density of tubulin and using $a\gamma c_T^* = \tilde{v}_s(l^*)$ yields

$$\bar{\rho}_T^{apex} = \frac{l_c}{aV_0} + \frac{\tilde{v}_s(l_c)}{a\gamma} = \sqrt{\frac{2v_m V_0}{k_{on}}} \left(\frac{1}{aV_0} + \frac{k_{on}}{2\gamma} \bar{\rho}_M \right). \tag{2.52}$$

This shows that there is a linear relation between the motor density $\bar{\rho}_M$ and tubulin density at the apex, $\bar{\rho}_T^{apex}$ [red line Fig. 2.18(c)]. Note that this provides a good approximation of the upper edge of

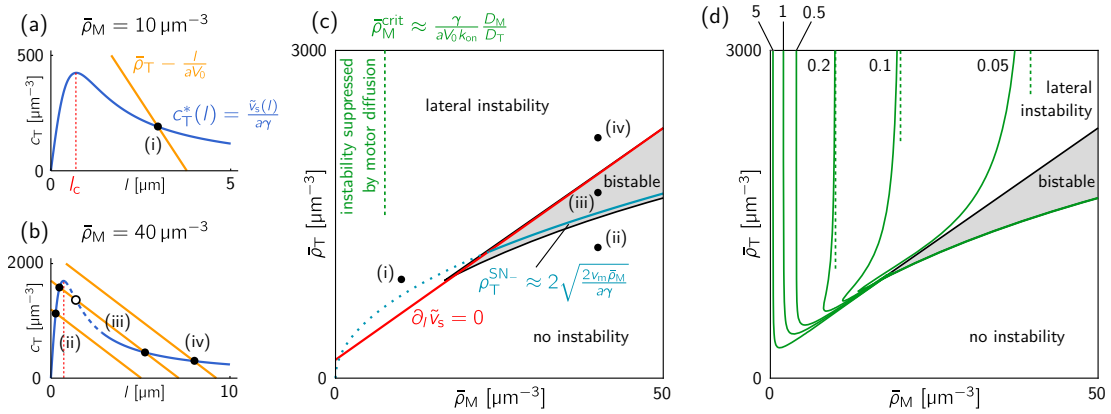

Figure 2.18: Homogeneous steady states and linear stability analysis for the point-like filament approximation, Eqs. (2.48a)–(2.48e). (a), (b) l–c_T phase plane analysis showing the graphical construction of the homogeneous steady states in the monostable case (a) and the bistable case (b). Homogeneous steady states are fixed points (black disks) of the length-regulation dynamics, found as intersection points of the nullcline $c_T^*(l) = \tilde{v}_s(l)/(a\gamma)$ (blue line) and the mass-conservation constraint for tubulin (orange line), $c_T = \bar{\rho}_T - l/(aV_0)$. The red dashed line marks the apex of the nullcline at l_c. (c) Stability diagram in the $\bar{\rho}_M$–$\bar{\rho}_T$ plane. Black points labelled (i)–(iv) correspond to the scenarios shown in (a) and (b). The bistable regime (shaded in gray) is delimited by limit point bifurcations (black lines). The red line, given by Eq. (2.52), separates the regions of positive and negative nullcline slope. Negative nullcline slope is a necessary condition for lateral instability. In addition lateral instability requires sufficiently large motor density $\bar{\rho}_M > \bar{\rho}_T^{crit}$, which is set by the diffusivity ratio D_T/D_M [see panel (d)]. Below this threshold, instability is suppressed by motor diffusion as explained in the main text. (d) Contour lines of the critical diffusivity ratio D_T/D_M above which the system is laterally unstable [cf. Eq. (2.65)]. For large $\bar{\rho}_T$, this ratio becomes independent of $\bar{\rho}_T$ and sets a threshold for the minimal motor density $\bar{\rho}_T^{crit} \propto D_M/D_T$ as indicated by the dashed green lines [cf. panel (b)].

the bistable regime.

To estimate lower edge of the bistable regime, we approximate consider the limit $l^* \gg l_c$. To lowest order, this yields $l^* \approx aV_0\bar{\rho}_T$ and $\partial_l \tilde{v}_s \approx ak_{on}l_c/l^2$. These approximations, substituted in to the criterion $\partial_l \tilde{v}_s = -\gamma/V_0$ yield

$$\bar{\rho}_T^{SN-} \approx 2\sqrt{\frac{2v_m\bar{\rho}_M}{a\gamma}}, \tag{2.53}$$

which is plotted as a teal line in Fig. 2.18(c).

Together, the estimates Eq. (2.52) and Eq. (2.53) reveal how the boundaries of the bistable regime depend on the system parameters. Increasing the polymerization rate γ moves the bistable regime to lower tubulin densities and reduces its size while increasing the motor velocity v_m move the bistable regime to higher tubulin densities. The attachment rate k_{on} and volume per filament V_0 only affect the upper boundary of the bistable regime, moving it to higher tubulin densities when increased.

LINEAR STABILITY ANALYSIS

Let us now analyse the stability of the homogeneous steady states against spatial perturbations. For a more compact notation, we combine the field variables into the vector $\mathbf{u} = (l, c_T, \rho_M)$. The homogeneous steady states are then $\mathbf{u}^* = (l^*, c_T^*, \bar{\rho}_M)$. Writing the spatial perturbations in terms of Fourier modes

$$\mathbf{u}(x,t) = \mathbf{u}^* + \delta\mathbf{u}_q e^{i\mathbf{q}\cdot\mathbf{x}+\sigma t}, \tag{2.54}$$

where $\mathbf{q}$ denotes the wave vector, and linearizing Eqs. (2.48) for small $\delta\mathbf{u}_q$ yields an eigenvalue problem for the growth rates $\sigma(q)$

$$J(q)\delta\mathbf{u}_q = \sigma(q)\delta\mathbf{u}_q \tag{2.55}$$

with the Jacobian (or stability matrix)

$$J(q) = \begin{pmatrix} -\partial_l \tilde{v}_s & a\gamma & -\partial_{\rho_M}\tilde{v}_s \\ \partial_l \tilde{v}_s/(aV_0) & -\gamma/V_0 - D_T q^2 & \partial_{\rho_M}\tilde{v}_s/(aV_0) \\ -D_M q^2 \partial_l \tilde{c}_M & 0 & -D_M q^2 \partial_{\rho_M}\tilde{c}_M \end{pmatrix}_{\mathbf{u}^*}. \tag{2.56}$$

In the following, we omit the subscript $\mathbf{u}^*$, with the understanding that all expressions are evaluated in the homogeneous steady state.

For spatially uniform perturbations, $q = 0$, the last row of the Jacobian vanishes and the eigenvalues of $J(0)$ are given by

$$\sigma_1 = \sigma_2 = 0, \quad \sigma_3 = -\partial_l \tilde{v}_s - \frac{\gamma}{V_0}. \tag{2.57}$$

The two zero eigenvalues correspond to perturbations that would change the average total densities $\bar{\rho}_T$ and $\bar{\rho}_M$, respectively. In a closed system with conservation of mass, however, these disturbances are not possible. Thus, the remaining eigenvalue σ_3 determines the stability to homogeneous perturbations that respect conservation of mass. One finds an instability for $\partial_l \tilde{v}_s < -\frac{\gamma}{V_0}$, which confirms the geometric criterion (in the in the l–c_T phase space) discussed above.

In general, the stability of a spatially uniform steady state against spatial perturbations with a wave number q is determined by the dispersion relation $\sigma(q)$; a typical dispersion relation in the laterally unstable parameter regime is shown in Fig. 3(a) in the main text.

While the eigenvalues of the full 3×3 Jacobian Eq. (2.56) can in principle be found analytically, the resulting expressions are not insightful. We therefore determine the eigenvalues numerically. Notably, we find that the instability is always of long-wavelength type, i.e., the band of unstable modes extends to $q \to 0$. Next, we will further analyze this long-wavelength limit. Further below, we will also consider the limit of well-mixed tubulin. In both these limits the resulting effective Jacobians are 2×2 matrices which allows us to find closed expressions for the instability criteria.

Long-wavelength limit: Since we numerically find that instability onset is always at long wavelengths, i.e. in the limit $q \to 0$, we can determine the instability criterion by considering the limit of small wavenumbers q. In this long-wavelength limit, we can make the local quasi-steady state approximation $l(x,t) \approx l^*(x,t)$, $c_\mathrm{T}(x,t) \approx c_\mathrm{T}^*(x,t)$, where the local equilibrium (l^*, c_T^*) depends on the local total densities ρ_T, ρ_M. The dynamics for the tubulin density is obtained by adding the equations for l and c_T, Eqs. (2.48)(a,b). Using the local quasi-steady state approximation then yields

$$\partial_t \rho_\mathrm{T} = D_\mathrm{T} \nabla^2 c_\mathrm{T}^*(\rho_\mathrm{T}, \rho_\mathrm{M}) \,, \tag{2.58a}$$

$$\partial_t \rho_\mathrm{M} = D_\mathrm{M} \nabla^2 \tilde{c}_\mathrm{M}[l^*(\rho_\mathrm{T}, \rho_\mathrm{M}), \rho_\mathrm{M}] \,. \tag{2.58b}$$

The respective long-wavelength (LW) Jacobian is given by

$$J_\mathrm{LW}(q) = -q^2 \begin{pmatrix} D_\mathrm{T} \partial_{\rho_\mathrm{T}} c_\mathrm{T}^* & D_\mathrm{T} \partial_{\rho_\mathrm{M}} c_\mathrm{T}^* \\ D_\mathrm{M} \partial_{\rho_\mathrm{T}} \tilde{c}_\mathrm{M} & D_\mathrm{M} \partial_{\rho_\mathrm{M}} \tilde{c}_\mathrm{M} \end{pmatrix} , \tag{2.59}$$

and its eigenvalues read (as for any 2×2 matrix)

$$\sigma_{1,2}(q) = \frac{1}{2} \Big[\operatorname{tr} J_\mathrm{LW}(q) \pm \sqrt{\big(\operatorname{tr} J_\mathrm{LW}(q)\big)^2 - 4 \det J_\mathrm{LW}(q)} \Big] \,. \tag{2.60}$$

Therefore, there is an instability (positive eigenvalue σ_i) either when the trace $(\sigma_1 + \sigma_2)$ is positive or when the determinant $(\sigma_1 \cdot \sigma_2)$ is negative. Moreover, when the determinant is positive, $\det J_\mathrm{LW} > 0$, the eigenvalues' real parts cross zero as a pair of complex conjugates when $\operatorname{tr} J_\mathrm{LW}$ crosses zero. This indicates an oscillatory instability (Hopf bifurcation) where the oscillation frequency is determined by the imaginary part of the eigenvalues. (Further away from the onset of instability, imaginary part vanishes for the fastest growing mode, so the instability loses it's oscillatory character; see Fig. 3(a) in the main text.) $J_\mathrm{LW}(q)$ has a positive trace if

$$D_\mathrm{T} \partial_{\rho_\mathrm{T}} c_\mathrm{T}^* + D_\mathrm{M} \, \partial_{\rho_\mathrm{M}} \tilde{c}_\mathrm{M} < 0 \,. \tag{2.61}$$

We will discuss this instability criterion below. Since, $\det J_\mathrm{LW} > 0$, the instability will be oscillatory near onset, as noted above.

A positive eigenvalue could also result from a negative determinant. However, numerically, we find that the determinant seems to be always positive, although we could not show this analytically. There is also a physical reasoning why the determinant should always be positive. First, observe that the diffusion constants can be factored out. The remaining term, which then determines the sign of the determinant is independent of the diffusion constants. Therefore, if this term were negative, it would imply an instability independent of the diffusion constants. This is at odds with physical intuition for a diffusion driven lateral instability, in particular, because sufficiently fast motor diffusion will always act to suppress lateral instability.

Let us now analyze the stability criterion Eq. (2.61). First consider the case $D_\mathrm{M} = 0$. Then the instability condition simply reads $\partial_{\rho_\mathrm{T}} c_\mathrm{T}^* < 0$, which can be understood as follows. When $D_\mathrm{M} = 0$, the total motor density remains constant under the dynamics and therefore spatially uniform (by choice of initial condition). The only dynamic variable in the long-wavelength limit is then the tubulin density, governed by

$$\partial_t \rho_\mathrm{T} = D_\mathrm{T} \nabla^2 c_\mathrm{T}^*(\rho_\mathrm{T}, \bar{\rho}_\mathrm{M}) = \nabla \big[D_\mathrm{T} \partial_{\rho_\mathrm{T}} c_\mathrm{T}^*(\rho_\mathrm{T}, \bar{\rho}_\mathrm{M}) \nabla \rho_\mathrm{T} \big] , \tag{2.62}$$

where we used the chain rule for the second equality. This is a diffusion equation with effective diffusion constant $D_\mathrm{T} \partial_{\rho_\mathrm{T}} c_\mathrm{T}^*$. Thus, if $\partial_{\rho_\mathrm{T}} c_\mathrm{T}^*$ is negative, there is an instability corresponding to effective "anti-diffusion." This is the basic mechanism underlying mass-redistribution instability in the

long-wavelength limit [213]. This shows that the basic mechanism of the instability is the same as in protein-based pattern forming systems like the ones discussed in [211].

In the main text, we discuss the stability condition based on the nullcline slope $\partial_l \tilde{v}_s$. To relate the derivative $\partial_{\rho_T} c_T^*$ to the nullcline slope $\partial_l \tilde{v}_s$, we apply the derivative ∂_{ρ_T} to the fixed point equations Eq. (2.51) which yields

$$\partial_{\rho_T} c_T^* = \frac{\partial_l \tilde{v}_s}{\frac{\gamma}{V_0} + \partial_l \tilde{v}_s}. \tag{2.63}$$

Thus, along sections of the nullcline where $\partial_l \tilde{v}_s > -\gamma/V_0$ (implying stability against homogeneous perturbations), the lateral instability condition $\partial_{\rho_T} c_T^* < 0$ is analogous to the slope condition $\partial_l \tilde{v}_s < 0$ discussed in the main text. In the $\bar{\rho}_M$–$\bar{\rho}_T$ plane, the line $\bar{\rho}_T^{\text{apex}}(\bar{\rho}_M)$, marks the nullcline apex where $\partial_l \tilde{v}_s = 0$ [red line in Fig. 2.18(c)]. Above this line, the nullcline slope is negative, and therefore, the homogeneous steady state is laterally unstable. In other words, a sufficiently high tubulin density compared to the motor density is required for the instability to occur.

In the bistable regime, we have to distinguish between the two stable steady states. Notably, the nullcline slope is always negative for the large-l fixed point (see Fig. 2.18(c). Therefore, this fixed point always laterally unstable. In contrast the low-l fixed point is unstable only in a very narrow regime due to the high nullcline curvature near its apex. In the stability diagram in Fig. 3(b) in the main text, we show the stability of the large-l fixed point.

The above conditions for lateral instability are necessary and sufficient in the case $D_M = 0$. Let us now turn to the case $D_M > 0$. As we heuristically argued in the main text, motor diffusion generally counteracts lateral instability. Indeed, the stability threshold $\operatorname{tr} J_{LW} = 0$ obtained from the above linear stability analysis gives

$$D_T \partial_{\rho_T} c_T^* = -D_M \partial_{\rho_M} \tilde{c}_M \,. \tag{2.64}$$

Substituting Eq. (2.63) for $\partial_{\rho_T} c_T^*$ and using $\partial_{\rho_M} \tilde{c}_M = \tilde{c}_M/\bar{\rho}_M$ [cf. Eq. (2.48d)], we can write this condition as

$$\frac{D_T}{D_M} = \frac{\tilde{c}_M}{\bar{\rho}_M} \frac{\frac{\gamma}{V_0} + \partial_l \tilde{v}_s|_{l^*}}{-\partial_l \tilde{v}_s|_{l^*}}\,, \tag{2.65}$$

determining the threshold value for the ratio of the diffusion constants D_T/D_M. For diffusivity ratios below this threshold, i.e. for too fast motor diffusion, the instability is suppressed [see red lines in Fig. 2.19]. In Fig. 2.18(d), contour lines show the instability threshold in the $\bar{\rho}_M$–$\bar{\rho}_T$ plane for several diffusivity ratios.

Notably, for sufficiently large $\bar{\rho}_T$, the threshold becomes independent of $\bar{\rho}_T$. The critical motor density $\bar{\rho}_M^{\text{crit}}$ in this regime is indicated by the he dashed green lines in Fig. 2.18(c,d). To obtain an estimate for this critical motor density D_T/D_M, we approximate Eq. (2.65) in the limit $l^* \gg l_c$ and solve for $\bar{\rho}_M$:

$$\bar{\rho}_M^{\text{crit}} \approx \frac{\gamma}{a k_{on} V_0} \frac{D_M}{D_T}. \tag{2.66}$$

This shows that the critical motor density is proportional to the diffusivity ratio D_M/D_T. A higher motor diffusivity requires a higher motor density for the instability to occur. At first glance, this may seem somewhat counterintuitive. The reason for this effect is that increasing the motor density increases the magnitude of the nullcline slope since $\tilde{v}_s \propto \rho_M$. This, in turn, increases the growth rate of the tubulin-mass-redistribution instability [cf. Eq. (2.62)], which allows it to overcome the stabilizing effect of motor diffusion. Physically, a steeper nullcline slope means that gradients in the filament length lead to steeper gradients in cytosolic tubulin concentration.

Substituting the values for a, γ, and k_{on} from Table 2.1 into Eq. (2.65) yields the condition for the number of motors per filament, $V_0 \bar{\rho}_M \gtrsim 0.57 D_M/D_T$, as given in the main text. In the $\bar{\rho}_M$–$\bar{\rho}_T$ diagram, Eq. (2.66) sets an approximate lower bound for the unstable region [see dashed green lines in Fig. 2.18(c,d)]. Below this threshold, the instability is suppressed by motor diffusion. In the

limit $D_T \gg D_M$, the critical value $\bar{\rho}_M^{crit}$ goes to zero. For physiological parameters and the estimated diffusivity ratio $D_T/D_M \approx 6$, the threshold is at about $V_0\bar{\rho}_M^{crit} \approx 0.1$ motors per filament.

Well-mixed cytosolic tubulin: Above, we have analyzed the long-wavelength limit, where the polymerization kinetics can be assumed to be in a local quasi-steady state. We now turn to the dynamics at short wavelengths, where cytosolic diffusion of tubulin is faster than the polymerization kinetics. Relaxation to the local steady state length happens at the rate $\sigma_{poly} = \gamma/V_0 + \partial_l \tilde{v}_s$, which we derived in the stability analysis for homogeneous perturbations above. The rate of diffusive transport for modes with wavenumber q is given by $D_T q^2$. Thus, for wavenumbers $q \gg \sqrt{|\sigma_{poly}|/D_T}$, the cytosolic tubulin density can be assumed well-mixed. (A detailed discussion of this "*reaction-limited regime*" and the complementary "*diffusion-limited regime*" at large wavelengths is given in Ref. [213] in the context of mass-conserving two-component reaction–diffusion equations.)

For spatial non-uniform perturbations ($q \neq 0$), a well-mixed (WM) cytosolic tubulin implies $\delta c_T = 0$. Thus, the reduced Jacobian is obtained by removing the central row and column from the full Jacobian J, Eq. (2.56), and reads

$$J_{WM}(q) = \begin{pmatrix} -\partial_l \tilde{v}_s & -\partial_{\rho_M} \tilde{v}_s \\ -D_M q^2 \partial_l \tilde{c}_M & -D_M q^2 \partial_{\rho_M} \tilde{c}_M \end{pmatrix}. \tag{2.67}$$

As above the eigenvalues of this 2×2 matrix can be obtained from its determinant and trace

$$\det J_{WM}(q) = D_M q^2 k_{on} \tilde{c}_M^2/\rho_M > 0\,, \tag{2.68}$$

$$\mathrm{tr}\, J_{WM}(q) = -\partial_l \tilde{v}_s - D_M q^2 \tilde{c}_M/\rho_M\,, \tag{2.69}$$

where we used $\tilde{v}_s \propto \tilde{c}_M \propto \rho_M$ [cf. Eq. (2.48d,e)] such that $\partial_{\rho_M} \tilde{c}_M = \tilde{c}_M/\rho_M$ and $\partial_{\rho_M} \tilde{v}_s = \tilde{v}_s/\rho_M$. Figure 3(a) in the main text shows that the dispersion relation derived $J_{WM}(q)$ agrees well with the dispersion relation of the full Jacobian, Eq. (2.56), for sufficiently large q. Since the $\det J_{WM}(q)$ is always positive, $J_{WM}(q)$ has an unstable eigenvalue if and only if $\mathrm{tr}\, J_{WM}(q) > 0$. Thus, if $-\partial_l \tilde{v}_s > 0$, there is a band of unstable modes $q \in (0, q_{max})$ with

$$q_{max}^2 = -\frac{\partial_l \tilde{v}_s}{D_M} \frac{\bar{\rho}_M}{\tilde{c}_M}. \tag{2.70}$$

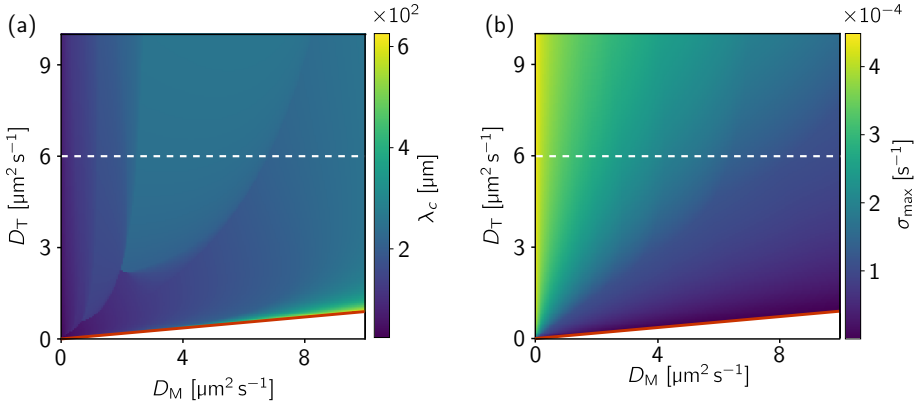

Figure 2.19: (a) Wavelength and (b) growth rate of the fastest growing mode in as a function of the diffusion constants D_M and D_T. The white dashed line indicates the physiological diffusion constant of tubulin. Remaining parameters are as in Fig. 4 in the main text. The boundary of the regime of instability is indicated by a red line, corresponding to the critical diffusivity ratio given by Eq. (2.65).

This shows that cytosolic motor diffusion suppresses a lateral instability on short length scales. In particular, the band of unstable modes vanishes in the limit $D_M \to \infty$. Therefore, an approximation in which both the cytosolic tubulin and the motors are assumed to be well-mixed will not reproduce the instability.

Equation (2.70), derived under the assumption of well-mixed cytosolic tubulin, only the approximates the band of unstable modes of the full Jacobian Eq. (2.56). This approximation is valid if $q_{max}^2 D_T \gg |\sigma_{poly}|$. Substituting the expressions and rearranging the terms yields the condition

$$\frac{D_T}{D_M} \gg \frac{\tilde{c}_M}{\bar{\rho}_M} \frac{\frac{\gamma}{V_0} + \partial_l \tilde{v}_s|_{l^*}}{-\partial_l \tilde{v}_s|_{l^*}} . \tag{2.71}$$

Comparing to Eq. (2.65) shows that the approximation is valid deep in the unstable regime, far from the instability threshold.

THE ROLE OF FINITE FILAMENT DIFFUSION:

In a general filaments diffuse with a diffusion constant that depends on filament length $D_{MT}(l)$, with longer filaments diffusing slower than shorter ones.

Within the framework of the point-like filament approximation, filament diffusion can be incorporated into the model by introducing an additional equation of motion for the filament minus end density $\rho_{MT}(\mathbf{x}, t)$. As filaments are neither produced nor destroyed this equation of motion is a simple diffusion equation with length dependent diffusion constant $D_{MT}(l)$.

$$\partial_t \rho_{MT}(\mathbf{x}, t) = \nabla [D_{MT}(l) \nabla \rho_{MT}(\mathbf{x}, l)] . \tag{2.72}$$

Linearizing this equation around the spatially homogeneous steady state $(l^*, c_T^*, \bar{\rho}_M, \bar{\rho}_{MT})$ results in

$$\partial_t \delta\rho_{MT}(\mathbf{x}, t) = D_{MT}(l^*) \nabla^2 \delta\rho_{MT}(\mathbf{x}, l) . \tag{2.73}$$

Notably, in the linearized dynamics, the length-dependent diffusion coefficient enters only via the steady state length l^*. Since this length is large, the corresponding diffusion coefficient will be much smaller than the monomer diffusion constant and can therefore be neglected in the linear stability analysis.

What would be the effect of such length-dependent filament diffusion beyond the linear regime? Consider a "phase-separated" state with low and high density regions. In the low density regions, filaments are short and therefore would diffuse rapidly, whereas filaments in the high density region are long and therefore diffuse slowly. Thus filament diffusion would lead to a net influx of short filaments into the high density regions while the long filaments remain (nearly) fixed in space. This influx of tubulin mass into high density regions would further amplify the phase separation process. In fact, density dependent diffusion alone is able to drive phase separation, if the diffusion coefficient decreases rapidly enough with increasing density. This is the mechanism underlying motility-induced phase separation of run-and-tumble particles [231]. To check if this intuitive understanding holds true we perform agent based simulations in a one-dimensional system containing filaments which diffuse with a length dependent diffusion coefficient. Explicitly we choose the functions $D_{MT}(l) = 0$ (Movie 3), $D_{MT}(l) = D_T/(1 + l/a)$ (Movie 4) and $D_{MT}(l) = D_T/\sqrt{1 + l/a}$ (Movie 5). The other parameters were chosen as in the main text. We find that the mass redistribution instability occurs for all chosen filament diffusion coefficient functions. Investigating the precise role of filament diffusion on the self-organized patterns and their dynamics (e.g. coarsening) is beyond the scope of this work.

THE ROLE OF FINITE TUBULIN NUCLEOTIDE EXCHANGE

In the cell, cytosolic tubulin cycles between a GTP-bound (active) and a GDP-bound (inactive) state. In general cytosolic tubulin that is incorporated into the microtobule is in the active state and upon depolymerization is released in the inactive state. Inactive cytosolic tubulin is then converted into GTP-tubulin by nucleotide exchange. In the model studied in the main text we assume a fast nucleotide exchange rate meaning that GDP-tubulin is rapidly converted into GTP-tubulin such that we can neglect the transient inactive state. In the following, we relax this assumption by extending the model to also account for inactive cytosolic tubulin and show under which conditions it can be neglected. The dynamic equations of this extended model read

$$\tilde{v}_\mathrm{s}(l,\rho_\mathrm{M}) = a\,k_\mathrm{on}\,l\,\frac{\rho_\mathrm{M}}{1+l^2/l_c^2}, \tag{2.74}$$

$$\partial_t l(\mathbf{x},t) = a\gamma\, c_\mathrm{TT}(\mathbf{x},t) - \tilde{v}_\mathrm{s}(\mathbf{x},t), \tag{2.75}$$

$$\partial_t c_\mathrm{TD}(\mathbf{x},t) = D_\mathrm{T}\nabla^2 c_\mathrm{TD}(\mathbf{x},t) - \omega c_\mathrm{TD}(\mathbf{x},t) + \frac{\tilde{v}_\mathrm{s}(\mathbf{x},t)/a}{V_0}, \tag{2.76}$$

$$\partial_t c_\mathrm{TT}(\mathbf{x},t) = D_\mathrm{T}\nabla^2 c_\mathrm{TT}(\mathbf{x},t) - \frac{\gamma c_\mathrm{TT}(\mathbf{x},t)}{V_0} + \omega c_\mathrm{TT}(\mathbf{x},t), \tag{2.77}$$

$$\partial_t \rho_\mathrm{M}(\mathbf{x},t) = D_\mathrm{M}\nabla^2 \tilde{c}_\mathrm{M}[l(\mathbf{x},t),\rho_\mathrm{M}(\mathbf{x},t)]\,, \tag{2.78}$$

where (c_TT) and (c_TD) denote the concentrations of GTP-bound and GDP-bound tubulin in the cytosol and ω is the nucleotide exchange rate. In the limit $\omega \to \infty$, this model reduces to the one discussed in the main text. We can estimate the typical time a GTP-bound tubulin spends in the cytosol before binding as V_0/γ. If this timescale is longer the typical time ω^{-1} before a GDP-bound tubulin is converted to the GTP-bound form, we can neglect the transient inactive state. For the parameters used throughout this work (see Tab. 2.1), this estimate suggests that finite nucleotide exchange is relevant for $\omega < \mathcal{O}(10^{-3}\mathrm{s}^{-1})$.

In order to investigate the extent to which the finite nucleotide exchange rate impacts the dynamics of the model even beyond this limit we perform a linear stability analysis of the extended model. Figure 2.20 shows the stability diagram in the $(\rho_\mathrm{M},\rho_\mathrm{T})$ parameter space for different nucleotide exchange rates ranging over 4 orders of magnitude ($\omega = 10^{-4}\ldots10^{-1}\,\mathrm{s}^{-1}$). For nucleotide exchange rates $\omega > 10^{-1}\,\mathrm{s}^{-1}$ the phase boundary coincides with the model used in the main text. A significant effect is found for $\omega \le 10^{-3}\,\mathrm{s}^{-1}$ (as estimated by the above dimension estimate), where the stability boundary is shifted towards larger total tubulin concentration $\bar{\rho}_\mathrm{T}$. This shift is caused by a significant amount of cytosolic tubulin being in its inactive form. This reduces the overall concentration of actively available tubulin, which must be compensated by an increase $\bar{\rho}_\mathrm{T}$.

To ensure that the long term dynamics remains qualitatively unchanged under finite nucleotide exchange we perform agent based simulations of the extended model. Figure 2.21 shows a time sequence obtained from the simulations. The characteristic features of the dynamics, namely phase separation into low and high tubulin density regions and filament plus-end accumulation at the interface between these zones remain unchanged under the modification of the model.

The nucleotide exchange rate for tubulin was reported to depend on the total tubulin concentration and ranges between $\omega = 0.02\,\mathrm{s}^{-1}$ at high tubulin concentration ($\rho_\mathrm{T} \ge 70\,\mu\mathrm{M}$) and $\omega = 0.15\,\mathrm{s}^{-1}$ at low tubulin concentrations ($\rho_\mathrm{T} \approx 10\,\mu\mathrm{M}$) [232, 233]. This means for tubulin concentrations discussed in the main text we can assume nucleotide exchange rates of order $\mathcal{O}(1\times10^{-1}\,\mathrm{s}^{-1})$. In this parameter range the phase diagram is well approximated by the equations used in the main text [cf. Fig. 2.18(d) and Fig. 2.20(b)].

FINITE-ELEMENT SIMULATIONS

To complement linear stability analysis, we performed numerical simulations of the point-like filament dynamics, governed by Eqs. (2.48). Specifically, a finite element method implemented in the

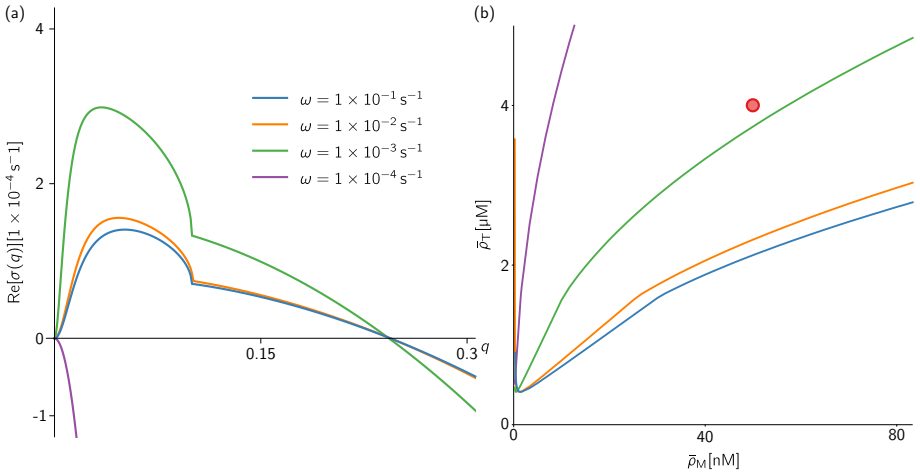

Figure 2.20: (a) Leading eigenvalue $\sigma(q)$ for different nucleotide exchange rates ω. Parameters are $\bar{\rho}_M = 50\,\mathrm{nM}$, $\bar{\rho}_T = 4\,\mu\mathrm{M}$ (marked by a red dot in (b)), $D_M = 0.5\,\mu\mathrm{m}^2\mathrm{s}^{-1}$ and $D_T = 6\,\mu\mathrm{m}^2\mathrm{s}^{-1}$; other parameters are specified in the Supplemental Material Sec. SI. Note the growth rate for low tubulin exchange rates increases since the growth rate increases as the stability threshold is approached (cf. Fig. 2.23). (b) Stability diagram in the $(\bar{\rho}_M, \bar{\rho}_T)$-parameter space. The legend is as in (a). The parameter choice for the dispersion relations in (a) is marked by the red dot.

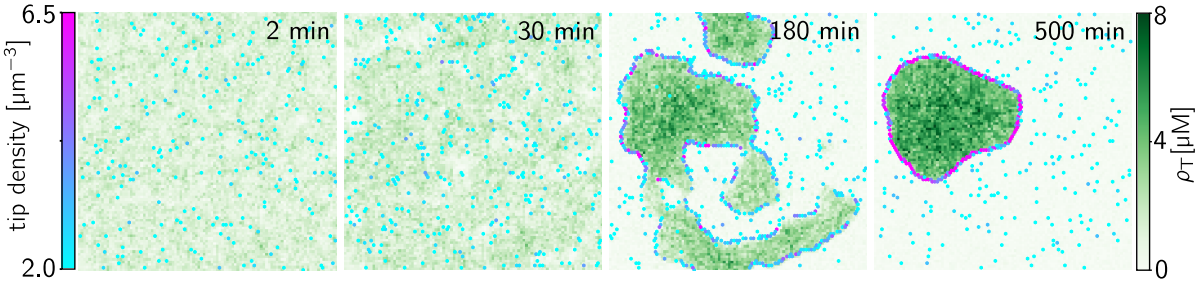

Figure 2.21: Snapshots of the total tubulin density $\rho_T(\mathbf{x}, t)$ and the tip density including finite tubulin nucleotide exchange $\omega = 0.01$. Parameters are $(\bar{\rho}_T, \bar{\rho}_M) = (2.75\,\mu\mathrm{M}, 30\,\mathrm{nM})$; $L_x = L_y = 100\,\mu\mathrm{m}$ other parameters are as specified in Tab. 2.1.

software COMSOL Mulitphysics was used (see point-like-filament-PDEs.mph). To ensure numerical stability, we add a small diffusion term (diffusion constant $1 \times 10^{-2}\,\mu m^2\,s^{-1}$) to the dynamics of $l(\mathbf{x}, t)$. This is necessary because sharp interfaces emerge rapidly around the long-filament clusters that from the initial instability (Fig. 2.22). Because of these sharp gradients, the assumption of point-like filaments underlying these simulations is no longer valid. Still, it is instructive to discuss the dynamics in this regime as it shares some of the features with the agent-based simulations with spatially extended filaments.

The interfaces of clusters that emerge from the initial instability propagate such that the regions of long filaments become smaller. This propagation is driven by the diffusive influx of motors from the regions where filaments are short, and therefore, most motors are in the cytosol. The motors diffusive into the long-filament regions, where they rapidly attach near the interface. This drives depolymerization of filaments near the interface, causing the long-filament regions to shrink. The released tubulin units then diffuse in the cytosol and drive further growth of filaments in the long-filament regions.

In fact, the propagation of interfaces is already indicated by the dispersion relation. As we discussed below Eq. (2.60), a positive determinant of J_{WM} implies that the eigenvalues are a pair of complex conjugates near the onset of instability. In the dispersion relation, this means that $\sigma(q)$ has a non-zero imaginary part near the zero crossing of its real part at $q = q_{\max}$ [see Fig. 3(a) in the main text]. In a previous study on mass-conserving reaction diffusion systems, we found that the properties of interfaces can be inferred from the right edge of the dispersion relation [213]. Specially, non-zero imaginary part at $q_{\max}$ indicates that the mode that defines the interface is propagating.

In the point-like filament approximation, interfaces will continue to propagate until the long-filament clusters have completely disappeared. Subsequently, new clusters will emerge from lateral instability. And these clusters will again collapse due to interface propagation, driven by diffusive flux of motors into the clusters. In contrast, in agent-based simulations with spatially extended filaments, advective transport of motors along filaments counteracts diffusive influx of motors into the clusters. This is because the net orientation of the filaments is aligned with the density gradients and leads out of the clusters. As a result of this advective motor transport, interface motion arrests

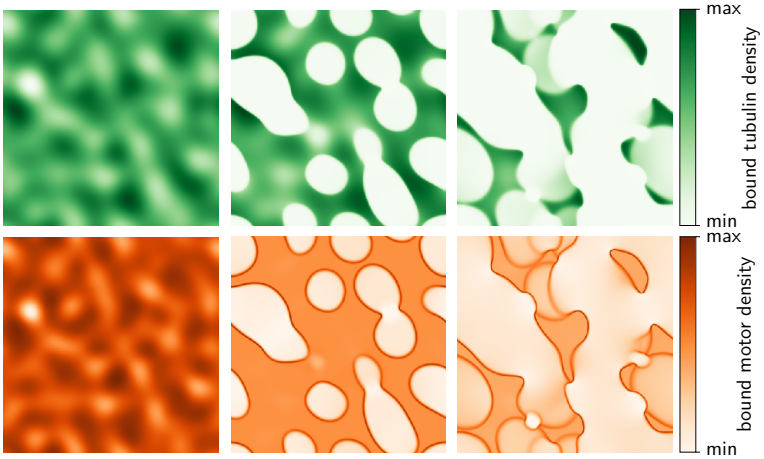

Figure 2.22: Snapshots from finite-element simulations of Eqs. (2.48a)–(2.48e) at times 1.8×10^4, 2.5×10^4, and 3.1×10^4 from left to right. Top row: Filament length l (bound tubulin density). The color bar ranges [min, max], are [4,7], [0,15], [0,32] from left to right. Bottom row: Filament-bound motor density $\tilde{M}$. The color scheme is logarithmic, with ranges $[10^{1.1}, 10^{1.2}]$, $[10^0, 10^3]$, and $[10^0, 10^3]$ from left to right. Note that the concentration of bound motors is highest around the perimeter of regions with long filaments (high bound tubulin density). Domain size $L_x = L_y = 500\,\mu m$. Remaining parameters as in Figs. 4 and 5 in the main text.

eventually, thus producing the final, aster-like steady state structure (see Movie 1 and Fig. 4 in the main text).

FASTEST-GROWING MODE IN AGENT-BASED SIMULATION

Within the framework of the point-like filament approximation we found a long-wavelength instability driven by polymerization kinetics of filaments that is controlled by a the local densities of depolarizing motors and cytosolic tubulin. To obtain a quantitative comparison between the agent-based simulation, which includes spatially extended filaments and the point like filament approximation we determine the growth rate as well as the wavelength of the initial dynamics starting from a homogeneous steady state. As the linear stability of the model does not depend on dimensionality we restrict the analysis to a quasi one dimensional setting, where filaments can be either left or right oriented. This would correspond to a nematically ordered filaments in two dimensions. This is done for the sake of computational cost as agent based simulations in the two dimensional setting are time-intensive. By performing a Fast Fourier transformation of the density field we obtain the fastest growing mode. Thereby we find the maximal growth rate $\sigma(q_c)$ and the corresponding wavelength λ_c. The laterally stable parameter regime is characterized by a maximal growth rate of zero $\sigma(q_c) = 0$.

We find that the boundary of the laterally stable parameter regime is well approximated by the point like filament approximation (see Fig. 2.23). It also correctly predicts the qualitative dependence of the growth rate on total motor and tubulin concentration (see Fig. 2.23).

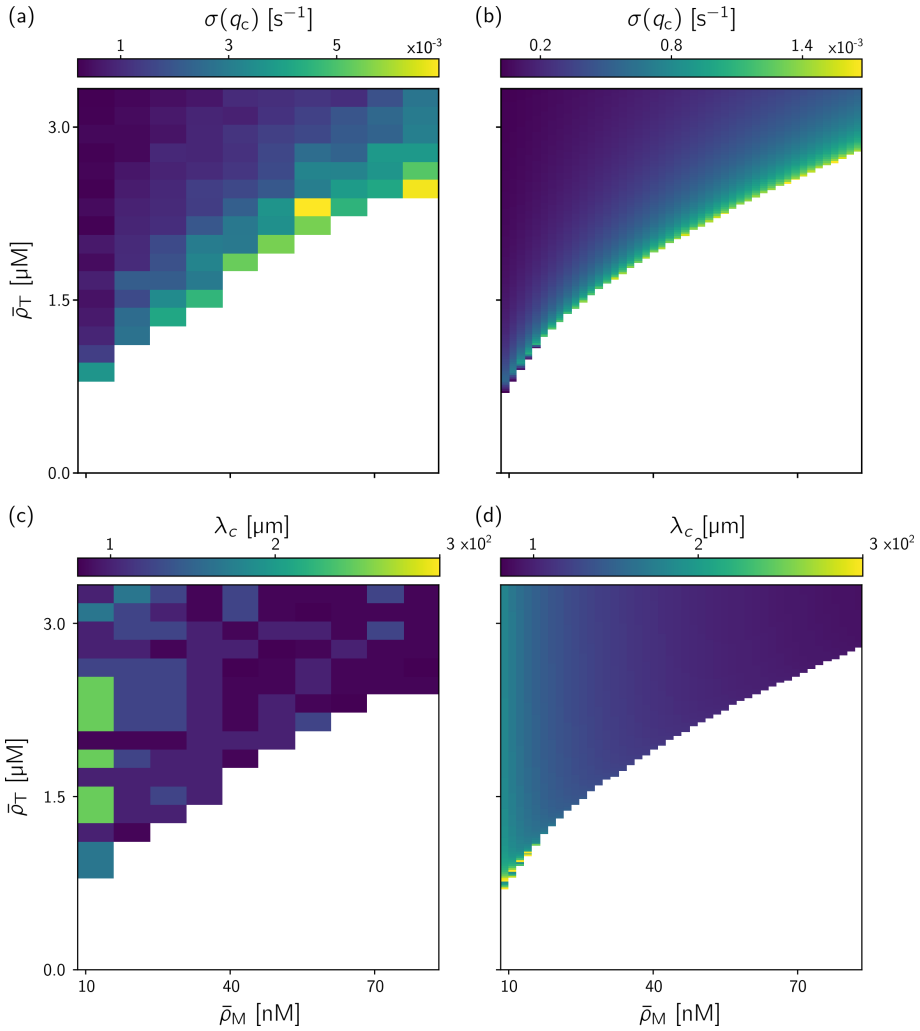

Figure 2.23: Growth rate $\sigma(q_c)$ and wavelength $\lambda_c = 2\pi/q_c$ of the fastest growing mode obtained form (a,c) agent-based simulations and (b,d) linear stability analysis of the point-like filament approximation Eq. 2.48. White areas indicate regions where the homogeneous states are stable against spatial perturbations. Note that, counterintuitively, the growth rate of the fastest growing mode increases towards the instability threshold. This is because the stability threshold is set by a saddle-node bifurcation where the laterally unstable steady-state branch disappears. We find a good agreement for the boundary of the laterally stable parameter regime. Moreover the qualitative dependence on the total motor and tubulin concentration is correctly predicted by linear stability analysis [cf. Fig. 2.18(b,d)]. Parameters: $L = 500\,\mu$m, $k_{\text{on}} = 0.22\,\mu\text{m}^3\text{s}^{-1}\mu\text{m}^{-1}$ all other parameters are as specified in Tab. 2.1.

Algorithm 1 Approximative simulation scheme

while $t < t_{\max}$ **do**
  for motor position = $\{s_1, s_2, \ldots\}$ **do**
    $s_i \rightarrow s_i + v_{\mathrm{m}} \Delta t$
    if $s_i > l$ **then**
      # cytosolic motors += 1
      # cytocolic tubulin += 1
      filament length −= a
  r =random_real ∈ $(0, 1)$
  if $r < k_{\mathrm{on}} l \Delta t$ (#cytosolic motors) **then**
    s_k =random_real ∈ $(0, l)$
    motor_positions.append(s_k)
    # cytosolic motors −= 1
  r = random_real ∈ $(0, 1)$
  if $r < \gamma \Delta t$ (#cytosolic tubulin) **then**
    l += a
    # cytosolic tubulin −= 1

Algorithm 2 Filament growth dynamics

for position (x_i, y_i) in free tubulin positions = $\{(x_0, y_0), \ldots\}$ **do**
  reaction time $\tau_k = \Delta t$
  filament plus ends in range = EuclidianDistance[(x_i, y_i), plus_end_position] < r_{T}
  for filament plus end **in** filament plus ends in range **do**
    $\tau_k^{\mathrm{new}} \rightarrow \gamma \exp(\gamma t)$
    if $\tau_k^{\mathrm{new}} < \tau_k$ **then**
      $\tau_k = \tau_k^{\mathrm{new}}$
      remember filament plus end
  if remembered filament plus end != empty **then**
    grow filament
    remove tubulin position from free tubulin positions
  else
    x_i += $\sqrt{24 D_{\mathrm{T}} \Delta t} \cdot$ (random_real ∈ $(-0.5, 0.5)$)
    y_i += $\sqrt{24 D_{\mathrm{T}} \Delta t} \cdot$ (random_real ∈ $(-0.5, 0.5)$)

Algorithm 3 Free motor dynamics

for position (x_i, y_i) in free motor positions = $\{(x_0, y_0), \ldots\}$ **do**
    reaction time $\tau_k = \Delta t$
    filaments in range = all filaments that intersect with a circle of radius
    r_M around (x_i, y_i) (see Fig. 2.15)
    for filament **in** filaments in range **do**
        calculate Δl
        $\tau_k^\mathrm{new} \rightarrow k_\mathrm{on} \Delta l \exp(k_\mathrm{on} \Delta l\, t)$
        if $\tau_k^\mathrm{new} < \tau_k$ **then**
            $\tau_k = \tau_k^\mathrm{new}$
            remember filament
    if remembered filament ! = empty **then**
        attach motor to remembered filament at random position within Δl
        set motor state to filament-bound
    else
        x_i += $\sqrt{24 D_\mathrm{M} \Delta t} \cdot$ (random_real $\in (-0.5, 0.5)$)
        y_i += $\sqrt{24 D_\mathrm{M} \Delta t} \cdot$ (random_real $\in (-0.5, 0.5)$)

3

COLLECTIVE FILAMENT MOTION IN ACTIVE FILAMENT BUNDLES

3.1. BIOLOGICAL BACKGROUND

In the living cell, cytoskeletal filaments are constantly reorganized and moved. This motion is caused by molecular motors that cross-bridge neighboring filaments [177]. Thereby they can exert force on the filaments. The most important motors involved in the motion of microtubules are dynein and members of the kinesin family [19, 34, 179]. The functionality of the cell relies crucially on this mechanical reorganization of filaments. An example is the mitotic spindle where the knockout of dynein results in unfocused spindles that lack spindle poles [183, 184] and the knockout of kinesin-5 to monopolar spindles with chromosomes at the periphery [180–182].

To understand the complex interplay between motor proteins that cross-link and slide neighboring filaments, it has proven informative to study isolated interactions between individual filaments (or filament bundles) and cross-linking motor proteins in reconstituted systems. This work will focus mainly on kinesin-5 (or kinesin-5 like) motor proteins. Kinesin-5 has the ability to simultaneously bind to two different microtubules and walk on them [95]. The motion of the motor domains is directed towards the filament plus end; see Fig. 3.1 (b). The directed motion and ability to cross-link adjacent filaments lead to distinct behavior for microtubules with their plus end oriented in the same (parallel filaments) or opposite (anti-parallel filaments) direction. If the filaments are parallel oriented, the two motor heads move in the same direction (see Fig. 3.1 (c)). Thereby their relative distance remains the same, and the two motor domains can walk towards their destination, the plus end, without inducing strain in the motor. In contrast, if the motor heads are attached to anti-parallel filaments the motor domains move apart. Instead, this results in filament motion as opposed to the direction of motor motion (see Fig. 3.1 (b)). Together this results in filament sliding that depends on the relative orientation of adjacent filaments; see Fig. 3.1 (b), (c). *In vivo* kinesin-5 mediated filament sliding yields a constant microtubule flux of spindle microtubules from the center of the spindle towards the poles [97, 98, 234]. *In vitro* the mechanistic hypotheses for kinesin-driven filament sliding was studied using assays of stabilized microtubules with fluorescently labeled minus ends to track their relative filament orientation; see Fig. 3.1 (a) top. It was observed that anti-parallel filaments move in the direction of their minus ends at a relative speed of $\sim 35\,\mathrm{nms}^{-1}$ which is approximately twice the velocity of Kinesin-5 ($v_\mathrm{m} \approx 20\,\mathrm{nms}^{-1}$). In contrast, parallel filaments remained static; see Fig. 3.1 (a) bottom [95].

Therefore, on the basis of single filament experiments, the filament velocity seems to be inherently linked to the relative orientation of interacting filaments. However, this conclusion is challenged by observations in the mitotic spindle. Measurements have shown that the fraction of parallel to anti-parallel filament pairs varies significantly inside the spindle, with primary parallel filaments at the spindle poles and a large number of anti-parallel filaments in the spindle center [98,

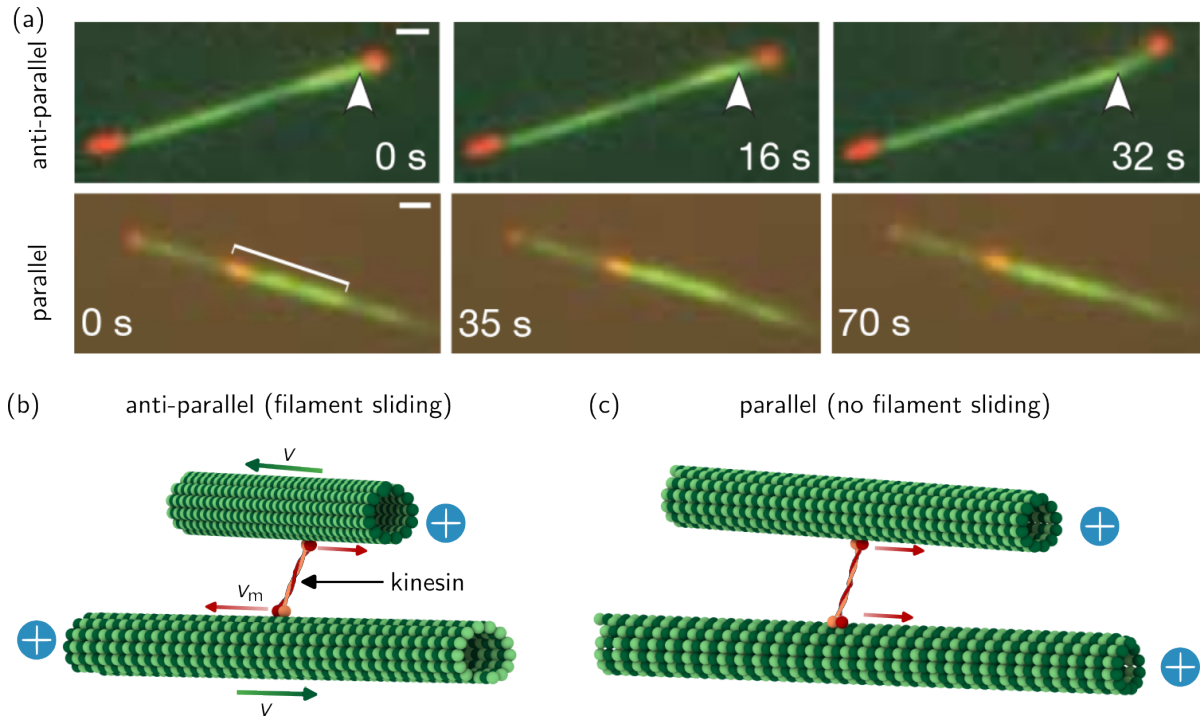

Figure 3.1: (a) *In vitro* assay of stabilized microtubules (green) with purified Eg5 (kinesin-5). Minus ends of microtubules are fluorescently labeled in red. Top panel: Anti-parallel microtubules move in the direction of their minus end. The arrow white arrow marks the plus end of the long microtubule, which has the minus end at the left. The two minus ends move apart at a speed of 35 nm/s which is approximately twice the velocity of Eg5 (~ 20 nm/s). Bottom panel: Parallel microtubules remain static. One is marked with a white line. The scale bar is 1 µm (b) Illustration of a Kinesin tetramer (yellow) that cross-links two anti-parallel microtubules (green) and moves simultaneously on them (yellow arrow). The motor domains move in opposite direction. As a result, the filaments slide in the opposite direction to the motor motion. (c) Illustration of a kinesin tetramer that cross-links two parallel microtubules. The motor domains of the kinesin tetramer move in the same direction and the cross-linked microtubules remain static. Panel (a) adapted from [95] and reproduced with permission from Springer Nature; License Number: 5614280563769.

184]; see Fig. 3.2 (b),(c). At the same time, those experiments have shown that microtubules slide at constant speed towards the spindle poles independent of their position in the spindle [96–98]; see Fig. 3.2 (b). How do the collective dynamics of many filaments cross-linked by motor proteins play out to behave differently than the individual components on their own?

In this chapter, we will focus on the question of how the dynamics of an ensemble of filaments emerge from the collective interplay between cross-linking of filaments and the directed motion of the motor proteins on the filaments. To this end, we will focus on stabilized filaments of fixed length ℓ, i.e., we disregard length regulation dynamics.

3.1.1. MODELING APPROACH

To assess the complex dynamics of motor-driven filament networks, we first aim to build a conceptual model on the basis of single filament experiments (two cross-linked filaments). First, we neglect possible correlations between different protofilaments of the microtubule and model filaments by an effectively one-dimensional structure of fixed length ℓ; see Fig. 3.3 (a). Motivated by the large persistence length of microtubules that exceeds the filament length by orders of magnitude [25] we

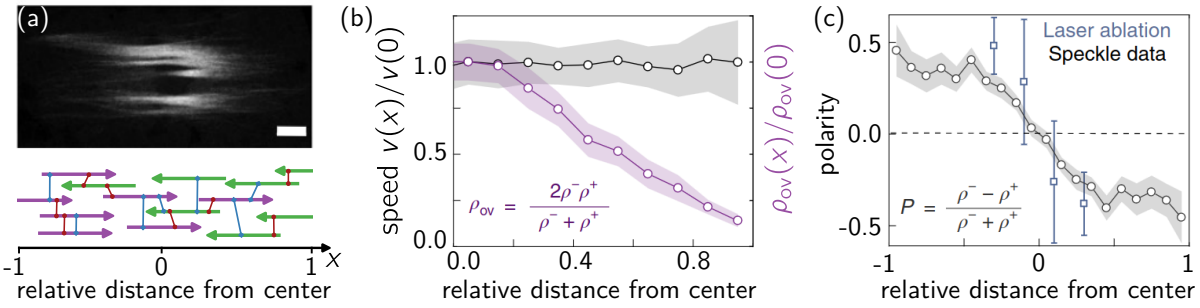

Figure 3.2: (a) Top: Fluorescent spindle labelled with Atto565 pig tubulin. Dynein was inhibited using p150-CC1, resulting in unfocused spindle poles. Schematic illustration of microtubules in the spindle. Microtubules can be cross-linked by molecular motors (red) or passive-cross-linkers (blue). The relative fraction of right (purple) and left (green) oriented filaments is not spatially uniform in the spindle. The scale bar is 10 µm. (b) The magnitude of the sliding speed of filaments as a function of their position. The speed is independent of the overlap of left $\rho^-(x)$ and right $\rho^+(x)$ oriented filaments. (c) Local polarity is defined as the relative fraction of left and right-oriented filaments in the spindle obtained by two different experimental techniques. Panel (a) top, (b), and (c) adapted with permission from [98], which is an open access article distributed under the terms of the Creative Commons CC BY license, which permits unrestricted use, distribution, and reproduction in any medium, provided the original work is properly cited.

model the filaments by rigid rods. The two cross-linked filaments are aligned along the $x-axis$ and can be oriented in direction $n_i = \pm 1$. The direction n_i of a filament is defined in the direction of the filament plus end; see Fig. 3.3 (a). We will assume a well-mixed cytosolic pool of components in the following, i.e., we do not account explicitly for the diffusive redistribution of motor proteins. Cytosolic motors can bind to a filament at rate $k_{\text{on}} c_{\text{m}}$ and cross-link two adjacent filaments. We model a cross-linking motor by two motor domains connected by a Hookean spring with stiffness κ; see Fig. 3.3 (a). A filament bound motor head moves along the arc-length $s \in [-\ell/2, \ell/2]$ in direction n_i of the filament; see Fig. 3.3 (b). For now, we consider motor proteins that detach immediately upon reaching the filament plus end. We will relax this restriction in Sec. 3.2. The speed of the motor head on filament i, $V_{m,i}(f)$, depends linear on the force $f(t)$ applied to the motor at time t [196]; see Fig. 3.3 (b),(c):

$$V_{\text{m,i}}(f) = n_i v_{\text{m}} \left(1 + \frac{n_i f(t)}{f_{\text{s}}}\right) \tag{3.1}$$

Here, v_{m} denotes the unloaded speed of motors and f_{s} the stall force of motors. This means if a force acts on the motor head against the motor's direction of motion (n_i), it slows down. For symmetry reasons, we assume that a motor can exceed its unloaded velocity v_{m} when it is pulled; see Fig. 3.3 (c). However, this can easily be adapted to the cases where a motor can not exceed its unloaded speed. Filament-bound motors detach from the filament at rate K_{off}. In general, this detachment rate can be force dependent [235]

$$K_{\text{off}}(f) = k_{\text{off}} \mathrm{e}^{\frac{|f(t)|}{f_{\text{u}}}}. \tag{3.2}$$

We next aim to derive a coarse-grained description of filament-filament interactions mediated by many cross-linking motor proteins.

DERIVATION OF A COARSE-GRAINED FILAMENT-FILAMENT INTERACTION

In this section, we aim to derive an effective interaction between filament 1 and filament 2 as a result of many cross-linking interactions of the motor proteins. As a result of the motor-mediated interactions, filament 1 will move at speed $v_1(t)$ and filament 2 at speed $v_2(t)$. Now consider a

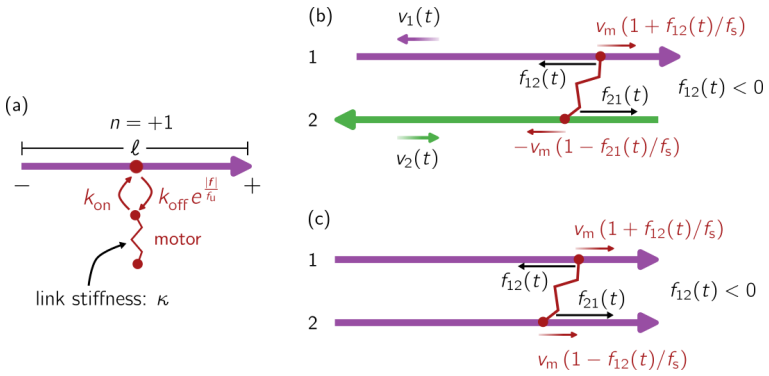

Figure 3.3: (a) Schematic representation of a filament with orientation $n = +1$ (purple) and a cross-linking motor (red). Filaments have fixed length ℓ. Motors are modeled as two motor domains that are connected by a Hookean spring with stiffness κ. Unbound motor heads can attach to the filament at rate k_{on}. Filament-bound motor heads detach at a rate $K_{\text{off}} = k_{\text{off}} e^{|f|/f_{\text{u}}}$ which is, in general, force dependent. (b) Two filaments oriented in direction $n_1 = 1$ (purple) and $n_2 = -1$ (green), that are cross-linked by a motor protein. The filament bound motor heads move in the direction of the filament plus end at speed $V_{\text{m},i} = n_i v_{\text{m}}(1 + n_i f_{ij}(t)/f_{\text{s}})$ if $n_i f_{ij}(t) < 0$ and $V_{\text{m},i} = n_i v_{\text{m}}$ else. This means motors are slowed down by an applied force that acts against their direction of motion but do not exceed their unloaded speed v_{m}. As a result of the motor motion, the spring gets strained. Therefore the motor exerts a force on $f_{12}(t)$ on filament 1. The force on filament 2, $f_{21}(t)$, has equal magnitude and opposite direction. As a result of many motor interactions, the filaments will slide at speed $v_1(t)$ and $v_2(t)$. (c) The analog situation for two parallel filaments. The leading filament head (here on filament 1) will be slowed down the motor head lagging behind moves at speed the unloaded speed v_{m}.

specific molecular motor that cross-links the two anti-parallel filaments; see Fig. 3.3 (b). At the time $t = 0$ the motor cross-links the two filaments in a relaxed state. As a result of the relative motor head motion and the relative filament velocity, the motor will get strained. The distance $\Delta x(t)$ between the motor heads is given by

$$\Delta x(t) = \int_0^t \mathrm{d}t' \, v_{\text{m}}(n_1 - n_2) - \frac{v_{\text{m}}}{f_{\text{s}}} \left(f_{12}(t') - f_{21}(t') \right) + \Delta v_{12}(t') \tag{3.3}$$

here $f_{12}(t)$ denotes the force the cross-linker exerts on filament 1 as a result of the interaction to filament 2. The first terms account for the velocity difference of the motor heads, and the last term for the velocity difference $\Delta v_{12}(t) = v_1(t) - v_2(t)$ of the filaments. The force applied by the motor heads, at time t, on the filaments is given by

$$f_{12}(t) = -\kappa \Delta x(t) = -f_{21}(t) \,. \tag{3.4}$$

Substituting Eqs. 3.3 in 3.4 yields a self-consitency equation for the the force $f_{12}(t)$

$$\partial_t f_{12}(t) + 2 v_{\text{m}} \kappa \frac{f_{12}(t)}{f_{\text{s}}} = 2 v_{\text{m}} \kappa \left[\frac{n_2 - n_1}{2} + \frac{\Delta v_{21}(t)}{2 v_{\text{m}}} \right] . \tag{3.5}$$

With the initial condition $f_{12}(0) = 0$. The solution to this equation is given by $f_{12}^*(t, v_{21}(t))$. In an ensemble of many motors, that cross-linking filament 1 and filament 2 each of them will have a different age τ since when it cross-links the filaments. As a result, each of the cross-linking motors will exert a different force $f_{12}(\tau)$ on the filaments. We are interested in the average force a motor exerts on the filaments. The motors that cross-link filament 1 and filament 2 at time t must have

been attached in the past and not detached yet. We denote the survival probability of a bond by $S(\tau)$. The average force a motor exerts between the filaments is then given by

$$F_{12}(t) = \frac{1}{\mathcal{N}} \int_0^\infty \mathrm{d}\tau S(\tau) f_{12}^*[\tau, v_{21}(t-\tau)] \tag{3.6}$$

The normalization constant $\mathcal{N}$ is given by

$$\mathcal{N} = \int_0^\infty \mathrm{d}\tau S(\tau) = \langle \tau \rangle \,.$$

The total force exerted between filament 1 and filament 2, which are cross-linked by $M_{12}(t)$ motors at time t, is then given $M_{12}(t)F_{12}(t)$ assuming overdamped dynamics this force has to be balanced by fluid drag:

$$\gamma v_1(t) = M_{12}(t)F_{12}(t) = -\gamma v_2(t) \,. \tag{3.7}$$

In principle Eq. 3.5, Eq. 3.6, and Eq. 3.7 forms a closed set of equations for the filament sliding velocities $v_1(t)$ and $v_2(t)$.

Here, we make an adiabatic approximation and assume that the relative filament sliding velocity $\Delta v_{21}(t) \approx \Delta \tilde{v}_{21}$ varies slowly on the timescale of individual detachment events. Using the adiabatic approximation, we find the solution $f_{12}^*[t, \Delta \tilde{v}_{21}]$ to be given by

$$f_{12}^*[\tilde{t}, \tilde{v}_{21}] = f_\mathrm{s}\left(1 - \mathrm{e}^{-A\tilde{t}}\right)\left(\frac{n_2 - n_1}{2} + \frac{\Delta \tilde{v}_{21}}{2v_\mathrm{m}}\right) \tag{3.8}$$

where we re-scaled time in units of the unloaded bond breakage rate $\tilde{t} = 2k_\mathrm{off}t$. Note the factor of two appears since both heads can detach from a filament. The dimensionless constant $A = v_\mathrm{m}\kappa/(f_\mathrm{s}k_\mathrm{off})$, quantifies the ratio of the average force a motor would exert in the absence of stalling, $v_\mathrm{m}\kappa/k_\mathrm{off}$, to the stall force f_s of motors.

Substitution into Eq. 3.6 yields

$$F_{12}(\Delta \tilde{v}_{21}) = f_\mathrm{s}\left(\frac{n_2 - n_1}{2} + \frac{\Delta \tilde{v}_{21}}{2v_\mathrm{m}}\right)\left[1 - \frac{1}{\langle \tilde{\tau} \rangle}\int_0^\infty \mathrm{d}\tilde{\tau} S(\tilde{\tau}, \Delta v_{21})\mathrm{e}^{-A\tilde{\tau}}\right] \tag{3.9}$$

We derived a force-velocity relation for motor-mediated interactions between the filaments in dependence on the relative filament velocity $\Delta \tilde{v}_{21}$. Note, to first order, this force-velocity relation is always linear in $\Delta \tilde{v}_{21}$. However, in general, the survival probability $S(\tilde{t}_\mathrm{u})$ might depend on $\Delta \tilde{v}_{21}$, and we get nonlinear corrections to the linear force-velocity relation. This is the case for force-dependent detachment. In principle, it is possible to derive the waiting time distribution for force-dependent detachment in the Supplemental Material Sec. 3.2.3 we give some examples. Here, we will consider force-independent detachment. The survival probability is then given by

$$S(\tilde{\tau}) = \mathrm{e}^{-\tilde{\tau}} \,. \tag{3.10}$$

In that case, the force-velocity relation, $F_{12}(\Delta v_{12})$ simplifies to

$$F_{12}(\Delta v_{21}) = f_\mathrm{s}\frac{A}{1+A}\left(\frac{n_2 - n_1}{2} + \frac{\Delta \tilde{v}_{21}}{2v_\mathrm{m}}\right) \tag{3.11}$$

$$= F_\mathrm{m}\left(\frac{n_2 - n_1}{2} + \frac{\Delta \tilde{v}_{21}}{2v_\mathrm{m}}\right) \tag{3.12}$$

Figure 3.4 shows the motor force amplitude, $F_\mathrm{m} = f_\mathrm{s}A/(1+A)$, as a function of $A = v_\mathrm{m}\kappa/(f_\mathrm{s}k_\mathrm{off})$ and the force-velocity relation $F_{12}(\Delta v_{21})$ as as function of Δv_{21}. The motor exerts a maximal force between the filaments if they do not move relative to each other, and the force declines to 0 if the two anti-parallel filaments slide apart at a relative velocity $2v_\mathrm{m}$. The amplitude, F_m, of the exerted force becomes zero for $v_\mathrm{m}\kappa/k_\mathrm{off} \ll f_\mathrm{s}$. This can be understood in the limit $k_\mathrm{off} \to \infty$. In this limit, motors will detach immediately and can not exert force on the filament. On the opposite limit, $k_\mathrm{off} \to 0$ motors will walk on the filament until they stall, i.e., they always exert the stall force on the filaments.

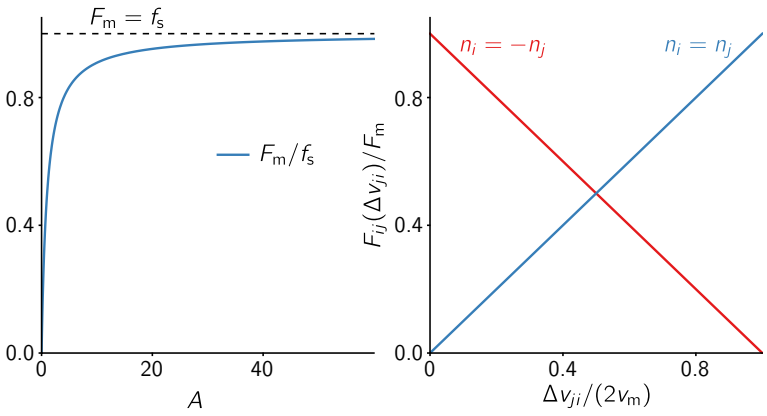

Figure 3.4: (a) Force amplitude F_m in units of the stall force as a function of $A = v_m\kappa/(f_s k_{off})$ and (b) coarse-grained force-velocity relation $F_{ij}(\Delta v_{ij})$ for a motor that detaches at a constant rate k_{off}. (a) Persistent motors ($k_{off} \to 0$) can exert a maximal force that is equivalent to their stall force. In the limit of fast detachment ($k_{off} \to \infty$), the motors detach before they are strained resulting in zero force amplitude. (b) Average force $F_{ij}(\Delta v_{ji})$ a motor exerts on two anti-parallel (red) and parallel (blue) filaments i and j in dependence of the relative velocity Δv_{ji} of the filaments.

A coarse-grained filament-filament interaction: We can summarize the force-velocity relation of a motor-mediated filament-filament interaction between filaments with orientation n_i and n_j in the equation

$$F_{ij} = \frac{F_m}{2}\left(n_j - n_i + \frac{v_j - v_i}{v_m}\right). \tag{3.13}$$

Substituting Eq. 3.13 into Eq. 3.7 allows to solve for the filament sliding velocities

$$v_i(t) = \frac{n_j - n_i}{2}\frac{v_m}{1 + \gamma v_m/(F_m M_{ij}(t))} = -v_j(t)\,. \tag{3.14}$$

For typical parameters, we obtain drag coefficients in the range of $\gamma = 0.1 - 0.8\,\mathrm{pNs\mu m^{-1}}$, resulting in fluid drag on the order of $10^{-2} - 10^{-1}\,\mathrm{pN}$. Compared to the motor force amplitudes on the order of 1 pN the term $\gamma v_m/(F_m M_{ij}(t))$ becomes negligible. The speed of the filaments then depends only on their relative orientation. For two parallel filaments $n_i = n_j$ the filament velocities are zero. Two anti-parallel filaments, $n_i = -n_j$, slide approximately at the speed of motors $v_i \approx -n_i v_m$ as observed in *in vitro* experiments; cf. Fig. 3.1.

While the derived force-velocity relation is consistent with the observed *in vitro* dynamics at a single filament level, can it also account for the puzzling observation that filaments in the spindle apparatus slide at a speed that is independent of the local number of parallel and anti-parallel interactions; cf. Fig. 3.2? Can we learn something about the necessary requirements for large filament bundles to contract or expand?

In the remainder of this chapter, we will approach those questions by deriving consequences for ensembles of filaments that are cross-linked by motor proteins that obey a force-velocity relation as described by Eq. 3.13.

3.2. BRIDGING SCALES IN FILAMENTOUS ACTIVE MATTER

3.2.1. SIGNIFICANCE

Assemblies of cytoskeletal filaments and associated proteins form diverse, dynamic structures that play essential roles in many intracellular processes. An important factor in the emergent self-organization of these networks is their ability to exert force and re-arrange. At the collective level, those forces are reflected in active extensile or contractile stresses that drive the network dynamics. On the macroscopic level, the consequences of those stresses are understood in terms of active field theories built on symmetry arguments. However, how microscopic interplay between the various components results in extensile or contractile filament networks is not well understood.

Here, we address this question using a minimal but generic theoretic model for bundles of rigid filaments cross-linked by motor proteins or passive cross-linkers. Starting from a general microscopic model, we derive a formalism to evaluate the contribution of a motor cross-linker to the propensity of a filament bundle to contract or expand. Based on the derived formalism, we can make general, statements about the ability of a motor cross-linker to promote extensile or contractile stress. First, a a motor whose microscopic dynamics result in a homogeneous density profile along the contour of a filament can neither contribute to extensile or contractile stress in the system. Second, in the absence of bundling agents or other cross-linkers, a single type of motor can only exert contractile stress. In mixtures of different motor cross-linker types, the inhomogeneity of the motor profiles and the total population of different cross-linker types control the filament bundle tension.

We proceed to use our theoretical framework to investigate the physics of filament-motor-mixtures composed of motors that can cross-link and walk on neighboring filaments and crowding agents that bundle filaments together. In addition, we allow for motors to dwell at the filament end they are walking to. This set of constituents resembles a minimal model for a broad range of experimentally studied *in vitro* filament motor mixtures, which are usually composed of filaments, crowding agents, and motors that might or might not dwell at the filament end [38, 40, 75–79, 87, 88, 90–93]. We identify two mechanisms that control the propensity of the filament bundle to contract or extend. First, contractile tension is predominantly caused by motor proteins that dwell at the filament tip and cross-link parallel filaments. Therefore, the contraction of the filament bundle relies on the ability of the motors to dwell at the filament end. Second, internal friction, e.g., from passive cross-linkers, is required for the filament bundle to generate extensile stress. The extensile stress can be increased by increasing the internal friction. This yields the counterintuitive prediction that holding individual filaments in the bundle together increases the materials' propensity to expand. Using our theoretic framework, we can summarize those requirements in a set of coarse-grained parameters that control the propensity of the filament bundle to contract or extent. By specifying a minimal microscopic model, we relate those parameters to the kinetic and mechanical properties of the network constituents, thereby bridging the gap between the microscopic and macroscopic dynamics of the filament bundle. This allowed us to identify three external control parameters of the filament bundle dynamics. First, the number of motors per filament. Second, the number of passive cross-linkers per filament, and third the filament length. We predict that the filament bundle is extensile at high concentrations of passive cross-linker and for long filaments. In contrast, high concentrations of motors and short filaments promote the propensity of the filament bundle to contract. All those predictions are in line with recent *in vitro* experiments [75, 78, 79, 91–93]. Last, we verify our predictions using agent-based computer simulations.

3.2.2. RESULTS

An essential ability of cytoskeletal filament structures is to exert force. Often, this force is generated by an extending or contracting network of cross-linked filaments. Prominent examples are the mitotic spindle, which relies on the ability to extend to segregate chromosomes during cell division [17, 19] and the actin cortex, which, in collaboration with myosin II, promotes contractile tension

that drives changes in cell shape, e.g., during tissue morphogenesis [100, 102, 105, 236]. Moreover, reconstituted systems of filaments and cross-linkers show a broad range of behavior. This includes characteristics of contractile dynamics like global and local network contraction or aster formation [193, 194, 205, 237], as well as characteristics of extensile dynamics like filament bundle extension, bundle buckling, network buckling, and turbulent-like dynamics [38, 75, 78, 87, 91].

Although the constituents of those materials are known, we lack an understanding of which microscopic properties of the constituents determine the contractile or extensile nature of filament motor mixtures. There is increasing experimental evidence that the propensity of a filament network to contract or extent can be tuned by changing the length of the filaments [75, 88, 93], the concentration of motors [79, 92], the concentration of passive cross-linkers or depletants in the system [79, 88, 91, 238] or by mixing different motor proteins and cross-linkers [75, 88]. However, how those changes in the microscopic constituents of the filament network control the propensity of a filament bundle to expand or contract on the collective level is not well understood.

On a phenomenological level, the collective dynamics of filament-motor mixtures have been studied by hydrodynamic theories that are built on symmetry arguments [48, 49, 51, 52, 86, 239]. In those theories, activity is included in models of passive nematics by active currents with coefficients characterizing the strength of activity. However, those coefficients are hard to measure and relate to the microscopic interactions of the constituents.

How to bridge the gap between properties of the microscopic constituents and the collective dynamics is an open question that has recently come into the focus of interest [76, 237, 240–242]. This question has been addressed using coarse-grained models derived from minimal microscopic interactions [240, 241, 243–248] or large scale computer simulations [39, 75, 93, 249–252].

Here we focus on this question using a minimal but generic theoretical model. We identify three essential parameters that control the propensity of the filament bundle to contract or expand: First, the ratio of motors bound to the filament end to motors bound to the filament bulk. Second, the strength of internal friction (passive cross-linkers) to motors bound to the filament bulk. Third, the anisotropy of filament-bound motors along the arc-length of the filament. Using our theoretical framework, we summarize those requirements in a set of coarse-grained control parameters. By specifying a minimal microscopic model, we relate all coarse-grained control parameters to the kinetic and mechanical properties of the network constituents. Thereby we were able to identify three experimentally accessible parameters that control the propensity of the filament bundle to contract or expand. First, the concentration of active motors. Second, the concentration of passive cross-linkers, and third the filament length. We predict that the filament bundle is extensile at high concentrations of passive cross-linker and for long filaments. In contrast, high concentrations of motors and short filaments promote the propensity of the filament bundle to contract. All those predictions are in line with recent *in-vitro* experiments [75, 78, 79, 91–93]. Lastly, we verify the predictions of our minimal model with the help of computer simulations.

MINIMAL BIOPHYSICAL MODEL

We consider a homogenous filament bundle composed of filaments of fixed length ℓ, which are aligned along the $x-$axis. The filaments $i = 1 \dots N_{\mathrm{Mt}}$ have center of mass position x_i and can take orientation $n_i = \pm 1$, which they maintain throughout the dynamics. The orientation n_i of a filament is defined in the direction of the filament plus end; see Fig. 3.5 (c). Filaments in the bundle can be cross-linked by motor cross-linkers or passive cross-linkers of different types; see Fig. 3.5 (c). We denote the different types of motor cross-linkers in the filament bundle by X. We consider motor cross-linkers and passive cross-linkers that exert a force linear to their extent Δx (see Fig. 3.5 (a)), i.e., motor cross-linkers that can be modeled by a Hookean spring with respective spring stiffness κ;

$$f[\Delta x(t)] = \kappa \Delta x(t)\,. \tag{3.15}$$

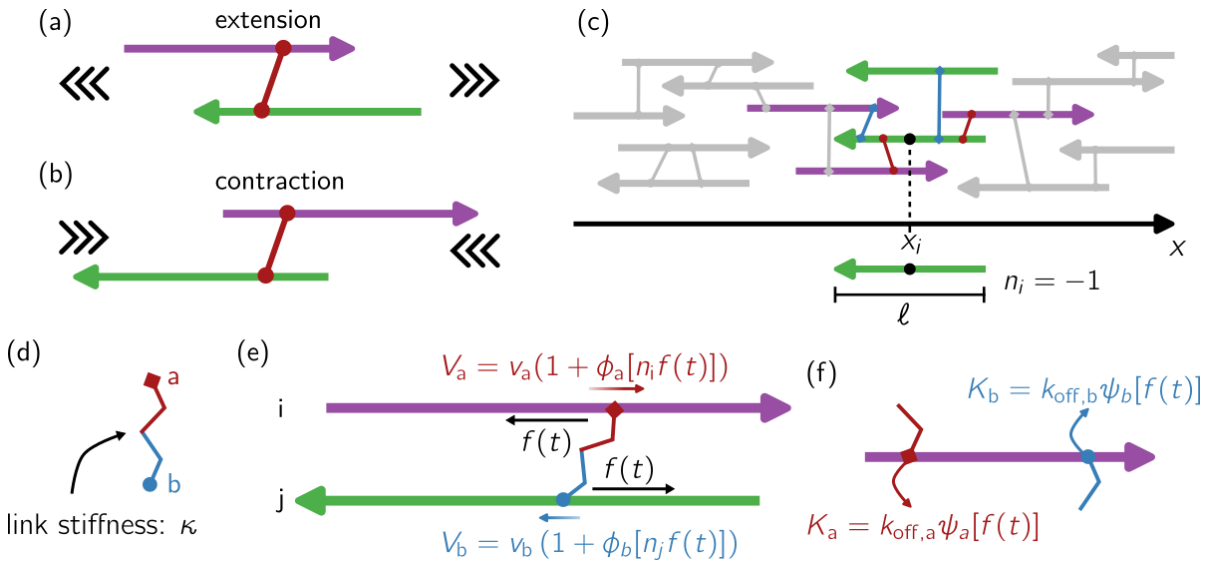

Figure 3.5: Depending on their relative position, a pair of interacting filaments can be (a) extensile or (b) contractile. In a homogeneous filament bundle, either configuration is equally likely. To generate net extensile or contractile stress, this symmetry has to be broken. (c) Filament bundle comprised of filaments of length ℓ. The filaments are aligned along the x-axis and have center of mass position x_i and orientation $n_i = \pm 1$. The interaction partners of filament i are depicted in color and the remaining filament bundle in gray. The filament bundle is cross-linked by a set of motor cross-linkers or passive cross-linkers. (d) We consider a general class of motor cross-linker. The two motor domains a and b are connected by a Hookean spring with spring stiffness κ. (e) The motor heads move at an unloaded speed v_a and v_b respectively. Positive motor velocities denote a motion in the direction of the filament plus end. The velocity V_a and V_b of the motor heads depends on the applied force $f(t)$ at time t and if the force is applied in or opposed to the motor heads' direction. The force dependency of the velocity is characterized by the function $\phi[f(t)]$. The detachment rates K_a and K_b of the motor cross-linker can be force dependent. The force dependence is characterized by the function $\psi[f(t)]$.

Motor cross-linkers are characterized by their ability to cross-link two neighboring filaments and walk directionally on them, either in the direction of the filament, n_i (plus-end-directed), or opposed to it, $-n_i$ (minus-end-directed). However, the motor cross-linkers may be asymmetric or symmetric. A biologically important example of a symmetric motor cross-linker is tetrameric Kinesin-5, which can cross-link and walk on two neighboring filaments [95]. An example of an asymmetric motor cross-linker is Kinesin-4, which can cross-link neighboring filaments but has one immobile microtubule-binding domain and one mobile motor domain. Another important class of asymmetric motor cross-linkers are motors that dwell at the filament end they are walking to. This is because they have, by definition, one immobile motor domain at the filament end and one mobile motor domain cross-linked to the bulk (arc-length) of a neighboring filament. A representative member of this class of motor cross-linkers is dynein [193]. We denote the two motor domains of the cross-linker X by (a) and (b). The walking speed V_a and V_b of the cross-linker along the arc-length $s \in [-\ell/2, \ell/2]$ of the filament depends on the force $f(t)$ applied to the motor head at time t, and if the force is applied in or opposed to the direction of motion of the motor head [196]. We characterize this response to a force by the dimensionless functions $\phi_a[nf]$ and $\phi_b[nf]$. The walking speed of the motor domain (a) cross-linked to filament i and motor domain (b) cross-linked to filament j

are then given by

$$V_\mathrm{a}[n_i f(t)] = v_\mathrm{a}(1+\phi_\mathrm{a}[n_i f(t)])$$
$$V_\mathrm{b}[n_j f(t)] = v_\mathrm{b}(1+\phi_\mathrm{b}[n_j f(t)])\,.$$

with the unloaded motor speeds v_a and v_b, such that $\phi_\mathrm{a}[0] = \phi_b[0] = 0$; see Fig. 3.5 (e). The sign convention is such that positive velocities denote a motor head motion in direction of the filament (plus-end-directed), and negative velocities are opposed to it (minus-end-directed). The motor head (a) and (b) can detach from the filament they are bound to at rate K_a and K_b. In general, those detachment rates have been shown to depend on the force applied to the motor head and, eventually, if the force is applied in the direction of motion of the motor cross-linker or opposed to it [235]. We characterize the response of the detachment dynamics of the motor cross-linker to an applied force by the dimensionless functions $\psi_\mathrm{a}[nf(t)]$ and $\psi_\mathrm{b}[nf(t)]$ and define the force-dependent detachment rates

$$K_\mathrm{a}[n_i f(t)] = k_\mathrm{off,a}\psi_\mathrm{a}[nf(t)]$$
$$K_\mathrm{b}[n_j f(t)] = k_\mathrm{off,b}\psi_\mathrm{a}[nf(t)]\,.$$

where $k_\mathrm{off,a}$ and $k_\mathrm{off,b}$ denote the unloaded detachment rates of the motor heads (a) and (b), such that $\psi_\mathrm{a}[0] = \psi_\mathrm{b}[0] = 1$; see Fig. 3.5 (f).

MEAN-FIELD MOTOR INTERACTIONS

Here we restrict the discussion to a linear sub-class of a more general theory presented in the Supplemental material Sec. 3.2.3. This linear sub-class is represented by motor cross-linkers which detach at a force-independent rate, $\psi_\mathrm{a}[nf(t)] = \psi_\mathrm{a}[nf(t)] = 1$ and which slow down linear to a force applied against their direction of motion

$$\phi_\mathrm{a}[nf(t)] = \mathrm{sgn}(v_\mathrm{a})\frac{nf(t)}{f_\mathrm{s,a}}$$
$$\phi_\mathrm{b}[nf(t)] = \mathrm{sgn}(v_\mathrm{b})\frac{nf(t)}{f_\mathrm{s,b}}\,.$$

Here f_s denotes a characteristic force at which the motor slows down to zero, commonly referred to as stall force. Note this implies that the motor heads can speed up above their unloaded velocities v_a and v_b. Relaxing this assumption changes some prefactors of the equations but not their functional form. The more general theory presented in the Supplemental material does not rely on these restrictions. However, the results presented here have the advantage of being analytically traceable and, thereby, easier to interpret.

Consider two filaments i and j which are cross-linked by the motor X, with motor head (a) attached to filament i and motor head (b) attached to filament j. The two filaments i and j move at time t at velocities $v_i(t)$ and $v_j(t)$. As a result of the relative filament motion $\Delta v_{ij}(t) = v_i(t) - v_j(t)$ and the relative motion of motor heads the motor cross-linker will be stretched, and therefore the motor heads exert a force on each other. This force is given by

$$f_\mathrm{ab}(t) = -\kappa\Delta x(t) = -\kappa\int_0^t \mathrm{d}t'[n_i V_\mathrm{a}[n_i f_\mathrm{ab}(t')] - n_j V_\mathrm{b}[n_j f_\mathrm{ba}(t')] + \Delta v_{ij}(t')]\,. \tag{3.16}$$

with $f_\mathrm{ab}(t) = -f_\mathrm{ba}(t)$. Here, we make the assumption that the motor cross-linker attached to the filaments at time $t = 0$ in a relaxed state, which, on average, will be true since binding is an equilibrium process. We make a time-scale separation argument, where we assume that the bond breakage of the cross-linker is fast compared to the time scale at which the filaments i and j change their speed

and denote the relative quasi-steady-state velocity by $\Delta\tilde{v}_{ij}$. In the following, we will drop the tilde. In the supplement (see Supplemental Material Sec. 3.2.3), we show that the average force this class of cross-linkers mediates, as a result of many cross-linking interactions, is given by the force-velocity relation

$$F_{\mathrm{ij,a}}(\Delta v_{ji}) = \Gamma_{\mathrm{X}}\left(n_j v_{\mathrm{b}} - n_i v_{\mathrm{a}} + \Delta v_{ji}\right) . \tag{3.17}$$

The notation $F_{\mathrm{ij,a}}$ denotes that head a is bound to filament i. This force-velocity relation can be seen as a mean-filed representation of the motor cross-linker X, which is valid in an ensemble of many motor cross-linkers of this type cross-linking the filaments i and j. The force-velocity relation is reciprocal under the exchange of filaments and motor heads; $F_{\mathrm{ij,a}}(\Delta v_{ji}) = -F_{\mathrm{ji,b}}(\Delta v_{ij})$. The constant Γ_{X} has units of force per velocity and represents an effective friction coefficient of the motor cross-linker, which is given by (see Supplemental Material Sec. 3.2.3)

$$\Gamma_{\mathrm{X}} = \frac{f_{\mathrm{s,a}} f_{\mathrm{s,b}}}{f_{\mathrm{s,b}}|v_{\mathrm{a}}| + f_{\mathrm{s,a}}|v_{\mathrm{b}}|} \frac{A}{1+A} . \tag{3.18}$$

Here A is a dimensionless constant that quantifies the relative force a motor would exert in the absence of stalling to the stall force of the motor heads:

$$A = \frac{\kappa}{k_{\mathrm{off,a}} + k_{\mathrm{off,b}}} \left(\frac{|v_{\mathrm{a}}|}{f_{\mathrm{s,a}}} + \frac{|v_{\mathrm{b}}|}{f_{\mathrm{s,b}}} \right) \tag{3.19}$$

It is easiest interpreted for a symmetric motor $a = b$, then it reads $A = \kappa v_{\mathrm{a}}/(k_{\mathrm{off,a}} f_{\mathrm{s,a}})$. For $\kappa v_{\mathrm{a}}/k_{\mathrm{off,a}} \ll f_{\mathrm{s}}$ the motor cross-linker detaches before it can exert a significant force and thereby does not impose friction between the filaments. In contrast, for $\kappa v_{\mathrm{a}}/k_{\mathrm{off,a}} \gg f_{\mathrm{s}}$ the friction coefficient of the symmetric motor cross-linker saturates at $\Gamma_{\mathrm{X}} = f_{\mathrm{s}}/v_{\mathrm{m}}$, i.e., is determined by the stall-force of the motor.

The force-velocity relation Eq. 3.17 depends on the relative orientation of the filaments. Since the filament bundle respects parity symmetry, we consider filament i with orientation $n_i = +1$ without loss of generality in the following and denote parallel interactions by $++$ and anti-parallel interactions by $+-$. The force-velocity relation for parallel and anti-parallel interactions then reads

$$F^{++}_{\mathrm{ij,a}}(\Delta v_{ji}) = \Gamma_{\mathrm{X}}\left(\Delta v_x + \Delta v_{ji}\right) \tag{3.20a}$$

$$F^{+-}_{\mathrm{ij,a}}(\Delta v_{ji}) = \Gamma_{\mathrm{X}}\left(-v_x + \Delta v_{ji}\right) . \tag{3.20b}$$

Here we introduced the sum $v_{\mathrm{x}} = (v_{\mathrm{a}} + v_{\mathrm{b}})$ and difference $\Delta v_{\mathrm{x}} = v_{\mathrm{b}} - v_{\mathrm{a}}$ of unloaded motor head velocities. We note that the average force a motor cross-linker of type X mediates between two filaments i and j does vanish if the relative motion of filaments and motor heads is such that it does not induce strain in the cross-linking motor.

FILAMENT SLIDING VELOCITY

We are first interested in the velocity v_i at which filament i moves in the filament bundle. Assuming overdamped dynamics, the velocity of filament i is determined by the total force acting on it as a result of motor cross-linker interactions and fluid drag. The total force mediated by a motor cross-linker of type X acting on the filament i is given by

$$F_{\mathrm{X,i}} = \sum_{j\neq i} X^{++}_{ij,a} F^{++}_{\mathrm{ij,a}} + X^{++}_{ij,b} F^{++}_{\mathrm{ij,b}} + X^{+-}_{ij,a} F^{+-}_{\mathrm{ij,a}} + X^{+-}_{ij,b} F^{+-}_{\mathrm{ij,b}} . \tag{3.21}$$

Here $X^{++}_{ij,a}, X^{+-}_{ij,a}, X^{++}_{ij,b}, X^{+-}_{ij,b}$ denote the population of a heads and b heads mediating a parallel $(++)$ or anti-parallel $(+-)$ interacton of the motor cross-linker X to filament j. In general, those populations depend on the density of filaments in the vicinity of filament i and, thereby, on space.

However, since we consider a homogenous filament bundle, it is reasonable to assume that the total number of motor cross-linker heads on filament i is equal for all filaments $i = 1,\dots,N_{\mathrm{Mt}}$, i.e., $\sum_{j\neq i} X^{++}_{ij,a} = X^{++}_a$ for all filaments (and analog for other populations). The total force mediated by the motor cross-linker X acting on a filament with orientation $n_i = +1$ is, therefore, the same for all filaments with equal orientation in the filament bundle. Hence, all filaments with equal orientation will have the same sliding velocity, and we can drop the subscript i. Filaments with opposite orientations have sliding velocities with an equal magnitude but opposite signs, which is already implied by parity symmetry. By definition we use $v_0^{\pm} \equiv \mp v_0$. Thereby, we obtain the total force applied by motor cross-linkers of type X to a filament with orientation $n = +1$, which is given by

$$F_{\mathrm{X}} = F_{\mathrm{X}}^{++}|_0 + F_{\mathrm{X}}^{+-}|_{2v_0}\,.$$

Here, the notation $|_x$ indicates where to evaluate the force-velocity relation. Before specifying those terms, this relation holds true for a general non-linear cross-linker, as shown in the Supplemental Material Sec. 3.2.3. For a linear cross-linker the terms $F_{\mathrm{X}}^{++}|_0$ and $F_{\mathrm{X}}^{+-}|_{2v_0}$ are given by

$$\begin{aligned} F_{\mathrm{X}}^{+-} &\equiv \Gamma_x v_{\mathrm{x}} (X_{\mathrm{a}}^{+-} + X_{\mathrm{b}}^{+-}) \left(-1 + \frac{2v_0}{v_x}\right) \\ F_{\mathrm{X}}^{++} &\equiv \Gamma_x \Delta v_{\mathrm{x}} (X_{\mathrm{a}}^{++} - X_{\mathrm{b}}^{++})\,. \end{aligned}$$

The total force acting on a filament with orientation $n = +1$ in a set of different cross-linkers is then given by

$$F = \sum_X \left(F_{\mathrm{X}}^{++}|_0 + F_{\mathrm{X}}^{+-}|_{2v_0}\right)$$

Those forces have to be balanced, either between each other or by drag imposed by the surrounding fluid. Force balance then implies

$$\gamma v_0 + \sum_X F_{\mathrm{X}}^{+-}|_{2v_0} = -\sum_X F_{\mathrm{X}}^{++}|_0\,. \tag{3.22}$$

Here, γ denotes the drag to the surrounding fluid. Note the only approximation made up to this point was a time-scale separation argument between the detachment dynamics of the cross-linkers and the dynamics of the filaments. Equation 3.22 is a good approximation even in the sparse limit of two filaments. The only requirement is that the filaments are cross-linked by sufficiently many cross-linkers to construct a mean-field representation of the motor. To interpret Eq. 3.22 let us consider a filament bundle cross-linked by a single symmetric motor cross-linker with $a = b$. For a symmetric motor cross-linker, we obtain $F_{\mathrm{X}}^{++}|_0 = 0$ and $F_{\mathrm{X}}^{+-}|_0 = -2\Gamma_{\mathrm{x}}(-v_a + v_0)$. Substitution in Eq. 3.22 yields $v_0 = v_{\mathrm{a}}/(1 + \gamma/(2\Gamma_X))$. Thus, if the effective friction Γ_{X} of the motor cross-linker dominates of external friction γ the motor will slide the filaments approximately at its unloaded speed, as observed in experiments for different types of motor cross-linkers [76, 95, 193]. This means if external friction is small, forces due to anti-parallel interactions balance each other, and motors do not get strained. This means that filaments have to be slowed down compared to the unloaded motor velocity to generate strain in the cross-linking motor. This hints at the fact that we need a finite amount of friction in the system to slow filaments down to generate tension in the motors and, thereby, the tension in the filament bundle. This is consistent with theoretical works studying specific examples of filament bundles cross-linked by symmetric motors [253, 254]. We now aim to explore this idea and understand the possible origin of the extensile or contractile tension in bundles of cross-linked filaments.

FILAMENT BUNDLE TENSION

The propensity of a filament bundle to contract or extend is revealed by its internal tension $\mathscr{T}$. A negative bundle tension ($\mathscr{T} < 0$) corresponds to a filament bundle under compression, i.e., the

bundle is extensile. In contrast, a positive bundle tension ($\mathcal{T} > 0$) corresponds to a filament bundle under tension, i.e., the bundle is contractile. In the following, we refer to the two possibilities as extensile ($\tilde{\mathcal{T}} < 0$) and contractile ($\tilde{\mathcal{T}} > 0$) tension. The tension in the filament bundle is revealed by the integrated force to one side of the bundle cross-section. Since the forces over the length of an individual filament balance in a homogenous filament bundle (cf. Eq. 3.22) the tension is given by the integrated force over all filaments that penetrate the cross-section; see Fig. 3.6 (d). In a homogenous

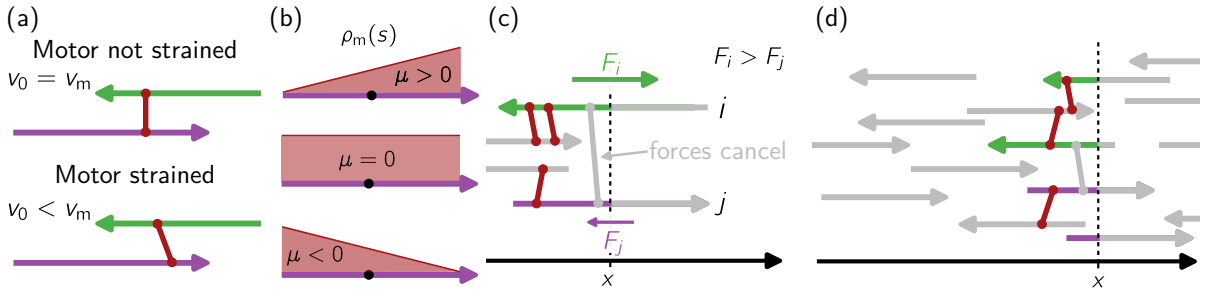

Figure 3.6: (a) If the filaments move at the speed of motors $v_0 = v_m$ opposed to the motor motion, the motor is not strained. (b) Schematic representation of the anisotropy factors. An asymmetric motor profile yields an anisotropy factor $\mu > 0$ if more motors are placed towards the plus end. A negative anisotropy factor indicates more motors at the minus end. (c) To obtain the bundle tension, we integrate over all forces to the left of a bundle cross-section. If more motors are centered towards the filament plus end ($\mu > 0$), the accumulated force to the right F_i is larger than the force to the left F_j. Interactions between filaments that pass through the plane cancel since $F_{ij,a} = -F_{ji,b}$. (d) Filaments in the bundle that pass through a bundle cross-section plane are shown in color. Filament-filament interactions that contribute to the bundle tension are also shown in color.

bundle of filaments with fixed length ℓ and density ρ_0 there will be $\rho_0\ell$ filaments that penetrate the bundle cross-section at different arc-length positions. To obtain the bundle tension, we introduce the force densities $f_X^{+-}(s)$ and $f_X^{++}(s)$ that stem from parallel and anti-parallel interactions of the motor cross-linker X at arc length position s. In mean-field, they are given by

$$f_X^{+-}(s) = \rho_{x,a}^{+-}(s) F_a^{+-}|_{2v_0} + \rho_{x,b}^{+-}(s) F_b^{+-}|_{2v_0}$$
$$f_X^{++}(s) = \rho_{x,a}^{++}(s) F_a^{++}|_0 + \rho_{x,b}^{++}(s) F_b^{++}|_0 \,.$$

Here $\rho_{x,a}^{+-}(s), \rho_{x,b}^{+-}(s), \rho_{x,a}^{++}(s), \rho_{x,b}^{++}(s)$ denote the arc-length density of the (a) and (b) heads mediating parallel and anti-pararallel interactions of the motor cross-linker X respectively. They obey $\int_{-\ell/2}^{\ell/2} ds \rho_{x,\alpha}^{\beta}(s) = X_\alpha^\beta$ with $\alpha = \{a, b\}$ and $\beta = \{++, +-\}$. The filament bundle tension $\mathcal{T}$ is then given by

$$\mathcal{T}_X = -\frac{\rho_0}{2} \int_{-\ell/2}^{\ell/2} d\xi \left[\int_{-\ell/2}^{\xi} ds f_X^{+-}(s) + f_X^{++}(s) + \int_{\xi}^{\ell/2} ds f_X^{-+}(s) + f_X^{--}(s) \right] . \tag{3.23}$$

making use of parity symmetry and substituting the explicit form of the force-velocity equation (Eq. 3.20), we find

$$\mathcal{T}_X^{+-}/(\rho_0\ell) = \Gamma_x v_x \left(-1 + \frac{2v_0}{v_x} \right) \left[\mu_a^{+-} X_a^{+-} + \mu_b^{+-} X_b^{+-} \right] \tag{3.24a}$$
$$\mathcal{T}_X^{++}/(\rho_0\ell) = \Gamma_x \Delta v_x \left[\mu_a^{++} X_a^{++} - \mu_b^{++} X_b^{++} \right] , \tag{3.24b}$$

where we introduced the anisotropy factors

$$\mu_\alpha^\beta \equiv \frac{1}{2} - \frac{1}{\ell X_\alpha^\beta} \int_{-\ell/2}^{\ell/2} d\xi \int_{-\ell/2}^{\xi} ds \rho_\alpha^\beta(s). \tag{3.25}$$

The anisotropy factors are in the range $\mu_\alpha^\beta \in [-1/2, 1/2]$. Where $\mu_\alpha^\beta = 1/2$ represents a delta-peaked distribution at the plus end and $\mu_\alpha^\beta = -1/2$ a delta peaked distribution at the minus end, $\mu_\alpha^\beta = 0$ represents a symmetric density profile; see Fig. 3.6 (b). Moreover, it should be noted that the anisotropy factor reverses the sign if we reverse the direction of motion of the cross-linker head as a result of the emergent density profile. Therefore, for a single type of motor cross-linker in the filament bundle, the sign and magnitude of the bundle tension are conserved under the inversion of motor head velocities.

The total filament bundle tension in a set of different motor cross-linkers is then given by

$$\mathcal{T} = \sum_X \mathcal{T}_X \,. \tag{3.26}$$

Note that the contribution of the individual motor cross-linker X to the total filament-bundle tension Eq. 3.24 is a function of the filament sliding velocity v_0 and thereby coupled to all other cross-linkers in the system via the force-balance condition Eq. 3.22. It should be appreciated that Eq. 3.24 expresses the contribution of a whole class of cross-linking motor proteins to the filament bundle tension. Thereby, we obtained a simple framework that can give insight into the physics that controls the propensity of a filament bundle to contract or expand. This allows us to make general statements about the features of a motor cross-linker to promote extensile or contractile stress, as well as to study specific examples "out of the box" upon specifying a microscopic model of the cross-linkers, by defining the kinetic constants ($v_\mathrm{a}, v_\mathrm{b}, k_\mathrm{off,a}, k_\mathrm{off,b}$) and the mechanical property of the motor cross-linker κ. Before we study specific examples and combine different motor cross-linkers we would like to explore general features of the contribution $\mathcal{T}_X$ of a specific cross-liner to the bundle tension.

INTERPRETATION OF THE BUNDLE TENSION

Interestingly, we find that a motor cross-linker X, which has symmetric density profiles ($\mu_\alpha^\beta = 0$), can neither promote extensile nor contractile tension. This is consistent with filed theories derived from the dilute limit on the basis of simplified interaction rules. In those theories, asymmetric filament-filament scattering interactions have to be imposed to obtain extensile stress [241, 247]. A second important observation is that symmetric motors ($a = b$) contribute only via anti-parallel interactions ($+-$) to the bundle tension. Moreover, in the absence of different motor cross-linkers, they can only promote extensile tension. Active nematic filament-motor mixtures with motors that do not dwell at the filament-end fall into this class of systems [38, 76, 87]. Somewhat surprisingly, we find that the magnitude of the extensile tension in those systems is increased as the sliding speed of individual filaments is decreased. This means the material's propensity to expand increases as the components of the material are slowed down. While being a surprising effect, it is consistent with recent *in vitro* experiments that demonstrate that an active nematic filament bundle can exhibit strong extensile stresses in the absence of relative filament sliding [90]. On a physical basis, this can be explained as follows: If the filaments slide at the unloaded speed of the motor, they slide across the motor without inducing strain in the motor, which in turn prevents the build-up of tension in the material. Moreover, Eq. 3.24a clearly shows that the broken symmetry in extensile and contractile stress, which was previously observed in computer simulations of symmetric motor cross-linkers [250], arises as a result of anisotropic motor density profiles, which in turn are caused by the directed motion of motor proteins. The need for anisotropic density profiles to promote extensile tension can be understood when we consider a pair of filaments with orientation $n_i = -1$ and $n_j = +1$ that penetrates the cross-section of interest; see Fig. 3.6 (c). Interactions between the filaments i and j do not contribute to the bundle tension as they have equal magnitude but opposite signs. The only interactions that contribute to the bundle tension are filament-filament interactions between a filament that penetrates the bundle cross-section and filaments that do not penetrate the

bundle cross-section; see Fig. 3.6 (d). If the motor densities are asymmetric, the symmetry between contractile and extensile forces is broken; see Fig. 3.6 (c).

Turning our attention to asymmetric motors, we observe that asymmetric motors can promote a contribution to the filament bundle tension that stems from parallel interactions of filaments. This contribution can be extensile or contractile depending on the anisotropy factors and motor head populations. Importantly, this tension is independent of the filament sliding velocity v_0, i.e., asymmetric motors can promote tension on their own, and there is no need for internal friction. This implies that if an active filament motor mixture is cross-linked by asymmetric motors, there can be an extensile or contractile tension associated with polar filament-filament interactions. This is in line with a recent field theory derived on the behavior of end-dwelling motors, which shows the existence of active polar stress [255] and not only apolar stress, as usually imposed by active nematic field theories [50, 80–85].

Relaxing the assumption of a homogenous filament bundle, we can make statements about a filament bundle that has homogenous density but spatially varying ratios of parallel and anti-parallel interaction partners. We previously showed that in such a filament bundle, the sliding speed v_0 of filaments is independent of the local ratio of parallel and anti-parallel interaction partners [2]. However, the populations of parallel and anti-parallel motor cross-linkers on a filament X_α^β will depend on the local number of parallel and anti-parallel filaments. Thus, extensile tension is expected to be highest in apolar regions and contractile tension in polar filament bundle regions, independent of the specific type of motor cross-linker.

We next use our general framework Eq. 3.24 and Eq. 3.22 to evaluate the contribution of some biologically relevant motor proteins to the bundle tension.

EXAMPLES

Symmetric bulk motors We first consider a symmetric bulk motor named M, which is a motor with equal head domains that does not dwell at the filament-end it is walking towards. We consider a plus-end oriented motor, which has the unloaded motor head velocities $v_\mathrm{a} = v_\mathrm{b} = v_\mathrm{m} > 0$ and the motor head populations $X_\mathrm{a}^{+-} = X_\mathrm{b}^{+-} = M/2$. The contribution of this type of motor crosslinker is then given by

$$F_\mathrm{M} = 2M\Gamma_\mathrm{m} v_\mathrm{m}\left(-1+\frac{v_0}{v_\mathrm{m}}\right) \tag{3.27a}$$

$$\mathscr{T}_\mathrm{M}^{+-}/(\rho_0\ell) = 2\Gamma_\mathrm{m} v_\mathrm{m} M\mu_\mathrm{m}\left(-1+\frac{v_0}{v_\mathrm{m}}\right). \tag{3.27b}$$

Since we consider a plus-end-oriented motor, the emergent anisotropy factor will be $\mu_\mathrm{m} > 0$. Moreover, in the absence of other motor cross-linkers, $v_0 \leq v_\mathrm{m}$, hence the motor can only contribute an extensile or neutral contribution. A prominent example of this class of motor-cross-linkers is Kinesin-5 [95].

Asymmetric bulk motors Another relevant biological example are motor cross-linkers that have one motor domain and one immobile microtubule-binding domain. An example is, e.g., kinesin-14 [256]. We consider a minus end-directed motor with $v_\mathrm{a} < 0$ and $v_\mathrm{b} = 0$. An analysis of the mean-field density profile as presented in the Supplemental Material Sec 3.2.3 implies a symmetric density profile of the immobile head domain and therefore $\mu_\mathrm{b}^{++} = \mu_\mathrm{b}^{+-} = 0$. Moreover, in a homogenous

filament bundle, we may assume $X_a^{+-} = X_b^{+-} = A/2$ and $X_a^{++} = X_b^{++} = A/2$. Thereby we obtain

$$F_a = \Gamma_a v_a A \left(-1 + \frac{2v_0}{v_a}\right)$$
$$\mathcal{T}_a^{+-}/(\rho_0 \ell) = \Gamma_a v_a \mu_a^{+-} \frac{A}{2}\left(-1 + \frac{2v_0}{v_a}\right)$$
$$\mathcal{T}_a^{++}/(\rho_0 \ell) = -\Gamma_a v_a \mu_a^{++} \frac{A}{2}\,.$$

In the absence of other motor cross-linkers, the maximal sliding velocity mediated by a minus end-directed motor cross-linker with only one motor domain is $-v_0/2$. If the filaments slide at this speed, the tension steming from anti-parallel interactions is zero. Else anti-parallel interactions mediate an extensile tension $\mathcal{T}_a^{+-} < 0$. Parallel interactions of an asymmetric bulk motor are always extensile ($v_a < 0$ and $\mu_a^{++} < 0$), $\mathcal{T}_a^{++} < 0$, This is an example of a motor which is capable of exerting extensile tension even in the absence of internal friction. If the anisotropy factor of parallel and anti-parallel interactions is equal, the resulting tension looks similar to the result for a symmetric bulk motor. However, with the difference that the maximal filament sliding speed is $|v_0| \leq v_a/2$. If there are more parallel interaction partners available, they are more efficient in promoting an extensile tension. This is consistent with a previous numerical analysis [257].

Tip dwelling motors An important class of asymmetric motors are motors that dwell at the filament tip. Examples are, e.g., Kinesin-4 [40], which dwells at the plus-tip, or dynein, which dwells at the minus-tip [193]. We consider a plus-end-oriented tip-motor with unloaded motor head velocities $v_a = v_m > 0$ and $v_b = 0$. The motor domain dwelling at the filament plus-end has delta-peaked density distribution at the filament plus-end, hence $\mu_b^{+-} = \mu_b^{++} = 1/2$.

$$F_t = \Gamma_t v_m (X_a^{+-} + X_b^{+-})\left(-1 + \frac{2v_0}{v_m}\right) - \Gamma_t v_m (X_a^{++} - X_b^{++}) \tag{3.28a}$$
$$\mathcal{T}_t^{+-}/(\rho_0 \ell) = \Gamma_t v_m \left(-1 + \frac{2v_0}{v_m}\right)\left[1/2 X_b^{+-} + \mu_a^{+-} X_a^{+-})\right] \tag{3.28b}$$
$$\mathcal{T}_t^{++}/(\rho_0 \ell) = \Gamma_t v_m \left[1/2 X_b^{++} - \mu_a^{++} X_a^{++}\right]\,, \tag{3.28c}$$

If we further assume that the tip-motor is symmetric in the bulk we may assume $X_a^{++} = X_b^{++}$ and $X_b^{+-} = X_b^{+-}$.

Passive cross-linkers Passive cross-linkers are motor cross-linkers without motor activity $v_a = v_b = 0$. On a mean-field level, they have the anisotropy factors 0 consistent with passive dynamics. Thus, they promote neither contractile nor extensile tension. However, an effective friction force between filaments

$$F_C = 2\Gamma_c v_0 C\,. \tag{3.29}$$

Where we denoted used $X^{+-} = X^{++} = C$. Note if $v_a = v_b = 0$ the effective friction coefficient has to be evaluated as presented in the Supplemental Material Sec. 3.2.3.

UNDERSTANDING ACTIVE FILAMENT BUNDLES IN MIXTURES OF DIFFERENT MOTOR CROSS-LINKERS

Having evaluated the contribution of specific examples of cross-linking motor proteins, we turn our attention to mixtures of different cross-linking motor proteins. In particular, we are interested in a specific set of agents that have recently received increased experimental attention. These are filament-motor mixtures composed of microtubules, and motors that are capable of cross-linking and walking on the cross-linked microtubules and a crowding agent. Often as a crowding agent,

polyethylene glycol (PEG) or the passive cross-linker PRC1 is used. In addition in some of the experiments, motors are used that dwell at the filament tip. Those *in vitro* systems show rich physical behavior. In the absence of tip-dwelling, the filament motor mixtures display turbulent-like dynamics, that are characterized by a repeating sequence of buckling, breaking, and fusing filament bundles associated with an extensile stress [38, 76, 87]. It has been shown that the Euler-like buckling instability of the filament bundles can be controlled by the crowding agent or passive cross-linker [78, 91, 238]. If motor cross-linkers are used that dwell at the filament tip these systems show transitions from contractile to extensile dynamics, that is controlled by the total number of motors and crowding agents [40, 79] and the average length of the filaments [75, 88]. In the presence of tip dwelling, those filament motor mixtures sometimes show puzzling dynamics to first show features associated with extensile stress and then contract in the long run [40].

We, therefore, conclude that those systems provide an interesting test case of our theoretical framework and see if we can gain insight into the macroscopic dynamics from the mesoscopic scale of an individual filament bundle. We use a minimal set of constituents that resembles the general features of the agents used in the experiments. First, a symmetric plus-end directed bulk motor. We denote the population of symmetric bulk motor heads on the filaments by M (cf. Eg. 3.27) and the anisotropy factor by μ_m (there is only one). The unloaded motor velocity is given by v_m. This motor is capable of dwelling at the filament tip (plus-end). The detachment dynamics at the filament tip can differ from the bulk detachment dynamics (cf. Eq. 3.28), hence, $\Gamma_\mathrm{m} \neq \Gamma_t$. Since the tip-motors are symmetric in the bulk we use $X_\mathrm{a}^{++} = X_\mathrm{b}^{++} \equiv M_\mathrm{t}^{++}$ and $X_\mathrm{b}^{+-} = X_\mathrm{b}^{+-} \equiv M_\mathrm{t}^{+-}$. Last we model the crowding agent by a passive cross-linker (cf. Eq. 3.29). While a depletant like PEG is not precisely a passive cross-linker, it has been shown to cause effective friction between neighboring filaments [258]. We re-scale velocities in units of the unloaded motor velocity $v \equiv v_0/v_\mathrm{m}$ and define the force amplitudes $F_\mathrm{m} \equiv 2\Gamma_\mathrm{m} v_\mathrm{m}$, $F_\mathrm{t} \equiv \Gamma_\mathrm{t} v_\mathrm{m}$, $F_\mathrm{c} \equiv 2\Gamma_\mathrm{c} v_\mathrm{m}$ and $F_\mathrm{s} = \gamma v_\mathrm{m}$ and re-scale the bundle tension by $\tilde{\mathcal{T}} = \mathcal{T}/(\rho_0 \ell)$. Combining the different terms yields the force balance equation Eq. 3.22 and the total bundle tension (Eq. 3.26)

$$0 = F_\mathrm{s} v + F_\mathrm{m} M(-1+v) + 2F_\mathrm{t} M_\mathrm{t}^{+-}(-1+2v) + F_\mathrm{c} C v \tag{3.30a}$$

$$\tilde{\mathcal{T}} = F_\mathrm{m} M(-1+v)\mu_\mathrm{m} + F_\mathrm{t} M_\mathrm{t}^{+-}(-1+2v)(\mu_t^{+-}+1/2) + F_\mathrm{t} M_\mathrm{t}^{++}(1/2-\mu_\mathrm{t}^{++}) \tag{3.30b}$$

When active forces dominate over dissipation to the surrounding fluid ($F_\mathrm{s} \ll (F_\mathrm{m} M + 2F_\mathrm{t} M_\mathrm{t}^{+-})$ we find the solution of the force balance condition to be given by

$$v = \frac{1+2\bar{m}}{1+4\bar{m}+\bar{c}}\,. \tag{3.31}$$

where we introduced the ratio of anti-parallel tip-to-bulk motor forces $\bar{m} = F_\mathrm{t} M_\mathrm{t}^{+-}/(F_\mathrm{m} M)$ and the ratio of internal friction forces to bulk motor forces $\bar{c} = F_\mathrm{c} C/(F_\mathrm{m} M)$. We note that the filament sliding velocity is determined by a competition between active forces and internal friction caused by the passive cross-linker. Moreover, tip motors can contribute to a frictional element. This is because they are outpaced by the cross-linked filaments whose motion is driven by the symmetric bulk motors, which promote a relative sliding velocity of $2v_\mathrm{m}$ instead of v_m for tip motors. The motion of the motor is plus-end directed, thus we expect $0 < \mu_\mathrm{m} < 1/2$, $0 < \mu_\mathrm{t}^{+-} < 1/2$ and $0 < \mu_\mathrm{t}^{++} < 1/2$. Hence, as expected the bulk motors contribute an extensile tesnion. Anti-parallel tip-motor interactions can contribute to extensile or contractile tension, depending on the filament sliding velocity. For $v < 1/2$ the tension is extensile, else contractile. This is because if $v > 1/2$, the relative filament sliding out paces tip motors and they will resist the relative motion of filaments and contribute a contractile tension. Last, parallel tip motors always contribute to contractile tension. However, they do not contribute to the total force acting on a filament, i.e., they cancel only when integrated over the entire arc length of the filament. Moreover, we note that

the contribution of parallel tip-motor interactions is independent of the sliding speed v. This offers an interesting pathway to control the relative strength of extensile and contractile tension in the filament bundle. If the relative motion of filaments is slowed down by increasing the number of bundling agents, the extensile tension in the filament bundle can be increased, in particular if anti-parallel tip motors also contribute extensile tension. In contrast, by increasing the number of tip motors in the system, we can increase the propensity of the filament bundle to contract.

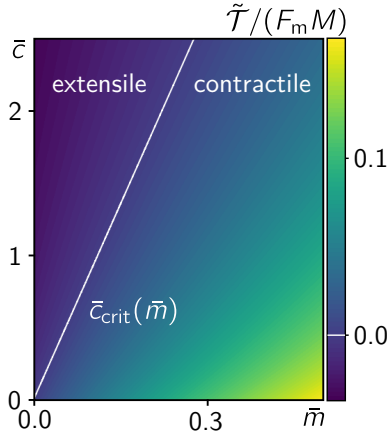

Figure 3.7: Filament bundle tension in the $(\bar{c}, \bar{m})$ parameter plane for a filament bundle cross-linked by plus-end directed motor cross-linker that dwell at the filament tip and passive cross-linkers. The filament bundle tension changes sign at a critical concentration of bundling agents $\bar{c}_{crit}(\bar{m})$. If the ratio of tip-to-bulk motor forces $\bar{m}$ is large the filament bundle is contractile.

To get an intuition about the underlying physics that determines the propensity of the filament bundle to contract or expand, we investigate the case of equal populations of parallel and anti-parallel tip motors $M_t^{+-} = M_t^{++} = M_t/2$ and equal anisotropy factors $\mu_m = \mu_t^{+-} = \mu_t^{++} = \mu$. We then find the critical ratio of internal friction to active bulk motor forces $c_{crit}(\bar{m})$ at which the bundle tension switches from contractile to extensile. Which is given by

$$\bar{c}_{crit}(\bar{m}) = \left(\frac{1}{2\mu} - 1\right)\bar{m}\,. \tag{3.32}$$

Figure 3.7 shows the bundle tension in the $(\bar{c}, \bar{m})$ parameter plane. For $\bar{c} < \bar{c}_{crit}(\bar{m})$ the sign on the bundle tension is positive, and the filament bundle is contractile, and for $\bar{c} > \bar{c}_{crit}(\bar{m})$ the filament bundle has an extensile tension. As long as the motor cross-linker has an asymmetric profile ($\mu > 0$), which is expected to be true as a result of the plus-end directed motion of the motor, the system can be tuned from contractile to extensile by increasing the internal friction in the filament bundle. In contrast, by increasing the population of tip-dwelling motors, the propensity of the filament bundle to contract can be increased. In summary, we found three mechanisms that determine the propensity of the filament bundle to contract or extent: First, in the absence of tip-dwelling of motors, the filament bundle is either neutral ($\tilde{\mathcal{T}} = 0$) or extensile ($\tilde{\mathcal{T}} < 0$). A finite amount of friction is needed for the filament bundle to be extensile. In particular, internal friction, which is caused, for example, by passive cross-linkers, allows one to tune the sign of the bundle tension and its magnitude. The second requirement for extensile filament bundles is an anisotropic profile of motors along the filaments, with more motor mass towards the filament plus end ($\mu > 0$). The filament bundle is neutral for symmetric motor profiles, $\mu = 0$. Third, end-dwelling motors promote the propensity of the filament bundle to contract. Those characteristics are reflected in the set of coarse-grained parameters $(F_m M, F_t M_t^{+-}, F_t M_t^{++}, \mu_m, \mu_t^{+-}, \mu_t^{++})$.

But how do those characteristics emerge from the microscopic interplay of the bundle constituents? Tip-motors and bulk motors are ultimately the same type of motor thus, their total number $M_{tot} = M_t^{+-} + M_t^{++} + M$ must be conserved. But which mechanisms control their ratio? Moreover, a motor must move through the bulk to reach the filament tip. However, the movement through the bulk is what sets the anisotropy factor of the motor. In the next section, we aim to identify how parameters that control the microscopic dynamics, like the binding and unbinding rate of proteins and the velocity of the motors, set the coarse-grained control parameters.

RELATING COARSE-GRAINED PARAMETERS TO THE MICROSCOPIC DYNAMICS

We first aim to identify which physical mechanisms control the tip-to-bulk motor ratio. Mass conservation requires

$$M_{\mathrm{tot}} = M + M_{\mathrm{tip}}^{\mathrm{pp}} + M_{\mathrm{tip}}^{\mathrm{ap}} \,. \tag{3.33}$$

However, this equation is under-determined, and we can choose any combination of populations that satisfies this condition. This seems at odds with physical intuition since motors must move through the bulk to reach the filament tip. Therefore, there has to be a connection relating to their relative populations. To obtain those relations, we investigate the microscopic dynamics of the mean-field motor expressed by the force-velocity relation Eq. 3.20. As a result of the average force the motor exerts between the filaments, it will adopt an average velocity $\langle V_\alpha^\beta \rangle$ that depends on the force of the respective interaction the motor mediates. In the case of our linear motor cross-linker, bulk motors will adapt the mean velocities

$$\langle V_{\mathrm{m}}^{+-} \rangle = v_{\mathrm{m}} \left[1 - \frac{F_{\mathrm{m}}}{f_{\mathrm{s}}} (1 - v) \right] \tag{3.34a}$$

$$\langle V_{\mathrm{m}}^{++} \rangle = v_{\mathrm{m}} \,. \tag{3.34b}$$

In the limit of $v_{\mathrm{m}} \kappa k_{\mathrm{off}}^{-1} \gg f_s$, i.e., when motors operate at their stall force ($F_{\mathrm{m}} = f_{\mathrm{s}}$), the velocity of motorheads attached to anti-parallel filaments will adapt the filament velocity $v_0 = v_{\mathrm{m}} v$. In contrast, parallel bulk motors do not exert force between the filaments they cross-link. Hence, they move at their unloaded speed. The directed motion of motor heads along the arc-length, $s \in [-\ell/2, \ell/2]$, of a filament at speed V_{m}^x in combination with attachment of motors at rate k_{on} and detachment from the filament at rate k_{off} can be described by a reaction-convection equation

$$\partial_t \rho_{\mathrm{x}}(s,t) = -\langle V_\alpha^\beta \rangle \partial_s \rho_\alpha^\beta(s,t) + k_{\mathrm{on}} - k_{\mathrm{off}} \rho_\alpha^\beta(s,t) \,, \tag{3.35}$$

With $\alpha = \{\mathrm{m}, \mathrm{t}\}$ and $\beta = \{++, +-\}$ Note k_{on} has units per time per unit length of the filament. Moreover we use the boundary condition $\rho_{\mathrm{x}}(-\ell/2) = 0$. In steady state this equation is solved by

$$\rho_\alpha^\beta(s) = \frac{M^\beta}{\mathcal{N}_\alpha^\beta \ell} \left(1 - \mathrm{e}^{-(s/\ell + 1/2)\lambda_{\mathrm{m}}^\beta} \right) , \tag{3.36}$$

here we defined

$$\lambda_\alpha^\beta = \ell / l_{\mathrm{run}} = \ell k_{\mathrm{off}} / \langle V_\alpha^\beta \rangle . \tag{3.37}$$

as the ratio of filament length to the motor run length $l_{\mathrm{run}} = V_\alpha^\beta / k_{\mathrm{off}}$. The dimensionless normalization, $\mathcal{N}_\alpha^\beta$, is chosen such that $\int_{-\ell/2}^{\ell/2} \mathrm{d}s \rho_\alpha^\beta(s) = M_\alpha^\beta$, i.e., the total population of anti-parallel bulk and tip motors. Here, we assume them to be equal $M^{+-} = M^{++} = M/2$. In steady state, the flux of bulk motor heads onto the filament tip $\langle V_\alpha^\beta \rangle \rho_\alpha^\beta(\ell/2)$ has to be balanced by the off flux due to tip detachment $k_{\mathrm{off,tip}} M_{\mathrm{t}}^\beta$, with $\beta = \{++, +-\}$:

$$0 = -k_{\mathrm{off,tip}} M_{\mathrm{t}}^\beta + \langle V_{\mathrm{m}}^\beta \rangle \frac{M/2}{\mathcal{N} \ell} \left(1 - e^{-\lambda_{\mathrm{m}}^\beta} \right) . \tag{3.38}$$

Thereby, we can express the population of parallel and anti-parallel tip motors as a function of the bulk motor population. However, they are all connected via the filament sliding velocity v. Taken together, we obtain a set of four coupled equations which has to be solved self consistently

$$\begin{aligned} M_{\mathrm{tot}} &= M_{\mathrm{t}}^{++} + M_{\mathrm{t}}^{+-} + M \\ M_{\mathrm{t}}^\beta &= \frac{M}{2} \frac{\omega}{\mathcal{N}_{\mathrm{m}}^\beta \lambda_{\mathrm{m}}^\beta} \left(1 - e^{-\lambda_{\mathrm{m}}^\beta} \right) \\ v &= \frac{1 + 2\bar{m}}{1 + 4\bar{m} + \bar{c}} \,. \end{aligned}$$

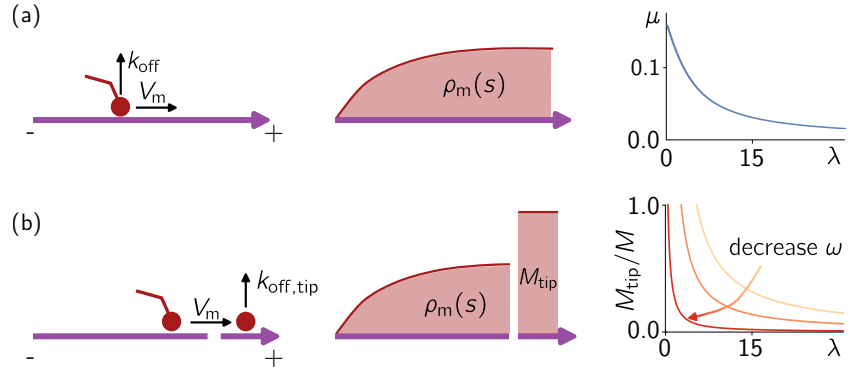

Figure 3.8: (a) Schematic representation of the dynamics of a motor head along the arc-length s of the filament. The average speed of motors V_m and the detachment rate k_{off} of motors determine their density profile and, thereby, the anisotropy factor. Note the velocity V_m depends on the relative orientation of the cross-linked filaments and whether the other motor head is attached to a filament tip or the filament bulk. (b) The number of tip motors is determined by a flux balance between the flux of motors onto the filament tip due to advection and the off-flux due to tip detachment at rate $k_{off,tip}$. Increasing the tip-detachment rate provides the simplest mechanism to reduce the number of tip-motors.

with $\bar{m} = F_t M_t^{+-}/(F_m M)$ and $\bar{c} = F_c C/(F_m M)$ and the bulk-to-tip detachment rate ratio $\omega = k_{off}/k_{off,tip}$. Taken together, we have a closed set of equations for the different motor populations (M, M_t^{+-}, M_t^{++}), the filament sliding speed v and the motor head velocities V_m^β. Figure 3.9 shows the resulting populations for a fixed set of kinetic parameters and the filament sliding velocity v_0 as a function of passive cross-linkers C per total number of motors M_{tot}. As the number of passive cross-links (internal friction) is increased, the number of anti-parallel tip motors is decreased. This is because the speed of anti-parallel bulk motors decreases as a function of the filament sliding velocity (cf. Eq. 3.34). This, in turn, reduces the flux of bulk motors onto the filament tip and, thereby, the number of anti-parallel tip motors M_t^{+-}. The increase in parallel tip-motors M_t^{++} and anti-parallel bulk motors M is due to mass conservation.

It is now straightforward to derive the anisotropy factors by substituting the solution for the density (Eq. 3.36) in the definition of the motor anisotropy (Eq. 3.25)

$$\mu_\alpha^\beta = \frac{1}{2} - \frac{e^{\lambda_\alpha^\beta}(1+\lambda_\alpha^\beta(\lambda_\alpha^\beta/2-1))-1}{\lambda_\alpha^\beta + e^{\lambda_\alpha^\beta}(\lambda_\alpha^\beta-1)\lambda_\alpha^\beta} \tag{3.39}$$

For $\lambda_\alpha^\beta \to 0$, i.e., for persistent motors, we obtain $\mu_\alpha^\beta = 1/6$, which corresponds to a linear profile, and for $l_{run} \ll \ell$, the anisotropy factors become $\mu_\alpha^\beta = 0$ since passive attachment/ detachment dynamics dominates over the active, directed motion of motors (the motor density saturates quickly). Figure 3.9 (b) shows the resulting anisotropy factors and the average velocities V_α^β of anti-parallel bulk, anti-parallel tip, and parallel tip motors for a fixed set of kinetic parameters as a function of C/M_{tot}. As internal friction is increased, anti-parallel motor cross-links have to operate against a higher load. As a result, they slow down. This in turn reduces their run length $l_{run} = \langle V_m^{+-}\rangle/k_{off}$ and therefore "flattens" the motor profile.

Taken together, we derived all mesoscopic control parameters as a function of the total number of motors and passive cross-linkers per filament and the filament length. Therefore, besides the kinetic parameters the remaining set of control parameters is (M_{tot}, C, ℓ)

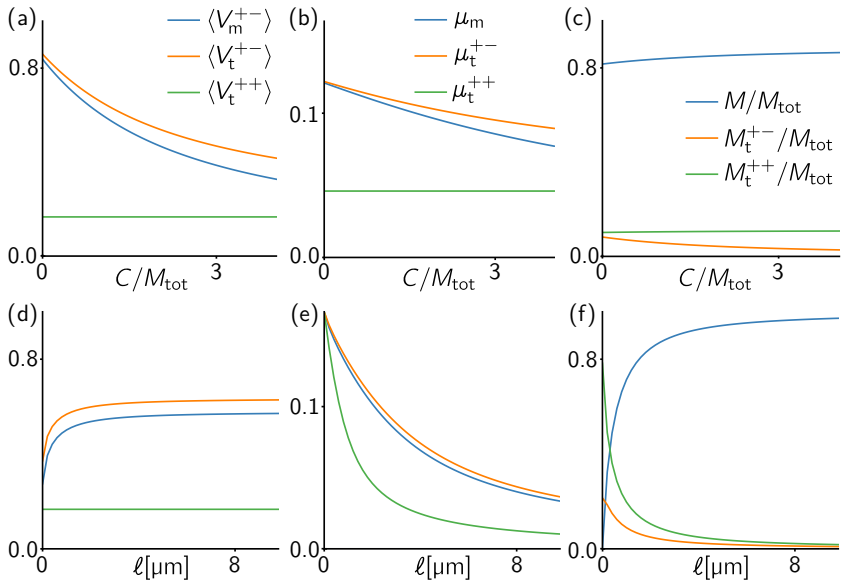

Figure 3.9: (a) Average motor head velocities of the different populations as a function of the motor-to-passive cross-linker ratio; C/M_{tot}. As the number of passive cross-links (internal friction) is increased, the number anti-parallel motor populations slows down to adapt to the decreasing sliding speed of filaments (cf. Eq. 3.34). Parallel cross-linked motors move at a speed independent of the filament sliding speed and, therefore, independent of C/M_{tot}. (b) As a result of the changing motor velocity, the anisotropy factors change. (c) Relative motor head populations. The decreased speed of anti-parallel cross-linked motors in the bulk decreases the influs into anti-parallel tip configurations. As a result, the number of anti-parallel tip motors M_t^{+-} decreases. (d) Mean motor velocities as a function of the filament length ℓ, the motor velocities remain approximately constant. (e) The motor anisotropies as a function of the filament length. Since the motor velocities are constant, longer filaments promote a "flatter" profile. Therefore, the motor anisotropies decrease. (e) The population of tip and bulk motors as a function of the filament length ℓ. The tip motor populations are proportional to $(1-\exp(-\lambda))/\lambda$. Thereby, the tip-motor populations decrease as a function of the filament length. As a result of mass conservation, the bulk motor concentration increases. Parameters: $k_{\text{off}} = k_{\text{off,tip}} = 0.8\,\text{s}^{-1}$ and $M_{\text{tot}} = 10$ other parameters are given in Table 3.2. Moreover, I accidentally used $\kappa_c = 100\,\text{pN}/\mu\text{m}$.

EMERGENT FILAMENT BUNDLE TENSION

For a given type of motor cross-linker, the set of kinetic parameters is fixed. However, what can be tuned externally is the total number of passive cross-linkers per filament C, the total number of motors per filament M_{tot}, and the filament length ℓ. We, therefore, study the bundle tension as a function of those parameters while keeping all other parameters fixed. Moreover, we investigate the impact of tip detachment since it provides the simplest mechanism to change the tip-to-bulk motor ratio. Figure 3.10 shows the filament bundle tension as a function of $(C, M_{\text{tot}}, \ell, \omega)$. In the (ω, C) parameter plane, the result is reminiscent of the $(\bar{m}, \bar{c})$ parameter plane of the coarse-grained description; Fig. 3.10 (a) and Fig. 3.7. However, the anisotropy factors and the relative ratio of the different populations differ, resulting in a different phase boundary. In the (M_{tot}, C) parameter plane, we find that the filament bundle is contractile for large total motor numbers, M_{tot}, and low internal friction and extensile for large internal friction and low motor numbers; see Fig. 3.10 (b). This switch in the sign of the bundle tension is controlled via the filament sliding velocity v. If the ratio of passive cross-linkers to active motors, C/M_{tot}, is increased, v_0/v_m is reduced. This, in turn, increases the extensile contribution to the bundle tension and reduces the contractile contribution

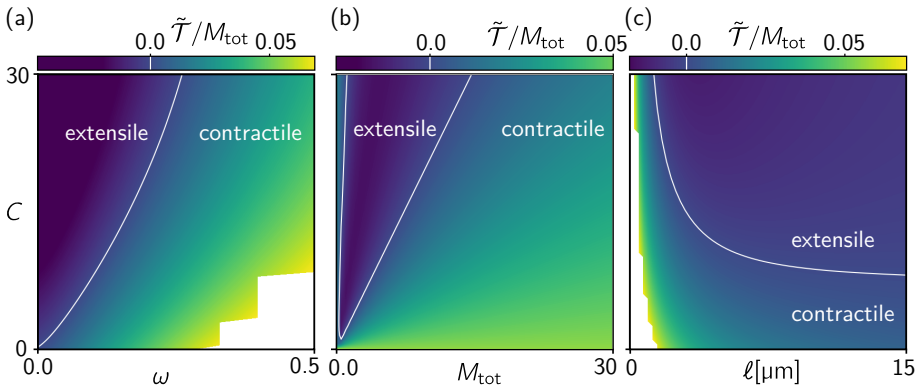

Figure 3.10: (a)-(c) Filament bundle tension obtained from the microscopic model for a fixed set of kinetic parameters. (a) Bundle tension as a function of passive cross-linkers C and the tip-detachment rate ω; $M_{\mathrm{tot}} = 13$. The tip-detachment rate provides a way to control the number of tip-bound motors without affecting other control parameters a lot. The result is reminiscent of Fig. 3.6 as expected. (b) Filament bundle tension as a function of the total number of doubly linked motors and cross-linkers per filament. (c) Filament bundle tension as a function of the filament length ℓ and the number of doubly-linked passive cross-linkers per filament; $M_{\mathrm{tot}} = 10$. Parameters: See Tab. 3.2.

of anti-parallel tip motors. For $v < 1/2$, the contribution of anti-parallel tip motors even changes sign and becomes extensile. Last, in the (ℓ, C) parameter plane, we find that the filament bundle is contractile for short filaments and low internal friction and extensile for long filaments and high internal friction; see Fig. 3.10 (c). This change is controlled in a more subtle way. For a fixed set of kinetic parameters and fixed $c = C/M_{\mathrm{tot}}$ the motor velocities $\langle V_{\mathrm{m}}^{\beta} \rangle$ are approximately constant; see Fig. 3.9. Together with a constant off rate, this yields a constant run length l_{run}. Therefore, $\lambda = \ell / l_{\mathrm{run}}$ will increase as the filament length is increased. The parallel and anti-parallel tip motor populations are proportional to $\rho_{\mathrm{m}}^{\beta} \sim (1 - \exp(-\lambda))/\lambda$, with $\beta = \{++, +-\}$. As a result of mass conservation, this increases the number of bulk motors m; see Fig. 3.9. Thereby, increasing the filament length, ℓ, increases the extensile contribution to the bundle tension and decreases the contractile contributions. This effect is counteracted but not compensated by a decrease in motor anisotropies due to the increase of λ; see Fig. 3.9 (e).

Taken together, we found that the propensity of a filament bundle to contract or expand can be controlled by three external control parameters: (i) The concentration of passive cross-linkers, (ii) the concentration of active motors, and (iii) the length of filaments. All those possibilities have been observed experimentally. In [91, 92, 238], it has been shown that a nematically aligned filament network can be tuned toward an Euler-type buckling instability by increasing the passive cross-linkers in the system. This is characteristic of a material under compression (negative tension). Similar behavior has been observed for depletion agents instead of passive cross-linkers [78, 91]. While depletion agents are not the same as passive cross-linkers it has been shown that they cause friction between neighboring filaments [258]. Therefore, they also provide a possibility to reduce v. In [79], it has been shown that a filament network can be tuned from extensile filament bundles resembling turbulent-like dynamics on the macroscopic scale to a contractile network that self-organized into asters by increasing the number of motors in the system and vice versa by increasing the concentration of a depletion agent. In [75, 88], it was shown that a network of dynamic filaments can be tuned from a contractile aster-forming dynamics to an extensile filament motor mixture by increasing the concentration of tubulin and, thereby, the mean filament length.

In the next section, we aim to explore the different impacts of tip and bulk motor populations on the macroscopic dynamics of the filament bundle with the help of agent-based computer simula-

tions.

COMPARISON TO AGENT-BASED SIMULATIONS

This section is a work in progress. Here, I will show some preliminary simulation results. Unfortunately, I simulated motors and passive cross-linkers with force-dependent detachment dynamics, making a direct comparison to the analytic result not possible at the moment. However, all predictions of our analytic derivation are recapitulated on a phenomenological level by the agent-based simulation. So far, I have used the number of passive cross-linkers and the tip detachment rate as control parameters. I used cytosim [249] to simulate the filament bundle. Unfortunately, the most reason version on Git `https://gitlab.com/f-nedelec/cytosim` *does not support the option to change the tip and bulk detachment rate separately. I, therefore, used an older version where the authors of Cytosim extended their code for a study to allow for plus-end specific detachment rates. The older version is also on Git* `https://github.com/nedelec/cytosim-2017`.

We derived a condition for the tension in a nematic filament bundle with periodic boundary conditions. But how does an extensile or contractile tension impact the macroscopic dynamics of the filament bundle? If the bundle tension is positive, $\tilde{\mathcal{T}} > 0$, we expect that the filament bundle is contractile in the axial direction. Then, if the magnitude of the bundle tension is sufficiently large, we expect that this can cause the bundle to rupture. The remaining structures should subsequently shorten. Our theory does not predict the subsequent dynamics and an emerging steady state structure. However, we can make an educated guess based on our theory. As a thought experiment, let us consider filaments that do not interact sterically and can move only along the x-axis, as our minimal model considers. In such a system, contraction driven by tip motors should yield bundle rupture and subsequent polarity sorting such that the tips of filaments point into the emerging structures. If steric interactions are taken into account, we expect similar dynamics. However, filaments should splay to account for steric exclusion.

In contrast, for $\tilde{\mathcal{T}} < 0$, the filament bundle is extensile along the axial direction. If the magnitude of the extensile tension exceeds the filament bundle's flexural rigidity, we expect the bundle to become unstable toward buckling. However, it should be noted that our theory makes no predictions about the physical properties that set the flexural rigidity of the filament bundle. On an intuitive level, one might expect that the flexural rigidity increases with increasing passive cross-linker concentration since more passive cross-links between the filaments should increase the ability of the filament bundle to resist deformation. It would therefore be striking to see if the filament bundle can be tuned towards buckling by adding more passive cross-linkers to the system. Next, we set up an agent-based model to investigate those possibilities.

AGENT-BASED MODEL

We use the open-source software cytosim [249] to implement an agent-based model to test our theory. The model consists of three classes of constituents: (i) stabilized microtubules of fixed length ℓ, (ii) molecular motors that can cross-link two microtubules and simultaneously move towards the plus end of both microtubules it cross-links, and (iii) passive cross-linkers mediating an attractive force between neighboring filaments; see Fig. 3.11. In detail, we use an agent-based model containing a finite number of filaments (N_{Mt}), active motors (N_{m}), and passive cross-linkers (N_{c}) in a thin box geometry with periodic boundary conditions in $x-$ and $y-$direction and reflective boundary conditions in $z-$direction. Each individual filament $i = 1,\ldots,N_{\mathrm{Mt}}$ is represented by a directed semi-flexible rod of fixed length ℓ, center of mass position $\boldsymbol{x}_i$, and orientation $\boldsymbol{n}_i$. The orientation $\boldsymbol{n}_i$ is defined in the direction of the filament plus-end. The rigidity of filaments is chosen large such that the end-to-end distance of filaments is always close to ℓ (cytosim has no implementation of rigid filaments). Close-by filaments repel each other via soft-core interaction if they are

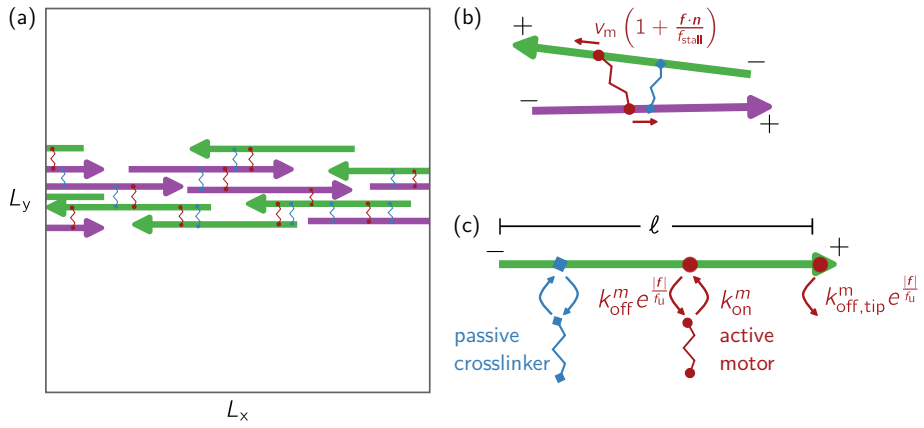

Figure 3.11: (a) Sketch of the agent-based simulation setup. We initialize the filament bundle in a thin slap geometry with periodic boundary conditions in x and $y-$direction and reflective boundary conditions in $z-$direction. We choose $L_x = L_y = 12\ell$, and the $z-$direction is chosen such that $3-4$ filaments can be stacked on top of each other. The system contains N_{Mt} microtubules, N_m motors, and N_c passive cross-linkers. Initially, microtubules can be oriented in $\pm\boldsymbol{e}_x$ direction and are placed in a thin rectangle in the center of the simulation volume. (c) Model constituents and their basic interactions. Filaments have a fixed length ℓ and orientation $\boldsymbol{n}$ in the direction of their plus end. Active motors (red) are modeled as two head domains connected by a Hookean spring. Passive cross-linkers (blue) are modeled analog as two microtubule binding domains (heads) connected by a Hookean spring. Active motors (passive cross-linkers) with no head attached are assumed to be well mixed in the cytosol and can bind to any filament at rate k^m_{on} (k^c_{on}). If one head is attached to a filament, the second head can attach to a filament within the range r_m (r_c). Motor (passive cross-linker) heads detach at a force-dependent rate $k^m_{off}e^{|\boldsymbol{f}|/f^m_u}$ ($k^c_{off}e^{|\boldsymbol{f}|/f^c_u}$). (b) Motor heads attached to a microtubule move directional towards the plus end at a force-dependent speed $v_m\left(1+\boldsymbol{f}\cdot\boldsymbol{n}/f_{stall}\right)$. Passive cross-linker heads do not move on the microtubule they are bound to.

closer than a distance d_{Mt}; for details on the implementation see [249]. Active motors consist of two head domains connected by a Hookean spring with stiffness κ_m and passive cross-linkers are modeled as two microtubule-binding domains (heads) connected by a Hookean spring with stiffness κ_c. Both active motors and passive cross-linker with no head attached to a filament are assumed to be well-mixed in the simulation volume. They can attach to any filament in the system with rate k^m_{on} and k^c_{on}, respectively. Active motors (passive cross-linkers) with one head attached to a filament can bind their second head to another filament within distance r_m (r_c). If the spring connecting the motor (passive cross-linker) heads becomes stretched, a corresponding force ($\boldsymbol{f}$) acts on the motor (passive cross-linker) heads. The heads are assumed to detach at a load-dependent rate $k^m_{off}e^{|\boldsymbol{f}|/f^m_u}$ ($k^c_{off}e^{|\boldsymbol{f}|/f^c_u}$) [235]; see Fig. 3.11. Filament-bound motor heads move towards the plus-end at a load-dependent speed $v = v_m(1+\boldsymbol{f}\cdot\boldsymbol{n}/f_{stall})$ [196] and passive cross-linkers remain static; see Fig. 3.11. Motor heads that reach the filament plus-end remain bound until they detach at rate force dependent rate $k_{off,tip}e^{|\boldsymbol{f}|/f_u}$.

We initialize the system at a low volume fraction of filaments $\phi \approx N_{Mt}\pi d^2_{MT}\ell/(4L_xL_yLz) = 2\times10^{-2}$ but position the filaments in a thin nematic band where they can be oriented in direction $\pm\boldsymbol{e}_x$; see Fig. 3.11.

In the following, we will use the total number of passive cross-linkers, N_c and the total number of motors, N_m. We aim to tune the population of tip motors by varying the bulk-to-tip detachment rate ratio ω via $k_{off,tip}$. Note that N_c/N_{Mt} and N_m/N_{Mt} are not equivalent to the number of doubly bound motors M and doubly bound cross-linkers C since not all motors and passive cross-linkers will be in a doubly bound state, some might be singly bound or unbound. We keep all other parameters

fixed unless specified otherwise. The simulation parameters as summarized in Tab. 3.1.

STABILITY OF THE NEMATIC BAND IN THE ABSENCE OF MOTORS

We first characterize the stability of the nematic filament band in the absence of active motors. Since we initialize the filament network at a volume fraction ϕ below the Onsager ordering threshold for rigid rods [259], we expect that the nematic band is unstable at low passive cross-linker concentrations and dissolves due to the diffusion of filaments. Figure 3.12 shows snapshots of the filament band at different doubly linked passive cross-linker numbers. The filament band dissolves as expected at passive cross-linker numbers $N_c < 3$; see Fig. 3.12. As the number of passive cross-linkers

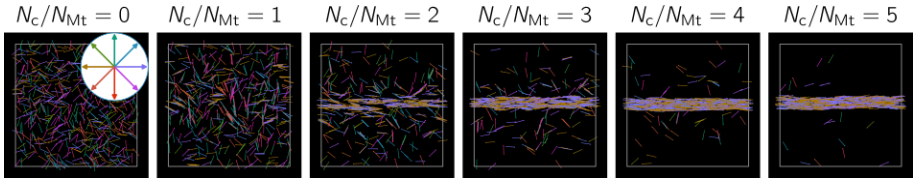

Figure 3.12: Snapshots obtained from the agent-based simulation for $N_m/N_{Mt} = 0$ the number of passive cross-linkers per filament is indicated at the top. All other parameters are as specified in Tab. 3.1. Filaments are shown in color. The color wheel indicates the orientation of the filaments. The simulation box is shown in gray. We initialize the filaments in a thin rectangle centered in the simulation volume. At low passive cross-linker numbers, the filament bundle dissolves ($N_c/N_{Mt} = 0-3$). For $N_c \gtrsim 3$ the filament bundle remains stable against thermal noise.

is increased, the filaments in the band percolate, and the filament band remains stable against thermal noise. In the following, we choose passive cross-linker numbers $N_c \geq 5$, but add motors to the filament bundle.

Before we investigate the competition between contractile and extensile tension, we study the cases of dominant tip and dominant bulk motor interactions.

FROM AXIAL CONTRACTION TO ASTERS AND MICELLES

We first investigate the possibility of axial contraction of the filament bundle. Our theory predicts that axial contraction is only present for a finite number of tip motors. Guided by our analysis for the minimal model (cf. Fig. 3.10) we expect that the filament bundle will be contractile over a large range of passive cross-linker numbers if the bulk-to-tip detachment rate ratio $\omega = k_{off}/k_{off,tip}$ is large. Moreover, we expect the magnitude of the contractile tension to be larger for a low number of passive cross-linkers in the system. Here we choose $\omega = 1$, $N_c/N_{Mt} = 9$ and $N_m/N_{Mt} = 16$. Considering the attachment/ detachment rates of passive cross-linkers and motors, this should yield $cf_c < 1$; cf. tab. 3.1. However, since the detachment rates are force dependent, there is no one-to-one correspondence between the agent-based model and the minimal model. Figure 3.13 shows a time sequence obtained from the simulation.

First, the filament bundle contracts in the axial direction (see Fig. 3.13 $t = 5\,s$), followed by bundle rupture (see Fig. 3.13 $t = 15\,s$). The remaining filament structures shorten further and contract to a single aster, where filament plus ends point towards the aster center (see Fig. 3.13 $t = 30\,s$). This aster splits and opens up in the subsequent dynamics to self-organize into micell-like assemblies (see Fig. 3.13 $t = 150\,s$). Those structures show a striking similarity to filament assemblies observed in *Xenoupus* egg extract with taxol-stabilized microtubules, which were referred to as "pineapple" filament assemblies [94]. In addition, similar filament structures have recently been observed in a hydrodynamic field theory derived from minimalistic scattering interactions that are modeled on the behavior of end-dwelling motors.

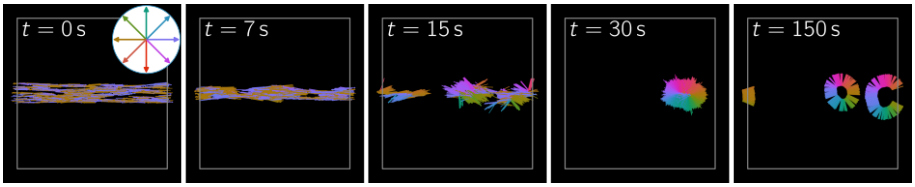

Figure 3.13: Snapshots obtained from the agent-based simulation for $\omega = k_{\text{off}}/k_{\text{off,tip}} = 1$, $N_c/N_{\text{Mt}} = 9$ and $N_c/N_{\text{Mt}} = 16$ all other parameters are as specified in Tab. 3.1. Filaments are shown in color. The color wheel indicates the orientation of the filaments. The simulation box is shown in gray. We initialize the filaments in a thin rectangle centered in the simulation volume. The filament bundle undergoes axial contraction and ruptures; see $t = 7$ s and $t = 15$ s. In the subsequent dynamics, the filaments form an aster-like structure where filament plus ends point inwards; see $t = 30$ s cf. the color wheel. Thereafter the filament aster "opens up" to form micelles. Such filament structures have been observed in *Xenoupus* egg extract with stabilized microtubules [94].

Having confirmed that the filament bundle undergoes axial contraction if tip motors are dominant, we turn toward the case where bulk motors dominate.

FROM AXIAL EXTENSION TO BUCKLING AND ACTIVE TURBULENCE

We now investigate the possibility of axial extension of the filament bundle. To this end, we choose a small bulk-to-tip detachment rate ratio $\omega = k_{\text{off}}/k_{\text{off,tip}} \approx 0.05$. Comparison to our theory implies that the filament bundle is always extensile; cf. Fig. 3.10 (a). Figure 3.14 (a) shows the time sequence obtained from the agent-based simulations for $N_c/N_{\text{MT}} = 5$ and $N_m/N_{\text{MT}} = 16$. The nematically aligned filament bundle remains stable. In the subsequent dynamics, the filaments in the bundle

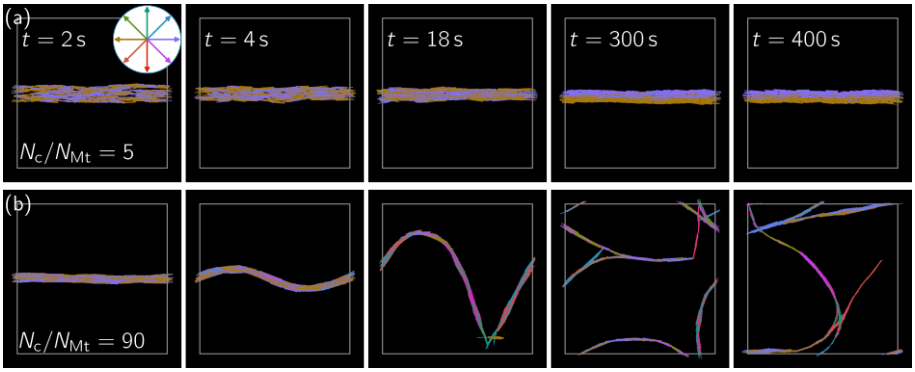

Figure 3.14: Time evolution of the filament bundle at a low ratio of bulk-to-tip detachment rates $\omega = 0.05$. The number of passive cross-linkers per filament is specified in the first panel. The number of motors per filament is $N_m/N_{\text{Mt}} = 16$. Filaments are color-coded according to their orientation; see the first panel in (a). (a) If the number of passive cross-linker per filament is low, the nematic band remains stable, and filaments in the band sort into polar domains (t=400 s). (b) If the number of passive cross-linkers per filament is increased, the filament band becomes unstable toward buckling. The buckling of the filament band yields bundle breakage; see $t = 18$ s. The subsequent time evolution is characterized by a dynamic sequence of buckling, bundle breakage, and fusion of adjacent filament bundles.

sort into polar domains of left and right-oriented filaments, respectively; see Fig. 3.14 (a), t=400 s. Polarity sorting of filaments into polar lanes was previously observed in computer simulations of filaments and motors in the absence of a passive cross-linker [250, 260]. To test our assumption that the filament bundle can become unstable toward buckling, we increase the magnitude of the bun-

dle tension by increasing the number of passive cross-linkers in the system. Figure 3.14 (b) shows the time sequence of the filament bundle for $N_c/N_{MT} = 90$. Strikingly, we find that by increasing the number of passive cross-linkers in the system, the nematic filament band becomes unstable towards buckling; see Fig. 3.14 (b) $t = 4\,s$. For sufficiently strong buckling the filament band breaks; see Fig. 3.14 (b) $t = 18\,s$. A dynamic sequence of buckling, breaking, and fusion of the bundles characterizes the subsequent time evolution of the filament network. Phenomenologically this behavior is consistent with observations from *in vitro* experiments under similar experimental conditions [38, 87, 261]. Moreover, a phenomenologically similar buckling instability has been observed experimentally and shown to be controllable by varying the concentration of passive cross-linkers or depletants [78, 92, 238].

FROM AXIAL EXTENSION TO POLAR DOMAINS AND BACK TO CONTRACTION

So far, we have confirmed the prediction of our theory that the filament bundle is contractile if the bulk-to-tip detachment rate ratio and, thereby, the bulk-to-tip motor ratio is low; see Fig. 3.13 and cf. Fig. 3.10 (a). Moreover, we have confirmed that the contractility of the filament bundle is caused by tip motors since a decrease in the tip-to-bulk detachment rate ratio, and thereby a reduction of the tip-to-bulk motor population did counteract the bundle contractility. Increasing the number of passive cross-linkers in the system made it possible to increase the extensile tension in the bundle to the extent that it buckled. We next aimed to quantify if it is possible to turn the filament bundle from contractile to extensile by increasing the number of passive cross-linkers. To this end, we use an intermediate bulk-to-tip detachment rate ratio $\omega \approx 0.175$ and sweep over different numbers of passive cross-linkers. Figure 3.15 shows a time sequence of the bundle dynamics obtained from agent-based simulations at different passive cross-linker concentrations. At low passive cross-linker concentrations, the filament bundle contracts and shows similar dynamics as observed for dominating tip interactions; see Fig. 3.15 (a). However, the filament bundle does not rupture straight away, but filaments contract to dense polar clusters at the bundle boundary; see Fig. 3.15 (a) $t = 100\,s$. Moreover, we observe that the time it takes for the filament bundle to contract to a micell-like state is significantly increased (cf. Fig. 3.13), indicating that the magnitude of the contractile tension is decreased compared to the case of $\omega = 1$. The steady state structure is characterized by lined-up filament bundles; see Fig. 3.15 (a), $t = 400\,s$. Similar "lined-up" filament structures were also observed in *Xenoupus* egg extract with taxol-stabilized microtubules [94]. An increase in passive cross-linker concentration slows the contractile dynamics further down; see Fig. 3.15 (b).

If the passive cross-linker concentration is increased above some critical concentration, we observe buckling of the filament bundle; see Fig. 3.15 (c) $t = 40\,s$ and (d) $t = 20\,s$. If the passive cross-linker concentration is sufficiently high, bundle buckling yields bundle breakage (see Fig. 3.15 (d) $t = 40\,s$), as observed for dominant bulk motors (cf. Fig. 3.14). At the breakage point, we observe the contraction of filaments into dense polar clusters; see Fig. 3.15 (d) $t = 160\,s$. In the subsequent dynamics, the filaments line up into polar arrays Fig. 3.15 (d) $t = 400\,s$. We can understand these dynamics based on our minimal model: The parameters are chosen such that the homogenous filament bundle is extensile. This means in a homogenous filament bundle where parallel and anti-parallel filament interactions are equally likely, anti-parallel extensile filament interactions mediated by bulk motors dominate over contractile interactions mediated by tip motors. However, bundle breakage is associated with the transient formation of a polar-aligned filament domain at the breaking point; see Fig. 3.15 (d) $t = 40\,s$. Since bulk motors contribute only via anti-parallel interaction, the contractile tension of tip motors can dominate if polar domains emerge in the network. This means the homogenous filament bundle self-organizes, driven by the extensile tension, into a contractile network architecture.

Let us summarize the results obtained so far: Based on our minimal model, we made the following predictions: (i) If the ratio of tip-to-bulk motors is dominated by tip motors, the filament

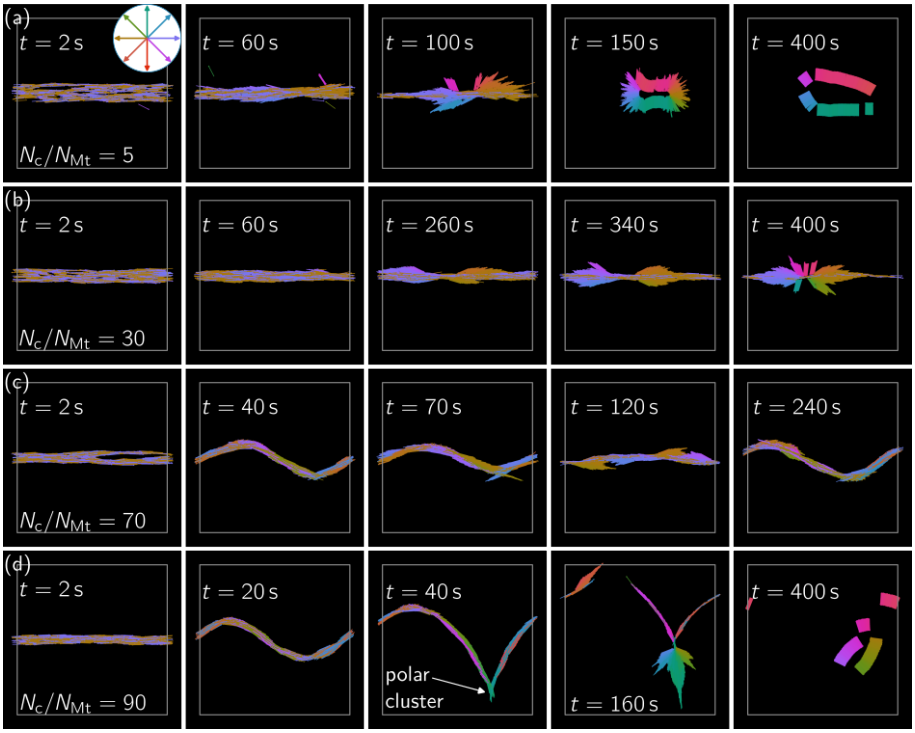

Figure 3.15: Time evolution of the filament bundle at intermediate ratio of bulk-to-tip detachment rates $\omega = 0.175$. The number of passive cross-linkers per filament is specified in the first panel. The number of motors per filament is $N_m/N_{Mt} = 16$. Filaments are color-coded according to their orientation; see the first panel in (a). (a) At low numbers of passive cross-linkers, the filament bundle shows axial contraction. In the long run, the filaments self-organize into a "lined-up" configuration; see $t = 400\,s$. (b) An increase in passive cross-linker concentration slows down the dynamics indicating that the magnitude of the contractile tension is decreased. (c) If the number of passive cross-linkers is sufficiently high, the filament bundle becomes unstable toward buckling. Transiently we observe polar configurations where contractile interactions dominate; see $t = 120\,s$. (d) At high passive cross-linker concentrations, bundle buckling yields bundle breakage. At the breakage point, filaments form polar clusters; see $t = 40\,s$. Since the extensile contributions to the tension stem from anti-parallel interaction, the contractile tension of parallel filament interactions can dominate in polar domains

bundle will be contractile. We confirmed this prediction by simulating a filament bundle with a high bulk-to-tip detachment rate ratio, ω. (ii) If the ratio of tip-to-bulk motors is dominated by bulk motors, the filament bundle is neutral or extensile, depending on the motor anisotropy. Moreover, the magnitude of the extensile tension can be increased by increasing the passive cross-linker concentration. We showed that the filament bundle is stable at a low tip-to-bulk motor ratio and becomes unstable toward buckling as the passive cross-linker concentration is increased. This is in line with our prediction. (iii) We predicted that the filament bundle could be tuned from being contractile to extensile by increasing the passive cross-linker concentration. We confirmed this prediction at an intermediate tip-to-bulk detachment rate ratio. Taken together, we were able to test and confirm the major predictions of our minimal model. The numerically obtained phase diagram is shown in Fig. 3.16. To compare the numerically obtained phase diagram to our theoretical results, we proceeded as follows: First, we measured the number of doubly bound passive cross-linkers and motor cross-linkers in the agent-based simulation since our theory is based on cross-linking proteins and does not take singly bound or unbound cross-linker into account. We

found that $M_{\mathrm{tot}} \sim 0.82 N_{\mathrm{m}}/N_{\mathrm{Mt}}$ and $C \sim 0.82 N_{\mathrm{m}}/N_{\mathrm{Mt}}$. The force-dependent detachment dynamics used in the agent-based simulations gives rise to a non-linear force-velocity relation. Using the general framework presented in the Supplemental Material 3.2.3 we calculate this force velocity relation numerically, both for motors and passive cross-linkers; see Supplemental Material Sec. 3.2.3. We then perform a linear fit to the non-linear force-velocity relation. For motors, we find that the force amplitude is well approximated by $F_{\mathrm{m}} \approx f_{\mathrm{s}} 0.52\,A/(1+0.52\,A)$, i.e., force-dependent detachment reduces the force amplitude (cf. Eq. 3.18). Force-dependent detachment has a significant impact on passive cross-linkers. This is because they can not adapt to the filament sliding velocity. To account for this, we perform a linear fit to the non-linear force-velocity relation and obtain a force amplitude of $F_{\mathrm{c}} \sim 2\,\mathrm{pN/(\mu m)}$ compared to $F_{\mathrm{c}} \sim 12\,\mathrm{pN/(\mu m)}$ in the absence of force-dependent detachment. To determine the anisotropy factors for anti-parallel bulk and tip motors and parallel tip motors, as well as the tip-to-bulk motor ratio, we perform the mean-field approximation

$$\langle K_\alpha^\beta \rangle \approx k_{\mathrm{off,m}} \exp\left(\frac{1}{f_{\mathrm{u}}} F_\alpha^\beta(v)\right). \tag{3.40}$$

With those mean-field detachment rates, we proceed as described in Sec. 3.2.2. Figure 3.16 shows the analytically obtained filament bundle tension in comparison to filament bundle behavior observed in agent-based simulations. We find strikingly good agreement between theory and agent-based simulation. It should be appreciated at this point that the analytic prediction is based on kinetic rates and mechanical properties of the cross-linking proteins. Those are quantities that are estimated from experiments. At a low bulk-to-tip detachment rate ratio and high ratio of passive cross-linkers to active motors, we observe buckling followed by turbulent-like dynamics of the filament network (red stars in Fig. 3.16). As the bulk-to-tip detachment rate is increased, the filament bundle still buckles. However, once polar domains have formed, the filament bundle stars to contract (green triangles in Fig. 3.16). At a low number of passive cross-linkers to active motors, the nematic band is stable if the bulk-to-tip detachment rate, ω, is low (yellow circles in Fig. 3.16) and becomes contractile if ω is increased (blue squares in Fig. 3.16). What remains to be done is to investigate the impact of filament length and total number of motors numerically. However, agent-based simulations in [93] indicate that longer filaments suppress contractile tension and show emerged turbulent-like dynamics turbulent-like dynamics in contrast to short filaments, which tend to form asters consistent with consistent with our theory (cf. 3.10 (c)) and *in vitro* experiments [75].

SUMMARY AND CONCLUSION

The ability of cytoskeletal filament assemblies to generate contractile or extensile tension is at the heart of many cellular processes. This includes prominent examples like the mitotic spindle, which relies on the ability to generate extensile tension to segregate chromosomes during cell division [17, 19, 262, 263], contraction of microtubule minus ends to form asters and spindle poles [96, 264, 265] or contraction of the actin-cortex which is essential to control cell shape [100, 104, 236].

In reconstituted systems of microtubules and motor proteins, extensile tension of filament bundles is the source that fuels turbulent-like dynamics observed at the macroscopic scale [38, 40, 87]. Moreover, reconstituted systems of end-dwelling motors and microtubules have been shown to promote the formation of asters [74, 193] and large-scale network contraction [193–195, 237]. These systems have become paradigmatic model systems for filamentous active matter [266].

To understand the collective dynamics of those systems on the macroscopic scale, active field theories have been developed on the basis of symmetry arguments [49, 51, 52, 86, 239]. Commonly, in those theories, active contractile or extensile stresses are introduced by an apolar active current that generates flux along or against the nematic curvature [241, 246]. Those theories have been successfully used to describe the macroscopic dynamics of active filament gels, in particular, the formation of steady-state structures and defect dynamics [50, 81–83]. However, how the introduced

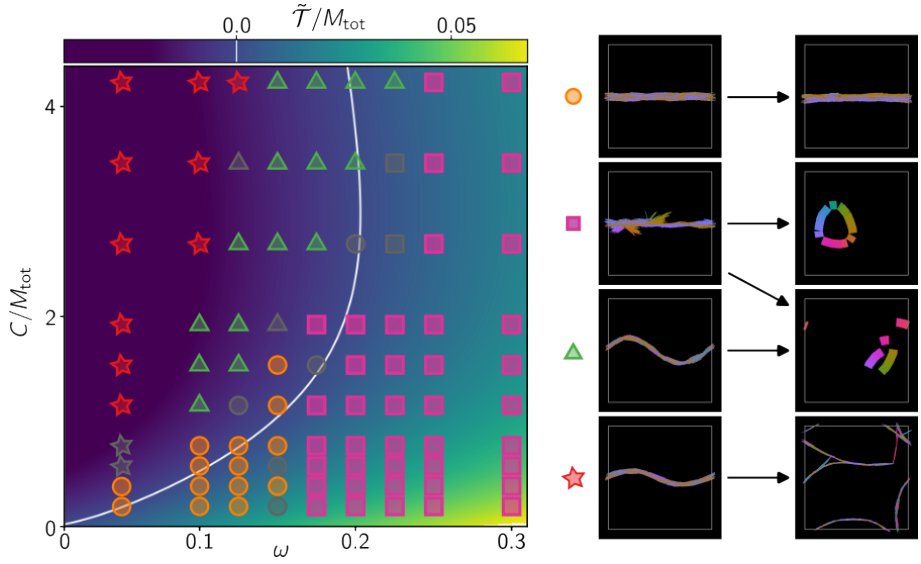

Figure 3.16: Phase diagram of the filament bundle in the $(\omega, C/M_{\mathrm{tot}})$ parameter plane obtained from the agent-based simulation. The number of motors per filament is $N_{\mathrm{m}}/N_{\mathrm{Mt}} = 16$. Other parameters are specified in Tab. 3.1. From the simulation, we measured the number of doubly bound motors $M_{\mathrm{tot}} \approx 0.82 N_{\mathrm{m}}/N_{\mathrm{Mt}}$ and doubly bound cross-linkers $C \approx 0.5 N_{\mathrm{c}}/N_{\mathrm{Mt}}$. The remaining analytical phase diagram is a fit-free prediction of our theoretical framework based on the kinetic rates of the cross-linking proteins and their force-response functions $\phi[nf]$ and $\psi[nf]$. We observe four different behaviors: (i) The filament bundle remains stable (yellow circles). (ii) The filament bundle contracts in the axial direction. Subsequently, the filament network self-organizes into micelles or "lined-up" filament configurations depending on the tip-to-bulk detachment rate ratio and the number of passive cross-linkers in the system (blue squares). (iii) The filament bundle buckles and breaks, followed by the self-organization into contractile polar domains (green triangles). (iv) The filament bundle buckles and breaks. The subsequent time evolution is characterized by a dynamic sequence of buckling, bundle breakage, and fusion of adjacent filament bundles (red stars). Gray symbols are parameter points where the dynamics were unclear, the tendency is indicated by the symbol, eventually, the simulation time was not long enough ($t_{\mathrm{max}} = 400\,\mathrm{s}$).

currents arise from microscopic interactions of the network constituents and which properties of the network constituents set the strength of this current is not well understood.

To close the gap between the microscopic and macroscopic dynamics large-scale computer simulations have been used [39, 75, 93, 218, 249–252, 260, 267]. However, this approach comes to its limits when collections of different types of motors and passive cross-linkers are considered due to the rapidly increasing number of model parameters and computational complexity.

In this work, we have used a complementary approach and developed a minimal but generic theoretical framework to study active tension generation in disordered bundles of filaments cross-linked by an arbitrary ensemble of cross-linking motors and passive cross-linkers. The basis of this theoretical framework is a force-velocity relation quantifying an average filament-filament interaction mediated by a cross-linking protein. By specifying a microscopic model, this relation can be derived from the kinetic interactions of the cross-linker with filaments and its mechanical properties. In the Supplemental Material Sec. 3.2.3, we present a general formalism. The minimal design of our model allowed us to derive a general expression for the contribution of a motor cross-linker to the filament bundle tension. Based on our general theoretical framework, we can make two restrictive predictions about the capability of a motor to promote an extensile or contractile tension in the filament bundle. First, a motor that has a homogenous density profile along the contour of

a filament can neither promote extensile nor contractile tension; see Eq. 3.71. Second, a symmetric motor cross-linker can only promote contractile tension in the presence of external or internal friction. Otherwise, filaments slide across the motor at its unloaded speed, and the motor does not get strained, which prevents the build-up of tension in the motors and, thereby tension in the filament bundle. This restriction is relaxed in mixtures of motors if they have different unloaded speeds. Then, the anisotropy factor (a measure for the inhomogeneity of the motor density) and the total population of different cross-linker head types define a mesoscopic set of control parameters determining the sign of the bundle tension and, thereby, the bundle's propensity to contract or expand.

We demonstrate this for a symmetric motor cross-linker that dwells at the filament end mixed with passive cross-linkers that cause internal friction in the filament bundle. In this case, the ratio of bulk-to-tip motors, the ratio of passive cross-linkers to bulk motors, and the motor anisotropy factors control the propensity of the filament bundle to contract or expand. Strikingly, we find that the extensile tension in a filament bundle is increased by increasing the internal friction in the filament bundle, i.e., holding individual filaments together increases the materials' property to expand. This prediction is consistent with recent photo-bleaching experiments in filaments bundled by the crowding agent polyethylene glycol (PEG), which demonstrate strong extensile stresses in the absence of relative filament sliding [90]. The contractile nature of the filament bundle is controlled by the ratio of tip-dwelling motors to bulk motors. For large populations of tip-motor proteins, we predict the filament bundle to be contractile.

By specifying a microscopic model on the basis of kinetic reactions and mechanical properties of the individual network constituents, we relate the set of coarse-grained control parameters to the kinetic rates defining the interactions between motors (passive cross-linkers) and filaments and the mechanical properties of the cross-linking proteins. Within this set of network constituents, we identify three experimentally accessible parameters that control the propensity of the filament bundle to contract or expand. First, the total number of passive cross-linkers which promote extensile tension. Second, the total number of motors per filament, with an increasing number of motors promoting the network's propensity to contract. Lastly, the filament length, with longer filaments promoting the network's propensity to expand. All those predictions are in line with recent *in vitro* experiments [75, 78, 79, 91–93].

We confirmed our theoretic predictions by agent-based simulations of a nematic filament bundle in a three-dimensional slap geometry. Consistent with our theoretic predictions, the nematic filament bundle contracts when tip-motors dominate. Caused by contraction, the nematic filament bundle ruptures and self-organizes into micell-like structures or "lined-up" filament configurations depending on the population of tip-motors and passive cross-linkers. Those structures are reminiscent of filament assemblies found in *Xenoupus* egg extract with taxol-stabilized microtubules [94]. Moreover, such structures were recently predicted by an active field theory derived from simplifying interactions modeled on the behavior of end-dwelling motors [255]. In contrast, if bulk motors dominate over tip motors, the nematic filament bundle remains stable at low passive cross-linker concentrations. As the internal friction in the filament bundle was increased by increasing the number of passive cross-linkers in the system, we observed an Euler-type bucking instability consistent with the behavior of a material under compression, i.e., an extensile tension in the filament bundle consistent with our theory. At sufficiently high passive cross-linker concentrations, the buckling of the filament bundle yields bundle breakage consistent with an increase in extensile tension. The long-term dynamics is then characterized by a repeating sequence of bundle-buckling, breakage, and fusion reminiscent of turbulent-like network dynamics as observed in *in vitro* experiments of filament motor mixtures in the absence of end-dwelling motors [38, 87, 91]. The pathway from buckling of nematic filament-bundles to dry active turbulence was recently discussed in terms of an active field theory [241, 247]. Last, we confirmed our prediction that the filament bundle

can be tuned from a contractile state to an extensile state by increasing the internal friction in the bundle. Strikingly, at intermediate passive cross-linker concentrations, where contractile tension mediated by polar tip-motors interactions and apolar extensile tension mediated by bulk motors compete, we observe that the nematic filament band becomes fist unstable towards buckling and even breaks, implying dominant extensile tension. However, buckling and band breakage are associated with the transient formation of polar domains. Consistent with our theory, the filament band started to contract, where polar filament clusters had formed due to the dominant contractile tension caused by parallel tip-motor interactions. Strikingly, a similar pathway from buckling of nematic bands to contraction and bilayer formation was recently observed in *in vitro* experiments of filament networks, cross-linked by a tip-dwelling motor. Somewhat surprisingly the theoretically predicted phase boundary between bundle contraction and bundle extension agrees quite well with the agent-based simulations, indicating that elastic contributions to the emergent bundle dynamics play a subordinate role, as they are not taken into account by our theoretical framework. We speculate that this might be caused by the relatively high number of active motors used in the agent-based simulations, such that the active stress is always dominant and only its sign matters. An alternative explanation is given by recent work, that used spars learning algorithms to learn the continuum equations governing the spatio temporal dynamics of active nematic filament gels based on experimental data [268, 269]. Starting from up to 246 terms allowed by symmetry a minimal set of equations were learned that describe the time evolution of the system. Interestingly no contributions which can be derived from a free energy, including those due to elasticity were identified [269]. Instead a force balance condition of the form $\nabla \cdot (\sigma_v + \sigma_a) = 0$ was identified as the dominant equation driving the system dynamics, where σ_a and σ_v are active and viscous stresses respectively. Such an equation is reminiscent of the force balance Eq. 3.22 derived here. Further work will be needed to understand how to to properly draw the link between the filament bundle tension derived here and active stresses that fuel the macroscopic dynamics.

Taken together, we were able to provide a framework that systematically bridges the scale between the microscopic dynamics of the filament bundle constituents, controlled by kinetic and mechanical constants, and the scale of the filament bundle itself. A nematic filament bundle, in turn, resembles the minimal building block of large-scale filament motor mixtures. Those systems are described in terms of active nematic field theories, which contain an unspecified apolar active stress, which describes the contractile or extensile tension exerted by the active particles [50, 80–86]. In an arbitrary mixture of filaments, active and passive cross-linkers our theoretical framework provides insight how the various components act together to determine the sign and the magnitude of this stress. Thereby, our theoretical framework shines light on the question of how the microscopic dynamics of cross-linking motors and passive cross-linkers impact the large-scale physics of filament motor mixtures.

3.2.3. APPENDIX: BRIDGING SCALES IN FILAMENTOUS ACTIVE MATTER

MEAN FIELD CROSS-LINKER FORCE

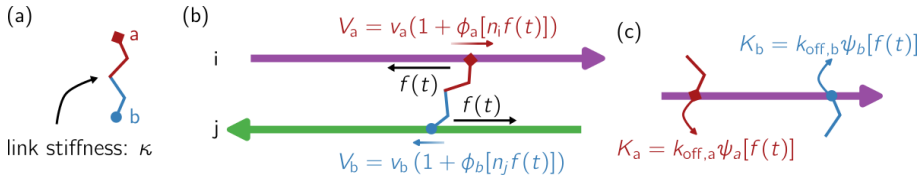

Figure 3.17: (a) We consider a cross-linker modeled as two head domains a and b. The head domains might be different. (b) The cross-linker head a can move on the filament it is attached to at speed V_a and head b at speed V_b. V_a and V_b are functions of the force applied on the motor head a and b, respectively. Therefore, they depend implicitly on time via $f_{ab}(t)$. (c) Head domain a detaches from the filament at rate $K_a(t)$ and head domain b at rate $K_a(t)$). The detachment rates depend implicitly on time via $f_{ab}(t)$.

In this section, we will derive the force-velocity relation of a general motor cross-linker that exerts a force that is linear in the extent $\Delta x(t)$ of the motor at time t. A non-linear force generator, i.e., a motor that generates a force that depends in a non-linear way on its extend $\Delta x(t)$, can be taken into account as long as the function $f[\Delta x(t)]$ quantifying the force as a function of the motor extent $\Delta x(t)$ can be inverted. This means a motor cross-linker that generates a force which is a discontinuous function of the cross-linker extent, might be a challenging task to consider. Here we use

$$f[\Delta x(t)] = \kappa \Delta x(t)\,, \tag{3.41}$$

i.e., we consider motor cross-linkers modeled by a Hookean spring. We denote our general linear motor cross-linker as X. The motor has two head domains (a) and (b) connected by the Hookean spring. Motor head (a) has the unloaded velocity v_a, and head (b) has the unloaded velocity v_b, at which they move along the arc-length $s \in [-\ell/2, \ell/2]$ of the filament they are cross-linked to. Head (a) and head (b) can detach from the filament they are bound to. We do not specify the explicit detachment dynamics at this point. In general, the velocity of the cross-linker may depend on the arc-length position s. If we take this into account, the derivation of the filament bundle tension will include the first moments in the unloaded motor head velocity, which read

$$\langle v_a(s)\rangle = \int_{-\ell/2}^{\ell/2} \mathrm{d}s\, v_a(s)\rho_a(s) \tag{3.42}$$

where $\rho_a(s)$ denotes the normalized motor head density along the arc-length s of the filament. I will explain why we do not take arc-length dependent velocities into account in terms of two biologically relevant examples, where the unloaded motor head velocity depends on the arc-length position. We already encountered an example in the main text of a motor that has an arc-length dependent velocity, namely when we considered a symmetric motor cross-linker that dwells at the filament end. Such a motor has the unloaded velocity $v_a(s) = v_b(s) = v_m\theta(s-(\ell/2-\epsilon))\theta(s+\ell/2)$, i.e., the velocity is v_m in the bulk and 0 at the tip region ϵ. This means the velocity distribution of the motor head is bimodal with peaks at 0 and v_m. Trying to characterize a bimodal distribution in terms of its first moment will not recapitulate the underlying physics but yield completely wrong results. Another example would be high particle occupations on the filament, where protein crowding on the filament plays a role. Motor crowding can lead to arc-length dependent unloaded motor head velocity $v_a(s)$ and $v_b(s)$ if steric exclusion of motors is taken into account. Importantly, the collective motor dynamics in such systems give rise to density profiles $\rho_a(s)$, which are characterized by a domain wall (a "discontinuous" motor head density). This, in turn, yields a bimodal distribution of

unloaded motor head velocities. Thus, again an example where a characterization in terms of the first moment fails.

From my perspective, a more promising approach is to split the arc-length of the filament into regions where the unloaded motor head velocity is approximately constant, and tread motors which are cross-linked to the different arc-length positions as different "types" of cross-linkers that obey different dynamics on the filament and therefore will have a different force-velocity relation. It is important to constraint those cross-linker populations to the arc-length domain they live on. In the main text, we did so for tip- and bulk-motors, by constraining tip motors via a delta-peaked arc-length density $\rho_b \sim \delta(s-\ell/2)$.

However, since the different populations are ultimately the same type of cross-linker, they will be coupled through particle conservation. This can be formulated in terms of flux-balance conditions and a mass conservation condition. We did present this formalism in the main text for tip and bulk-motors and present it in Sec 3.2.3 in a more general context. Therefore, we will consider v_a and v_b as independent of the arc-length position s in the following.

Consider two filaments i and j with orientation n_i and n_j. At time t, the two filaments move at velocity $v_i(t)$ and $v_j(t)$. The motor cross-links the two filaments with motor head (a) attached to filament i and motor head (b) attached to filament j. The loaded velocity of motor head (a) and (b) at time t depends on the force applied to the motor heads. We quantify the dependence of the motor head velocities in a dimensionless function $\phi[nf(t)]$ that characterizes the response of the motor velocity to an applied force with the constraint $\phi(0)=0$. Moreover, the response of the motor head will depend on whether the force is applied in the direction of the unloaded motor head velocity or opposed to it. Therefore it is a function of nf. Taken together, we write the motor head velocity as

$$V_\mathrm{a}[n_i f_\mathrm{ab}(t)] = v_\mathrm{a}(1+\phi_\mathrm{a}[n_i f_\mathrm{ab}(t)]) \tag{3.43}$$

$$V_\mathrm{b}[n_j f_\mathrm{ba}(t)] = v_\mathrm{b}(1+\phi_\mathrm{b}[n_j f_\mathrm{ba}(t)])\,. \tag{3.44}$$

here $f_\mathrm{ab}(t)$ denotes the force head (b) applies on head (a). Thus $f_\mathrm{ab}(t) = -f_\mathrm{ba}(t)$. The sign convention is such that positive motor head velocities characterize a movement of the motor head in the direction of the plus end of the filament. Negative motor head velocities denote movement towards the minus end. At time $t=0$, the two motor heads are attached, in a relaxed state, to two filaments i and j. This is not a restriction since attachment is an equilibrium process, which, on average, will yield zero cross-linker extension at the time of binding. The two filaments move at velocities $v_i(t)$ and $v_j(t)$. As a result of the relative filament motion $\Delta v_{ij}(t) = v_i(t) - v_j(t)$ and the relative motor head motion, the motor cross-linker will become stretched

$$\Delta x(t) = \int_0^t \mathrm{d}t'(n_i V_\mathrm{a}(t') - n_j V_\mathrm{b}(t') + \Delta v_{ij}(t')) \tag{3.45}$$

The force applied by head (b) on (a) is then given by

$$\begin{aligned} f_\mathrm{ab}(t) &= -\kappa \Delta x(t) \\ &= -\kappa \int_0^t \mathrm{d}t'[n_i V_\mathrm{a}(t') - n_j V_\mathrm{b}(t') + \Delta v_{ij}(t')]\,. \end{aligned}$$

This defines the self-consistency equation for f_ab. At the time t_u, one of the motor heads (a) or (b) will detach from the filament. We will now make an adiabatic approximation and assume that the relative filament sliding velocity is approximately constant during the time scale a motor cross-links the two filaments and denote the quasi-steady-state as $\tilde{v}_{ij}$. This is a valid assumption in an ensemble of many motors cross-linking the filaments i and j, and it is most certainly true in a bundle of cross-linked filaments. The self-consistency equation then reads

$$f_\mathrm{ab}(t) + \kappa \int_0^t \mathrm{d}t' \left(n_i v_\mathrm{a} \phi_\mathrm{a}[n_i f_\mathrm{ab}(t')] - n_j v_\mathrm{b} \phi_\mathrm{b}[-n_j f_\mathrm{ab}(t')]\right) = \kappa t (n_j v_\mathrm{b} - n_i v_\mathrm{a} + \Delta \tilde{v}_{ji})\,. \tag{3.46}$$

Upon specifying the functions ϕ_a and ϕ_b this function can be solved. The solution of this equation f^*_{ab} will be a function of t and $\Delta\tilde{v}_{ji}$; $f^*_{ab} = f^*_{ab}[t, \Delta\tilde{v}_{ji}]$.

A motor cross-linker of age τ, exerts the force $f^*_{ab}[\tau, \Delta\tilde{v}_{ji}]$ on the filaments. We define a bond-breakage event as a detachment of head (a) or head (b) from the respective filament and $S(\tau)$ as the survival probability of a bond of age τ. In an ensemble of many motor cross-linkers, which cross-link the filament i and j, there will be cross-linkers of different ages τ cross-linking the two filaments. The average force those motor cross-linkers exert on the filaments is then given by

$$F_{\mathrm{ij,a}}(\Delta\tilde{v}_{ji}) = \frac{1}{\mathcal{N}} \int_0^\infty \mathrm{d}\tau\, S(\tau) f^*_{ab}(\tau, \Delta\tilde{v}_{ji}) \tag{3.47}$$

with the normalization constant

$$\mathcal{N} = \int_0^\infty \mathrm{d}\tau\, S(\tau) = \langle\tau\rangle$$

In the second line, we used integration by parts. Here, we introduced the notation $F_{\mathrm{ij,a}}$ to denote that head a is attached to filament i. Equation 3.47 defines the average force a specific type of motor cross-linker exerts on filament i in an ensemble of many cross-linking interactions to filament j.

The remaining task is to derive an expression for the survival probability of a bond of age τ. The survival probability of a bond depends on the rate K_a and K_b at which head (a) and (b) detach from the filaments, respectively. In general, the rates depend on the applied force and the direction of the force. We define the detachment rates of head a and b as

$$K_a[n_i f_{ab}(t)] = k_{\mathrm{off,a}} \psi_a[n_i f_{ab}(t)]$$
$$K_b[n_j f_{ba}(t)] = k_{\mathrm{off,b}} \psi_b[n_j f_{ba}(t)]$$

Here $k_{\mathrm{off,a}}$ and $k_{\mathrm{off,b}}$ denote the unloaded detachment rate of cross-linker head (a) and (b) respectively, and $\psi_a\left[n_i f^*_{ab}(t)\right]$ and $\psi_b\left[n_j f^*_{ba}(t)\right]$ is a function quantifying the response of the detachment rate to the applied force, with the constraint $\psi_a[0] = 1$ and $\psi_b[0] = 1$. We define the rate of bond breakage of the motor cross-linker

$$K\left[f^*_{ab}(t)\right] = k_{\mathrm{off,a}} \psi_a\left[n_i f^*_{ab}(t)\right] + k_{\mathrm{off,b}} \psi_b\left[-n_j f^*_{ab}(t)\right]. \tag{3.48}$$

Note, the solution to the self consistency equation (Eq. 3.46), $f^*_{ab}(t)$, is a function of $\Delta\tilde{v}_{ji}$. Therefore $\psi\left[f^*_{ab}(t)\right]$ depends implicitly on $\Delta\tilde{v}_{ji}$ if $\psi_a[n_i f^*_{ab}(t)] \neq 1$ or $\psi_b[-n_j f^*_{ab}(t)] \neq 1$.

Consider the time interval $[t, t + \mathrm{d}t]$ and let $S(t)$ be the probability that no detachment event occurred up to time t (the survival probability), the probability that the motor cross-linker bond survives up to time $(t + \mathrm{d}t)$ is then

$$\begin{aligned} S(t + \mathrm{d}t) &= \mathrm{Prob}\{\text{“no bond breakage until t”} \wedge \text{“no bond breakage in [t, t + dt)”}\} \\ &= S(t)\left(1 - K\left[f^*_{ab}(t)\right]\mathrm{d}t\right) \end{aligned}$$

Expanding for small $\mathrm{d}t$ we obtain an ODE, using the initial condition $S(0) = 1$ we find the solution

$$S(\tau) = \exp\left(-\int_0^\tau \mathrm{d}t K\left[f^*_{ab}(t)\right]\right).$$

The general expression for the force-velocity relation then reads

$$F_{\mathrm{ij,a}}(\Delta v_{ji}) = \frac{1}{\langle\tau\rangle} \int_0^\infty \mathrm{d}\tau\, \mathrm{e}^{-\int_0^\tau \mathrm{d}t K\left[f^*_{ab}(t)\right]} f^*_{ab}[\tau, \Delta\tilde{v}_{ji}]. \tag{3.49}$$

It is important to note that the general force-velocity relation Eq. 3.49 is reciprocal under the operation $i \to j, \mathrm{a} \to \mathrm{b}$

$$F_{\mathrm{ij,a}}(\Delta\tilde{v}_{ji}) = -F_{\mathrm{ji,b}}(\Delta\tilde{v}_{ij})\,. \tag{3.50}$$

Taken together, upon specifying the functions $\phi_a[nf(t)], \phi_b[nf(t)], \psi_{\mathrm{a}}\left[nf\right], \psi_{\mathrm{b}}\left[nf\right]$ and the kinetic constants $(v_{\mathrm{a}}, v_{\mathrm{b}}, k_{\mathrm{off,a}}, k_{\mathrm{off,b}})$ and the link-stiffness κ the self consistency equation Eq. 3.46, and the force-velocity relation Eq. 3.49 form a closed set of equations that define $F_{\mathrm{ij,a}}(\Delta v_{ji})$ for an general motor or passive cross-linker. Section 3.2.3 contains a set of exemplary motor cross-linkers to illustrate how to derive the force-velocity relation for a specific motor or passive cross-linker based on the self-consistency Eq. 3.46 and the general force-velocity relation Eq. 3.49.

MEAN FIELD MOTOR HEAD DENSITIES

The general force-velocity relation Eq. 3.49 is a mean-field representation of a general cross-linker. This means it represents the mean force a specific type of cross-linker mediates between two filaments it cross-links as a result of many averaged cross-linking interactions. It is, therefore, valid in an ensemble of many motor cross-linkers linking filaments i and j. To bridge the scale between an individual motor or passive cross-linker interaction to the scale of the filament, we have to evaluate the emergent density profiles $\rho_{\mathrm{a}}(s)$ and $\rho_{\mathrm{b}}(s)$ of the mean-field motor cross-linker heads (a) and (b). Those density profiles will depend on the average velocity $\langle V_{\mathrm{a}}[n_i f^*_{ab}(t)]\rangle$, $\langle V_{\mathrm{b}}[n_i f^*_{ba}(t)]\rangle$ as well as the average detachment rates $\langle K_{\mathrm{a}}[n_i f^*_{ab}(t)]\rangle$ and $\langle K_{\mathrm{b}}[n_i f^*_{ba}(t)]\rangle$.

The mean velocities of the cross-linker heads a and b on filament i with orientation n_i are given by

$$\begin{aligned}\left\langle V_{\mathrm{a}}[n_i f^*_{\mathrm{ab}}(t)]\right\rangle &= v_{\mathrm{a}}\left(1 + \left\langle \phi_{\mathrm{a}}[n_i f^*_{\mathrm{ab}}(t)]\right\rangle\right)\\ \left\langle V_{\mathrm{b}}[n_i f^*_{\mathrm{ba}}(t)]\right\rangle &= v_{\mathrm{b}}\left(1 + \left\langle \phi_{\mathrm{b}}[n_i f^*_{\mathrm{ba}}(t)]\right\rangle\right)\,.\end{aligned}$$

If the functions $\phi_{\mathrm{a}}(nf)$ and $\phi_{\mathrm{b}}(nf)$ are linear in nf then $\left\langle \phi_{\mathrm{a}}[n_i f^*_{\mathrm{ab}}(t)]\right\rangle = \phi_{\mathrm{a}}(n_i F_{ij,a})$. However, this is not true if $\phi_{\mathrm{a}}(nf)$ is a non-linear function of (nf) then $\langle V_{\mathrm{a}}[n_i f^*_{\mathrm{ab}}(t)]\rangle$ will contain higher order moments of $n_i f^*_{\mathrm{ab}}(t)$.

We proceed analog for the detachment rates, which are given by

$$\begin{aligned}\left\langle K_{\mathrm{a}}[n_i f^*_{\mathrm{ab}}(t)]\right\rangle &= k_{\mathrm{off,a}}\left\langle \psi_{\mathrm{a}}[n_i f^*_{\mathrm{ab}}(t)]\right\rangle\\ \left\langle K_{\mathrm{b}}[n_i f^*_{\mathrm{ba}}(t)]\right\rangle &= k_{\mathrm{off,b}}\left\langle \psi_{\mathrm{b}}[n_i f^*_{\mathrm{ba}}(t)]\right\rangle\,.\end{aligned}$$

To keep the notation compact, we write $\left\langle V_{\mathrm{a}}[n_i f^*_{\mathrm{ab}}(t)]\right\rangle = \langle V_{\mathrm{a}}\rangle$ in the following (and analog for the other ensemble-time averages). Note the mean velocity and the mean detachment rate will depend on the relative orientation of the cross-linked filaments via the self-consistency equation Eq. 3.46. This is because the average force the cross-linker exerts between the filaments depends on the relative orientation, and the speed of the cross-linker depends on the force (same argumentation for the detachment rates). We introduce the notation $++$ $(+-)$ to denote that filament i with orientation $n_i = +1$ is cross-linked, by the mean-field cross-linker, to filament j with orientation $n_j = \pm 1$. We obtain four mean velocities and four mean detachment rates of cross-linker heads on filament i with orientation $n_i = +1$, which are given by $\langle V_{\mathrm{a}}^{+-}\rangle, \langle V_{\mathrm{a}}^{++}\rangle, \langle V_{\mathrm{b}}^{+-}\rangle, \langle V_{\mathrm{b}}^{+-}\rangle$ and analog for the mean detachment rates.

To keep the notation compact, we introduce the subscript $\alpha = \{\mathrm{a}, \mathrm{b}\}$ superscript $\beta = \{++, +-\}$ to indicate the cross-linker head type and the type of interaction (parallel or anti-parallel with respect to filament i with orientation $n_i = +1$).

Having identified the mean velocity and detachment rate of the mean-field cross-linker, we can derive the cross-linker head density profiles $\rho^{\beta}_{\alpha}(s) = \{\rho^{++}_a(s), \rho^{+-}_a(s), \rho^{++}_b(s), \rho^{+-}_b\}$ along the arc-length

$s \in [-\ell/2, \ell/2]$ of filament i with orientation $n_i = +1$. The directed motion of the mean-field cross-linker head along the arc length of the filament, in combination with detachment, can be expressed in terms of a reaction advection equation

$$\partial_t \rho_\alpha^\beta(s) = -\left\langle V_\alpha^\beta \right\rangle \partial_s \rho_\alpha^\beta(s) + k_{\mathrm{on},\alpha} - \left\langle K_\alpha^\beta \right\rangle \rho_\alpha^\beta(s) \tag{3.51}$$

with appropriate boundary conditions, which we will specify later. Note since we assumed that the unloaded velocities and detachment rates are arc-length independent, we can put $\langle V_\mathrm{a} \rangle$ outside the derivative. We will construct the solution for arc-length-dependent velocities or rates in the next step. Since we already made an adiabatic approximation separating the timescale of cross-linker dynamics and filament dynamics, we evaluate Equations 3.51 in a quasi-steady state. The quasi-steady state solution is given by

$$\rho_\alpha^\beta(s) = \frac{k_\mathrm{on}}{\left\langle K_\alpha^\beta \right\rangle} + A_\alpha^\beta \, \mathrm{e}^{-s/l_{\mathrm{run},\alpha}^\beta} \tag{3.52}$$

with A_α^β a constant, which is determined by an appropriate boundary condition and the mean run length, $l_{\mathrm{run},\alpha}^\beta = \langle V_\alpha^\beta \rangle / \langle K_\alpha^\beta \rangle$. Note the attachment rate $k_{\mathrm{on},\alpha}$ has units per time per unit length of the filament and does not depend on the applied force. Therefore it does not depend on the type of interaction $\beta = \{++, +-\}$ but only on the type of cross-linker head $\alpha = \{a, b\}$.

The remaining task is to specify appropriate boundary conditions. A cross-linker head with mean velocity $\langle V_\alpha^\beta \rangle > 0$ will have zero density at the minus end of the filament, and a cross-linker head with unloaded velocity $\langle V_\alpha^\beta \rangle < 0$ will have zero density at the plus end of the filament

$$\begin{aligned} \rho_\alpha^\beta(s)(-\ell/2) = 0 \quad &\text{if } \langle V_\alpha^\beta \rangle > 0 \\ \rho_\alpha^\beta(s)(\ell/2) = 0 \quad &\text{if } \langle V_\alpha^\beta \rangle < 0 \,. \end{aligned}$$

The solution to Eq. 3.52 is then given by

$$\rho_\alpha^\beta(s) = \frac{X_\alpha^\beta}{\mathcal{N}\ell}\left(1 - \mathrm{e}^{-(s/\ell + 1/2)\lambda}\right) \quad \text{if } \langle V_\alpha^\beta \rangle > 0 \tag{3.53}$$

$$\rho_\alpha^\beta(s) = \frac{X_\alpha^\beta}{\mathcal{N}\ell}\left(1 - \mathrm{e}^{-(s/\ell - 1/2)\lambda}\right) \quad \text{if } \langle V_\alpha^\beta \rangle < 0 \tag{3.54}$$

The dimensionless normalization $\mathcal{N}$ is chosen such that

$$X_\alpha^\beta = \int_{-\ell/2}^{\ell/2} \mathrm{d}s \, \rho_\alpha^\beta(s) \tag{3.55}$$

and X_α^β denotes the total population of parallel ($\beta = ++$) and anti-parallel ($\beta = +-$) a motor heads ($\alpha = a$) and b motor heads ($\alpha = b$) on filament i.

The cross-linker head generally does not just fall off the filament-end it is walking to (minus or plus end, depending on the direction of motion), i.e., we have a second boundary condition at $\rho_\mathrm{q}(\pm\ell/2)$ which is determined by the detachment dynamics of the motor cross-linker at the filament tip it is walking towards. However, since Eq. 3.51 is just a first-order differential equation, the boundary value problem is overdetermined. We can account for this problem by constructing a solution at the filament end the cross-linker head is walking towards. The solution still has to obey Eq. 3.51 however, with $\left\langle V_\alpha^\beta \right\rangle = 0$ since motors dwelling at a filament end are by definition immobile. Since the tip region ϵ (units of length) is small, we approximate the influx of motors into the tip by $k_{\mathrm{on},\alpha}\epsilon \approx 0$. However, we have an additional influx of cross-linker heads due to the advective transport of bulk motor heads into the tip region, which is given by $\langle V_\alpha^\beta \rangle \rho_\alpha^\beta(s)(\pm\ell/2)$. In general,

the detachment dynamics of tip motors differ from the detachment dynamics of bulk motors (the detachment dynamics along the arc-length). This yields a flux balance condition for the tip motor population which reads

$$\langle V_\alpha^\beta \rangle \rho_\alpha^\beta(\ell/2) = X_{\alpha,\mathrm{tip}}^\beta \left\langle K_{\alpha,\mathrm{tip}}^\beta \right\rangle \quad \text{if } \langle V_\alpha^\beta \rangle > 0$$
$$\langle V_\alpha^\beta \rangle \rho_\alpha^\beta(-\ell/2) = X_{\alpha,\mathrm{tip}}^\beta \left\langle K_{\alpha,\mathrm{tip}}^\beta \right\rangle \quad \text{if } \langle V_\alpha^\beta \rangle < 0\,.$$

where $X_{\alpha,\mathrm{tip}}^\beta$ denotes the population of cross-linker heads of type α mediating an interaction of type β at the filament tip and $\left\langle K_{\alpha,\mathrm{tip}}^\beta \right\rangle$ the respective mean detachment rate at the filament tip. Since the different motors head populations are ultimately the same type of cross-linker, they are constrained by mass conservation

$$X_{\mathrm{tot}} = X_{\mathrm{a}}^{+-} + X_{\mathrm{a}}^{++} + X_{\mathrm{b}}^{+-} + X_{\mathrm{b}}^{++} + X_{\mathrm{a,tip}}^{+-} + X_{\mathrm{a,tip}}^{++} + X_{\mathrm{b,tip}}^{+-} + X_{\mathrm{b,tip}}^{++}\,. \tag{3.56}$$

It is important to keep in mind that all of those cross-linker head populations X_α^β and $X_{\alpha,\mathrm{tip}}^\beta$ obey different force-velocity relations. Therefore, when we construct the filament bundle tension, they will be treated as different types of cross-linker interactions, which are ultimately connected through particle number conservation 3.56. Moreover, note the same strategy as used for tip motors can also be applied if the motor velocities or binding rates differ in different bulk regions of the filament. Then the different solutions of Eq. 3.51 have to be connected at the interface between the regions using flux balance. The obtained density profile can then be discontinuous (as is the case for tip and bulk motors).

A GENERAL FORMALISM TO CONSTRUCT THE BUNDLE TENSION FOR AN ARBITRARY SET OF MOTOR CROSS-LINKERS

In this section, we will present a general framework to construct the filament bundle tension for an arbitrary mixture of different motor proteins and passive cross-linkers.

Without loss of generality, we consider the force applied to filament i with orientation $n_i = +1$. We consider a motor or passive cross-linker denoted as X. In the following, we will refer to the motor or passive cross-linker as motor. In general, the motor might be asymmetric, with two microtubule-binding domains a and b (see Fig. 3.17 (a)) that have different dynamics along the arc-length $s \in [-\ell/2, \ell/2]$ of the cross-linked filament. As a result, they might evolve different density profiles along the arc-length of the cross-linked filaments, which might as well depend on the relative orientation of the filament. Since we consider a filament with orientation $n_i = +1$ we denote anti-parallel interactions by $(+-)$ and parallel interactions by $(++)$. Taken together we obtain four different density profiles $\rho_{x,a}^{++}(s)$, $\rho_{x,a}^{+-}(s)$, $\rho_{x,b}^{++}(s)$ and $\rho_{x,b}^{+-}(s)$ on filament i. The total population of cross-linker heads of those types of interactions are then given by

$$X_{\mathrm{a}}^{+-} = \int_{-\ell/2}^{\ell/2} \mathrm{d}s \rho_{x,a}^{+-}(s)$$
$$X_{\mathrm{a}}^{++} = \int_{-\ell/2}^{\ell/2} \mathrm{d}s \rho_{x,a}^{++}(s)$$
$$X_{\mathrm{b}}^{+-} = \int_{-\ell/2}^{\ell/2} \mathrm{d}s \rho_{x,b}^{+-}(s)$$
$$X_{\mathrm{b}}^{++} = \int_{-\ell/2}^{\ell/2} \mathrm{d}s \rho_{x,b}^{++}(s)\,.$$

An example we discussed in the main text are end-dwelling motors which have one walking motor domain a and one immobile motor domain b at the filament tip. As a result of the different dynamics, tip motors have emergent density profiles $\rho_{t,a}(s)$ and $\rho_{t,b}(s) = M_{\mathrm{tip}}\delta(s - \ell/2)$.

The asymmetric motor cross-link obeys the general force-velocity relation (Eq. 3.49) $F_{ij,a}(\Delta v)$ with the constraint

$$F_{ij,a}(\Delta v_{ji}) = -F_{ji,b}(\Delta v_{ij})\,. \tag{3.57}$$

Note here we do not restrict the discussion to a linear force-velocity relation as in the main text but consider the general form.

In a homogenous filament bundle, the relative sliding velocity of two anti-parallel filaments will always be given by $\Delta v^{+-} = v_0^- - v_0^+ = 2v_0$ and for parallel filaments $\Delta v_{++} = 0$. By convention, we choose $v_0^\pm = \mp v_0$. Though v_0 might be positive or negative depending on the type of cross-linkers in the filament bundle. The force density at arc-length position s of filament i with orientation $n_i = +1$ that stems from cross-linking interactions of the motor X is then given by

$$f_X^{+-}(s) = \rho_{x,a}^{+-}(s)F_\mathrm{a}^{+-}|_{2v_0} + \rho_{x,b}^{+-}(s)F_\mathrm{b}^{+-}|_{2v_0} \tag{3.58}$$

$$f_X^{++}(s) = \rho_{x,a}^{++}(s)F_\mathrm{a}^{++}|_0 + \rho_{x,b}^{++}(s)F_\mathrm{b}^{++}|_0\,. \tag{3.59}$$

here $F_\mathrm{a}^{+-}|_{2v_0}$ denotes that we evaluate the force-velocity relation at $\Delta v = 2v_0$. Note if $2v_0 = v_\mathrm{a} + v_\mathrm{b}$ then $F^{+-}|_{2v_0} = 0$; cf. Eq. 3.46 and Eq.3.47.

Total force acting on filament i caused by the motor X: The total force acting on filament i caused by cross-linking interactions of the motor X is then given by

$$F_X = F_X^{+-} + F_X^{++} = \int_{-\ell/2}^{\ell/2} \mathrm{d}s f_X^{+-}(s) + f_X^{++}(s) \tag{3.60}$$

with

$$F_X^{+-}(v_0) \equiv F_\mathrm{a}^{+-}|_{2v_0} X_\mathrm{a}^{+-} + F_\mathrm{b}^{+-}|_{2v_0} X_\mathrm{b}^{+-} \tag{3.61}$$

$$F_X^{++} \equiv F_\mathrm{a}^{++}|_0 X_\mathrm{a}^{++} + F_\mathrm{b}^{++}|_0 X_\mathrm{b}^{++}\,. \tag{3.62}$$

This means the total force depends only on the total number of cross-linking head populations on filament i and not on the explicit profile of the cross-linking head.

Tension profile on filament i caused by the motor X: The tension $T^+(\xi)$ on filament i with orientation $n_i = +1$ at arc-length position ξ that stems from cross-linking interactions of the motor X is given by

$$T_X^+(\xi) = T_X^{+-}(\xi) + T_X^{++}(\xi) = -\int_{-\ell/2}^{\xi} \mathrm{d}s f_X^{+-}(s) + f_X^{++}(s) \tag{3.63}$$

with

$$T_X^{+-}(\xi) \equiv -x_\mathrm{a}^{+-}(\xi)F_\mathrm{a}^{+-}|_{2v_0} - x_\mathrm{b}^{+-}(\xi)F_\mathrm{b}^{+-}|_{2v_0} \tag{3.64}$$

$$T_X^{++}(\xi) \equiv -x_\mathrm{a}^{++}(\xi)F_\mathrm{a}^{++}|_0 - x_\mathrm{b}^{++}(\xi)F_\mathrm{b}^{++}|_0 \tag{3.65}$$

where we defined the number of the different cross-linker head populations up to arc-length position ξ on filament i

$$x_\mathrm{a}^{+-}(\xi) \equiv \int_{-\ell/2}^{\xi} \mathrm{d}s \rho_{x,a}^{+-}(s)$$

$$x_\mathrm{a}^{++}(\xi) \equiv \int_{-\ell/2}^{\xi} \mathrm{d}s \rho_{x,a}^{++}(s)$$

$$x_\mathrm{b}^{+-}(\xi) \equiv \int_{-\ell/2}^{\xi} \mathrm{d}s \rho_{x,b}^{+-}(s)$$

$$x_\mathrm{b}^{++}(\xi) \equiv \int_{-\ell/2}^{\xi} \mathrm{d}s \rho_{x,b}^{++}(s)\,.$$

Bundle tension caused by the motor X: The contribution of the motor X to the tension in a homogeneous filament bundle of density ρ_0 with filaments of fixed length ℓ is given by (cf. Fig. 3.6)

$$\begin{aligned}
\mathcal{T}_X &= \frac{\rho_0}{2}\int_{-\ell/2}^{\ell/2} \mathrm{d}\xi \left(T_X^+(\xi) - \int_\xi^{\ell/2} \mathrm{d}s f_X^{-+}(s) + f_X^{--}(s) \right) \\
&= \frac{\rho_0}{2}\int_{-\ell/2}^{\ell/2} \mathrm{d}\xi \left(T_X^+(\xi) + \int_\xi^{\ell/2} \mathrm{d}s f_X^{+-}(s) + f_X^{++}(s) \right) \\
&= \frac{\rho_0}{2}\int_{-\ell/2}^{\ell/2} \mathrm{d}\xi \left(T_X^+(\xi) + F_X - \int_{-\ell/2}^{\xi} \mathrm{d}s f_X^{+-}(s) + f_X^{++}(s) \right) \\
&= \frac{\rho_0}{2}\int_{-\ell/2}^{\ell/2} \mathrm{d}\xi \left(F_X + 2T_X^+(\xi) \right) \\
&= \frac{\rho_0 \ell}{2} F_X + \rho_0 \int_{-\ell/2}^{\ell/2} \mathrm{d}\xi\, T_X^+(\xi)\,.
\end{aligned}$$

Here we used $f_X^{-+}(s) = -f_X^{+-}(s)$ and $f_X^{--}(s) = -f_X^{++}(s)$. Next, we introduce the anisotropy factors for the different motor populations

$$\begin{aligned}
\mu_\mathrm{a}^{+-} &\equiv 1/2 - \frac{1}{\ell X_\mathrm{a}^{+-}} \int_{-\ell/2}^{\ell/2} \mathrm{d}\xi\, x_\mathrm{a}^{+-}(\xi) \\
\mu_\mathrm{a}^{++} &\equiv 1/2 - \frac{1}{\ell X_\mathrm{a}^{++}} \int_{-\ell/2}^{\ell/2} \mathrm{d}\xi\, x_\mathrm{a}^{++}(\xi) \\
\mu_\mathrm{b}^{+-} &\equiv 1/2 - \frac{1}{\ell X_\mathrm{b}^{+-}} \int_{-\ell/2}^{\ell/2} \mathrm{d}\xi\, x_\mathrm{b}^{+-}(\xi) \\
\mu_\mathrm{b}^{++} &\equiv 1/2 - \frac{1}{\ell X_\mathrm{b}^{++}} \int_{-\ell/2}^{\ell/2} \mathrm{d}\xi\, x_\mathrm{b}^{++}(\xi)\,.
\end{aligned}$$

using those definitions we evaluate the integral over $T^+(\xi)$. Taken together, we obtain

$$\begin{aligned}
\mathcal{T}_X/(\rho_0\ell) = {} & \mu_\mathrm{a}^{+-} X_\mathrm{a}^{+-} F_\mathrm{a}^{+-}|_{2v_0} + \mu_\mathrm{b}^{+-} X_\mathrm{b}^{+-} F_\mathrm{b}^{+-}|_{2v_0} \\
& + \mu_\mathrm{a}^{++} X_\mathrm{a}^{++} F_\mathrm{a}^{++}|_0 + \mu_\mathrm{b}^{++} X_\mathrm{b}^{++} F_\mathrm{b}^{++}|_0\,.
\end{aligned} \tag{3.66}$$

It is important to note that we did not specify the functional form of the force-velocity relation at any point. Thus Eq. 3.66 can be applied to an arbitrary non-linear force-velocity relation. Moreover, note the fact that we have to evaluate the non-linear force-velocity only at $\Delta v = 0$ and $\Delta v = 2v_0$ is of significant advantage if we consider the general form of the force-velocity relation (Eq. 3.49). Even if we can not solve the integrals analytically, we only have to approximate them numerically at $\Delta v = 0$ and $\Delta v = 2v_0$.

Total force applied to filament i in mixtures of different cross-linking proteins: In a mixture of different cross-linking proteins $X = \{X_1, X_2, X_3, \ldots\}$, the total force on filament i is then given by

$$F = \sum_X F_X\,. \tag{3.67}$$

In the limit where forces of cross-linking proteins dominate over dissipation to the solvent, those forces have to balance

$$F = \sum_X F_X = 0\,. \tag{3.68}$$

If they do not dominate over dissipation to the solvent, the force balance condition reads

$$F = \sum_X F_X = -\gamma v_0 \,. \tag{3.69}$$

where γ denotes the drag coefficient. Note the minus sign is there because by convention we used $v_0^+ = -v_0$ and we consider a right-oriented filament. This sets a condition for the filament sliding velocity v_0 in dependency on the different total populations of cross-linking heads on the filament,

$$\gamma v_0 + \sum_X F_X^{+-}(v_0) = -\sum_X F_X^{++} \,. \tag{3.70}$$

Filament bundle tension in mixtures of different cross-linking proteins: The accumulated bundle tension caused by different cross-linking proteins is given by

$$\mathcal{T} = \sum_X \mathcal{T}_X \,. \tag{3.71}$$

It is important to note that Eq. 3.71 provides a general expression for the bundle tension in a homogenous filament bundle with an arbitrary set of cross-linkers that might obey non-linear force-velocity relations. Having a general expression for the filament bundle tension, the remaining task is to derive how the different populations of cross-linker heads on a filament depend on each other. This is because most motor proteins have a speed V_X that depends on the applied load. This force will depend on the filament sliding velocity v_0 and, thereby, on all populations of cross-linker heads on the filament via Eq. 3.70. However, since the force applied on parallel and anti-parallel cross-links differs, this affects the number of parallel and anti-parallel cross-links on a filament, in particular, if force-dependent detachment is considered. The resulting set of equations has to be solved self-consistently.

EXAMPLES

Force independent detachment and linear stalling As an example of our general theory, we discuss a class of minimal models for motor proteins that detach at a force-independent rate and slow down linear to a force applied against their unloaded direction of motion. The kinetic constants in the absence of force are given by $(v_\mathrm{a}, v_\mathrm{b}, k_\mathrm{off,a}, k_\mathrm{off,b})$ and the functions characterizing the response to the applied force are given by

$$\begin{aligned}
\phi_a[nf] &= \mathrm{sgn}(v_a)\frac{nf}{f_\mathrm{s,a}} \\
\phi_b[nf] &= \mathrm{sgn}(v_b)\frac{nf}{f_\mathrm{s,b}} \\
\psi_a[nf] &= 1 \\
\psi_b[nf] &= 1
\end{aligned}$$

Note we assume here that a motor head can seed up above its unloaded velocity v_a (v_b) if the applied force pulls the motor in its direction of motion. This is done to keep the notation compact. Changing this assumption yields slightly different prefactors for parallel and anti-parallel interactions but no change in the functional form.

We re-scale time in units of the bond breakage rate $\tilde{t} = (k_\mathrm{off,a} + k_\mathrm{off,b})\,t$. Therefore,

$$\tilde{K}[f_\mathrm{ab}^*] = 1 \,.$$

Substitution in the self-consistency equation Eq. 3.46 yields

$$\partial_{\tilde{t}} f_\mathrm{ab}(\tilde{t}) + \frac{\kappa}{k_\mathrm{off,a} + k_\mathrm{off,b}}\left(\frac{|v_\mathrm{a}|}{f_\mathrm{s,a}} + \frac{|v_\mathrm{b}|}{f_\mathrm{s,b}}\right) f_\mathrm{ab}^*(\tilde{t}) = \frac{\kappa}{k_\mathrm{off,a} + k_\mathrm{off,b}}\left(n_\mathrm{j} v_\mathrm{b} - n_\mathrm{i} v_\mathrm{a} + \Delta v_{ji}\right) \tag{3.72}$$

with the initial condition $f^*_{ab}(0) = 0$ this is solved by

$$f^*_{ab}(t) = \frac{f_{s,a} f_{s,b}}{f_{s,b}|v_a| + f_{s,a}|v_b|}\left(1 - e^{-A\tilde{t}}\right)\left(n_j v_b - n_i v_a + \Delta v_{ji}\right). \tag{3.73}$$

with the dimensionless constant A given by

$$A = \frac{\kappa}{k_{off,a} + k_{off,b}}\left(\frac{|v_a|}{f_{s,a}} + \frac{|v_b|}{f_{s,b}}\right). \tag{3.74}$$

Substitution in the general form of the force-velocity equation (Eq. 3.49) yields

$$F_{ij,a}(\Delta v_{ji}) = \Gamma_m(n_j v_b - n_i v_a + \Delta v_{ji})$$

with

$$\Gamma_m = \frac{f_{s,a} f_{s,b}}{f_{s,b}|v_a| + f_{s,a}|v_b|}\frac{A}{1+A}. \tag{3.75}$$

Note Γ_m has units of force per velocity, i.e., it is an effective friction constant of the motor cross-linker, which is determined by a competition between bond-breakage events and stalling of the motor heads. For $\kappa|v_{a,b}|/(k_{off,a} + k_{off,b}) \ll f_{s,\{a,b\}}$ it is dominated by spring relaxation, i.e., bond breakage, and the effective friction coefficient of the cross-linker is low. In contrast, the effective friction coefficient of the motor cross-linker saturates at $(f_{s,a} f_{s,b})/(f_{s,b}|v_a| + f_{s,a}|v_b|)$ for persistent motors (low detachment rates).

To evaluate the contribution of this class of cross-linkers to the bundle tension, we need to evaluate the force-velocity relation for $F_a^{++}|_0, F_a^{+-}|_{2v_0}, F_b^{++}|_0, F_b^{+-}|_{2v_0}$, which results in

$$\begin{aligned} F_a^{+-}|_{2v_0} &= \Gamma_x(-v_x + 2v_0) \\ F_b^{+-}|_{2v_0} &= \Gamma_x(-v_x + 2v_0) \\ F_a^{++}|_0 &= \Gamma_x \Delta v_x \\ F_b^{++}|_0 &= -\Gamma_x \Delta v_x \end{aligned}$$

here we introduced the relative unloaded motor head velocity $\Delta v_x = v_b - v_a$ and the sum unloaded motor head velocity $v_x = v_b + v_a$.

The contribution to the total force acting on a filament in the bundle that comes from interactions with this class of cross-linkers is given by (see Eq. 3.60)

$$F_X = \Gamma_x v_x (X_a^{+-} + X_b^{+-})\left(-1 + \frac{2v_0}{v_m}\right) + \Gamma_x \Delta v_x (X_a^{++} - X_b^{++}) \tag{3.76}$$

The contribution to the filament bundle tension of this class of motor cross-linkers, that steam from parallel (++) and anti-parallel (+-) interactions, is then given by (see Eq. 3.66)

$$\mathcal{T}_X^{+-}/(\rho_0 \ell) = \Gamma_x v_x \left(-1 + \frac{2v_0}{v_x}\right)\left[\mu_a^{+-} X_a^{+-} + \mu_b^{+-} X_b^{+-})\right] \tag{3.77}$$

$$\mathcal{T}_X^{++}/(\rho_0 \ell) = \Gamma_x \Delta v_x \left[\mu_a^{++} X_a^{++} - \mu_b^{++} X_b^{++}\right] \tag{3.78}$$

The motor cross-linker types discussed in the main text are members of this class of cross-linkers.

Symmetric bulk motor (Kinesin-5): We consider a symmetric bulk motor ($a = b$) with unloaded speed $v_a = v_b$. A representative member of this class of cross-linkers is Kinsesin-5 [95]. Since the motor cross-linker is symmetric we find $\Delta v_x = 0$ and $v_x = 2v_m$ Moreover, we use $X_a^{+-} = X_b^{+-} = X^{+-}/2$ and $X_a^{++} = X_b^{++} = X^{++}/2$ and $\mu_a^{+-} = \mu_b^{+-} = \mu^{+-}$. Thus,

$$\begin{aligned} F_X &= 2\Gamma_x v_a X^{+-}\left(-1+\frac{v_0}{v_a}\right) \\ \mathcal{T}_X^{+-}/(\rho_0\ell) &= 2\Gamma_x v_a X^{+-}\left(-1+\frac{v_0}{v_a}\right)\mu^{+-} \\ \mathcal{T}_X^{++}/(\rho_0\ell) &= 0\,. \end{aligned}$$

Note the unloaded speed of the motor can be positive (plus-end directed) or negative (minus-end directed). In the absence of other motor cross-linkers, plus-end directed motors will cause a filament sliding velocity $v_0 > 0$, and minus-end directed motors a filament sliding velocity $v_0 < 0$. Plus end directed motors will have an anisotropy factor $\mu^{+-} \leq 1/2$, and minus end-directed motors will have an anisotropy factor $\mu^{+-} \geq 1/2$. Therefore, in the absence of other motor cross-linkers, the sign and magnitude of $\mathcal{T}_X^{+-}$ is equal under the transformation $v_a \to -v_a$ as expected.

Asymmetric bulk motor (Kinesin-4, Dynein): We consider an asymmetric bulk motor with $v_b = 0$ and v_a. Hence $\Delta v_x = -v_a$ and $v_x = v_a$. Members of this class of motor cross-linkers are Dynein $v_a < 0$ and kinesin-4 $v_a > 0$ [193]. The analysis presented in Sec 3.2.3 implies a homogenous density profile of the immobile head domain. Thus, $\mu_b^{+-} = \mu_b^{++} = 0$. Therefore

$$F_X = \Gamma_x v_a (X_a^{+-} + X_b^{+-})\left(-1+\frac{2v_0}{v_a}\right) - \Gamma_x v_a (X_a^{++} - X_b^{++}) \tag{3.79}$$

$$\mathcal{T}_X^{+-}/(\rho_0\ell) = \Gamma_x v_a X_a^{+-}\left(-1+\frac{2v_0}{v_a}\right)\mu_a^{+-} \tag{3.80}$$

$$\mathcal{T}_X^{++}/(\rho_0\ell) = -\Gamma_x v_a X_a^{++}\mu_a^{++}\,. \tag{3.81}$$

This implies that an asymmetric bulk motor contributes an extensile tension, which is equal to or stronger than a symmetric bulk motor with equal kinetic parameters since the motor velocity on parallel filaments will be faster and therefore $\mu_a^{++} \leq \mu_a^{+-}$. This is consistent with previous theoretic models for an explicit asymmetric motor [257]. Again sign and magnitude of the bundle tension are conserved under the transformation $v_a \to -v_a$ in the absence of other cross-linkers.

Tip dwelling motor (Kinesin-4,Dynein): Tip-dwelling motors are, by definition, asymmetric motors since they have one immobile motor domain dwelling at the filament tip $v_b = 0$ and one mobile motor domain with v_a. Hence $\Delta v_x = -v_a$ and $v_x = v_a/2$. Members of this class of motor cross-linkers are dynein $v_a < 0$ and kinesin-4 $v_a > 0$. dynein is a "super persistent" motor, in particular at the filament tip [193]. Tip motors have a delta-peaked density distribution of immobile motor domains at the respective filament end. Therefore we find the anisotropy factors

$$\begin{aligned} \mu_b^{+-} = \mu_b^{++} &= 1/2 \quad \text{for } v_a > 0 \\ \mu_b^{+-} = \mu_b^{++} &= -1/2 \quad \text{for } v_a < 0 \end{aligned}$$

For $v_a > 0$ we obtain

$$F_X = \Gamma_x v_a (X_a^{+-} + X_b^{+-})\left(-1+\frac{2v_0}{v_a}\right) - \Gamma_x v_a (X_a^{++} - X_b^{++}) \tag{3.82}$$

$$\mathcal{T}_X^{+-}/(\rho_0\ell) = \Gamma_x v_a \left(-1+\frac{2v_0}{v_m}\right)\left[(1/2-\mu_a^{+-})X_a^{+-} + 1/2 X_b^{+-}\right] \tag{3.83}$$

$$\mathcal{T}_X^{++}/(\rho_0\ell) = -\Gamma_x v_a \left[(1/2-\mu_a^{++})X_a^{++} - 1/2 X_b^{++}\right]\,. \tag{3.84}$$

If we further use $X_a^{++} = X_b^{++}$ and $X_a^{+-} = X_b^{+-}$ we recover the results used in the main text.

For $v_a < 0$ we obtain

$$F_X = \Gamma_x v_a (X_a^{+-} + X_b^{+-}) \left(-1 + \frac{2v_0}{v_a}\right) - \Gamma_x v_a (X_a^{++} - X_b^{++}) \tag{3.85}$$

$$\mathcal{T}_X^{+-}/(\rho_0 \ell) = \Gamma_x v_a \left(-1 + \frac{2v_0}{v_a}\right) \left[\mu_a^{+-} X_a^{+-} - 1/2 X_b^{+-})\right] \tag{3.86}$$

$$\mathcal{T}_X^{++}/(\rho_0 \ell) = -\Gamma_x v_a \left[\mu_a^{++} X_a^{++} + 1/2 X_b^{++}\right] . \tag{3.87}$$

Note again, those expressions respect parity symmetry under the transformation $v_a \to -v_a$, since $v_a \to -v_a \Rightarrow \mu \to -\mu$ (in the absence of other motor cross-linkers).

Constructing the bundle tension The filament bundle tension caused by this class of cross-linking proteins can now be constructed by first solving

$$\gamma v_0 + \sum_X F_X = 0 . \tag{3.88}$$

then relating tip and bulk motor contributions via mass conservation and flux balance as presented in Sec. 3.2.3 and substituting the self-consistent solution for v_0 into

$$\mathcal{T} = \sum_X \mathcal{T}_X|_{v_0} . \tag{3.89}$$

Note the constants Γ_m differ for all different cross-linkers.

Linear stalling with exponential detachment. We now want to consider some examples of cross-linking proteins with force-dependent detachment. We re-scale time in units of the unloaded motor head detachment rates $\tilde{t} = (k_{off,a} + k_{off,b})t$. In particular, we are interested in slip-bonds, i.e., detachment dynamics, where an applied force accelerates the detachment dynamics. As a classical result, the dissociation dynamics can be estimated as

$$K[nf(t)] = k_{off} e^{\frac{|nf|}{f_u}} . \tag{3.90}$$

with an characteristic unbinding force f_u. For the sake of simplicity, we assume equal force-response functions of a and b head unbinding dynamics, such that

$$\psi_a[nf] = e^{\frac{|nf|}{f_u}} = \psi_b[nf] .$$

The self-consistency equation Eq. 3.46 is not affected by force-dependent detachment. We therefore still obtain the solution (in the case of linear stalling)

$$f_{ab}^*(t) = \frac{f_{s,a} f_{s,b}}{f_{s,b}|v_a| + f_{s,a}|v_b|} \left(1 - e^{-A\tilde{t}}\right) \left(n_j v_b - n_i v_a + \Delta v_{ji}\right) . \tag{3.91}$$

with the dimensionless constant

$$A = \frac{\kappa}{k_{off,a} + k_{off,b}} \left(\frac{|v_a|}{f_{s,a}} + \frac{|v_b|}{f_{s,b}}\right) . \tag{3.92}$$

Substitution in the general form of the force-velocity relation yields

$$F_{ij,a}(\Delta v_{ji}) = \frac{f_{s,a} f_{s,b}}{f_{s,b}|v_a| + f_{s,a}|v_b|} \left(n_j v_b - n_i v_a + \Delta v_{ji}\right) \left[1 - \frac{1}{\langle\tilde{\tau}\rangle} \int_0^\infty d\tilde{\tau}\, S(\tilde{\tau}, \Delta v_{ji}) e^{-A\tilde{\tau}}\right] .$$

This means to first order any motor cross-linker that stalls linear will obey a linear force-velocity relation. For force-independent detachment, the survival probability is given by $\exp(-\tilde{\tau})$. For force-dependent detachment, we have to find the survival probability using the general formula.

The re-scaled bond-breakage rate reads

$$\tilde{K}[|f^*_{\mathrm{ab}}(\tilde{t})|] = \exp\left[B|n_j v_\mathrm{b} - n_\mathrm{i} v_\mathrm{a} + \Delta v_{ji}|\left(1-\mathrm{e}^{-A\tilde{t}}\right)\right] \tag{3.93}$$

with

$$B = \frac{1}{A}\frac{\kappa}{k_{\mathrm{off,a}}+k_{\mathrm{off,b}}}\frac{1}{f_\mathrm{u}} \tag{3.94}$$

which has units of one over velocity. Substitution in the general form for the survival probability yields

$$S(\tilde{\tau}) = \exp\left\{-\int_0^{\tilde{\tau}} \mathrm{d}t \exp\left[B|n_j v_\mathrm{b} - n_\mathrm{i} v_\mathrm{a} + \Delta v_{ji}|\left(1-\mathrm{e}^{-A\tilde{t}}\right)\right]\right\} \tag{3.95}$$

We evaluate the integral with the help of Mathematica and find

$$\begin{aligned} S(\tilde{\tau},\Delta v_{ji}) = \exp\Bigg\{&-\left[\frac{1}{A}\mathrm{e}^{B|n_j v_\mathrm{b} - n_\mathrm{i} v_\mathrm{a} + \Delta v_{ji}|}\right] \\ &\left(\mathrm{Ei}(-B|n_j v_\mathrm{b} - n_\mathrm{i} v_\mathrm{a} + \Delta v_{ji}|)\right) - \mathrm{Ei}\left(-B\mathrm{e}^{-A\tilde{\tau}}|n_j v_\mathrm{b} - n_\mathrm{i} v_\mathrm{a} + \Delta v_{ji}|\right)\Bigg\} \end{aligned}$$

with the exponential integral $\mathrm{Ei}(z) = -\int_z^\infty \mathrm{d}t\, \mathrm{e}^{-t}/t$.

Taken together, we obtain the force-velocity relation for a motor cross-linker with exponential force-dependent detachment, as used in many agent-based simulation software. The remaining integral over $\tilde{\tau}$ has to be approximated numerically. An example for a symmetric bulk motor with parameters used in the agent-based simulation (see Tab. 3.1) is given in Fig. Fig. 3.18 (a),(b).

Care has to be taken if one considers a passive cross-linker, which has, by definition, zero motor activity, i.e., $v_\mathrm{a} = v_\mathrm{b} = 0$ and $\phi_a[nf] = \phi_b[nf] = 0$. Then the self-consistency equation Eq. 3.46 is solved by

$$f^*_{\mathrm{ab}}(\tilde{t}) = \frac{\kappa}{k_{\mathrm{off,a}}+k_{\mathrm{off,b}}}\tilde{t}\Delta v_{\mathrm{ji}}\,. \tag{3.96}$$

which yields the force-velocity relation

$$\begin{aligned} F_{\mathrm{ij,a}}(\Delta v_{ji}) &= \frac{1}{2}\frac{\kappa}{k_{\mathrm{off,a}}+k_{\mathrm{off,b}}}\Delta v_{ji}\int_0^\infty \mathrm{d}\tilde{\tau}\,\tilde{\tau}^2\,\tilde{w}(\tilde{\tau},\Delta v_{ji}) \\ &= \frac{\kappa v_\mathrm{m}}{k_{\mathrm{off,a}}+k_{\mathrm{off,b}}}\frac{\Delta v_{ji}}{2v_\mathrm{m}}\frac{\langle\tilde{\tau}^2\rangle}{\langle\tilde{\tau}\rangle} \end{aligned}$$

We decided to measure the velocity of filaments in units of the relative unloaded motor head velocity $2v_\mathrm{m}$ of some motor in the system. For force-independent detachment ($\tilde{w} = \exp(-\tilde{\tau})$), we obtain the result used in the main text. Using symmetric force-dependent detachment as we did for motor cross-linkers, we obtain the waiting time distribution

$$\tilde{w}(\tilde{\tau}) = \exp\left[\frac{1}{D}\frac{2v_\mathrm{m}}{|\Delta v_{21}|}\left(1-\mathrm{e}^{D\frac{|\Delta v_{21}|}{2v_\mathrm{m}}\tilde{\tau}}\right) + D\frac{|\Delta v_{21}|}{2v_\mathrm{m}}\tilde{\tau}\right] \tag{3.97}$$

with the dimension less constant

$$D = \frac{\kappa v_\mathrm{m}}{2k_\mathrm{off}}\frac{1}{f_\mathrm{u}}\,. \tag{3.98}$$

The resulting non-linear force-velocity relation alongside a linear fit to it is shown in Fig. 3.18 (c).

Since we assumed a homogeneous density profile of the passive cross-linker, the direct contribution to the bundle tension is zero (anisotropy factor of 1/2), and it enters only via the filament sliding velocity v_0.

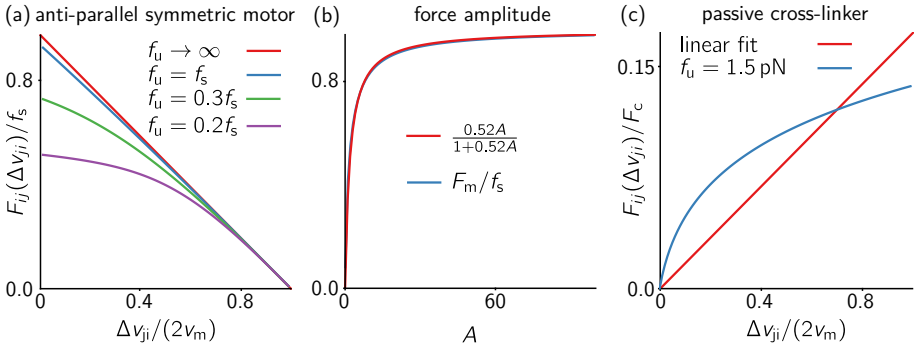

Figure 3.18: (a) Non-linear force-velocity relation $|F_{ij}|(|\Delta v_{ji}|/(2v_m))$ for motor cross-linkers with exponential force-response detachment functions $\psi[nf] = \exp(|f(t)|/f_u)$. The dimensionless parameter was chosen to be $A = 37.5$. For $f_u \to \infty$, the result for force-independent detachment is recovered ($\psi[nf] \to 1$). If the unbinding force is less than the stall force, the motor cross-linker can not operate at the stall force since it detaches before reaching it. Hence, we get increasing deviations from the linear force-velocity relation as the unbinding force is decreased. (b) Force amplitude F_m/f_s as a function of the dimensionless constant A. Obtained from a linear fit of the form $F_m/f_s \Delta v_{ji}/(2v_m)$ to the non-linear force-velocity relation for $f_s = f_u$ (as in the agent-based simulation). We find $F_m/f_s \approx 0.52A/(1+0.52A)$, i.e., compared to force-independent detachment motor-cross-linkers with force dependent-detachment have a lower force amplitude. (c) Force velocity relation for a passive cross-linker as used in the agent-based simulation (blue curve) and linear fit to the non-linear force-velocity relation (Tab. 3.1). To compare the agent-based simulations to our theoretical prediction (Fig. 3.16), we used the linear fit to the non-linear force-velocity relations. We tend to overestimate the strength of passive cross-linkers since they enter the filament bundle tension only via the filament sliding velocity v_0/v_m and anti-parallel filament-filament interactions, which tend to have a relative sliding velocity $\Delta v_{ji} > v_m$. A

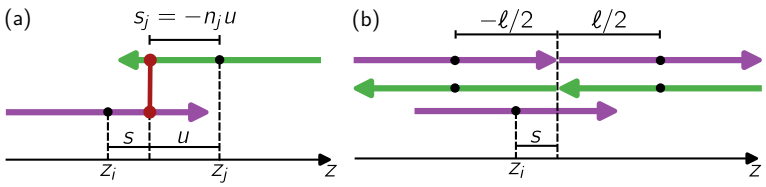

Figure 3.19: (a) Motor cross-linker interaction between filament i with center of mass-position z_i and filament j with center of mass position $z_j = z_i + s_i + u$. The potential interaction partners of a motor cross-linker at arc-length position s_i are distributed in the intervall $u \in [-\ell/2, \ell/2]$; see (b)

FORCE DENSITY AND FILAMENT BUNDLE TENSION IN AN INHOMOGENOUS FILAMENT-BUNDLE

In this section, we discussed the physics of a homogenous filament bundle cross-linked by different motor cross-linkers. A natural next step is to analyze the physics of an inhomogenous filament bundle. What is the impact of local variations in the bundle polarity or the bundle density? To answer this question, we have to formulate our theoretical framework for spatially varying fields. Here, we will provide the governing equations but do not discuss the physical consequences.

We denote the spatial coordinate by z and the center of mass densities of filaments with orientation $n_i = +1$ and $n_i = -1$ by $\rho^+(z)$ and $\rho^-(z)$ respectively. As before, we denote the arc-length density profiles of doubly linked motor cross-linkers by $\rho_a^{++}, \rho_a^{+-}, \rho_b^{++}, \rho_b^{++}$. However, since the filament bundle is inhomogenous $\rho_a^{++} = \rho_a^{++}(z,s)$, with

$$X_\alpha^\beta(z) = \int_{-\ell/2}^{\ell/2} \mathrm{d}s\, \rho_\alpha^\beta(z,s) \tag{3.99}$$

where $\alpha = \{\mathrm{a},\mathrm{b}\}$ and $\beta = \{++,+-\}$. The filament sliding velocities $v^{\pm}$ become functions of space as well $v^{\pm} = v^{\pm}(z)$. A motor cross-link on a filament with the center of mass position z at arc-length s of the filament can mediate an interaction with other filaments in the range $[z+s-\ell/2, z+s+\ell/2]$. Consider the situation in which the motor with head a attached to filament i with the center of mass position z mediates an interaction to a filament with orientation $n_j = -1$, which has a center of mass position $z+s+u$ with $u \in [-\ell/2, \ell/2]$. We assume that this interaction takes place with probability $\rho^{-}(z+s+u)\rho^{+-}_{X,a}(z,s)$ and analog for other interactions. The force densities due to the different interaction types at arc-length position s of the filament are then given by

$$f_a^{+-}(z,s) = \frac{X_a^{+-}(z)}{\mathcal{N}_a^{+-}(z)} \int_{-\ell/2}^{\ell/2} \mathrm{d}u\, \rho^{-}(z+s+u)\rho^{+-}_{\mathrm{x,a}}(z,s)\left[-v_{\mathrm{x}} + v^{-}(z+s+u) - v^{+}(z)\right]\Gamma_{\mathrm{x}} \tag{3.100a}$$

$$f_a^{++}(z,s) = \frac{X_a^{++}(z)}{\mathcal{N}_a^{++}(z)} \int_{-\ell/2}^{\ell/2} \mathrm{d}u\, \rho^{+}(z+s+u)\rho^{++}_{\mathrm{x,a}}(z,s)\left[\Delta v_{\mathrm{x}} + v^{+}(z+s+u) - v^{+}(z)\right]\Gamma_{\mathrm{x}} \tag{3.100b}$$

$$f_b^{+-}(z,s) = \frac{X_b^{+-}(z)}{\mathcal{N}_b^{+-}(z)} \int_{-\ell/2}^{\ell/2} \mathrm{d}u\, \rho^{-}(z+s+u)\rho^{+-}_{\mathrm{x,b}}(z,s)\left[v_{\mathrm{x}} + v^{-}(z+s+u) - v^{+}(z)\right]\Gamma_{\mathrm{x}} \tag{3.100c}$$

$$f_b^{++}(z,s) = \frac{X_b^{++}(z)}{\mathcal{N}_b^{++}(z)} \int_{-\ell/2}^{\ell/2} \mathrm{d}u\, \rho^{+}(z+s+u)\rho^{++}_{\mathrm{x,b}}(z,s)\left[-\Delta v_{\mathrm{x}} + v^{+}(z+s+u) - v^{+}(z)\right]\Gamma_{\mathrm{x}} \tag{3.100d}$$

with the normalization

$$\mathcal{N}_\alpha^{\beta}(z) = \int_{-\ell/2}^{\ell/2} \mathrm{d}s \int_{-\ell/2}^{\ell/2} \mathrm{d}u\, \rho^{\beta[1]}(z+s+u)\rho^{\beta}_{\mathrm{x},\alpha}(z,s) \tag{3.101}$$

where $\beta[1] = +$ if $\beta = ++$ and $\beta[1] = -$ if $\beta = +-$. The normalization is chosen such that the total force on a filament at position z that stems from interactions parallel and anti-parallel motor interactions of the cross-linker head α is proportional to the total population on the filament X_α^β.

The total force on a filament with orientation $n = +1$ at position z is then given by

$$F^{\beta}_{X,\alpha}(z) = \int_{-\ell/2}^{\ell/2} \mathrm{d}s\, f_\alpha^{\beta}(z,s) \tag{3.102}$$

and the bundle tension by

$$\mathcal{T}^{\beta}_{X,\alpha} = \int_{-\ell/2}^{\ell/2} \mathrm{d}\xi\, \rho^{\beta[1]}(z+\xi) \int_{-\ell/2}^{\xi} \mathrm{d}s\, f_\alpha^{\beta}(z,s)\,. \tag{3.103}$$

The analysis presented in the main text corresponds to a zeroth-order gradient expansion of the equations presented above.

PARAMETERS

	Parameter name	Value
System parameters:		
$x-$Extent	L_x	$24\,\mu m$
$y-$Extent	L_y	$24\,\mu m$
$z-$Extent	L_z	$0.2\,\mu m$
Viscosity	—	$0.02\,pN\mu m^{-2}$
Filament parameters:		
Filament length	ℓ	$2\,\mu m$
Rigidity	—	$30\,pN\mu m^2$
Steric radius	d_{Mt}	$0.05\,\mu m$
Steric force constant	—	$50\,pN\mu m^{-1}$
Motor parameters:		
Motor velocity	v_m	$0.25\,\mu m\,s^{-1}$
Attachment rate	k_{on}	$5\,s^{-1}$
Detachment rate	k_{off}	$0.2\,s^{-1}$
End-detachment rate	$k_{off,tip}$	$0.2-4\,s^{-1}$
Unbinding force	f_u	$5\,pN$
Stall force	f_{stall}	$5\,pN$
Link stiffness	—	$150\,pN\mu m^{-1}$
Rest length	—	$0.1\,\mu m$
Passive cross-linker parameters:		
Attachment rate	k_{on}	$5\,s^{-1}$
Detachment rate	k_{off}	$1\,s^{-1}$
Unbinding force	f_u	$1.5\,pN$
Link stiffness	—	$50\,pN\mu m^{-1}$
Rest length	—	$0.1\,\mu m$
Simulation parameters:		
Time step	dt	$5\times10^{-3}\,s^{-1}$
Filament segmentation	—	$0.1\,\mu m$

Table 3.1: Parameters specifying the microscopic dynamics of the constituents in the agent-based simulation. At a pacing fraction of $\phi \approx N_{Mt}\pi d_{MT}^2 \ell/(4L_xL_yLz) = 2\times10^{-2}$ we have 576 filaments in the system. We keep most parameters fixed and use the total number of motors, passive cross-linkers, and the tip detachment rate as control parameters. When indicated, we changed the motor velocity or the bulk detachment rate of motors to change the motor anisotropy.

	Parameter name	Value
Filament parameters:		
Filament length	ℓ	$2\,\mu m$
Motor parameters:		
Motor velocity	v_m	$0.25\,\mu m\,s^{-1}$
Detachment rate	k_{off}	$0.2\,s^{-1}$
End-detachment rate	$k_{off,tip}$	$0.8\,s^{-1}$
Stall force	f_{stall}	$5\,pN$
Link stiffness	κ_m	$100\,pN\mu m^{-1}$
Passive cross-linker parameters:		
Detachment rate	k_{off}	$5\,s^{-1}$
Link stiffness	κ_c	$60\,pN\mu m^{-1}$

Table 3.2: Kinetic and mechanical parameters specifying the minimal microscopic model. If not stated otherwise, we used those parameters in the following.

3.3. A MECHANISTIC VIEW OF COLLECTIVE FILAMENT MOTION IN ACTIVE NEMATIC NETWORKS

3.3.1. SIGNIFICANCE

Assemblies of cytoskeletal filaments and associated proteins form a diverse range of dynamic structures that play essential roles in many intracellular structures and processes. A decisive factor in the ability of these networks to self-organize is the dynamic rearrangement of filaments driven by motor proteins. However, there is still a large gap in our knowledge of how the various components act together to establish and modulate these dynamic structures.

Here, we address this general question using a minimal but generic theoretical model. We identify a robust physical mechanism for the relationship between filament velocity and ambient/local network polarity. This mechanism explains previous results of experiments on Xenopus egg extracts [96, 97] as well as experiments with defined systems containing purified components [99]. Moreover, we suggest how our predictions can be tested by in-vitro experiments.

Our understanding of the mechanistic origin of filament dynamics in mixtures with motors is largely based on experimental studies of the interactions of purified components. A basic fact that has emerged from such studies is that two isolated antiparallel microtubules are pushed past one another by the action of sliding motors (kinesin-5 family), while parallel filaments remain static [95]. When this finding is applied to an ensemble of filaments cross-linked by motors, one would intuitively expect that the filament dynamics should strongly depend on the local number of anti-parallel filaments. While this intuition is supported by existing theories for dilute filament networks [240, 250], it is clearly contradicted by experimental observations on the mitotic spindle [97, 98] (see Fig. 3.2) as well as in vitro structures consisting of filaments cross-linked by motors [99]. Strikingly, in these systems, the local filament velocity is largely independent of the local number of anti-parallel filaments, i.e., network polarity. How can one resolve this riddle? What is the underlying mechanism that explains the difference in filament dynamics between the two network types?

To answer these questions, we develop a theoretical framework for filament motion in networks cross-linked by motor proteins. By deriving a continuum description from mesoscopic interactions, we identify a mechanism for collective filament motion: Owing to the cross-linking in the network, motion is propagated through it over a characteristic length. This characteristic length is set by the antagonism between drag and motor-driven forces and is a control parameter of the filament dynamics.

Intriguingly, for biologically realistic parameters, we can explain the qualitative behaviour observed in the spindle [96, 97] and in recent in vitro experiments [99]. In addition, our theory predicts how the ratio between the spectra of polarities and velocities depends on the characteristic length. We suggest an in vitro experiment which uses this prediction to test our theory. The feasibility of this experiment is assessed with the help of computer simulations and an accompanying theoretical analysis.

Taken together, our work offers a new perspective on the emergence of collective active motion in nematic filament networks, and constitutes a significant step towards the establishment of a concise theoretical framework for the dynamics in filament networks.

3.3.2. PUBLICATION

This section is based on the publication

A mechanistic view of collective filament motion in active nematic networks

by
M. Striebel[1,*], **Isabella R. Graf**[1,*] **and E. Frey**[1]
[1] Arnold Sommerfeld Center for Theoretical Physics and Center for NanoScience, Department of Physics, Ludwig-Maximilians-Universität München, Theresienstrasse 37, D-80333 Munich, Germany

Biophysical Journal **118**, 313-324 (2020).

DOI: 10.1016/j.bpj.2019.11.3387
Also available on bioRxiv: bioRxiv:10.1101/732909

Supplementary material: The supplemental material can be found in Sec. 3.6.

Author contributions: Isabella R. Graf and I contributed equally to this work. Isabella R. Graf, Erwin Frey and I conceptualized the study. Isabella R. Graf and I performed the analytic analysis. I performed the numerical analysis, date analysis and date visualization. Isabella R. Graf, Erwin Frey and I wrote the manuscript. Erwin Frey supervised the research.

A mechanistic view of collective filament motion in active nematic networks

Abstract

Protein filament networks are structures crucial for force generation and cell shape. A central open question is how collective filament dynamics emerges from interactions between individual network constituents. To address this question we study a minimal but generic model for a nematic network where filament sliding is driven by the action of motor proteins. Our theoretical analysis shows how the interplay between viscous drag on filaments and motor-induced forces governs force propagation through such interconnected filament networks. We find that the ratio between these antagonistic forces establishes the range of filament interaction, which determines how the local filament velocity depends on the polarity of the surrounding network. This force propagation mechanism implies that the polarity-independent sliding observed in Xenopus egg extracts, and in vitro experiments with purified components, is a consequence of a large force propagation length. We suggest how our predictions can be tested by tangible in vitro experiments whose feasibility is assessed with the help of simulations and an accompanying theoretical analysis.

Living cells have the remarkable ability to actively change their shape, and to generate forces and motion. A key component enabling cells to exhibit these stunning mechanical properties is the cytoskeleton. This structure is built out of various proteins and forms diverse functional networks consisting of polymer filaments such as actin and microtubules, motor proteins, and associated proteins [6, 9]. The motor proteins expend chemical energy to generate forces that act on the cytosceletal filaments [34, 190, 191]. In particular, motors that have two binding domains, e.g. kinesin-5, can walk along two filaments at once, causing filaments of opposite polarity to slide past one another [95].

To understand the non-equilibrium physics underlying the dynamics of motor–filament systems, it has proven fruitful to study reconstituted systems of purified components *in vitro* [38, 74, 75, 205]. Despite their reduced complexity, these systems still self-organize into intricate patterns and structures reminiscent of those found in living cells. But how is their collective behavior at the macroscopic level linked to the interactions between individual filaments and motors? What are the underlying mechanisms? To provide an answer, we focus here on a generic class of systems in which filaments exhibit nematic order and motors drive relative sliding of filaments. A prominent representative of this class is the poleward flux of microtubules in Xenopus mitotic spindles [97, 234, 270]. This process has been attributed to antiparallel, motor-driven interactions between filaments, especially if the motor protein dynein is inhibited [19, 96, 234]. A quite puzzling observation made in these systems was the correlation — or rather, the lack of correlation — between filament speed and network polarity, i.e. the ratio of parallel to antiparallel filaments. Although filament motion is induced by sliding antiparallel filaments past each other, polarity was observed to have barely any influence on the filament speed [96, 184, 271]. This surprising behavior was recently replicated in a system of purified components composed of the kinesin-14 XCTK2 and microtubules, and interpreted in terms of a hydrodynamic theory for heavily crosslinked filament networks [99]. These observations are at variance with previous predictions for dilute filament networks, where filament motion depends linearly on the local polarity [206, 250, 272]. How can these conflicting results be reconciled? What are the biophysical mechanisms determining the relation between filament speed and network polarity?

To gain insight into these important questions we study a minimal but generic model consisting of nematically ordered cytoskeletal filaments (like microtubules) and molecular motors (like

kinesin-5) that are capable of crosslinking and sliding antiparallel filaments apart. Our mathematical analysis of this theoretical model shows that the interplay between motor-induced forces and viscous drag acting on the filaments determines the relation between filament velocity and the polarity of filaments. Depending on the relative strengths of these forces, we find that the velocity–polarity relation varies continuously between a local and a global law. Our theory reveals the mechanism that underlies this relation between filament velocity and network polarity: For high motor-induced forces and small fluid drag, local forces on the filaments propagate through the strongly interconnected network without dissipation and thereby influence the overall network dynamics. In contrast, for small motor–induced forces or high fluid drag, local forces are quickly damped and only influence the local dynamics. This mechanism provides a deeper understanding of the link between collective filament dynamics and molecular interactions. Moreover, it reconciles previously conflicting results for the velocity-polarity relation in the limit of dilute [206, 250, 272] and heavily crosslinked systems [96, 99, 273]. Strikingly, our theoretical analysis shows that the insensitivity of filament velocities to changes in the network polarity, which was reported for the spindle [96, 271] and *in vitro* systems [99], occurs in a biologically relevant parameter range. In addition our theory predicts how the ratio between the spectrum of measured polarities and filament speeds depends on the ratio of drag to motor-induced forces in the system. We suggest an *in-vitro* experiment to validate those predictions. The feasibility of this experiment is assessed with the help of computer simulations and an accompanying theory.

BIOPHYSICAL AGENT-BASED MODEL OF MOTOR-INDUCED FILAMENT MOVEMENT

We are interested in understanding how the interplay between viscous drag and molecular forces between cytoskeletal filaments, mediated by molecular motors, drives the internal dynamics of filament networks. Specifically, we focus on reconstituted *in vitro* systems consisting of microtubules and motors capable of crosslinking neighboring filaments and sliding them apart, c.f. Fig. 3.20 A, B. Such motor proteins can walk on both filaments simultaneously, so that the forces generated between filaments depend on their relative orientation (Fig. 3.20 A). *In vitro* such microtubule-motor mixtures were observed to self-organize into a nematic network, where neighboring filaments may be disposed approximately parallel or antiparallel [99].

Motivated by the nematic order of these filament networks, we set up a biophysical agent-based model, which is effectively one-dimensional. We consider a system of size S where the filaments (microtubules) are assumed to be rigid polar rods of fixed length L, oriented with their plus end either to the left (+) or right (−); see Fig. 3.20 C. Hence, the dynamics of each polar filament i is determined (solely) by its velocity $v_i^{(\pm)}$. Relative motion between filaments is caused by molecular motors that walk on these crosslinked filaments and thereby exert forces. In-vitro assays involving pairs of isolated microtubules cross-linked by kinesin-5 motors reveal that: (a) Kinesin-5 has the ability to walk simultaneously on both microtubules with approximately the zero-load velocity V_m, (b) antiparallel microtubules are pushed apart with a relative velocity of $\sim 2V_\mathrm{m}$, and (c) parallel microtubules remain static [95]. Integrating this information with experiments showing a linear force-velocity relation for kinesin motors [274–277], we assume that the forces between two crosslinked parallel ($\pm\pm$) and antiparallel ($\pm\mp$) filaments per motor are given by

$$F_{ij}^{(\pm\pm)} = F_\mathrm{m}\left(\frac{v_j^{(\pm)} - v_i^{(\pm)}}{2\,V_\mathrm{m}}\right), \qquad F_{ij}^{(+-)} = -F_{ji}^{(-+)} = F_\mathrm{m}\left(1 + \frac{v_j^{(-)} - v_i^{(+)}}{2\,V_\mathrm{m}}\right). \tag{3.104}$$

Here F_{ij} denotes the force that filament j exerts on filament i, with F_m signifying the motor stall force; due to force balance $F_{ij} = -F_{ji}$. These forces vanish if the relative motion of the filaments does not induce strain in the crosslinking motors. While for parallel filaments this is the case if the filaments move at the same speed, a motor walking on antiparallel filaments is not strained if these

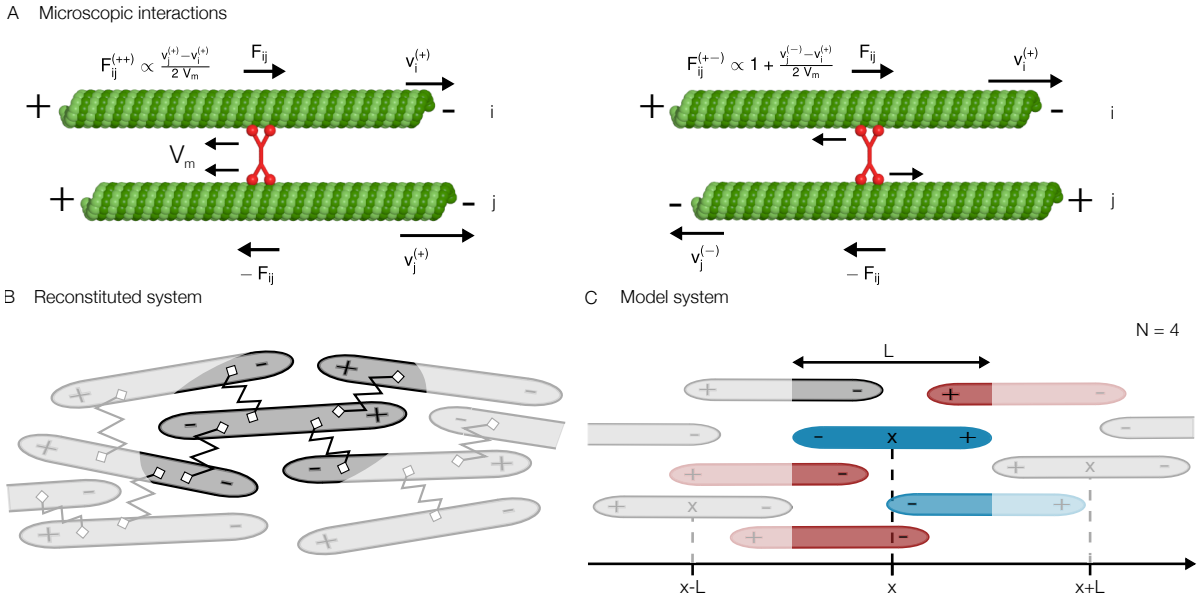

Figure 3.20: Biophysical model for motor-driven filament motion. (**A**) Microscopic, motor-mediated interactions between microtubules. Neighboring microtubules are connected by motors (red) which walk towards the microtubule's (green) plus end with velocity V_m. A motor exerts zero force if filament motion is such that the motor is not stretched. (**A -left**) A motor connecting two parallel microtubules counteracts relative motion between the filaments. (**A -right**) In contrast, two antiparallel microtubules connected by a motor are slid apart. The force falls to zero once their relative velocity equals twice the motor velocity ($-2\ V_m$). (**B**) Sketch of a microtubule-motor mixture in a nematically aligned state. The springs denote motors crosslinking neighboring filaments. The highlighted region includes all interactions of the center microtubule. (**C**) The one-dimensional model system. Possible interaction partners of the microtubule in the center (dark blue) are in the highlighted region. To account for the reduced number of interaction partners in the experimental filament network, we draw on average N out of all possible partners to interact (interaction partners are highlighted in color, parallel interaction partners in light blue and antiparallel interaction partners in light red).

slide apart with relative velocity $2V_\mathrm{m}$, i.e. $v_i^{(+)} - v_j^{(-)} = 2V_\mathrm{m}$. On the other hand, the maximal force between two filaments corresponds to the stall force, F_m, which is defined as the force between two antiparallel filaments fixed at their relative position ($v_i^{(-)} = v_j^{(+)}$). In that case the motor heads move apart until the motor stalls and exerts its maximal force on the filaments. An analogous situation occurs if a motor is attached to two parallel filaments which move with a relative speed $v_j^{(\pm)} - v_i^{(\pm)} = 2\,V_\mathrm{m}$. So the corresponding force is also F_m.

The velocity $v_i^{(\pm)}$ of a specific microtubule i in the network is determined by the force balance equation

$$\gamma v_i^{(\pm)} = \sum_j n_{ij}\, F_{ij}^{(\pm\pm)} + \sum_k n_{ik}\, F_{ik}^{(\pm\mp)}\,, \tag{3.105}$$

where γ denotes the fluid drag coefficient and n_{ij} the number of motors crosslinking microtubule i and j. The sums run over all parallel and antiparallel interaction partners of microtubule i, respectively. In general, the number of interaction partners as well as the strength of their interaction can depend on a variety of factors. For example, the interactions are influenced by the density of motors in the cytosolic volume as well as along the filament, or the local structure of the filament network. Inclusion of all these factors would lead to a microscopic description with many unknown parameters. Focusing on the mechanistic basis of filament motion here, we make the following two assumptions (c.f. Fig. 3.20 C): First, we consider a homogeneous motor density in the cytosolic volume and along the microtubules. Thus, we describe motors effectively by a constant density, with on average N_m motors per filament. Second, we assume that all filaments have on average N interaction partners that are drawn randomly. This on average accounts for the limited number of neighbors in the three-dimensional network structure.

A LOCAL MEAN-FIELD APPROXIMATION PREDICTS STRONG VELOCITY-POLARITY SENSITIVITY

To gain initial insight into the dynamics of microtubules, we simplify the system even further using a local, continuum mean-field approximation that neglects any lateral displacement between crosslinked filaments. In the continuum description, each microtubule i is identified by its midpoint position x_i. As a crude simplification, we assume that all crosslinked, equally oriented filaments passing through position x move at (roughly) the same velocity $v^{(\pm)}(x)$. This entails that the forces between all parallel filaments, $F^{(\pm\pm)}(x)$, vanish. Denoting the fraction of filaments at position x oriented in $(\pm)$ direction by $\varphi^{(\pm)}(x)$, Eq. 3.105 then simplifies to $\gamma v^{(+)}(x) = N_\mathrm{m}\varphi^{(-)}(x)F^{(+-)}(x)$ and $\gamma v^{-}(x) = N_\mathrm{m}\varphi^{(+)}(x)F^{(-+)}(x)$ with N_m denoting the number of motors per filament as above. Inserting the force velocity equation, Eq. 3.104, and solving for the velocity yields $v^{(+)}(x) \propto 1 - P(x)$ and $v^{(-)}(x) \propto 1 + P(x)$, where we defined $P(x) = \varphi^{(+)}(x) - \varphi^{(-)}(x)$ as the local network polarity at position x. Hence, the central result of this local mean-field analysis, which will ultimately turn out to be oversimplified, is a linear dependence of the local velocities on the local polarity. This result corresponds to the intuition that forces between filaments — and their relative motions — strongly depends on their relative orientation. In particular, while antiparallel interactions between two filaments introduce motion of both filaments, parallel filaments remain static. As a consequence, filaments with a higher number of antiparallel interactions are expected to exhibit an enhanced speed. However, as we will see next, this intuition is in conflict with numerical simulations (in the biologically relevant parameter regime) as well as with experimental findings for heavily crosslinked filament gels [99].

THE AGENT-BASED MODEL CAN DESCRIBE THE WEAK VELOCITY-POLARITY SENSITIVITY

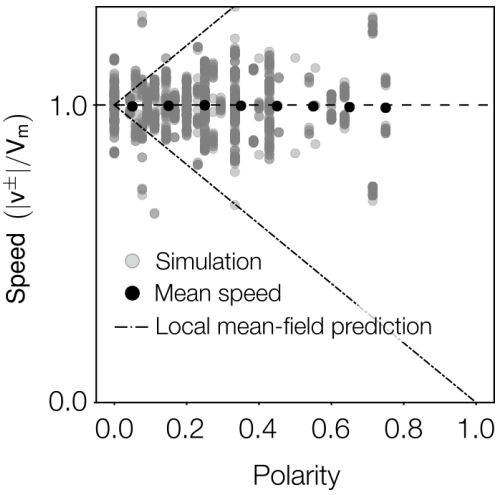

Figure 3.21: Local microtubule speed vs. local polarity obtained by numerically solving the full set of coupled linear equations (Eq. 3.105) for a one-dimensional microtubule network. The microtubule network is generated as described in section 3.3.2. Gray dots represent individual measurements, black dots show the average speed binned for local polarities (bin size $\Delta P = 0.1$). In contrast to the oversimplified discussion (dashed - dotted lines), the velocity does not depend linearly on the local polarity. Instead, the average speed is mostly independent of the local polarity. Note that the vertical stripes are artefacts arising from the discrete nature of the agent-based simulation: Due to the finite number of filaments in an interval $[x, x+\Delta x]$ the polarity can only take on discrete values.

To test whether our model is capable of describing the observations in heavily crosslinked filament networks, we solved the full set of coupled linear equations (Eq. 3.105) for a one-dimensional network numerically.

In order to compare our results to experimental data, we assessed the model parameters as follows: First, we determined the mean number of interaction partners per filament. The typical maximal distance between two microtubules connected by a sliding motor is estimated to be of the order of the tail length of kinesin-5, $\sim 0.1 \mu m$, [34] plus two times the microtubule radius, $\sim 0.024\,\mu m$, [5]. Together with the typical microtubule length, estimated to be $\sim 6-7\,\mu m$, these values yield an interaction volume of approximately $1/3\,\mu m^3$. Fürthauer and collaborators argue that the number density of filaments in their experimental setup is approximately $17/\mu m^3$ [99]. So, all in all, we estimate that there are $N \approx 5.5$ interaction partners per filament. In an analogous manner, we assessed the number of microtubules in our one-dimensional representation of the experimental chamber of length $400\,\mu m$ to be ~ 400. Those filaments are placed randomly as described below (3.3.2) and experience a drag coefficient of $\gamma = 0.5\,pN\,s/\mu m$ [278–280]. As motor parameters we use $V_m = 20\,nm/s$ [95], $F_m \sim 1\,pN$ [34] and $N_m = 25$ as the average number of motors per filament [99]. Using these parameters we performed numerical simulations, and found good agreement with experimental results (compare Fig. 3.21 and Fig. 2 in Ref. [99]). In particular, the average filament speed (filled black circles in Fig. 3.21) is found to be independent of the local polarity. This clearly contradicts the local mean-field theory as discussed above (see section "3.3.2"). To assess why this simplified local view is misleading, we next give a comprehensive mathematical analysis of the full agent-based model.

NON-LOCAL CONTINUUM THEORY

It is evident that in the simplified local mean-field analysis discussed above we neglected the finite extension of filaments. Actually, two filaments which pass through the same location do not necessarily have the same midpoint position. While they share some overlap, they will interact with different neighbors at different positions. If all filaments have the same length L, a filament with midpoint at position x can interact with filaments whose midpoints lie in the interval $[x-L, x+L]$ (cf. Fig 3.20 C). In this way, the velocities of filaments located at different spatial positions are coupled, leading to non-local correlation effects that could explain the weak dependence of filament speed on local polarity.

Motivated by this heuristic argument, we set out to formulate a continuum theory that quantifies the non-local coupling between the filament velocities ($v^{\pm}(x)$) and densities ($\rho^{(\pm)}(x)$). To this end,

we rewrote the local balance equation, Eq. 3.105, assuming a continuum limit.

$$\gamma\, v^{(\pm)}(x) = \frac{1}{L}\int_{x-L}^{x+L} \mathrm{d}y\, \left\{ f^{(\pm\pm)}_{\text{parallel}}(x,y) + f^{(\pm\mp)}_{\text{antiparallel}}(x,y) \right\}, \tag{3.106}$$

where the local forces are given by

$$f^{(\pm\pm)}_{\text{parallel}}(x,y) = \hat{N}_{\text{m}}(x,y)\cdot N\varphi^{(\pm)}(y)\cdot F^{(\pm\pm)}(x,y)\,, \tag{3.107a}$$

$$f^{(\pm\mp)}_{\text{antiparallel}}(x,y) = \hat{N}_{\text{m}}(x,y)\cdot N\varphi^{(\mp)}(y)\cdot F^{(\pm\mp)}(x,y)\,. \tag{3.107b}$$

Here, the force a motor exerts on the filaments it crosslinks is simply given by the continuum version of Eq. 3.104, e.g. $F^{(\pm\pm)}(x,y) = F_{\text{m}}\,[v^{(\pm)}(y) - v^{(\pm)}(x)]/(2\,V_{\text{m}})$. The second factor in Eq. 3.107 accounts for the expected number of interaction partners at position y, given by the number fraction of filaments with the respective polarity $\varphi^{(\pm)}(y)$ multiplied by the average number N of interaction partners: $N\varphi^{(\pm)}(y)$. For this functional form to apply, we implicitly assumed that the filament network is not sparse, i.e., that there is always a sufficient number of interaction partners, namely more than N, available. The number fraction can be written in terms of the filament densities as $\varphi^{(\pm)} = \rho^{(\pm)}/(\rho^{(+)} + \rho^{(-)})$. The first factor in Eq. 3.107, $\hat{N}_{\text{m}}(x,y)$, specifies the average number of motor proteins mediating the interaction between a pair of filaments located at positions x and y. This number is determined by the size of the overlapping region, $L_{\text{ov}} = L - |x-y|$, and the number of motors per filament, N_{m}. Since all the available motors on a filament have to be shared among all of its N interaction partners, only N_{m}/N are available for the interaction with any specific filament. Hence, assuming a uniform motor distribution along each microtubule, the effective number of motors crosslinking a filament pair is on average given by $\hat{N}_{\text{m}}(x,y) = N_{\text{m}}/N\cdot L_{\text{ov}}/L$.

Based on this non-local continuum representation of our agent-based model, we seek a quantitative understanding of how the opposing forces in the filament network give rise to collective (uniform) motion. Ultimately, our goal is to provide an explicit expression relating the polarity and velocity fields.

ANALYTIC SOLUTION FOR MOTOR-INDUCED FILAMENT MOVEMENT

In this section, we present an analytic solution to our non-local continuum description (Eq. 3.106). We restrict our analysis to the limit where the system size is large compared to the filament length L and to all other intrinsic length scales of the system we might encounter in the course of the mathematical analysis. Making use of complex calculus, in this limit it is possible to find an explicit expression for the velocity field $v^{(\pm)}(x)$ in terms of the polarity field $P(x)$. This expression, thus, constitutes a velocity-polarity relation which quantifies how the polarity field affects the velocities.

In an experimentally reasonable parameter regime one finds an approximate expression which reads (for a detailed analysis see SI):

$$v^{(\pm)}(x) = \pm V_{\text{m}}\,(1-\alpha)\,\big(1 \mp \Pi(x)\big)\,, \tag{3.108a}$$

$$\Pi(x) = \frac{1}{2\,l_c}\int_{-\infty}^{\infty} \mathrm{d}y\, \mathrm{e}^{-|x-y|/l_c}\, P(y)\,. \tag{3.108b}$$

where $1/\alpha := 1 + 12\,(l_c/L)^2$; for biologically plausible parameter values one has $\alpha \ll 1$. Importantly, Eq. 3.108a shows that the motion of filaments is neither solely dependent on the local polarity nor fully independent of the polarity field. Instead, the local filament velocities, $v^{(\pm)}(x)$, now depend in a non-local way on the polarity, $P(y)$, as specified by the convolution integral (weighted average), $\Pi(x)$, with an exponential kernel (weight) $\sim \mathrm{e}^{-|x-y|/l_c}$. To emphasize this non-local dependence of

the velocities on the polarity, we refer to $\Pi(x)$ as the *ambient polarity* in the following. The characteristic interaction range l_c, over which the polarity field is averaged, is given by

$$l_c = L\sqrt{\frac{F_\mathrm{m} N_\mathrm{m}}{24\gamma V_\mathrm{m}}}\,. \tag{3.109}$$

It is set by the ratio of the total average force exerted by motors on a microtubule, $F_\mathrm{m} N_\mathrm{m}$, to the drag imposed on the microtubule by the surrounding fluid, γV_m. Furthermore, it can be interpreted as the length scale over which motion generated by antiparallel filament sliding is propagated by parallel filament interactions through the network. As a result, the interaction range l_c reflects the antagonism between the combined effect of motion-generating forces (antiparallel interactions) and motion-propagating forces (parallel interactions), and the attenuation of force propagation in the filament network mediated by viscous drag. This antagonism is captured by the spatial average of the polarity field which effectively corresponds to a low-pass filter. Due to averaging over local polarities, high-frequency fluctuations in the spatial polarity profile are filtered out and, hence, do not contribute to the velocity. Explicitly, by Fourier transforming Eq. 3.108b we find a Lorentzian Fourier weight

$$\Pi_k = P_k\,\frac{1}{1+(kl_c)^2}\,, \tag{3.110}$$

where k denotes the wave number. Hence, the characteristic frequency of the low-pass filter is proportional to the reciprocal of the characteristic length, $1/l_c$, implying that the larger l_c the stronger the filter and the less relevant local fluctuations in the polarity. To put it another way, the speed of a filament at position x depends only on the local "view" of the polarity field within a range defined by l_c (Fig. 3.22).

To gain an impression of how the interplay between the different forces in the network leads to the non-local effects, it is helpful to consider the limiting cases of large and small l_c, respectively. For large l_c, motor forces dominate viscous drag ($F_\mathrm{m}N_\mathrm{m} \gg \gamma V_\mathrm{m}$). Then, either due to weak dissipation or strong motor-mediated filament coupling, parallel crosslinked filaments translate the motion, generated by interactions between antiparallel filaments, over long distances ($\sim l_c$). As a result, motion generated at one position in the network propagates through the entire network. In the asymptotic limit $l_c \to \infty$, the velocity-polarity relation (Eq. 3.108a) reduces to $v^{(\pm)} = \pm V_m$[1], confirming recently published findings for a heavily crosslinked network [99]. In contrast, for small l_c ($F_\mathrm{m}N_\mathrm{m} \ll \gamma V_\mathrm{m}$) force generated at a certain position in the network has only a local effect. Forces generated by antiparallel interactions cannot propagate through the network either due to strong dissipation or a lack of parallel filament interactions. In this limit, the velocity-polarity relation reduces to the result obtained with the local mean-field theory discussed in 3.3.2. This relation agrees with the velocity-polarity relation found for dilute filament networks where only local bundles of filaments are considered [250, 272] [2].

INTERPRETATION OF THE VELOCITY-POLARITY RELATION

With regard to previous results, our considerations offer a solution to the seemingly contradictory behavior of dilute and heavily crosslinked networks. More specifically, our results identify a common mechanism for collective filament dynamics: Due to the finite extension of the microtubules, one microtubule can be crosslinked with several others whose center positions are spread over a

[1] for zero overall polarity

[2] Care has to be taken when comparing our result to the dilute limit: We restricted our discussion to the case of sufficient number of interaction partners, whereas usually for dilute systems disconnected patches of filaments are considered. For a more comprehensive discussion on how our results are related to results for dilute systems we refer the reader to the SI.

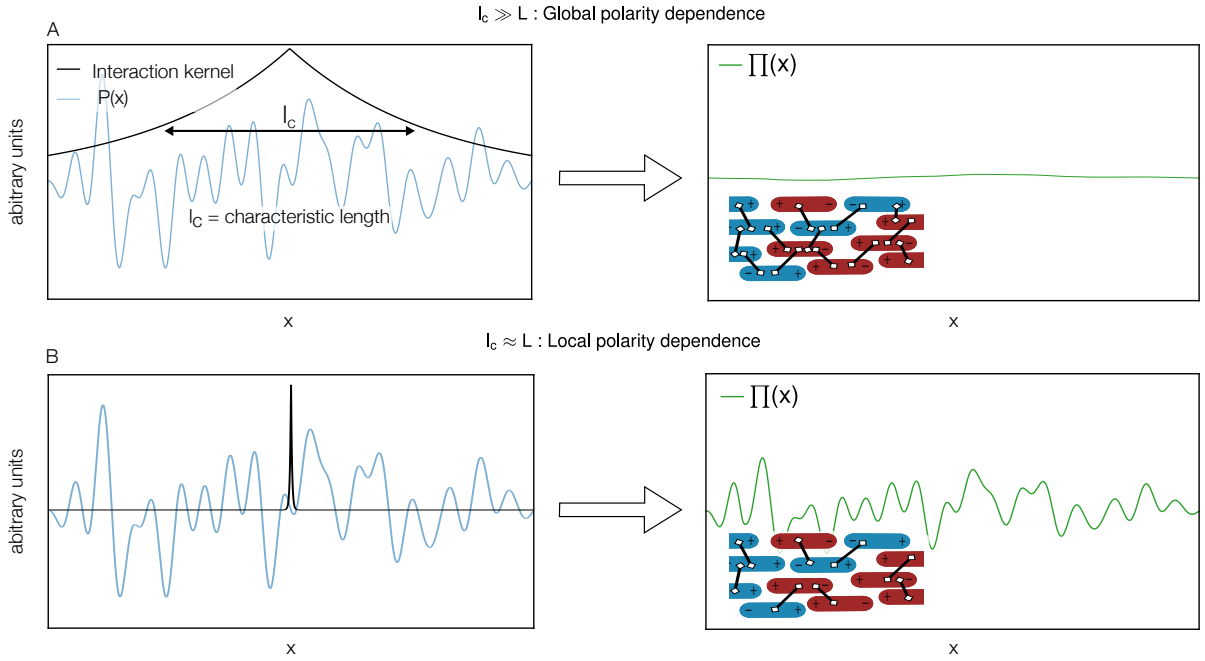

Figure 3.22: Typical polarity field, $P(x)$, and two choices of interaction kernel, $\exp(-|x-y|/l_c)$, characterizing global and local polarity dependence, respectively. Filaments positioned in a range of l_c around x contribute to the motion of microtubules at x. Depending on the ratio of average motor force exerted on a microtubule to attenuation (drag of microtubules in the fluid), the characteristic propagation length l_c takes different values. (**A**) For large l_c and polarity fields that vary randomly on length scales smaller than l_c, this averaging yields a roughly constant ambient polarity profile, $\Pi(x)$, and hence a roughly constant velocity profile. On a microscopic level, this corresponds to a heavily crosslinked filament network (inset). (**B**) In the limit of small l_c only the local environment, i.e., the direct interaction partners, has an influence on the microtubule motion. The ambient polarity field (velocity field) varies as the polarity field varies.

region up to twice the microtubule length (Fig. 3.20C). As a result, although microtubules at different positions might in fact not be directly linked by a motor, an interaction between them can be mediated by successive crosslinks through a chain of microtubules. In this way, the velocity of microtubules at one position influences the velocity at a different position and information on the local polarities propagates through the system. How far this information propagates (l_c) depends on how "effectively" movement at one position is translated into movement at a different position. The greater the efficiency, the smaller the ratio between the passive drag on microtubules in the fluid (and thus the attenuation) and the average maximal active force exerted on one microtubule by all motors linking it to other microtubules.

Taken together, our results shed light on the question of what determines the local speed of microtubules in a nematic network: Generally, it is neither the local polarity, $P(x)$, that determines the velocity of microtubules at a certain position nor the overall polarity in the system, P_{glob}. Instead the ambient polarity, $\Pi(x)$, is informative. The ambient polarity corresponds to an average of the polarity with a weight that decays exponentially with the distance from the position of interest (see Eq. 3.108b). The characteristic decay length, l_c, is proportional to the filament length L, and increases with the ratio of the motor-force on a microtubule, $F_m N_m$, to the fluid drag, γV_m. In general, for a finite decay length and a spatially varying polarity profile, the ambient polarity also varies in space. As can be inferred from Eq. 3.108b, for larger values of l_c, a larger region of space contributes to the ambient polarity (see also Fig. 3.22). Accordingly, the ambient polarity then corresponds to an average of the local polarity over more positions. As a result, for a fixed spatial polarity profile, the range of values of the ambient polarity decreases with increasing characteristic propagation length l_c. Due to the linear relationship between the velocities and the ambient polarity, Eq. 3.108a, the same holds true for the range of velocities.

In the following, we illustrate these predictions with the help of two examples. First, we consider a spatially linear polarity profile. Besides being an instructive case, this polarity profile is of biological relevance. It resembles the measured, approximately linear polarity profiles in the mitotic spindle (see 3.3.2). As a complement, the setup of the second example is designed to mimic typical *in vitro* experiments. In order to make testable predictions we analyze the suggested (idealized) experiment in detail and focus on quantities which we believe to be accessible in experiments.

A SIMPLE EXAMPLE: THE LINEAR POLARITY PROFILE

Our theory predicts that the range of velocities decreases with increasing characteristic propagation length, l_c. To demonstrate this correlation, we consider a linear polarity profile $P(x) = a\,(x - S/2)$ in a finite interval $x \in [0, S]$ (for details see SI). As motivated above, we describe the local polarity profile in terms of its Fourier coefficients $\hat{P}_k$. The wave numbers are now discrete, $k \in \mathbb{N}$, as the system is finite. The Fourier coefficients of the ambient polarity, $\hat{\Pi}_k$, are given by the Fourier coefficient of the local polarity, $\hat{P}_k$, times a k-dependent weighting factor: $\hat{\Pi}_k = \hat{P}_k / \left[1 + (2\pi k l_c/S)^2\right]$ (see SI). Correspondingly, the ratio between the range of the local polarity $2P_{\max} = aS$ and the range of the ambient polarity $2\Pi_{\max}$ can be approximated as (see SI)

$$\frac{\Pi_{\max}}{P_{\max}} \approx \frac{1}{1 + (\pi l_c/S)^2}. \tag{3.111}$$

This finding confirms the intuitive expectation that with increasing characteristic length l_c the ambient polarity range $2\Pi_{\max}$ (or analogously the velocity range $2\Pi_{\max} V_m(1-\alpha)$), should decrease relative to the local polarity range, $2P_{\max}$, and the spatial profile gets "squeezed" (Fig. 3.23). From the approximate expression, Eq. 3.111, we infer that for characteristic lengths of the same order as the system size, $l_c/S \sim \mathcal{O}(1)$, the range of the ambient polarity $2\Pi_{\max}$ is only a tenth of the range of the local polarity $2P_{\max}$. Due to the linear relationship between the velocity and ambient polarity, Eq. 3.108a, this small range of ambient polarities implies that also the velocity range for equally

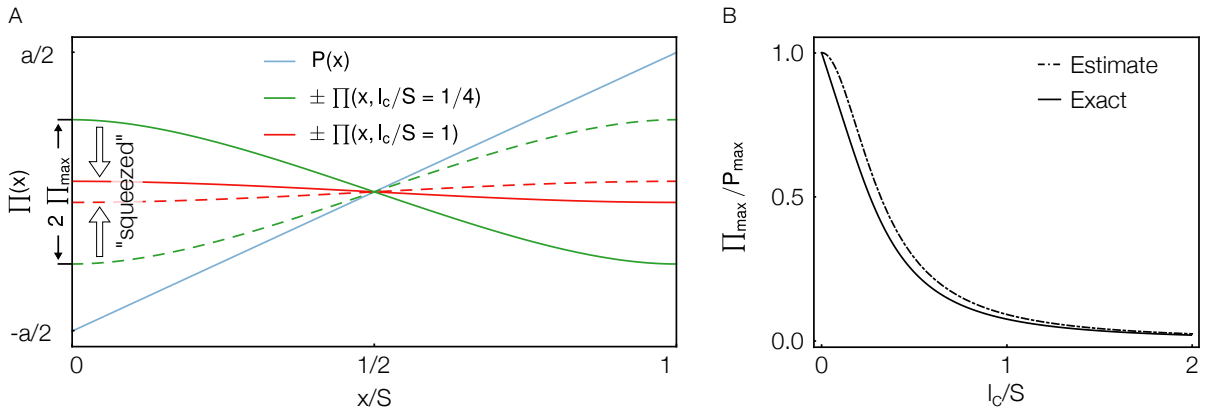

Figure 3.23: "Squeezing" of the ambient polarity in a finite system with reflecting boundary conditions. (**A**) Sketch of the linear spatial polarity profile, $P(x) = a\ (x - S/2)$, $x \in [0, S]$, together with the ambient polarity profile, $\Pi(x, l_c)$, for two different values of the characteristic length l_c/S (normalized by the system size S). The solid and dashed lines indicate the solutions relevant for (+) and (−) filaments, respectively. For larger l_c, the range of the ambient polarity, $2\Pi_{\max}$, becomes more restricted. (**B**) Ratio between the range of the ambient polarity $2\Pi_{\max}$ and the range of the local polarity $2P_{\max} = aS$ plotted against l_c/S. The curve is well approximated by a Lorentzian decay $1/(1 + (\pi l_c/S)^2)$ (estimate). For the exact expression, please refer to the SI. For larger l_c/S, the range of the ambient polarity relative to that of the local polarity falls off rapidly.

oriented microtubules is small. As a result, for $l_c \geq S$, all equally oriented microtubules move as a collective with approximately uniform velocity. In particular, there is also movement in regions where locally the polarity is $P(x) = \pm 1$, corresponding to stretches populated only by parallel microtubules.

For *in vitro* experiments with filament gels or reconstituted systems, it might not be feasible to get information on the entire spatial polarity and velocity fields. Instead, in typical experiments the local polarity and velocity are recorded only at single points in the filament gel [99, 184, 217]. Data obtained in this way is similar to that shown in Fig. 3.21 where one data point corresponds to a polarity-velocity pair measured at one location in the gel. In the next section, we thus perform an *in silico* experiment where we make single velocity and polarity measurements only and do not measure the entire spatial fields. Nevertheless, the key idea motivating the setup of the *in silico* experiment is the expectation that the spectrum of measured velocities is squeezed compared to the spectrum of local polarities: Due to the filtering of short-wavelength modes, extreme values of the local polarity are averaged out and the velocity profile is smoother than the local polarity profile. In the following, we thus focus on deriving a relation between the measured distribution of local polarities and velocities.

IN SILICO STUDY: RANDOM POLARITY FIELD

The goal of this section is to suggest an experimental setup that should permit the antagonism between the different forces in the system due to drag and motor-mediated interactions to be explored. To this end, we performed an *in silico* experiment intended to closely emulate the situation in experiments with *in vitro* filament gels. Photo-bleaching experiments have proven to be a feasible option to simultaneously determine sliding velocities and local gel polarity in filament gels [99, 184, 217]. In these experiments, the fluorescently labelled microtubules in the gel are photo-bleached along a line by laser light. Due to the motion of the filaments in the gel, the bleached line splits into two lines that move to the right (left) and correspond to left-oriented (right-oriented) microtubules, respectively. From the motion of the two lines, the local velocity and the local polarity can

be inferred simultaneously: The local velocity of the left-oriented (right-oriented) microtubules is directly obtained from the velocity of the respective line. Furthermore, the local polarity is determined from the ratio of the bleach intensities of the two lines. The data so obtained only contains local information about the velocity and polarity but no spatially resolved information. In order to make experimentally testable predictions, our goal is, therefore, to derive a relationship between the distribution of measured local polarities and the distribution of measured velocities for which spatial resolution is not necessary.

Setup of the *in silico* experiment: To illustrate how a given polarity distribution affects the velocity distribution, we consider a specific example, namely a polarity "environment" resulting from random filament assemblies; for details please refer to the SI. We assume that the filament network is nematically ordered and filaments are randomly oriented to the left or to the right, and therefore neglect the possibility that in the experimental system the spontaneous self-organization into the nematic state might involve some polarity sorting. More specifically, filaments are randomly placed in a chamber of size $S \gg L$ with periodic boundary conditions. Since for random filament assemblies there is no reason why the average number of left- and right-pointing filaments should differ, we choose the number density for both left- and right-pointing microtubules to be identical: $\mu^{(+)} = \mu^{(-)} = \mu$. Importantly, due to the finite extension of the microtubules, the polarity at different positions is not independent. Instead, one finds a positive covariance for the polarities at distances less than one microtubule length L apart (see SI). As a result, the polarity profile is not completely random but correlated on lengths smaller than the microtubule length L (for a typical profile please refer to the SI).

Signature of the ambient polarity in the velocity distribution: Based on our theoretical understanding, we expect that, depending on the characteristic length l_c, the distribution of velocities is squeezed compared to the polarity distribution. This is because, depending on the ratio of the antagonistic forces, filament motion arises from averaging the polarity over longer (large l_c) or shorter (small l_c) distances. As we expect the degree of averaging to be reflected in the distribution of velocities, the standard deviation of the microtubule velocities should be an interesting quantity to look at in experiments.

In order to predict the variance of the velocities (ambient polarities) analytically, we describe the local polarity field resulting from the random placement and orientation of filaments in the "experimental" chamber by a set of correlated random variables (see SI). Using their correlation structure, we average the local polarity according to the expression for the ambient polarity (Eq. 3.108b) and find (see SI)

$$\frac{\mathrm{Var}[v/V_m]}{\mathrm{Var}[P]} = (1-\alpha)^2 \left[1 - \frac{3l_c}{2L}\left(1 - \mathrm{e}^{-L/l_c}\right) + \frac{1}{2}\mathrm{e}^{-L/l_c}\right]. \tag{3.112}$$

Here, $\mathrm{Var}[P] = \mathrm{Var}[P(x)] = \langle P(x)^2\rangle - \langle P(x)\rangle^2$ denotes the variance of the local polarity, and $\mathrm{Var}[v/V_m] = \mathrm{Var}[v(x)/V_m]$ the variance of the (normalized) velocity v/V_m measured in units of the motor velocity. The above equation implies that the variance of the normalized velocity can be considerably smaller than the variance of the spatial polarity profile; see Fig. 3.24B. The ratio between the two only depends on the characteristic length l_c/L and quickly decays with respect to it. For larger l_c/L, the ambient polarity corresponds to an average over a larger region in space. Therefore, its variance decreases. Due to the linear relationship between the velocity and the ambient polarity, the variance of the velocity decreases to an equal extent.

In order to compare our results to *in vitro* experiments we assessed the values for both the one-dimensional number density of filaments 2μ and the characteristic length l_c. From recent experimental data [99], we estimated $2\mu = 6$ and $l_c/L \approx 10$; see also Section 3.3.2. Given these estimates,

our theory yields a standard deviation of the polarity distribution $\sigma[P] = \sqrt{\mathrm{Var}[P]} \approx 0.46$, corresponding to a broad range of observable polarities similar to what is seen in experiments. Using our theoretical results we predict the ratio between the standard deviations of the local polarity and the normalized velocity to be approximately $\sigma[P]/\sigma[v/V_m] = \sqrt{\mathrm{Var}[P]/\mathrm{Var}[v/V_m]} \approx 6.3$. Thus, we expect the mismatch between the widths of the two distributions to be clearly visible in experiments.

Polarity and velocity distribution in the *in silico* experiment: Figure 3.24A shows a comparison of the distribution of the local polarity and velocity, as measured in the *in silico* experiment (density plot and histograms) and as predicted analytically (black lines). The density plot shows the measured probability distribution for all combinations of local polarity and velocity. The histograms for both quantities were obtained as projections of the density plot onto the respective axis. While the local polarity takes values in a broad range between ±1 (histogram at top of Fig. 3.24A), the distribution of the velocity is squeezed to values of approximately $(1 \pm 0.2)V_m$ (histogram at right of Fig. 3.24A).

The disparity between the two distributions nicely illustrates the filtering of high-frequency modes

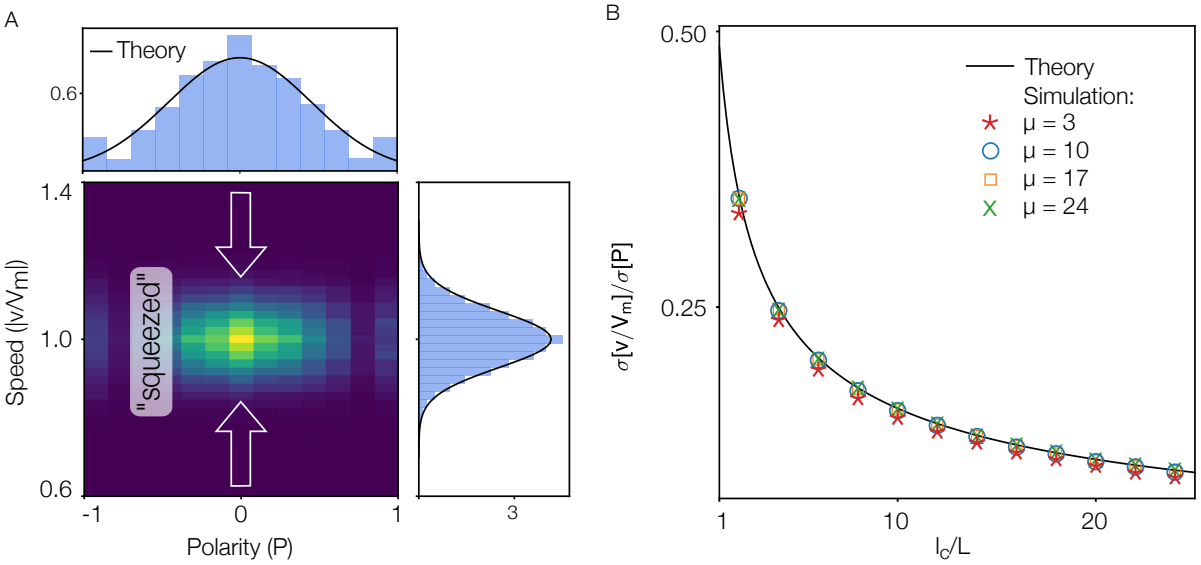

Figure 3.24: Results for the *in silico* experiment. (**A**) Density plot displaying the probability distribution for all combinations of local polarity, $P(x)$, and speed, $|v(x)/V_m|$, as measured in the *in silico* experiment described in section 3.3.2. The histograms at the top and on the right are projections of the density plot on the respective axis. In both cases, the solid line is the corresponding analytic prediction that was obtained by approximating the distributions by a normal distribution with the respective predicted mean and variance. In comparison to the local polarity (top), the velocity distribution (right) is less broad, i.e., it exhibits a smaller but non-zero standard deviation. The parameters are chosen to match the stochastic agent-based simulation described in section 3.3.2, namely $\mu = 3$ and $l_c/L = 10$. (**B**) Ratio between the standard deviations of the normalized velocity, $\sigma[v/V_m]$, and of the local polarity, $\sigma[P]$, plotted against normalized characteristic length, l_c/L. The results of the *in silico* experiments (symbols) for $\mu = \{3, 10, 17, 24\}$ (red stars, blue circles, yellow squares, green crosses) collapse onto one master curve. The solid line corresponds to the analytic prediction of the master curve. For larger characteristic length, the standard deviation of the velocity decreases relative to the standard deviation of the local polarity. Note that for small $\mu = 3$, there is a slight deviation from the master curve. In this case, the variance of the local polarity is so high that the corresponding, approximate normal distribution has not decayed to zero at $P = \pm 1$ (see histogram at top of A).

discussed in the section 3.3.2. This filtering is due to long-range interactions induced by the averaging of the polarity field over a length l_c. Since the filtering strongly depends on the characteristic length l_c, the ratio between the standard deviations of the local polarity and velocity distributions, $\sigma[P]/\sigma[v/V_m]$, decreases as l_c increases (Fig. 3.24B). It would be interesting to test this prediction experimentally by changing, for instance, the concentration of the molecular motors, or the drag in the fluid.

Figure 3.24B shows how the standard deviation of the velocity distribution, normalized to the standard deviation of the local polarity distribution, depends on the characteristic length l_c. For small $l_c \sim L$, the effective interaction range of microtubules l_c is small and the microtubule dynamics is predominantly determined by the local polarity at their respective position. Conversely, in the limit of large l_c, the dynamics of all microtubules is determined by the same average global polarity. Consequently, all microtubules then exhibit the same velocity and the standard deviation of the velocity $\sigma[v/V_m]$ decays to zero. Notably, the normalized curves for different values of the microtubule density, μ, collapse onto one master curve when plotted against l_c/L (see SI). Thus, in our thought experiment, where we make a certain assumption with regard to the spatial polarity profile, knowledge of the microtubule density is not necessary.

Experimental relevance In an experimental filament gel other factors also influence filament dynamics. For instance, as molecular motors randomly attach and detach from microtubules, even microtubules at the same position can interact with a different set of microtubules and thus experience different environments. As a result, different microtubules at the same position might actually have a (slightly) different velocity. Correspondingly, for two experimental realizations with an identical polarity profile, the respective average filament speeds at one position x might indeed differ. This effect is not captured by our continuum description, which assumes deterministic velocity profiles $v^{(\pm)}(x)$. Thus, we expect a broader distribution of velocities for *in vitro* measurements compared to our theoretical prediction. To gauge the strength of this effect, we compared our theoretical predictions with the results from stochastic agent-based simulations of the system (for details see SI). We find that the specific value of the width of the velocity distribution depends on details of the velocity measurement in the experiments. Nevertheless, irrespective of these details, the velocity distribution is significantly smaller than the width of the polarity distribution.

The *in silico* experiment considered here clearly simulates an idealized system insofar as we have assumed that there is no overall spatial structure. The analysis can be readily extended to a broader class of systems, in which knowledge of the covariance structure of the polarity field ($\mathrm{Cov}[P](x,y)$) is sufficient to predict the covariance structure of the velocity field ($\mathrm{Cov}[v/V_m](x,y)$) (see SI). Since this signature of our results is strongly dependent on the characteristic length, l_c, we expect such measurements to provide insight into network parameters. Actually, even low-resolution information on the spatial variation of the polarity field could be helpful to test our predictions. As we have seen above, the Fourier coefficients are suppressed by $1/(1+(2\pi l_c k/S)^2)$, $k \in \mathbb{Z}$, in a finite system of size S (or, equivalently, by $1/(1+(l_c k)^2)$, $k \in \mathbb{R}$, in the infinite system). So, for large l_c, the velocity modes with wave vector $k \geq 1/l_c$ should not be visible in experiments.

DISCUSSION AND CONCLUSION

In this work, we have considered a mesoscopic model for microtubule dynamics in a nematic, motor-crosslinked network. So far, research has focused on either the dilute or heavily crosslinked limit. Strikingly, the observed behavior in these two cases is qualitatively different: While in the dilute case the microtubule velocities strongly depend on the local network polarity [250, 272], in the heavily crosslinked case the velocity has been found to be independent of the polarity [96, 99, 271]). These distinct phenomenologies are puzzling, as the underlying microscopic motor-mediated mi-

crotubule interactions are presumably the same in both cases. Starting from these filament interactions, we have shown how the interplay between movement resulting from motor-crosslinking and the countervailing effects of fluid drag determines the sensitivity of the local filament dynamics to the network polarity. Thereby we provide a better understanding of the essential physical principles that lead to such diverse dynamics.

To this end, we derived a non-local mean-field theory of our system from the microscopic interactions. This theory enabled us to obtain an explicit analytic expression relating the local microtubule velocity to the spatial polarity profile. Our key result is that the local velocity depends on the local *ambient polarity*, which is given by the averaged polarity a microtubule senses in its environment. More specifically, the local velocity is given by the convolution of the polarity and an exponentially decaying interaction kernel with *characteristic propagation length*, l_c. Hence, it is not the local polarity at the position of a microtubule that determines its motion but rather the entire polarity profile in an environment of length l_c. This finding implies that a one-to-one mapping between the local velocities of microtubules and the local polarity as shown in Fig. 3.21 is not the whole story. Instead, in order to predict the velocity at a specific location, knowledge of the spatially varying polarity profile in the entire vicinity is needed. In general, such detailed spatial information appears to be inaccessible with current experimental techniques. Fortunately, in order to infer the distribution of velocities from the distribution of local polarities, such detailed information is not essential. For example, in a gel where microtubules are randomly placed in an experimental chamber and stochastically oriented, our theory predicts how the variances of the local polarity and of the velocity are related.

The relationship between the velocity and polarity distributions strongly depends on the characteristic propagation length l_c, which is an important emerging length scale in the system. It can be interpreted as a non-local interaction range of filaments, and is determined by the ratio between the average motor-driven force on a microtubule and the microtubule's drag in the fluid. Thus, this intrinsic length reflects how effectively motion generated at one position is propagated through the interconnected network of filaments. It strongly depends on the network properties.

We have identified a common mechanism explaining the microscopic origin of both uniform filament motion in percolated nematic networks and the strong polarity dependence of microtubule motion in dilute systems: Due to their finite extension, microtubules directly interact with several parallel and antiparallel neighbors within a spatial ranges equal to twice their filament length. Motors between parallel microtubules induce a resistance against relative motion and thus promote uniform motion of crosslinked microtubules. Thereby, motion generated by antiparallel interactions translates through the percolated network of microtubules even into regions with only parallel and no antiparallel interactions where *a priori* no motion is expected. The degree of efficiency of this propagation of motion is quantified by the characteristic propagation length l_c. Hence, it is influenced by the average number of motors per interaction and the drag of filaments in the fluid, among other factors. Filaments at distances larger than l_c apart can be considered to be part of disconnected patches. That is, for small l_c only motor-crosslinks between nearest neighbor filaments are relevant for filament motion, as in the dilute limit. For this case, we recover the linear relationship between local polarity and filament velocity [206, 250, 272]. On the other hand, in the limit of large l_c, which corresponds to systems where the patch size exceeds the system size, we find a dependence of the velocity on the global polarity only. Here, the velocity for equally oriented microtubules is the same everywhere in space. In particular, our results explain the weak sensitivity of the filament velocities to the local polarity observed in recent experiments [99] and in the spindle apparatus [96, 234, 271].

In particular we predict a strong dependency of the velocity distribution on the characteristic propagation length. In order to test this prediction, we suggest a practicable *in vitro* experiment

whose feasibility we assessed with the help of an *in silico* experiment intended to mimic the suggested *in vitro* experiment. Intriguingly, it is not necessary to determine the entire spatial polarity and velocity profile to check the validity of our theory. Instead, it suffices to determine the polarity and velocity distributions by measuring the local velocity and polarity at random positions in the filament gel. When plotting the ratio of the standard deviations of the polarity and velocity distribution against the characteristic length l_c, we expect the data to collapse onto a master curve, irrespective of the explicit number of filaments in the experimental chamber (Fig. 3.24). Furthermore, the ratio of the standard deviations of the polarity and velocity distributions for a specific experimental setup could be used to identify the characteristic propagation length l_c and, allow one to draw conclusions regarding network features (Eq. 3.109).

Microtubule motion in mitotic spindles formed in Xenopus egg extract is a prominent example for polarity-independent sliding. The polarity profile in these spindles is approximately linear, ranging from zero polarity in the center to highly polar regions at the spindle poles [184]. Nonetheless, microtubules drift with roughly constant velocity towards the spindle poles, especially if dynein is inhibited. Our theory can account for this behavior. In particular, the individual velocities deviate only slightly from the mean velocity if motor-crosslinking is strong, i.e. if the characteristic length exceeds the system size (see Sec. 3.3.2). Interestingly, for biologically plausible parameters the interaction range is of the same order as the length of the spindles formed in Xenopus egg extracts, $l_c \propto 30-80\ \mu m$. Correspondingly, as seen in Fig. 3.23(A), the velocity of the poleward moving microtubules is expected to be slightly smaller close to the pole than in the center of the spindle. This variation is due to the dependence of the velocity on the ambient polarity (the local polarity environment). Taken together, our results suggest that, depending on the value of the characteristic length compared to the spindle size, the spatial polarity profile and, in particular, the fact that the poles are highly polar, could be significant for the velocity profile as well. To examine this behavior experimentally, it would be instructive to investigate the velocity distribution of microtubules in a dynein-depleted, unfocused spindle as a function of the distance from the spindle boundary.

From a broader perspective, it would be interesting to extend our work on nematic networks to a more general description of filament gels. To this end, it could be promising to start from recent work on heavily crosslinked filament gels, where a sophisticated hydrodynamic framework has been established from microscopic properties [99]. This theoretical framework assumes an infinitely large characteristic length l_c, so that motion generated at one position propagates through the whole network without loss. Our results suggest that incorporating an exponential interaction kernel into this framework can provide a more comprehensive description of filament motion in crosslinked gels. Such a description would also offer the chance to understand the transition from heavily crosslinked to weakly coupled gels.

3.4. CONNECTIVITY TUNES FILAMENT VELOCITY IN FILAMENT-MOTOR MIXTURES

3.4.1. SIGNIFICANCE

Cytoskeletal filament assemblies form a diverse range of dynamic structures that play essential roles in many cellular processes, including cell division, cell motility, and intracellular transport. The variety of tasks performed by cytoskeletal filament assemblies makes it necessary that their size and shape vary enormously. How the interaction between filaments and their associated motor proteins occurs at the microscopic level to control the size and shape of these structures is not well understood. Previous studies have increased the awareness that an important factor that controls the large-scale physics of cytoskeletal filament assemblies is their cross-lining state. For example, it has been shown that the self-organization of the spindle is tied to the fact that its microtubules are highly connected.

Here, we address the question of how the degree of filament connectivity controls filament velocities in the system. To this end, we study a *in vitro* system composed of cross-lining motors, passive cross-linkers, and stabilized microtubules. On the basis of experimental observations and agent-based computer simulations, we derive a semi-analytical theory that shows how the local filament speed depends on the cross-linking state of the network.

3.4.2. MANUSCRIPT

This section is based on a manuscript in preparation

Connectivity tunes filament velocity in filament-motor mixtures

by
M. Striebel[1], **A. Sciortino**[2], **I. Maryshev**[1], **A. R. Bausch**[2] **and E. Frey**[1]
[1] Arnold Sommerfeld Center for Theoretical Physics and Center for NanoScience, Department of Physics, Ludwig-Maximilians-Universität München, Theresienstraße 37, D-80333 München, Germany
[2] Lehrstuhl für Biophysik (E27), Technische Universität München, D-85748 Garching, Germany; and Center for Protein Assemblies, 85747 Garching, Germany

Author contributions: A. S., M.S and E.F. conceptualized the study. A.S. designed and performed the experiments. M.S. performed the formal analysis and the numerical simulations in discussion with I.M. M.S. visualized the data. M.S., A.S. and E.F. wrote the manuscript. A.B. and E.F. supervised the research.

Connectivity tunes filament velocity in filament-motor mixtures

The cytoskeleton provides living cells with the remarkable ability to generate force and motion. Filaments such as actin and microtubules, molecular motors, and associated proteins represent the main building blocks of this structure [8, 9]. The capability of molecular motors to locally convert chemical energy into mechanical work enables the active remodeling of cytoskeletal filaments into structures such as microtubule asters or the spindle apparatus, which are essential for cell functionality [9, 281, 282].

To understand the complex interplay between filaments and molecular motors it has been proven fruitful to study reconstituted systems composed of purified components in controlled conditions [40, 74, 121, 205, 283]. Despite their reduced complexity, mixtures of microtubules, kinesin motors, and passive cross-linkers or depletion agents have been found to self-organize into patterns and structures reminiscent of those observed *in-vivo* [38, 40, 74, 75, 205]. This includes the formation of nematically ordered dynamic bundles exhibiting turbulent-like behavior [85, 119, 247, 284–286], polarity sorting of microtubules [38, 76] with the subsequent creation of asters or other polar structures [48, 75], and the emergence of active networks [218, 287–289]. On a phenomenological level, this behavior can be understood by hydrodynamic theories that are built on symmetry arguments [48, 49, 51, 52, 86, 239]. However, those theories come at a price and contain phenomenological parameters, which are hard to measure and relate to the microscopic interactions of the constituents.

How to bridge the gap between molecular scale interactions and large scale dynamics is an open question that has recently come into the focus of interest [76, 237, 240, 242]. This question has been addressed using coarse-grained models derived from minimal microscopic interactions [240, 241, 243–248] or large scale computer simulations [39, 75, 93, 249–252]. These studies have increased the awareness that an important property determining the large scale physics of filament-motor mixtures is their cross-linking state [242]. For example, it has been shown that the self-organization of the spindle is inherently tied to the fact that its microtubules are highly connected [98]. Moreover it has been shown that the number of passive cross-linkers in the filament network can control spatial instabilities of the large scale dynamics [91, 92]. Previous theoretical work examining how the number of cross-linkers influences the macroscopic behavior of filament networks has concentrated on dense highly cross-linked systems [2, 92, 99, 242, 290] or sparsely linked systems [206, 240, 243, 250]. However, not much is known about the intermediate cross-linking regime, which is likely describes a broad range of active biological systems. As an example, microtubule asters studied in cell extracts [291] are likely highly cross-linked in the bulk while sparsely towards their periphery [242].

Here we address the question how the degree of filament connectivity affects the overall speed of filaments in the network. To this end, we use an *in-vitro* reconstituted system composed of stabilized microtubules, molecular motors and passive cross-linkers. We find that an increase in the passive cross-linker concentration leads a non-monotonous change in the mean filament velocity. Surprisingly we find that an increase of passive cross-linkers can lead to an increase of filament velocities (Sec. 3.4.2). This is counterintuitive since passive cross-linkers impose friction on adjacent filaments. In Sec. 3.4.2 we proceed to develop a minimal agent-based model that reproduces our key experimental observations. Based on this model we relate the mean filament velocity to the network architecture and ultimately to the connectivity in the filament network (Sec. 3.4.2 and Sec. 3.4.2). Using large scale numerical simulations we identify previously reported physical properties of sparse and highly cross-linked networks at low and high cross-linker concentrations, respectively (Sec. 3.4.2). Specifically we show that the mean filament velocities become insensitive to the local network environment as the passive cross-linker concentration is increased; a feature which was predicted for highly cross-linked filament networks [2, 99]. Based on a minimal model we derive a semi-analytical theory that can encompass both sparse and highly cross-linked regimes and

predict the mean filament velocity as a function of the active motor and passive cross-linker concentration (Sec. 3.4.2). Last we compare our analytic results to measurements from the agent-based simulation (Sec. 3.4.2).

EXPERIMENTAL SYSTEM

To investigate the dynamics of active filament networks as the connectivity is increased, we use a three-dimensional system composed of active microtubule bundles on which molecular motors act exerting active forces. Briefly, as previously reported, we incubate short ($\approx 2\ \mu m$) fluorescently-labeled stabilized microtubules with engineered motors and crosslinkers. Motors are composed of two biotynilated kinesins (specifically, the fragment K401 of kinesin-1 [38]) bound together via streptavidin (Methods); see Fig. 3.25 (a). We refer to them as KSA for Kinesin-StreptAvidin. Each kinesin of the motor cluster can bind a microtubule, allowing the motor cluster to cross-link neighbouring microtubules and simultaneously walk towards the plus end of the microtubules it cross-links; see Fig. 3.25 (a),(b). If the microtubules are oriented in an anti-paralllel way, each half of the motor

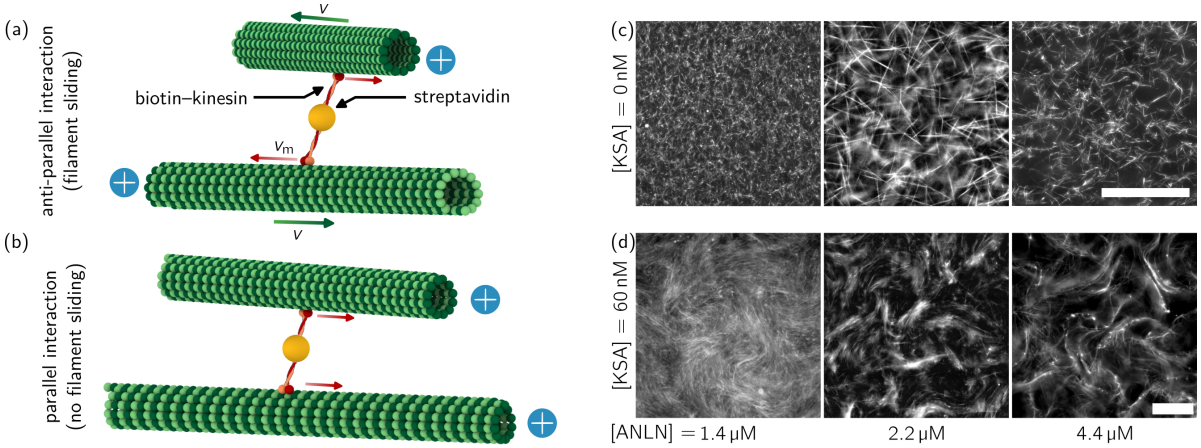

Figure 3.25: (a) Kinesin motor complexes are linked together by streptavidin forming a motor cluster that can simultaneously bind to two microtubules. The kinesin motors move directionally towards the microtubule plus end at speed v_m. If the microtubules cross-linked by a motor cluster are oriented in opposite direction (anti-parallel), the motor motion results in filament sliding opposed to the direction of motor movement. (b) If the microtubules are oriented in the same direction (parallel), the filaments do not move relative to each other. (c) A large field of view of the system under fluorescence microscopy in absence of motor clusters ([KSA] = 0 nM) at different concentrations of ANLN. We find that the peptide ANLN bundels microtubules in a concentration dependent way (left to right: [ANLN] = 1.4 µM, 2.2 µM, 4.4 µM). (d) Upon addition of motor clusters ([KSA] = 60 nM) and ATP the system assembles in active bundles whose architecture depends on the ANLN concentration (left to right: [ANLN] = 1.4 µM, 2.2 µM, 4.4 µM). Scale bar in (c) and (d) 100 µm

cluster attempts to walk in a different direction. In doing this, motors exert opposite forces on each of the two microtubules, resulting in extension of the filaments pair; see Fig. 3.25 (a). In contrast if the motor cluster is attached to parallel filaments the kinesins move in the same direction and the filaments remain static; Fig. 3.25 (b).

As a crosslinker, we choose to use a short peptide (ANLN) derived from the protein anillin [292]. While anillin is not a specific microtubule crosslinker, by adding it at various concentrations (from 0 to 5 μM) to a fixed concentration of microtubules (0.4 mg/ml) and motors (60 nM) we found that this fragment is able to bundle microtubules unspecifically. As the concentration of ANLN is increased, microtubule bundles become thicker and longer (Fig. 3.25 (c)). Differently from the commonly used cross-linkers (such as PRC-1 [261]) or depletion agents (such as PEG [87]) using

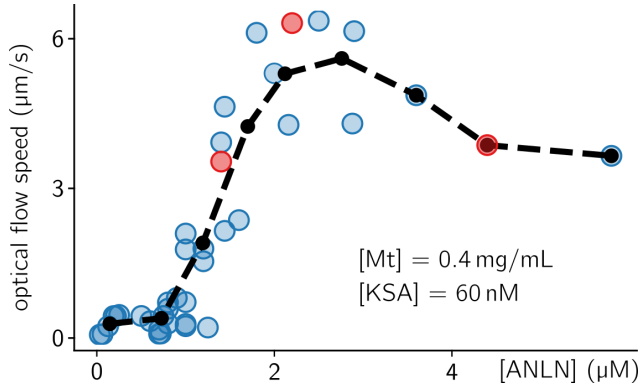

Figure 3.26: In plane optical flow speed of the active system extracted from microscopy images using an optical flow algorithm. As the ANLN concentration is increased we observe three characteristic phases of collective dynamics. First, no large-scale flow is observed ($v \approx 0\,\mu$m/s). Second, the macroscopic flow increases monotonously as a function of the ANLN concentration and reaches a maximum at $v_{\max} \approx 6\,\mu$m/s. Last, the macroscopic flow decreases as the ANLN concentration is increased further. Red circles correspond to snapshots in Fig. 3.25(d).

ANLN we can more finely tune the degree of filament-filament interaction (hence, their bundling) and avoid any adsorption to the surface that would be instead present if using a depletion agent. We then add molecular motors and ATP as a fuel to the mixture. In the presence of both ANLN, motors and ATP, filaments assemble into active bundles, i.e., bundles composed of filaments sliding against each other. We then perform an ANLN concentration series of the active system (Fig. 3.25 (d)) and observe, as the amount of ANLN is varied, distinct behaviors which we characterize by analyzing the architecture of the bundles and their speed v extracted from microscopy images of a given focal plane using an optical flow algorithm (Methods); see Fig. 3.26.

First, below a given threshold in the ANLN concentration ($[ANLN] < 1\ \mu M$), microtubules do not assemble into bundles and the system, while active at the microscopic scale, does not exhibit large-scale flow ($v \approx\ 0\ \mu m/s$); above such threshold, active bundles form and filament flow on a spatial scale much larger than individual filaments, albeit slow, can be observed; as ANLN is further increased ($1.5\,\mu M < [ANLN] < 3\,\mu M$), the speed of the filaments' flow finally increases and reaches a maximum value ($v \approx\ 6\ \mu m/s$); eventually, however, as the network further bundles due to the increase in ANLN ($[ANLN] > 3\,\mu M$) the speed declines again.

Thus, we show that by varying the ANLN concentration we can tune the overall activity, in terms of speed of the filaments flow, of the system. In addition, we find that there is an ANLN concentration leading to an optimum in such speed. We also note that the maximum attained speed is comparable to the maximum speed of filament-motors systems in similar conditions[38, 87, 88], indicating that the ANLN can be compared with previous results. As ANLN can clearly not induce activity itself we speculated that the macroscopic change in activity is tied to a change in the cross-linking state of the filament network. To understand how changes in connectivity can lead to a non-monotonic change in the global flow, we turned to theoretical and numerical studies.

MODEL SYSTEM

We build a minimal agent-based model based on the above described reconstituted *in vitro* system. The model consist of three classes of constituents: (i) stabilized microtubules of fixed length ℓ (ii) molecular motors that can cross-link two microtubules and simultaneously move towards the plus end of both microtubules it cross-links, and (iii) passive cross-linkers mediating an attractive force between neighbouring filaments; see Fig. 3.27. In detail, we use an agent-based model containing

a finite number of filaments (N_{MT}), active motors (N_{m}) and passive cross-linkers (N_{c}) in a thin box geometry with periodic boundary conditions in $x-$ and $y-$direction; see Fig. 3.27 (a). Each individual filament $i = 1,\ldots,N_{\mathrm{MT}}$ is represented by a directed semi-flexible rod of fixed length ℓ, center of mass position $\boldsymbol{x}_i$, and orientation $\boldsymbol{n}_i$. The orientation $\boldsymbol{n}_i$ is defined in direction of the filament plus-end. Close-by filaments repel each other via soft-core interaction if they are closer then a distance d_{Mt}; for details on the implementation see [249]. The system is simulated at a volume fraction $\phi = \pi d_{\mathrm{Mt}}^2/(4V_{\mathrm{system}}) \approx 0.03$. Active motors consist of two head domains connected by a Hookean spring. Due to our lack of knowledge how ANLN interacts with microtubules we decided to model passive cross-linkers similarly to active motors. They are modeled as two microtubule binding domains (heads) connected by a Hookean spring. Both active motors and passive cross-linker with no head attached to a filament are assumed to be well-mixed in the cytosol and can attach to any filament in the system with rate k_{on}^m and k_{on}^c, respectively. Active motors (passive cross-linkers) with one head attached to a filament can bind their second head to another filament within distance r_{m} (r_{c}). If the spring connecting the motor (passive cross-linker) heads becomes stretched a corresponding force ($\boldsymbol{f}$) acts on the motor (passive cross-linker) heads. The heads are assumed to detach at a load dependent rate $k_{\mathrm{off}}^m \mathrm{e}^{|\boldsymbol{f}|/f_{\mathrm{u}}^m}$ ($k_{\mathrm{off}}^c \mathrm{e}^{|\boldsymbol{f}|/f_{\mathrm{u}}^c}$) [235]; see Fig. 3.27 (b). Filament-bound motor heads move towards the plus-end at a load-dependent speed $v = v_{\mathrm{m}}(1+\boldsymbol{f}\cdot\boldsymbol{n}/f_{\mathrm{stall}})$ [196] and passive cross-linkers remain static; see Fig. 3.27 (c).

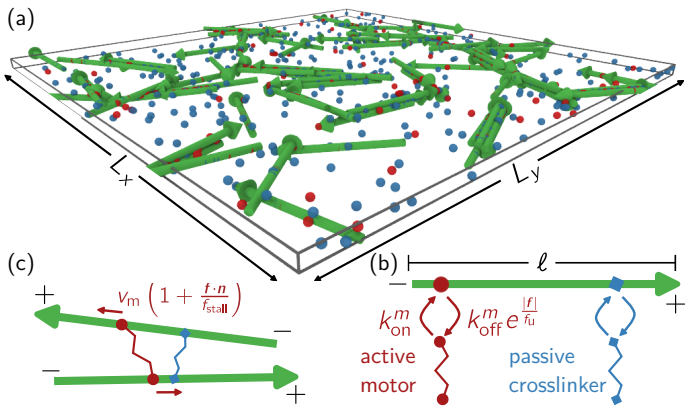

Figure 3.27: (a) Illustration of the agent-based model of the filament-motor mixture. Filaments are depicted in green, motors in red and passive cross-linkers in blue. All constituents are placed in a thin slab geometry of size (L_x, L_y, L_z) with periodic boundary conditions in $x-$ and y-direction and reflective boundary conditions in z-direction. The system contains N_{MT} microtubules, N_{m} motors and N_{c} passive cross-linkers (b) Model constituents and their basic interactions. Filaments (green) have a fixed length ℓ and orinetation $\boldsymbol{n}$ in direction of their plus end. Active motors (red) are modeled as two head domains connected by a Hookean spring. Passive cross-linkers (blue) are modeled analog as two microtubule binding domains (heads) connected by a Hookean spring. Active motors (passive cross-linkers) with no head attached are assumed to be well mixed in the cytosol and can bind to any filament at rate k_{on}^m (k_{on}^c). If one head is attached to a filament the second head can attach to a filament within range r_{m} (r_{c}). Motor (passive cross-linker) heads detach at a force dependent rate $k_{\mathrm{off}}^m \mathrm{e}^{|\boldsymbol{f}|/f_{\mathrm{u}}^m}$ ($k_{\mathrm{off}}^c \mathrm{e}^{|\boldsymbol{f}|/f_{\mathrm{u}}^c}$) (c) Motor heads attached to a microtubule move directional towards the plus end at a force dependent speed $v_{\mathrm{m}}\left(1+\boldsymbol{f}\cdot\boldsymbol{n}/f_{\mathrm{stall}}\right)$. Passive cross-linker heads do not move on the microtobule they are bound to.

RESULTS

FILAMENT ACTIVITY AND NETWORK ARCHITECTURE:

To test whether the minimal model is capable of reproducing the observations of our *in-vitro* experiments we simulated the agent-based model using the open-source software Cytosim [249]. To assess the filament flux in the simulation we measured the average filament activity $\overline{\alpha}$, defined as the average of filament velocities $\boldsymbol{v}_i$ along their director $\boldsymbol{n}_i$

$$\overline{\alpha} \equiv -\frac{1}{N_{\mathrm{MT}}} \sum_{i=1}^{N_{\mathrm{MT}}} \boldsymbol{n}_i \cdot \boldsymbol{v}_i / v_{\mathrm{m}}. \tag{3.113}$$

Note, since motors slide filaments in direction of their minus ends (opposed to $\boldsymbol{n}_i$, see Fig. 3.25 (a)) $\overline{\boldsymbol{n}_i \cdot \boldsymbol{v}_i} < 0$. The minus sign in Eq. 3.113 therefor ensures that $\overline{\alpha}$ is positive. Figure 3.28 (a) shows a typical profile of the average filament activity as a function of the number of passive cross-linkers (N_{c}) per filaments (N_{MT}), $c \equiv N_{\mathrm{c}}/N_{\mathrm{MT}}$, at a fixed number of active motors (N_{m}) number per filament; $m \equiv N_{\mathrm{m}}/N_{\mathrm{MT}}$. Consistent with experiments, we find a monotonic increase in filament activity below a number of passive cross-linker c^*; a detailed definition of c^* will be given later. At $c \approx c^*$, the activity starts to plateau followed by a monotonic decrease if the passive cross-linker concentration is increased further; see Fig. 3.28 (a).

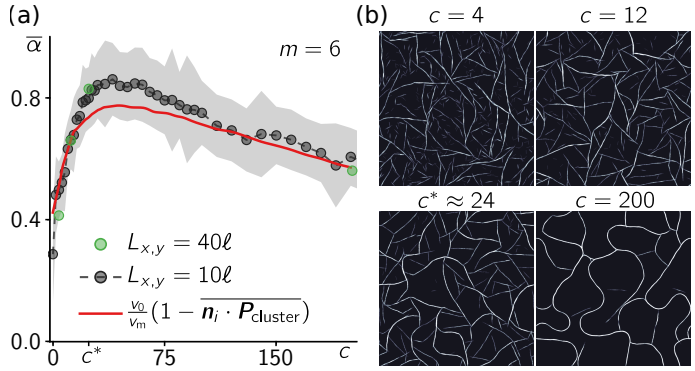

Figure 3.28: (a) Mean filament activity $\overline{\alpha} \pm$SEM as a function of the passive cross-linker number c for $m = 6$ obtained from numerical simulations of a system of size $L_x = L_y = 10\ell$. To obtain the mean filament activity we average the simulation results in the time interval $t \in [15\,\mathrm{min}, 30\,\mathrm{min}]$ and over 10 independent samples. Green circles are results for a larger system of size $L_x = L_y = 40\ell$; see (b) for snapshots of the system. The red curve represents our semi-analytic result derived in Sec. 3.4.2. (b) Representative snapshots of the filament density at passive cross-linker numbers $c = 4, 12, 24, 200$ and $m = 6$ for a system of size $L_{\mathrm{x}} = L_{\mathrm{y}} = 40\ell$.

The change in filament activity is accompanied by a macroscopic change in the network architecture. At low cross-linker concentrations ($c \ll c^*$) the network architecture is characterized by many kinks (junctions) and short disconnected filament bundles; see Fig. 3.28 (b) $c = 4, 12$. At the mesoscopic scale this network architecture results from a dynamic interplay of filament bundle expansion, buckling and immediate breaking. The breaking of filament bundles results in sharp kinks in the network; see Fig. 3.29 (a). Fragments of the broken filament bundles drift apart resulting in many small disconnected filament bundles at the macroscopic scale; see Fig. 3.29 (a) and Fig. 3.28 (b). Eventually bundle fragments fuse with other neighbouring filament bundles and the dynamic sequence of buckling, breaking and bundle fusion repeats. Phenomenologically this dynamic behaviour is consistent with observations from our *in vitro* experiments (see Fig. 3.29) and was also reported for similar experimental setups [38, 87, 261]. As the number of passive cross-linkers per filament c is increased above c^* the network architecture changes to long nematic filament bands

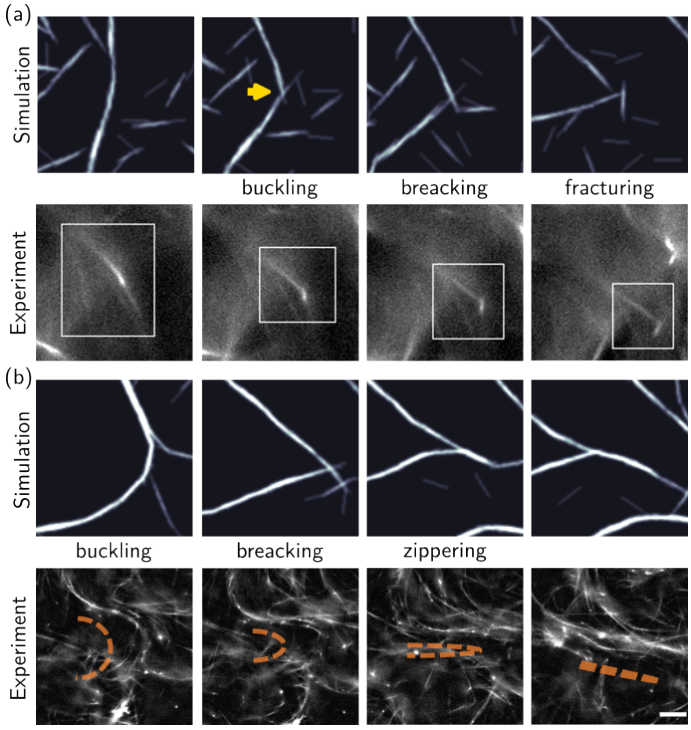

Figure 3.29: At the mesoscopic scale the dynamics is driven by filament bundle buckling, breaking and zippering. (a) Top panel: Example of simulation ssnapshots showing filament bundle breaking (indicated by the yellow arrow). The bundle fragments drift apart (right snapshot) at low passive cross-linker concentration. Simulations where performed at $(c,m) = (4,6)$. Bottom panel: Microtubule bundle breaking observed in the *in vitro* experiment ($[ANLN] = 2.5\ \mu M$, 0.4 mg/ml MTs, 60 nM KSA). (b) Top panel: Example of bundle buckling, breaking and immediate zippering of the bundle fragments. Simulations where performed at $(c,m) = (30,6)$. Bottom panel: Bundle buckling and zippering observed in the *in vitro* experiment ($[ANLN] = 5\ \mu M$, 0.4 mg/ml MTs, 60 nM KSA). All simulations where performed in a system of size $L_x = L_y = 40\ell$

whose dynamics is driven by extended periods of buckling, followed by filament band breaking, and immediate zippering of the band fragments; see Fig. 3.29 (b). On a macroscopic scale this results in a network architecture which is characterized by less junctions and long continuous filament bands with higher curvature (see Fig. 3.28 (b); $c = 24$). For $c \gg c^*$, almost all filaments are condensed in a single system spanning filament band which exhibits only very few junctions (see Fig. 3.28 (b); $c = 200$).

QUANTIFICATION OF THE NETWORK ARCHITECTURE:

Motivated by the observation that the network architecture changed alongside with the average filament activity, we asked whether the changing collective dynamics could be related to the cross-linking state of the network. Specifically we wondered whether the macroscopic change in filament activity is caused by a transition from a sparsely to a highly cross-linked filament network. To gain a deeper understanding of how the degree of network connectivity affects the collective filament dynamics we quantified the network architecture by monitoring the number and size of filament clusters in our agent-based simulations. As a filament cluster we define a group of $N_{\text{cluster}} \geq 2$ filaments connected by active motors, passive cross-linkers, or both. Figure 3.30 shows the normalized frequency distribution $\mathscr{P}(n_{\text{cluster}})$ of filaments being part of a filament cluster of size $n_{\text{cluster}} = N_{\text{cluster}}/N_{\text{MT}}$. Consistent with our phenomenological observation, that the network architecture is

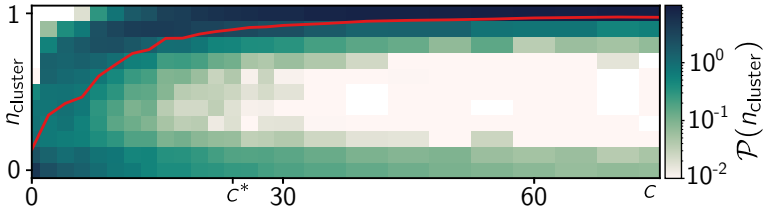

Figure 3.30: Normalized frequency distribution $\mathscr{P}(n_{\text{cluster}})$ of filaments being part of a filament cluster of size $n_{\text{cluster}} = N_{\text{cluster}}/N_{\text{MT}}$ obtained from agent-based simulations. Here $N_{\text{cluster}} \geq 2$ is the number of filaments connected by active motors, passive cross-linkers or both. We find that the filament network forms a giant component (cluster) as the passive cross-linker concentration is increased. At large passive cross-linker concentrations most filaments are condensed in a single filament cluster. The red curve shows the average cluster size a filament is part of.

characterized by small disconnected filament bundles at low passive cross-linker concentrations we find that the frequency distribution $\mathscr{P}_{\text{cluster}}$ is peaked at $n_{\text{cluster}} \approx 0$ at small passive cross-linker concentrations; see Fig. 3.30. Finally, at $c > c^*$, almost all filaments are part of a single large system spanning cluster; see Fig. 3.30 and Fig. 3.28 (b).

We now ask which physical properties of the filament network change as the network changes from sparsely linked system composed of many small filament clusters to a single, highly cross-linked, filament cluster. In particular we are interested in quantities that could affect the overall sliding velocity of filaments in the system.

NETWORK POLARITY, FILAMENT ALIGNMENT, AND FILAMENT SLIDING VELOCITY IN THE AGENT-BASED SIMULATION

Anti-parallel filaments slide past each other while parallel filaments do not move relative to each other; cf. Fig. 3.25 (a),(b). A natural hypothesis for a quantity that changes the sliding speed of a filament in the network is therefore the average number of parallel and anti-parallel interaction partners of a filament. To asses this hypothesis in our agent-based simulation we measure the local network polarity $\boldsymbol{p}(\boldsymbol{x})$ defined as the average orientation of filaments at a given position $\boldsymbol{x}$. To obtained the polarity field $\boldsymbol{p}(\boldsymbol{x})$ from the agent-based simulation we bin the system and evaluate the average orientation of filaments which pass trough each bin. Figure 3.31 shows snapshots of $|\boldsymbol{p}(\boldsymbol{x})|$ obtained from the agent-based simulation at different passive cross-linker numbers. Interestingly we find that the filament network is predominantly polar at low passive cross-linker concentrations. As the number of passive cross-links is increased the local polar order declines; see Fig. 3.31. To

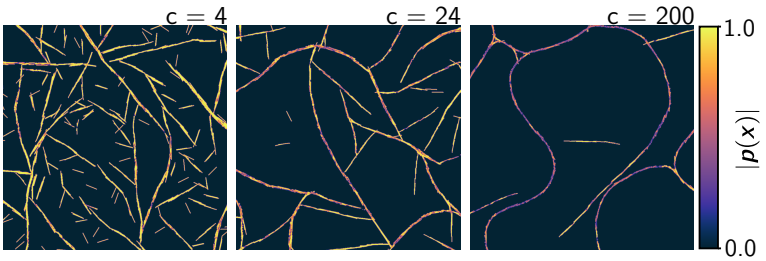

Figure 3.31: Snapshots of the absolute value of the local polarity $|\boldsymbol{p}(\boldsymbol{x})|$. To obtained the polarity field $\boldsymbol{p}(\boldsymbol{x})$ from the agent-based simulation we bin the system and evaluate the average orienation of filaments which pass trough each bin. For low local passive cross-linker number the system evolves into polar filament bundels. As the cross-linker number is increased the emerging filament bands become apolar. Snapshots show a field of view of size $(20\ell, 20\ell)$ of a system of size $L_x = L_y = 40\ell$.

quantify the change in the local polarity environment of filaments we measure the average alignment, $\overline{\boldsymbol{n}_i \cdot \boldsymbol{p}(\boldsymbol{x}_i)}$, in the network defined as

$$\overline{\boldsymbol{n}_i \cdot \boldsymbol{p}(\boldsymbol{x}_i)} \equiv \frac{1}{N_{\mathrm{Mt}}} \sum_{i=1}^{N_{\mathrm{Mt}}} \boldsymbol{n}_i \cdot \boldsymbol{p}(\boldsymbol{x}_i)\,. \tag{3.114}$$

A value of $\overline{\boldsymbol{n}_i \cdot \boldsymbol{p}(\boldsymbol{x}_i)} = 1$ corresponds to a fully polar network environment and $\overline{\boldsymbol{n}_i \cdot \boldsymbol{p}(\boldsymbol{x}_i)} = 0$ to an apolar network environment. We find that the average alignment $\overline{\boldsymbol{n}_i \cdot \boldsymbol{p}(\boldsymbol{x}_i)}$ decreases as a function of passive cross-linkers; see Fig. 3.32 (a). For $c < c^*$, filaments are predominantly polar aligned to their neighbours, making parallel filament-filament interactions more likely. As the passive cross-linker concentration is increased the local network environment of a filament becomes successively apolar favoring anti-parallel filament interactions; see Fig. 3.32 (a).

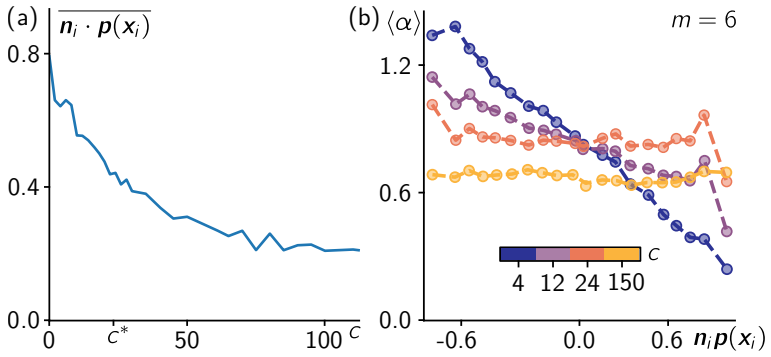

Figure 3.32: (a) Average local alignment $\overline{\boldsymbol{n}_i \cdot \boldsymbol{p}(\boldsymbol{x}_i)}$ of filaments as a function of passive cross-linkers per filament c at $N_{\mathrm{m}} = 6$. As the number of passive cross-linkers is increased the local network environment of a filament becomes less polar. (b) Sensitivity of the activity $-\boldsymbol{n}_i \cdot \boldsymbol{v}_i / v_{\mathrm{m}}$ to the local alignment $\boldsymbol{n}_i \cdot \boldsymbol{p}(\boldsymbol{x}_i)$ of a filament. At low passive cross-linker numbers filaments move fast in anti-aligned ($\boldsymbol{n}_i \cdot \boldsymbol{p}(\boldsymbol{x}_i) < 0$) and slow in aligned ($\boldsymbol{n}_i \cdot \boldsymbol{p}(\boldsymbol{x}_i) > 0$) network environments. As the passive cross-linker concentration is increased, the activity of filaments becomes insensitive to the network environment. Simulation results were averaged in the time interval $t \in [15\,\mathrm{min}, 30\,\mathrm{min}]$ and over 10 independent samples.

The decrease in polar order being monotonic whereas the activity is not, raises the question of whether the local alignment of filaments is indeed sufficient to explain the change in filament activity. To address this question we measured the activity of filaments, $\alpha_i = -\boldsymbol{n}_i \cdot \boldsymbol{v}_i / v_{\mathrm{m}}$, as a function of their local alignment to the filament network in our simulations, $\boldsymbol{n}_i \cdot \boldsymbol{p}(\boldsymbol{x}_i) \in [-1, 1]$ (see Fig. 3.32 (b)). A filament alignment $\boldsymbol{n}_i \cdot \boldsymbol{p}(\boldsymbol{x}_i) > 0$ ($\boldsymbol{n}_i \cdot \boldsymbol{p}(\boldsymbol{x}_i) < -1$) corresponds to a network environment of parallel (anti-parallel) filaments. At low passive cross-linker numbers, $c \ll c^*$, the filament activity depends linearly on the network environment; see Fig. 3.32 (b). As expected from our intuitive understanding that anti-parallel filament interactions induce filament motion filaments in a anti-parallel network environment ($\boldsymbol{n}_i \cdot \boldsymbol{p}(\boldsymbol{x}_i) < 0$) move faster as compared to filaments in a parallel network environment ($\boldsymbol{n}_i \cdot \boldsymbol{p}(\boldsymbol{x}_i) > 0$); see Fig. 3.32 (b) $c = 4, 12$. However as we increase the passive cross-linker concentration the filament activity becomes less sensitive to the local network environment. Ultimately at $c = c^*$ it becomes independent of the network environment (see Fig. 3.32 (b) $c = 24$); a feature which is was predicted for highly cross-linked filament networks [2, 99]. We therefore define the passive cross-linker number, c^*, at which the sliding velocity of filaments becomes insensitive to the local network environment as the transition to a highly cross-linked network.

Taken together our simulations show that as we increase the passive cross-linker number, the filament network changes its architecture from many small, disconnected filament clusters to a large interconnected filament cluster; see Fig. 3.28 and Fig. 3.30. Alongside the change in network

architecture, we observe a change in the average alignment, $\overline{\boldsymbol{n}_i \cdot \boldsymbol{p}(\boldsymbol{x}_i)}$, of filaments; see Fig. 3.32. Moreover, we observe that the sensitivity of filament sliding speeds to the local filament alignment changes with increasing passive cross-linker number from a linear dependence, as predicted for sparsely linked systems [240], to independent as predicted for highly cross-linked systems [2, 99]; see Fig. 3.32 (b). This suggests that our system transitions from a sparsely to a highly cross-linked filament network.

To get to the bottom of how the combination of the observed effects play together to affect the average filament activity $\overline{\alpha}$ in the system we aim to build a minimal biophysical model that relates the local polarity field $\boldsymbol{p}(\boldsymbol{x})$ to the local filament sliding velocity $\boldsymbol{v}(\boldsymbol{x})$.

A MINIMAL BIOPHYSICAL MODEL

In our agent based simulations we observed that filaments condense in quasi one-dimensional filament bands (cf. Fig. 3.28 (b)). Moreover the end-to-end distance of filaments in the simulation was $> 0.99\ell$. Motivated by those observations we limit the minimal biophysical model to a one-dimensional geometry and use a theoretical framework for rigid rods which we have successfully used in a previous work to describe collective filament motion in active nematic filament bands [2]. This is, for now, we ignore the fact that filament bands in the agent based simulations have non zero curvature. In section 3.4.2 we will relax this limitation in order to compare our analytic results to the data obtained from the agent-based simulation; cf. Fig. 3.27 (a).

In the minimal one-dimensional description filaments are aligned along the x-axis with center of mass position x_i and can take only two orientations $n_i = \pm 1$; see Fig. 3.33. Hence the dynamics of

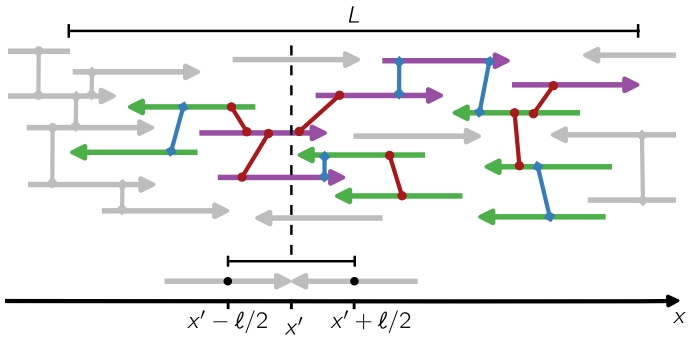

Figure 3.33: Skatch of the minimal biophysical model. Filaments can be either left ($n_i = -1$, green) or right ($n_i = +1$, purple) oriented. Filaments which are connected by a motor (red) or a passive cross-linker (blue) form a cluster. In the illustration the colored filaments form a cluster of extent L. The total number of all filaments with orientation $n_i = \pm 1$ that pass trough position x', $n^{\pm}_{\mathrm{Mt}}(x')$, is given by summing over all filaments with center of mass in the interval $[x' - \ell/2, x' + \ell/2]$; see Eq. 3.118.

a filament in the minimal model is determined solely by its velocity v_i. Instead of accounting for the explicit dynamics of motors and passive cross-linkers, we model motor (passive cross-linker) mediated interactions between filament i and j by an effective force-velocity relation $F^m_{ij}(\Delta v_{ij})$ ($F^c_{ij}(\Delta v_{ij})$) that depends on the relative velocity, $\Delta v_{ij} = v_j - v_i$, of filament i and j. Since $F_{ij} = -F_{ji}$ the force velocity relation can be only an odd function of Δv_{ij}. Here we restrict the discussion to a linear force-velocity relation. As previously described [2], we use

$$F^m_{ij}(\Delta v_{ij}) = \frac{F_m}{2}\left(n_j - n_i + \frac{v_j - v_i}{v_m}\right) \tag{3.115}$$

$$F^c_{ij}(\Delta v_{ij}) = \frac{F_c}{2}\frac{v_j - v_i}{v_m} \tag{3.116}$$

for motor and passive cross-linker mediated filament-filament interactions. F_m and F_c correspond to the average force amplitude exerted on the filaments by motors and cross-linkers respectively. The force velocity relations are designed to vanish if the relative motion of filaments does not induce strain in the cross-linking motor (or passive cross-linker). Passive cross-linkers are not strained if the filaments do not move relative to each other independent of the orientation of filament i and j; cf. Fig 3.27 (c). In contrast the force exerted by motors depends on the relative orientation of the filaments. For parallel filaments, $n_i = n_j$, motors act analog to cross-linkers and resist relative motion of the filaments. For anti-parallel filaments, $n_i = -n_j$, motors are not strained if the filaments move apart at a relative velocity of $2v_\mathrm{m}$.

Assuming overdamped dynamics the velocity v_i of filament i in the network is then determined by the force balance relation

$$\gamma v_i = \sum_{j\neq i} \left(M_{ij} F^m_{ij} + C_{ij} F^c_{ij} \right) , \tag{3.117}$$

where γ denotes the fluid drag, and M_{ij} and C_{ij} denote the number of motors and passive cross-linkers connecting filament i and j, respectively. The total number of motor (cross-linker) links of filament i is given by $\sum_j M_{ij} \equiv M_i$ ($\sum_j C_{ij} \equiv C_i$). In general M_i and C_i are functions of the filament density which depend on the attachment/detachment kinetics of motors and cross-linkers.

To understand how the network polarity impacts the filament velocity v_i we formulate Eq. 3.117 in the continuum limit. We denote the center of mass density of filaments at position x and orientation $n_i = \pm 1$ by $\rho^\pm(x)$. The number of filaments with orientation $n_i = \pm 1$, $n^\pm_\mathrm{Mt}(x)$, that pass trough position x can be expressed in terms of the center of mass filament density $\rho^\pm(x)$ (see Fig. 3.33)

$$n^\pm_\mathrm{Mt}(x) = \int_{-\ell/2}^{\ell/2} \mathrm{d}\xi \rho^\pm(x+\xi) . \tag{3.118}$$

On a mean field level the motor mediated links of filament i at arc-length position s to other filaments with orientation $n_j = \pm 1$ is given by $\rho_m(s)[n^\pm_\mathrm{Mt}(x_i+s)/n_\mathrm{Mt}(x_i+s)]$. Here $\rho_m(s)$ denotes the density of motors at arc-length position s that mediate an interaction to other filaments. The expression for passive cross-linkers reads the same with $\rho_\mathrm{c}(s)$ instead of $\rho_\mathrm{m}(s)$. For simplicity we assume a homogeneous density of motors and cross-linkers, i.e., $\rho_\mathrm{m}(s) = M_i/\ell$ and $\rho_\mathrm{c}(s) = C_i/\ell$. Using Eq. 3.115 we find the motor and cross-linker mediated force density acting on filament i that steam from parallel (pp) and anti-parallel (ap) interactions with other filaments

$$\begin{aligned} f^\mathrm{ap}_i(s) = \frac{\gamma}{n_\mathrm{Mt}(x_i+s)} \int_{-\ell/2}^{\ell/2} \frac{\mathrm{d}\xi}{\ell} \rho^\mp(x_i+s+\xi) \{ \mp 2 v_\mathrm{m} A_m \\ + (A_m + A_c)[v^\mp(x_i+\xi+s) - v^\pm_i] \} \end{aligned} \tag{3.119}$$

$$\begin{aligned} f^\mathrm{pp}_i(s) = \frac{\gamma}{n_\mathrm{Mt}(x_i+s)} \int_{-\ell/2}^{\ell/2} \frac{\mathrm{d}\xi}{\ell} \rho^\pm(x_i+s+\xi) \\ (A_m + A_c)[v^\pm(x_i+\xi+s) - v^\pm_i] , \end{aligned} \tag{3.120}$$

where we introduced $A_m = F_m M_i/(2v_\mathrm{m}\gamma)$ and $A_c = F_c C_i/(2v_\mathrm{m}\gamma)$ as dimensionless parameters quantifying the strength of active motor forces ($F_\mathrm{m} M_i$) and passive cross-linker forces ($F_\mathrm{c} C_i$) acting on filament i to dissipation to the surrounding fluid (γv_m). Taken together we find the continuum representation of Eq. 3.117 to be given by

$$\gamma v^\pm_i = \int_{-\ell/2}^{\ell/2} \mathrm{d}s \left(f^\mathrm{ap}_i(s) + f^\mathrm{pp}_i(s) \right) . \tag{3.121}$$

After applying the mean field assumption $v^\pm(x_i) = \langle v^\pm_i \rangle$, Eq. 3.121 together with Eq. 3.119 and 3.120 forms a set of coupled integral equations relating the filament velocities $v^\pm(x)$ to the number density $\rho^\pm(x)$ of filaments at position x.

ANALYTIC SOLUTION OF THE MINIMAL BIOPHYSICAL MODEL

In general the set of coupled integral equations (Eq. 3.121) is challenging to solve. In our agent-based simulation we observed that the total filament density $\rho(x) = \rho^+(x)+\rho^-(x)$ inside the filament bands (clusters) is approximately homogeneous (cf. 3.28 (b)). Therefor we assume a constant total filament density $\rho_0 = \rho^+(x) + \rho^-(x) = const.$ in the following, but allow for variations in the polarity defined as $p(x) = (1/\rho_0)[\rho^+(x) - \rho^-(x)]$. For constant filament density ρ_0, it is reasonable to assume $M_i = M$ ($C_i = C$), i.e., that all filaments have (on average) the same number of motor and passive cross-linker mediated interactions. Under those constraints it is possible to solve the set of integral equations (Eq. 3.121) using complex calculus. For details please refer to our previous work [2]. The result for the filament velocities $v^\pm(x)$ at position x reads

$$v^\pm(x) = \mp v_0[1 \mp \Pi(x)]\,, \tag{3.122}$$

$$\Pi(x) = \frac{1}{2l_c}\int_{-\infty}^{\infty} \mathrm{d}\xi\, p(x+\xi)\mathrm{e}^{-|\xi|/l_c}\,. \tag{3.123}$$

Here we have defined the characteristic length

$$l_c/\ell = \sqrt{\frac{1}{12}(A_m + A_c)}\,, \tag{3.124}$$

and the velocity of filaments in a homogeneous filament bundle:

$$v_0 = \frac{v_m}{1 + 1/A_m + A_c/A_m}\,. \tag{3.125}$$

To obtain Eq. 3.123 we assumed the system size to be large compared to the filament length ℓ and l_c. To account for filament clusters of finite size, as observed in the simulation, we mirror the polarity field $p(x)$ at the cluster boundaries. As before we define a filament cluster as a set of filaments connected by motors and passive cross-linkers.

As discussed in our previous work [2] Eq. 3.123 defines a weighted average of the polarity field along the contour of the filament cluster with a characteristic length l_c over which the polarity field is averaged. The characteristic length l_c defines a length scale over which locally generated momentum can be transferred in the filament cluster. This means in particular, if l_c is large, filament motion becomes independent of the local network environment; cf. Fig. 3.32 (b). The characteristic length is set by the competition of total motor and cross-linker forces acting on a filament, $F_m M + F_c C$, and dissipation to the surrounding fluid $2v_m\gamma$. For parameters used in the simulation, γv_m is small compared to the forces of motors and passive cross-linkers, i.e., l_c is large. If we consider a filament cluster of extend L (see Fig. 3.33) which spans the spatial region $[x - L/2, x + L/2]$ and $F_m M \gg v_m\gamma$ the ambient polarity Eq. 3.123 turns into an average of the polarity field along the extend of the filament cluster

$$\Pi(x) \approx P_{\text{cluster}} = \frac{1}{L}\int_{-L/2}^{L/2} \mathrm{d}\xi\, p(x+\xi)\,, \tag{3.126}$$

and the velocity amplitude v_0 is set by the motor velocity and a competition between active forces $F_m M$ and internal friction due to passive cross-linkers $F_c C$. Taken together, we find the velocity of filaments with orientation ± 1 inside the cluster to be given by

$$v^\pm(x) \approx \mp \frac{v_m}{1 + F_c C/(F_m M)}(1 \mp P_{\text{cluster}})\,. \tag{3.127}$$

Thereby we obtain an expression for the average filament activity in the system which reads

$$\overline{\alpha} = -\frac{1}{N_{\mathrm{Mt}}}\sum_i \frac{n_i v^{\pm}(x_i)}{v_{\mathrm{m}}} = \frac{1}{1+F_{\mathrm{c}}C/(F_m M)}\left(1-\overline{n_i P_{\mathrm{cluster}}}\right). \tag{3.128}$$

The term $\overline{n_i P_{\mathrm{cluster}}} \in [0,1]$ characterizes if filaments are on average part of polar or apolar filament clusters. Where the fully polar case corresponds to $\overline{n_i P_{\mathrm{cluster}}} = 1$.

Together with the network architecture Eq. 3.128 provides a possible explanation for the change in the sensitivity of the filament activity to the local network environment as the passive cross-linker concentration is increased; see Fig. 3.32 (b). At $c \ll c^*$, we observe a system composed of many small, disconnected, filament clusters. For such a network architecture, it is reasonable to coarse grain over the filament cluster and approximate $P_{\mathrm{cluster}} \approx p(x)$. Equation 3.128 then suggests a linear activity polarity relation, as observed for measurements from the agent-based simulation; cf. Fig. 3.32 (b) and predicted for sparsely cross-linked filament networks [240]. In contrast, if the network architecture changes to filament clusters composed of many filaments which span a large spatial region the local network polarity $p(x)$ becomes a bad approximation for the cluster polarity.

Moreover, Eq. 3.128 implies the presence of two, potentially competing, contributions to the average filament activity in the system. First, as the passive cross-linker number is increased the cluster polarity decreases (cf. Fig. 3.31), this increases the average filament activity since $(n_i P_{\mathrm{cluster}})$ decreases. Second, the competition between internal friction caused by passive cross-linkers and active motor forces in the filament clusters sets the pre-factor $1/(1+F_{\mathrm{c}}C/(F_m M))$, which decreases the filament activity with increasing passive cross-linker number. In particular, if $P_{\mathrm{cluster}} \approx 0$ for cross-linker numbers $c > c^*$ our theory suggest that the average filament activity is solely set by the ratio of passive cross-linker to active motor interactions of a filament.

COMPARISON TO THE AGENT-BASED SIMULATION

We now aim to relate findings of the minimal biophysical model to the agent-based simulations on a quantitative level. Ultimately, we are interested whether Eq.3.128 is indeed sufficient to account for the measured average filament-activity as a function of the passive cross-linker number. To this end we have to relax our assumption of straight filament clusters and have to define the cluster polarity in filament bands with non-zero curvature.

EVALUATION OF THE CLUSTER POLARITY IN THE AGENT-BASED SIMULATION

In order to compare Eq. 3.128 to direct measurements from the agent-based simulation (see Fig. 3.28 (a)) we have to evaluate the alignment of a filament i to its associated cluster, $\boldsymbol{n}_i \cdot \boldsymbol{P}_{\mathrm{cluster}}$, from the simulation data since we have no analytic prediction how the network architecture evolves dynamically from a initially homogeneous state.

For a curved filament cluster we define the alignment of a filament as the line integral of the polarity field $\boldsymbol{p}(\boldsymbol{r}(\sigma))$ along the contour $\boldsymbol{r}(\sigma)$ of the cluster. We denote $\boldsymbol{e}(\sigma)$ as the normalized tangential vector to the cluster at arc-length position σ of the cluster contour. We choose the direction of the cluster contour $\boldsymbol{e}(\sigma)$ to be aligned to the filament we consider; $\boldsymbol{n}_i \cdot \boldsymbol{e}(\sigma_i) = 1$. To obtain this average from the agent-based simulation we follow the cluster contour from the position of filament $\boldsymbol{r}(t_i)$ in steps of the filament length ℓ; see Fig. 3.34 (a). At each step $k = \pm 1, \pm 2\ldots$ we calculate the local cluster polarity defined as the average orientation of filaments in a square of length ℓ and cross section $(0.15\ell, L_z)$ centered at the cluster contour and calculate the projection on the local tangential vector $\boldsymbol{e}(\sigma + k\ell)$; see Fig. 3.34 (a). We stop if (i) the cluster ends (ii) we encounter a junction defined as two subsequent tangential vectors $\boldsymbol{e}(\sigma)$ which prescribe a relative orientation $\theta > \theta_{\mathrm{c}}$ or (iii) at a maximal k_{max} (see Fig. 3.34 (a)) $k_{\mathrm{max}}\ell$ can be seen as an approximative value for l_{c} (cf. Eq. 3.123). The choice of the angle θ_{c} at which a junction is defined is to a certain degree arbitrary. The assumption here is that motors that connect two filaments which prescribe a relative orientation $\theta > \theta_{\mathrm{c}}$ will will realign them rather then slide them apart. Here we use $\theta_{\mathrm{c}} = 45°$.

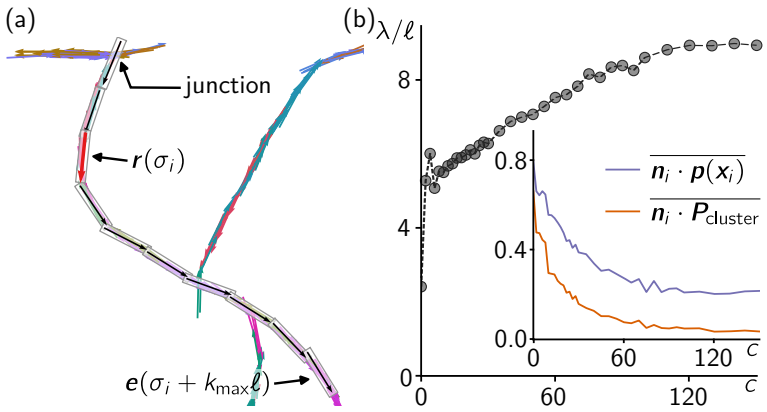

Figure 3.34: (a) Numeric evaluation of the alignment of filament i (red arrow) to the surrounding filament cluster. Starting from the filament position $\boldsymbol{r}(\sigma_i)$ we follow the cluster contour $\boldsymbol{r}(\sigma)$ in steps of ℓ. At each step k, we calculate the mean orientation of filaments inside a square of length ℓ and cross section $(0.15\ell, L_z)$ (gray squares) and project it on the local tangential vector $\boldsymbol{e}(\sigma + k\ell)$ of the cluster (black arrows); $\boldsymbol{e}(\sigma + k\ell) \cdot \boldsymbol{p}(\boldsymbol{r}(\sigma + k\ell))$. We stop if (i) the cluster ends, (ii) we encounter a junction, or (iii) at $k_{\max}$. We define the alignment of filament i to the cluster as the mean of the obtained values; cf. Eq. 3.129. (b) The average number of steps λ/ℓ before a junction or the cluster end is encountered as a function of passive cross-linkers; λ quantifies the length over which the polarity field is averaged. Inset: comparison between the average local alignment of filaments $\overline{\boldsymbol{n}_i \cdot \boldsymbol{p}(\boldsymbol{x}_i)}$ and the non-local alignment to the cluster $\overline{\boldsymbol{n}_i \cdot \boldsymbol{P}_{\text{cluster}}}$. As λ increases the polarity field is averaged over an extending spatial region. As a result of this non-local averaging high frequency fluctuations in the local polarity are suppressed and the filaments sense on average an apolar ($\overline{\boldsymbol{n}_i \boldsymbol{P}_{\text{cluster}}} = 0$) environment. Simulation results were averaged in the time interval $t \in [15\,\text{min}, 30\,\text{min}]$ and over 10 independent samples.

The average alignment of filaments to their cluster is then given by

$$\overline{\boldsymbol{n}_i \cdot \boldsymbol{P}_{\text{cluster}}} \equiv \frac{1}{N_{\text{MT}}} \sum_i \overline{\boldsymbol{e}(\sigma_i + k\ell) \cdot \boldsymbol{p}(\boldsymbol{r}(\sigma_i + k\ell))}\,. \tag{3.129}$$

We evaluate the average alignment of filaments to their cluster, $\overline{\boldsymbol{n}_i \cdot \boldsymbol{P}_{\text{cluster}}}$, for different values of $k_{\max}$ as a function of the number of passive cross-linkers. The mean length, λ, over which the polarity field is averaged can be approximated by the number of steps taken before either a junction or cluster end is reached. This length indicates how far locally generated momentum can be transferred in the filament network. We choose $k_{\max}\ell \gg \lambda$ such that the choice of $k_{\max}$ does not impact the result. Fig. 3.34 (b) shows the estimated length scale of momentum transfer λ, limited by either the cluster extension or junctions. We find three distinct regimes, which are related to the network architecture. Firstly, λ increases rapidly. This results from a rapid increase in the average filament cluster size; cf. Fig. 3.30. Secondly, λ continues to increase however at a slower rate. This goes along with the reduction of junctions in the network; cf. Fig. 3.28 (b). Lastly, the range of momentum transfer saturates at $\lambda \approx L$ indicating system-wide momentum transfer. The inset in Fig 3.34 (b) shows $\overline{\boldsymbol{n}_i \cdot \boldsymbol{P}_{\text{cluster}}}$ for $k_{\max} = 14\ell$ in comparison to the local filament alignment ($\overline{\boldsymbol{n}_i \cdot \boldsymbol{p}(\boldsymbol{x}_i)}$). As the length λ over which the polarity field is averaged increases fluctuations in the local polarity field are averaged out. Thereby the filament activity becomes insensitive to the local network polarity; cf. Fig. 3.32 (b).

THE HIGHLY CROSS-LINKED REGIME

At large passive cross-linker numbers $c > c^*$, filaments sense on average an apolar environment, $\overline{\boldsymbol{n}_i \cdot \boldsymbol{P}_{\text{cluster}}} \approx 0$, as a result of the non-local averaging of the polarity field; cf. Fig. 3.34 (b) inset. Equation 3.128 then implies that the average filament activity is then solely determined by

$$\overline{\alpha} = \frac{1}{1 + F_c C/(F_m M)} = \frac{1}{1 + K\, c/m}\,. \tag{3.130}$$

Here K is a fit constant that depends on the average force exerted by motors and passive cross-linkers and their attachment/detachment kinetics. Equation 3.130 then implies that the average filament activity is not sensitive to the absolute number of passive cross-linkers and motors but depends only on their ratio. If the number of motors is kept fixed the filament activity monotonically decreases as a function of passive cross-linkers due to internal friction. This is in line with our observation for $c > c^*$; cf. Fig. 3.28 (a). To compare our analytic prediction (Eq. 3.130) to the agent-based simulation we measure the average filament activity at different motor and cross-linker numbers. Consistent with the theoretic prediction we find that all data collapses on a single curve for $c \gtrsim c^*$ both in our simulations (see Fig. 3.35 (a)) and *in-vitro* experiments (Fig. 3.35 (b)).

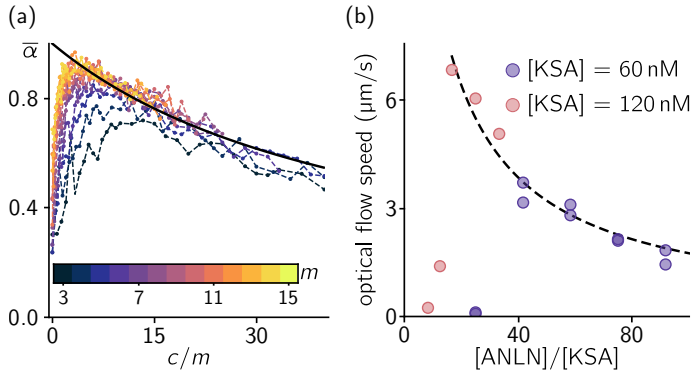

Figure 3.35: (a) Mean filament activity $\overline{\alpha}$ obtained from agent-based simulations for different active motor concentrations. In a highly cross-linked filament network the filament activity is predicted be $\overline{\alpha} = 1/(1 + K\, c/m)$ (black line), i.e., it depends only on the ratio of active motors to passive cross-linkers. We find good agreement in the regime where the filament activity declines. (b) Corresponding *in-vitro* measurements at [MT] = 0.8 mg/mL and different motor concentrations. The dashed line is a fit of the analytically predicted functional form $A_1/(1 + A_2[\text{ANLN}]/[\text{KSA}])$. As for the numerical data we find good agreement to the analytic predictions. Simulation results were averaged in the time interval $t \in [15\,\text{min}, 30\,\text{min}]$.

We fit Eq. 3.130 to the data obtained from the agent-based simulation for $c \gg c^*$. Thereby we obtain the fit constant ($K \approx 0.02$). This allows to write the pre-factor in Eq. 3.128 as a function of c/m only. Together with the numerical obtained value for the cluster polarity, Eq. 3.129, this allows to estimate the filament activity as a function of active motors and passive cross-linkers.

ESTIMATING THE FILAMENT ACTIVITY

Substituting the numerically obtained estimate of the cluster polarity (Eq. 3.129 and Fig. 3.34 (b) inset) into Eq. 3.128 allows to estimate the filament activity in terms of the passive cross-linker and motor number. The result is in good agreement with direct measurements from the agent-based simulation; see Fig. 3.28 (a) red curve. The fact that we recover a reasonable prediction of the simulation data (cf. Fig. 3.28 (a), red line) using (Eq. 3.128) together with the numerically extracted values of $\overline{\boldsymbol{n}_i \cdot \boldsymbol{P}_{\text{cluster}}}$ at each cross-linker concentration further shows that our framework is able to encompass the full connectivity range of the filament-motor mixture.

In summary, this result shows that the filament activity is controlled by two competing mechanisms as the passive cross-linker concentration is increased. The network architecture, in particular the connectivity of filaments, controls the length λ over which locally generated momentum can propagate in the filament network. This has major impact if the filament network shows local filament alignment ($\overline{\boldsymbol{n}_i \cdot \boldsymbol{p}(\boldsymbol{x}_i)} > 0$). Somewhat surprisingly the system studied here shows always local polar order; cf. Fig. 3.32 and Fig. 3.31. As the connectivity of the filament network is increased the length of momentum propagation λ (see Fig. 3.34 (b)) increases. Therefore, filament sliding velocities become less sensitive to local deviations in the number of parallel and anti-parallel interaction partners. On a coarse-grained level this is expressed in filaments sensing on average an apolar network environment (see Fig. 3.34 (b) inset), which in turn leads to higher filament activity (cf. Eq. 3.128). However, as the number of passive cross-linkers is increased, not only does the connectivity increase but so does the internal friction in the network, which decreases the filament activity in the system.

CONCLUSION

Here we have investigated an active *in-vitro* system of stabilized microtubules connected by molecular motors and passive cross-linkers under dilute conditions. We found that the filament activity increases with an increasing number of passive cross-linkers c, reaches a maximum at $c \approx c^*$, and declines upon a further increase. Using large scale computer simulations we were able to recapitulate this finding *in silico*. Based on the agent-based simulation we derived a semi-analytic theory that explains our observations.

The initially disordered filaments condense into filament clusters yielding dense bundles within the dilute system. Those filament bundles evolve through a repeating sequence of buckling, breaking, and fusion. Depending on the passive cross-linker concentration this dynamics leads to different microscopic order of the filament network. At low passive cross-linker concentrations filaments are predominantly polar aligned. Microscopically, motors can only slide anti-aligned filament pairs. However, as the passive cross-linker concentration is increased we find that the activity of filaments changes its dependence on the local polar order from linear, to independent (cf. Fig. 3.32).

This effect arises because the ability of the filament network to transmit locally generated force to different parts of the system depends on the network connectivity. At low passive cross-linker concentration, the filament network is sparsely linked and locally generated force can not propagate in the network. It follows that the filament velocities depend on the local number of anti-parallel filament interactions. In contrast at high passive cross-linker concentrations filaments immersed in regions of polar order, and therefore incapable of sliding relative to each other, can be transported by the netowork.

Hence, the overall filament activity of the system arises as an interplay between the microscopic generation of force from anti-polar interactions and the ability of the network to propagate such force. In our semi-analytic theory, the ability of the network to transfer force is characterized by the length λ. In the sparse cross-linking state λ is limited by the extent of disconnected filament clusters. As the network connectivity is increased λ increases and locally generated force can be transferred over large spatial regions, causing filament motion even in polar regions. In this latter parameter regime, filament sliding velocities do not depend on the local network environment but are only determined by a competition of active forces and internal friction due to passive cross-linkers. Filament sliding velocities are maximized by a balance of internal friction and length of force transmission λ.

For a long time, polarity has received little attention in the context of active filament gels. This is due to the success of active nematic theories which include an apolar active current that generates a particle flux along or against the nematic curvature [241, 246]. Those theories have been successfully used to describe the macroscopic dynamics of active filament gels, in particular, the formation

of steady-state structures and defect dynamics [50, 81–83]. However, at the microscopic level, nematic symmetry is hard to unify with activity that emerges from polar interactions. The success of our semi-analytic theory to describe the filament activity in terms of the cluster polarity rather the the local polarity might provide insight on this discrepancy. If the network is highly cross-linked the filament clusters span large spatial regions and polarity affects the filament activity only if large polar domains emerge in the filament network.

Recent experimental results in dense two-dimensional active gels show sliding velocities of microtubule pairs at approximately 30% of the sliding velocity of isolated bundles [76]. This appears to be in apparent contradiction to observations in 3D-aligned microtubule gels. However, computer simulations of a two-dimensional system composed of polar filaments and molecular motors suggest the existence of large polar domains in such systems [260]. Together with our theory, this might provide an explanation for the measured filament velocities; cf. Fig. 3.28(a).

On a broader perspective, the system studied here shows similarities to the liquid–solid transition found in cross-linked actin networks as their connectivity is varied [293, 294]. Similar to our result force propagation in those networks has been shown to be controlled by network connectivity [287]. However, in contrast to the system studied here actin, networks are predominately contractile. A possible origin for this difference is the flexibility of actin compared to microtubules, since filament buckling has been proposed as a microscopic mechanism underlying contractility in actin networks [295–297]. However recent experiments and simulations have shown that actomyosin networks are contractile even if the filament rigidity is increased [298]. For networks composed of rigid filaments the contractile vs. extansile nature of the network is likely to be controlled by asymmetries in the filament bound motor and/or cross-linker density [79, 93, 206, 218, 254]. In the context of our theoretic framework inhomogenous motor and passive cross-linker density profiles can be incorporated into Eq. 3.120 and 3.119. This might allow to understand the bending instability (cf. Fig. 3.29(b)). Investigating this will be an interesting avenue for further research.

3.5. SUMMARY & OUTLOOK

In this chapter, we have studied the collective dynamics of filament bundles driven by force-generating motor cross-links. Starting from a microscopic model for cross-linking motor proteins, we derive a coarse-grained, effective motor-mediated filament-filament interaction based on a time-scale separation argument. Based on this effective interaction, we studied the emergent dynamics of mesoscale filament bundles.

First, we addressed the question of how different types of motor cross-linkers control the propensity of a filament bundle to expand or contrast. *In vivo* nature exploits the ability of cytoskeletal filament networks to contract or expand to perform different tasks. Important examples are the mitotic spindle, which expands during anaphase to segregate chromosomes, or the actin cortex, which contracts to drive changes in cell shape. *In vitro* active filament networks show a broad range of dynamics, including large-scale network contraction, aster formation, and formation of active foams associated with contractile stresses, as well as filament bundle banding and turbulent-like dynamics associated with extensile stresses depending on the type or mixture of motor cross-linkers in the system. Previous studies have focused on emergent large-scale dynamics by using phenomenological hydrodynamic theories, which are based on symmetry arguments. In those theories, activity is introduced via an apolar active stress. However, how the introduced stress arises from the microscopic dynamics is an open question. In Section 3.2, we develop a minimal but generic framework to evaluate the contribution of a cross-linker to the filament bundles' propensity to generate contractile or extensile tension. Thereby, we were able to identify generic requirements for a filament bundle cross-linked by motors to generate extensile or contractile stress: First, a motor that has a homogenous density profile along the arc-length of a filament can neither generate contractile nor extensile stress. Second, symmetric motor cross-linkers can only generate extensile stress in the presence of external or internal friction. This friction can be caused by crowding agents or passive cross-linkers. Third, motors that dwell at the filament tip promote contractile tension through interactions of filaments with equal orientation. Using our general framework, we studied a minimal set of constituents given by a crowding agent and a symmetric motor that slides anti-parallel filaments. The motor is allowed to dwell at the filament end it is walking towards. This set of constituents resembles the main features of our general theory. We show that the contractile nature of the filament bundle is controlled by the ratio of tip-to-bulk motors, and the bundles' propensity to the extent is controlled by the number of bundling agents in the system. We relate those parameters to three experimentally accessible parameters: First, the total number of passive cross-linkers in the system, with more passive cross-linkers promoting expansile stress. Second, the total number of motors with an increasing number of motors promoting contractile stress. Lastly, the filament length, with longer filaments, increases the network's propensity to expand. To verify our theoretical predictions and to study the long-term dynamics of the system, we use agent-based computer simulations. All our predictions and the observed steady-state filament assemblies are in line with recent *in vitro* experiments [75, 78, 79, 91–93].

On the level of individual filaments, motor-induced filament sliding is tied to the relative orientation of the cross-linked filaments. While parallel filaments that are cross-linked do not move relative to each other, anti-parallel cross-linked filaments slide apart at approximately twice the unloaded speed of motors [95]. However, this observation on the level of an individual filament pair is in conflict with experimental observations in the spindle apparatus [96–98]. There, filaments seam to slide apart at a speed that is independent of the local number of parallel and anti-parallel interaction partners. Motivated by this puzzling observation, we sought to understand which mechanisms control the filament sliding speed in bundles of homogenous density but inhomogeneous polarity. In Section 3.3, we used our formalism to derive a continuum model for motor-induced filament sliding that relates the filament sliding velocity to the local network polarity. We show that the dependence between network polarity and filament sliding velocity is non-local. The locally generated force is

propagated through the network at a characteristic length that is set by the competition between active forces in the system and dissipation to the surrounding fluid. In the limit of low dissipation and large fluid drag, we recover the experimental findings that the filament velocity is independent of the local network polarity.

In Section 3.4, we asked how the ability of the filament network to propagate force depends on the network connectivity. To this end, we studied an *in vitro* reconstituted system composed of microtubules, passive cross-linkers, and active motors. By varying the concentration of passive cross-linkers in the system, we controlled the network connectivity. Interestingly, we find that an increasing number of passive cross-linkers in the system increases the average filament sliding velocity in the system, contradicting the intuition that passive cross-linkers promote friction between filaments. Using an agent-based model, we related the mean filament velocity to the network architecture and, in particular, to the network connectivity. We showed that by increasing the network connectivity, the filament sliding velocities become insensitive to the local number of parallel and anti-parallel interaction partners, as predicted by our previous work in the limit of highly cross-linked filament bundles. We derive a semianalytical theory that can encompass both the sparse and highly cross-linked parameter regimes.

Taken together, in this chapter, we studied the emergent dynamics in filament bundles cross-linked by force-generating motors. All our theoretical studies have in common that we considered stabilized filaments of fixed length. *In vivo* filaments are dynamic, and even in *in vitro* reconstituted systems of stabilized microtubules, filaments will have a distribution of length $p(\ell)$. A logical next step is to ask how a distribution of filament lengths will affect the physics of filament bundles. In Section 3.2, we found that the filament length can be a control parameter for the filament bundles' propensity to expand or contract. But how about a filament bundle composed of filaments of different lengths? Filaments of different lengths will definitely have different anisotropy factors and different tip-motor populations. Evaluating if it is possible to account for filaments of different lengths in a simple mean-field picture by treating all filaments as if they had the average length will be an interesting future research project. Let us turn our attention to dynamic filaments and consider a cross-linking motor that moves towards the plus end. Hence, on a static filament, the motor would have an anisotropy factor $\mu > 0$ (see Sec. 3.2). However, if the filament grows faster than the motor's walking speed, it is possible to shift the mass of filament-bound motors toward the minus end and obtain a motor anisotropy factor $\mu < 0$, which would turn the bundle tension from extensile to contractile. An indication that this is indeed possible is given by recent research on treadmilling actin filaments [254]. Evaluating if this is indeed possible will be an interesting avenue for further research.

An alternative direction for further research questions would be to consider stochastic effects caused by the demographic noise of motor cross-linker populations. To illustrate this idea, let us again consider the case of a filament bundle cross-linked by a plus-end oriented motor and a passive cross-linker. However, the number of motors per filament is low. Then, there is a high probability that a filament is only cross-linked by passive cross-linkers to neighboring filaments. If those neighbors have an opposite orientation to the filament itself, they drag them along as opposed to the direction of motion a motor cross-linker would induce. This, in turn, would yield an active diffusion of filaments that depends on the local polar order. Results of recent *in vitro* experiments hint at the existence of such an active diffusion contribution of cross-linking motors [76]. Studying how such an active, polarity-dependent diffusion impacts the dynamics on a collective level would also be an interesting future research question.

3.6. SUPPLEMENTAL MATERIAL

SUPPLEMENTAL MATERIAL: A MECHANISTIC VIEW OF COLLECTIVE FILAMENT MOTION IN ACTIVE NEMATIC NETWORKS

Agent-based simulation: To simulate the filament gel, we implement an agent-based simulation consisting of M_l left- and M_r right-oriented filaments. As described in detail in section In silico study: Random polarity field, we randomly place the filaments in a one-dimensional box with periodic boundary conditions. Next, a vector $\mathbf{I} \in \mathbb{R}^{M_r+M_l}$ consisting of the numbers of overlapping filaments for each filament i is generated. From this vector, a probability vector $\mathbf{p} \in \mathbb{R}^{M_l+M_r}$ is derived so that the average number of interaction partners per filament is given by $N = I_i\ p_i$. Out of the I_i possible interaction partners of filament i, we accept an interaction with probability p_i and reject it with probability $1-p_i$. Once the interactions are determined, we construct a set of M_l+M_r coupled linear equations on the basis of the force balance equation

$$\gamma\, v_i = \sum_j F_{ij}^{\text{parallel}} + \sum_k F_{ik}^{\text{antiparallel}}\,, \tag{3.131}$$

and weigh each interaction by the overlap between the filaments. Here j runs over the parallel interaction partners and k over the antiparallel interaction partners of filament i. The velocities of each filament i are then obtained using matrix inversion.

Continuum simulation: For the continuum simulation, we generate a polarity profile analogous to that in the agent-based simulation. Then we use our theoretical results (Eqs. 3.108a, 3.108b) but perform the integration numerically to obtain the velocity field.

A continuum model for motor-driven filament motion Here we derive a solution for our continuum model of filament motion. As a starting point, we use the coupled set of integral equations, Eqs. 3.106, in the main text which read

$$\gamma\, v^{(+)}(x) = \frac{N}{L}\int_{x-L}^{x+L} \mathrm{d}y\, \frac{\hat{N}_\mathrm{m}(x,y)}{2}\,\{(1+P(y))F^{(++)}(x,y) + (1-P(y))F^{(+-)}(x,y)\} \tag{3.132}$$

$$\gamma\, v^{(-)}(x) = \frac{N}{L}\int_{x-L}^{x+L} \mathrm{d}y\, \frac{\hat{N}_\mathrm{m}(x,y)}{2}\,\{(1-P(y))F^{(--)}(x,y) + (1+P(y))F^{(-+)}(x,y)\}\,, \tag{3.133}$$

where we used $\varphi^{(\pm)} = 1/2(1\pm P(y))$.

In general, it is quite challenging to provide an analytic solution to a set of coupled integral equations. Here, however, one can make use of the fact that the difference of the velocities, $v^{(+)} - v^{(-)}$, takes a quite simple form. Namely,

$$\begin{aligned} 2\,\gamma(v^{(+)}(x) - v^{(-)}(x)) = \frac{N}{L}\int_{x-L}^{x+L} \mathrm{d}y\, \hat{N}_\mathrm{m}(x,y)\{&(1+P(y))\,(F^{(++)}(x,y) - F^{(-+)}(x,y)) \\ &+(1-P(y))\,(F^{(+-)}(x,y) - F^{(--)}(x,y))\}\,. \end{aligned} \tag{3.134}$$

The difference of the contributing forces reads

$$F^{(++)}(x,y) - F^{(-+)}(x,y) = F^{(+-)}(x,y) - F^{(--)}(x,y) = F_\mathrm{m}\left(1 + \frac{v^{(-)}(x) - v^{(+)}(x)}{2V_\mathrm{m}}\right), \tag{3.135}$$

and is a function of x only.

Substituting Eq. 3.135 into Eq. 3.134 and performing the integration yields

$$v^{(+)}(x) - v^{(-)}(x) = 2\,V_\mathrm{m}\frac{1}{1+\frac{2\,V_\mathrm{m}\,\gamma}{F_\mathrm{m}N_\mathrm{m}}} \equiv 2\,V_\mathrm{m}(1-\alpha) = \text{const}\,. \tag{3.136}$$

As a result, $v^{(-)}$ is expressed in terms of $v^{(+)}$, and we can use this relation to decouple Eq. 3.132 and Eq. 3.133.
The resulting integral equation reads

$$\epsilon\, v^{(+)}(x) - V_\mathrm{m}\alpha = \int_{x-L}^{x+L} \frac{\mathrm{d}y}{L^2}\,(L-|x-y|)\left\{v^{(+)}(y) - v^{(+)}(x) - V_\mathrm{m}\alpha\, P(y)\right\}\,, \tag{3.137}$$

where we introduced $\epsilon = \frac{2\gamma V_\mathrm{m}}{F_\mathrm{m} N_\mathrm{m}}$.

To proceed further, we rewrite $v(y)$ and $P(y)$ in terms of their full Taylor expansions around x and shift $v^{(+)}$ by $\alpha/\epsilon\, V_\mathrm{m}$, i.e., $v^{(+)} \to v^{(+)} - \alpha/\epsilon\, V_\mathrm{m}$.

Performing the integration yields an ODE coupling the velocity to the polarity field. It reads:

$$\left(\epsilon - \sum_{k=1}^{\infty} \frac{2L^{2k}}{(2+2k)!}\left(\frac{\partial}{\partial x}\right)^{(2k)}\right) v^{(+)}(x) = -V_\mathrm{m}\alpha \sum_{k=0}^{\infty} \frac{2L^{2k}}{(2+2k)!}\left(\frac{\partial}{\partial x}\right)^{(2k)} P(x) \tag{3.138}$$

AN ANALYTIC SOLUTION FOR FILAMENT MOTION IN A NEMATIC NETWORK

To find a feasible expression relating the velocity and polarity field, we apply the Fourier transformation to Eq. 3.138. Our system - recast in $v^{(+)}(k)$ and $P(k)$ - becomes

$$v^{(+)}(k) = -2V_\mathrm{m}\alpha \underbrace{\left(\frac{1-\cos(Lk)}{\epsilon(Lk)^2 - 2 + (Lk)^2 + 2\,\cos(Lk)}\right)}_{\equiv \hat{K}(k)} P(k) = \mathrm{F}\{K\}\cdot\mathrm{F}\{P\}\,. \tag{3.139}$$

where F denotes the Fourier transformation operator[3]. From the convolution theorem, we directly find that $v^{(+)}(x)$ is given by the convolution of $K(x)$ and $P(x)$. So, in order to tackle our original equations, we are left with finding the Fourier back transformation of $\hat{K}(k)$, i.e., we need to solve

$$K(x) = \frac{1}{2\,\pi}\int_{-\infty}^{\infty} \mathrm{d}k \left(\frac{1-\cos(Lk)}{\epsilon(Lk)^2 - 2 + (Lk)^2 + 2\,\cos(Lk)}\right) \exp(ikx)\,. \tag{3.140}$$

To proceed further, we assume that the integral can be performed using the residue theorem, i.e.,

$$K(x) = \frac{1}{2\,\pi}\int_{-\infty}^{\infty} \mathrm{d}k \underbrace{\left(\frac{1-\cos(Lk)}{\epsilon(Lk)^2 - 2 + (Lk)^2 + 2\,\cos(Lk)}\right) \exp(ikx)}_{f(k)} = i\sum_j \mathrm{Res}_{k_j}\left\{f(k)\right\}\,, \tag{3.141}$$

with the sum running over all poles in the upper half-plane (lower half plane) if $x > 0$ ($x < 0$). In the following, we will restrict the discussion to the case $x > 0$ since the calculations for $x < 0$ are analogous. Note that we exclude the case $x = 0$ explicitly and assume a smooth solution at $x = 0$. For simplicity, we will use dimensionless variables in the following and recast $k \to kL$ and $x \to x/L$. To find the potential residues, we search for all solutions of the equation

$$0 \stackrel{!}{=} k^2(1+\epsilon) - 2 + 2\cos(k) = k^2(1+\epsilon) - 4\,\sin^2(k/2)\,. \tag{3.142}$$

in the complex plane. In the following, we will use $k = a + ib$ with $a, b \in \mathbb{R}$. Using this notation, the problem of finding possible residues of $f(k)$ has shifted to finding solutions to the equations

$$a\sqrt{1+\epsilon} = \pm 2\cosh(b/2)\,\sin(a/2) \tag{3.143}$$

$$b\sqrt{1+\epsilon} = \pm 2\sinh(b/2)\,\cos(a/2)\,. \tag{3.144}$$

We split the discussion into (i) real, (ii) imaginary and (iii) complex solutions of Eq.3.142. a^*, b^* will denote solutions of the above equation system.

[3] It is also possible to derive Eq. 3.139 by directly inserting the Fourier transforms of $v^{(+)}$ and P into Eq. 3.137.

(i) real solutions $(b^* = 0)$ The only real solution of Eq. 3.142 is given by $a^* = 0$.

(ii) imaginary solutions $(a^* = 0)$ Eq. 3.143 is always fulfilled for $a_0^* = 0$. Moreover, Eq. 3.144 always has two solutions for $\epsilon > 0$ which can be estimated as $b_0^* = \pm\sqrt{24\sqrt{1+\epsilon}-24}$ for small ϵ.

(iii) complex solutions $(a^* \neq 0, b^* \neq 0)$ The complex solutions are not trivial to find. First, note that the discussion can be split into positive and negative signs of the right-hand side of Eq. 3.143 and 3.144.

For a negative sign on the right-hand side, if $a, b > 0$, $\cos(a/2)$ and $\sin(a/2)$ have to be negative for the equation system to be solvable, i.e., we know $a \in (2n\pi, (2n+1)\pi)$ with $n = 1, 3, 5\ldots$.
Investigating Eq. 3.144 alone, the minimal $b^*(a)$ is found for $a = 2\pi n$ and can be estimated as $b^*_{min}(2n\pi) = \sqrt{24\sqrt{1+\epsilon}-24}$, i.e.,$b^*_{min}$ is close to 0 for small ϵ. Moreover, one finds that $b^*(a)$ is monotonically increasing in the interval $a \in (2n\pi, (2n+1)\pi)$ and $b^*(a \to (2n+1)\pi) \to \infty$.
Equation 3.143 implies that $\cosh(b/2)$ has to be sufficiently large if $a \in (2n\pi, (2n+1)\pi)$ with $n = 1, 3, 5\ldots$. Especially for large n this means that a^* has to be close to $(2n+1)\pi$ with $n = 1, 3, 5\ldots$, i.e., $\sin(a^*/2) \approx -1 \Rightarrow b^* \approx 2\text{arcosh}\left(\frac{2n+1}{2}\pi\sqrt{1+\epsilon}\right)$. Taken together, this yields

$$(a^*, b^*) \approx \left((2n+1)\pi, 2\text{arcosh}\left(\frac{2n+1}{2}\pi\sqrt{1+\epsilon}\right)\right) \quad \text{with } n = 1, 3, 5\ldots \tag{3.145}$$

A similar argumentation for a positive sign on the right-hand side of Eq. 3.143 and Eq. 3.144 and $a, b > 0$ yields the same result for $n = 2, 4, 5\ldots$. The cases $a > 0, b < 0$, $a < 0, b > 0$ and $a < 0, b < 0$ are analogous.
Taken together, we find the solutions

$$(a_n^*, b_n^*) \approx \left((2n+1)\pi, \pm 2\,\text{arcosh}\left(\frac{2n+1}{2}\pi\sqrt{1+\epsilon}\right)\right)$$
$$(a_n^*, b_n^*) \approx \left(-(2n+1)\pi, \pm 2\,\text{arcosh}\left(\frac{2n+1}{2}\pi\sqrt{1+\epsilon}\right)\right) \quad \text{with } n = 1, 2, 3\ldots$$

Figure 3.36 shows a comparison between the numerically found roots and our approximation for $\epsilon = 0.1$.

Since there is an infinite number of poles with arbitrarily large real part, one can not proceed as usual and use the residue theorem without any additional considerations. So, to make further progress, we continue as follows: First, we show

$$\int_{-\infty}^{\infty} \mathrm{d}k\, f(k) \approx \int_{-R}^{R} \mathrm{d}k\, f(k) \tag{3.146}$$

for sufficiently large R.
Second, we compute the integration along the path $\mathscr{C} = \{-R \to R \to C_1 \to C_2 \to -R\}$ according to the residue theorem:

$$\oint_{\mathscr{C}} f(k)\mathrm{d}k = 2\pi\, i \sum_j \text{Res}_{k_j}\{f(k)\}\,. \tag{3.147}$$

Third, we show that the path in the complex plane gives a vanishing contribution. Then the real Integral $\int_{-R}^{R} \mathrm{d}k\, f(k)$ can be estimated by

$$\int_{-R}^{R} \mathrm{d}k\, f(k) = 2\pi\, i \sum_{n=-M}^{M} \text{Res}_{k_n}\{f(k)\} \tag{3.148}$$

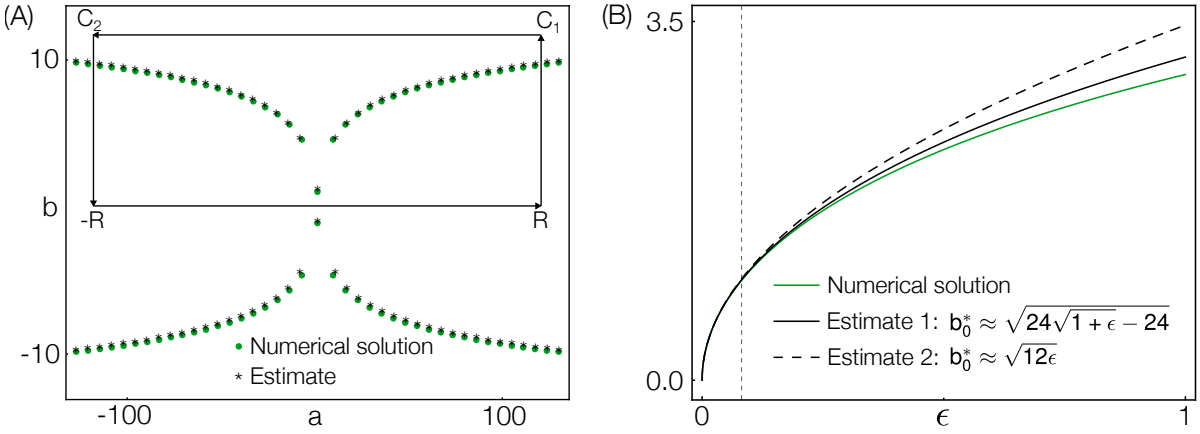

Figure 3.36: (**A**) Comparison of the estimate of the solutions of the equation system Eq.3.143,3.144 with the solutions obtained numerically (the results are compared exemplary for $\epsilon = 0.1$). (**B**) Comparison of two estimates for the imaginary pole with the corresponding numerical solutions. The gray dashed line indicates the $\epsilon-$value for which $l_c \approx L$.

where $k_n = k_{-M}...k_M$ denotes the poles in the interior of the integration path sorted by increasing real part. The notation is chosen so that k_0 denotes the purely imaginary pole.

The first step is straightforward since

$$\mathrm{Re}\left\{\int_R^\infty \mathrm{d}k \left(\frac{1-\cos(k)}{(1+\epsilon)k^2-2+2\cos(k)}\right)\exp(ikx)\right\} < \int_R^\infty \mathrm{d}k\,\frac{2}{k^2} = \frac{2}{R}\,, \tag{3.149}$$

i.e.,

$$\begin{aligned}&\int_{-\infty}^{\infty} \mathrm{d}k \left(\frac{1-\cos(k)}{(1+\epsilon)k^2-2+2\cos(k)}\right)\exp(ikx)\\ =&\int_{-R}^{R} \mathrm{d}k \left(\frac{1-\cos(k)}{(1+\epsilon)k^2-2+2\cos(k)}\right)\exp(ikx)+\mathcal{O}\left(\frac{1}{R}\right).\end{aligned}$$

Next, we aim on showing that there is a path $R \to C_1 \to C_2 \to -R$ so that the integration along that path gives zero contribution in the limit of large R.
Usually, if one deals with functions of the form $g(k)\,\exp(ixk)$ one can make use of Jordan's lemma which states that the integration along the semicircular contour in the upper half plan (lower half plan) for $x > 0$ ($x < 0$) aims to zero for the radius $R \equiv |k| \to \infty$. However, if $f(k)$ is rewritten in the form of $g(k)\,\exp(ixk)$ with $g(k) = (1-\cos(k))/((1+\epsilon)k^2 - 2(1-\cos(k)))$, we face the problem that $g(k)$ does not converge uniformly to zero since $g(k)$ has an infinite number of poles in the upper (and lower) half plane. So, to proceed further we aim on proving that there exists a path so that the contribution of the contour in the complex plane goes to zero for large radius.
First, note that

$$\mathrm{Re}\{\mathrm{Res}\{f(k)\}|_{k=a+ib}\} = -\mathrm{Re}\{\mathrm{Res}\{f(k)\}|_{k=-a+ib}\} \tag{3.150}$$

$$\mathrm{Im}\{\mathrm{Res}\{f(k)\}|_{k=a+ib}\} = \mathrm{Im}\{\mathrm{Res}\{f(k)\}|_{k=-a+ib}\}\,, \tag{3.151}$$

i.e., if the integration path is chosen in a way to symmetrically include the poles in the upper left and upper right quarter we know $\mathrm{Im}\{2\pi i \sum_j \mathrm{Res}_{k_j}\{f(k)\}\} = 0$. Hence, if the contour integral (Eq. 3.147) is calculated explicitly along such a path, the result has to be real. In the following, we

will make use of this fact. To prove that the integration along the contour in the complex plane goes to zero (for large R), we choose an explicit path along a rectangle as shown in Fig.3.36. More concretely, the vertices are defined by $R = 2n\pi$, $C_1 = 2n\pi + i2n\pi$ and $C_2 = -2n\pi + i2n\pi$ for $n \in \mathbb{N}$. Since the overall contour integral is real, we only care about terms which can give a real contribution, i.e., we investigate the real (imaginary) parts of the integrand for the integration paths parallel to the real (imaginary) axis:

$$\lim_{n\to\infty}\int_0^{2n\pi} \mathrm{d}b\, \mathrm{Im}\{f(k)|_{k=2n\pi+ib}\}$$
$$\lim_{n\to\infty}\int_{2n\pi}^{0} \mathrm{d}b\, \mathrm{Im}\{f(k)|_{k=-2n\pi+ib}\}$$
$$\lim_{n\to\infty}\int_{2n\pi}^{-2n\,\pi} \mathrm{d}a\, \mathrm{Re}\{f(k)|_{k=a+2n\pi\, i}\}\,.$$

To prove that those terms give zero contribution for $n \to \infty$ (and thereby $R \to \infty$), we aim on finding an integrable majorant of the above expressions, and then swap the integration and the limit. It is possible to show that

$$\mathrm{Im}\{f(k)|_{\pm 2n\pi+i\,b}\} < \exp(-b\,x)$$
$$\mathrm{Re}\{f(k)|_{a+2n\pi\,i}\} < \exp(-2n\pi\,x)\,.$$

Thus, we found an integrable majorant for both paths. Furthermore, since $\mathrm{Im}\{f(k)|_{2n\pi+i\,b}\} = -\mathrm{Im}\{f(k)|_{-2n\pi+i\,b}\}$, the discussion can be restricted to one of the paths $R \to C_1$ or $C_2 \to -R$. Moreover, as we found an integrable majorant for the parts of the contour in the complex plane, we can swap the integral and the limit. Since $\lim_{n\to\infty} |\mathrm{Im}\{f(k)|_{2n\pi+i\,b}\}| \to 0$, the paths $R \to C_1$ and $C_2 \to -R$ give zero contribution to the contour integral. The same holds true for the integration along the path $C_1 \to C_2$. Thus, the integration along the contour in the complex plane gives zero contribution for $n \to \infty$ and we can calculate the desired integral by

$$\int_{-\infty}^{\infty} \mathrm{d}k\, f(k) = 2\pi\, i \sum_j^{\infty} \mathrm{Res}_{k_j}\{f(k)\} = 2\pi\, \mathrm{Im}\left\{\left(\mathrm{Res}_{k_0}\{f(k)\} + 2\sum_{j=1}^{M} \mathrm{Res}_{k_j}\{f(k)\}\right)\right\}\,.$$

In the last step, we made use of Eq.3.150. In the following, we will denote the contribution of the k_0 residue to the integral as $f_0(x)$ and the contribution of the sum over all other poles as $f_\infty(x)$ Using the estimated expression for the poles of $f(k)$ and making use of the fact that b_n^* is large, we find an estimate for the imaginary part of the residue which reads

$$\mathrm{Im}\{\mathrm{Res}_{k_n}\{f(k)\}\} \approx \exp(-b_n x)\cos(a_n x)$$

for $n = 1...M$. Here, we assumed that $b_n x$ is sufficient large, i.e., we expect deviations for $x \to 0$. For k_0 we find the residue (for small ϵ)

$$f_0(x) = \mathrm{Res}_{k_0}\{f(k)\} \approx$$
$$\approx \frac{2\pi \sinh^2\left(\sqrt{24\sqrt{1+\epsilon}-24}\right)}{\sinh\left(\sqrt{24\sqrt{1+\epsilon}-24}\right) - (1+\epsilon)\sqrt{24\sqrt{1+\epsilon}-24}} \exp\left(-\sqrt{24\sqrt{1+\epsilon}-24}\,x\right)\,.$$

So, to find a closed form of the integral, we are left with finding an expression for the sum

$$
\begin{aligned}
f_\infty(x) &= 2\pi \sum_{n=1}^{\infty} \mathrm{Res}_{k_n}\{f(k)\} \\
&= 2\pi \sum_{n=1}^{\infty} \exp\left(-2\,\mathrm{arcosh}\left(\frac{2n+1}{2}\pi\sqrt{1+\epsilon}\right) x\right) \cos((2n+1)\pi\, x) \\
&\approx 2\pi \left(\frac{1}{\pi^2(1+\epsilon)}\right)^x \sum_{n=1}^{\infty} \frac{\cos((2n+1)\pi\, x)}{(2n+1)^{2x}} \\
&= \pi \left(\frac{1}{4\pi^2(1+\epsilon)}\right)^x \left[\exp(-3i\pi\, x)\ \phi(\exp(-2i\pi x, 2x, 3/2)) + \exp(3i\pi\, x)\ \phi(\exp(2i\pi x, 2x, 3/2))\right] .
\end{aligned}
\tag{3.152}
$$

For the approximation we used $\mathrm{arcosh}(x) \approx \ln(2x)$ for large x. Here, $\phi(z,s,\alpha) = \sum_{n=0}^{\infty} \frac{z^n}{n+\alpha}$ denotes the Lerch zeta function. Fig. 3.37 (A) shows a comparison between our analytic result and the sum over the first 5000 numerically obtained residues. For a better comparison, we also perform the sum over the approximated residue (Eq.3.152) for the first 5000 terms. Moreover, we compute the ratio of f_∞ / f_0 to get insight into how much f_∞ contributes to the overall integral.
Taken together, this yields the desired expression for the integral and, thereby, an expression for the interaction kernel in real space which reads

$$
\begin{aligned}
\int_{-\infty}^{\infty} \mathrm{d}k\, f(k) &= \frac{2\pi \sinh^2\left(\sqrt{24\sqrt{1+\epsilon}-24}\right)}{\sinh\left(\sqrt{24\sqrt{1+\epsilon}-24}\right) - (1+\epsilon)\sqrt{24\sqrt{1+\epsilon}-24}} \exp\left(-\sqrt{24\sqrt{1+\epsilon}-24}\, x\right) \\
&+ \pi \left(\frac{1}{4\pi^2(1+\epsilon)}\right)^x \left[\exp(-3i\pi\, x)\ \phi\left(\exp(-2i\pi x), 2x, \frac{3}{2}\right) + \exp(3i\pi\, x)\ \phi\left(\exp(2i\pi x), 2x, \frac{3}{2}\right)\right] .
\end{aligned}
\tag{3.153}
$$

This expression, however, is not particularly intuitive. Therefore, we seek for a simpler and more meaningful expression.
Fig. 3.37 (B) indicates that f_∞ is not particularly relevant for the overall integral, i.e., it is promising to use only the $0th$ residue to approximate the integral. Moreover, ϵ is known to be small for biologically meaningful parameters. In hindsight, one can argue that a value of $\epsilon > 1/12$ is not particularly meaningful since for $\epsilon < 1/12$ our result suggests an interaction range $l_c < L$, implying that the microtubules interact only over a distance smaller than one microtubule length. Therefore, it makes sense to consider the limit of small ϵ. Using only the $0th$ residue and considering the lowest order of ϵ yields

$$
f(x) \approx \pi \frac{\sqrt{3}}{\sqrt{\epsilon}} \exp(-\sqrt{12\epsilon}x) . \tag{3.154}
$$

Fig. 3.36 (B) shows the estimate of the imaginary pole in comparison to the more accurate estimate and the numeric result. Fig. 3.38 shows a comparison between the numerical solution of the integral, our analytic expression (Eq. 3.153) and the $0th$ residue approximation for small ϵ (Eq. 3.154).

Finally, making use of the convolution theorem, Eq. 3.154 and Eq. 3.139 yield the desired expression for the filament velocity. Going back to natural variables, i.e., $x \to x\, L$ and $v^{(+)} \to v^{(+)} + \frac{\alpha}{\epsilon} V_\mathrm{m}$ gives the expression used in the main text:

$$
v^{(+)}(x) = V_\mathrm{m}(1-\alpha)\left(1 - \frac{1}{2\, l_c} \int_{-\infty}^{\infty} \mathrm{d}y\, P(y) \exp\left(-\frac{|x-y|}{l_c}\right)\right)
$$

where we introduced $l_c = L/\sqrt{12\epsilon}$. The occurrence of the absolute value is due to the fact that an integration over the lower half plane gives an analogous result as compared to the one for the upper half-plane.

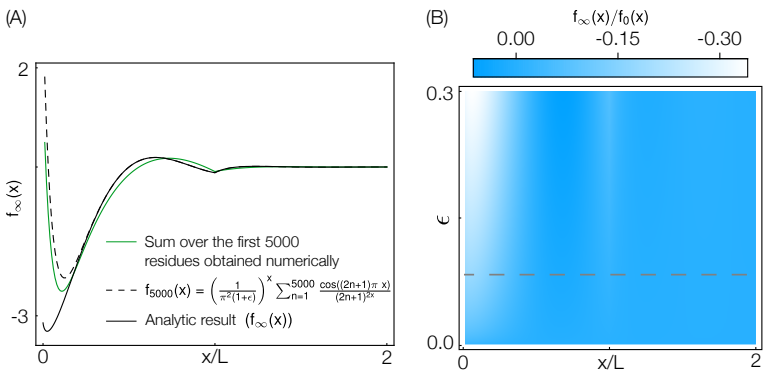

Figure 3.37: (**A**) Analytic result for the sum over the residues in the complex plane in comparison to the sum over the first 5000 numerically obtained residues. To provide a more accurate comparison, we also compute Eq.3.152 for the first 5000 terms. (**B**) To compare the contribution of the k_0 residue and the sum over the other residues to the overall integral, we plot the ratio $f_\infty(x)/f_0(x)$. The dashed line indicates the ϵ value where $l_c \approx L$

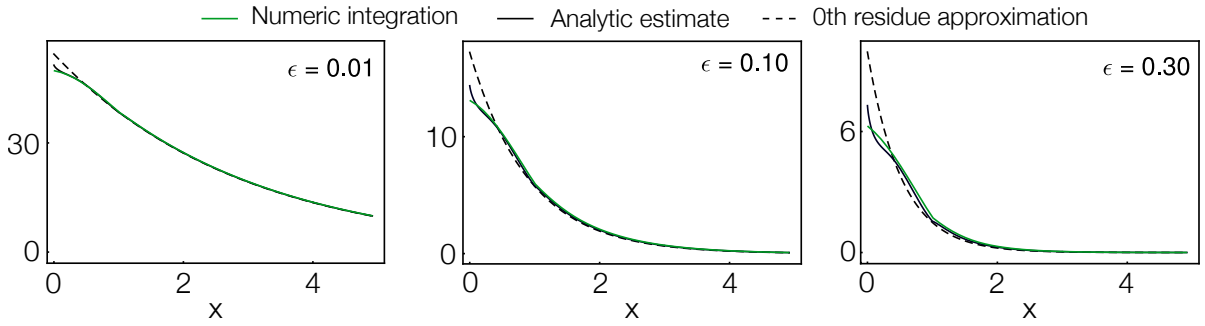

Figure 3.38: Comparison between numerical integration, analytic approximation and the 0th residue approximation used in the main text. Note that the deviation between the approximations for larger ϵ is manly caused by the wrong estimate of the k_0 residue.

Extension of the analysis to systems with several different types of crosslinking motors In the main text, we focus our analysis on the case where there is only one type of motor in the system, namely a crosslinking motor whose two heads are both active and walk to the plus end of the respective microtubule. However, there are also other types of crosslinking motors, for instance motors with only one active head and one passive one that does not move on the microtubule (see Fig. 3.39 for an illustration). Our analysis can be straightforwardly extended to such other types of crosslinking motors as long as the dominant part of their force generation still happens in the bulk of microtubules and not at the end:[4] More concretely, let us look at a system with five different types of motors (see also Fig. 3.39 for an illustration):

- one passive crosslinker with two passive heads: P
- two active crosslinkers with two active heads both moving to the $\pm$ end of the microtubule, respectively: $A_\pm$
- two types of crosslinkers ("mixed") with one passive head and one active head that moves to the $\pm$ end of the microtubule, respectively: $M_\pm$.

[4] The latter case is true for motors such as dynein which exhibit a much higher residence time at the microtubule minus ends as compared to the bulk (e.g. [96]).

Furthermore, we again assume a linear force-velocity relation for all motors.

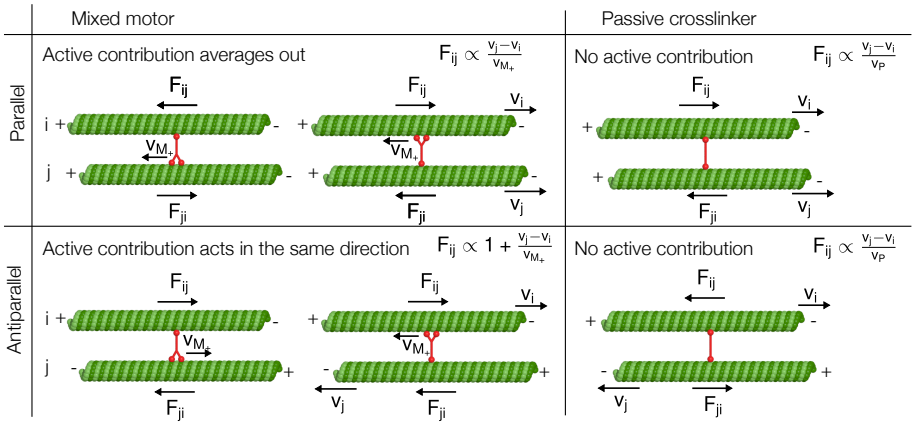

Figure 3.39: Microscopic, motor-mediated interactions between microtubules for different types of motors. Passive crosslinkers have two passive heads that do not move along the microtubule. “Mixed" motors have one active and one passive head.

The passive crosslinker does not exert any active forces between a pair of microtubules but resists relative motion of the two microtubules, irrespective of their relative orientation:

$$F_P^{(\pm\pm)}(x,y) = F_P\left(\frac{v^{(\pm)}(y) - v^{(\pm)}(x)}{v_P}\right)$$
$$F_P^{(\pm\mp)}(x,y) = F_P\left(\frac{v^{(\mp)}(y) - v^{(\pm)}(x)}{v_P}\right),$$

where $F_P^{(\pm\pm)}(x,y)$ is the force a $(\pm)$ microtubule at position y exerts on a parallel $(\pm)$ microtubule at position x. Similarly, $F_P^{(\pm\mp)}(x,y)$ denotes the force a $(\pm)$ microtubule at position y exerts on an antiparallel $(\mp)$ microtubule at position x. F_P denotes the motor force arising for a relative velocity v_P.

The active crosslinker with both heads moving to the $(+)$ end is the one we already described in the main text. It exerts an active force on antiparallel microtubules and resists relative motion of the two crosslinked microtubules, irrespective of the relative orientation:

$$F_{A_+}^{(\pm\pm)}(x,y) = F_{A_+}\left(\frac{v^{(\pm)}(y) - v^{(\pm)}(x)}{2v_{A_+}}\right)$$
$$F_{A_+}^{(\pm\mp)}(x,y) = F_{A_+}\left(\pm 1 + \frac{v^{(\mp)}(y) - v^{(\pm)}(x)}{2v_{A_+}}\right).$$

Similarly, the active crosslinker with heads moving towards the $(-)$ end exerts the following forces:

$$F_{A_-}^{(\pm\pm)}(x,y) = F_{A_-}\left(\frac{v^{(\pm)}(y) - v^{(\pm)}(x)}{2v_{A_-}}\right)$$
$$F_{A_-}^{(\pm\mp)}(x,y) = F_{A_-}\left(\mp 1 + \frac{v^{(\mp)}(y) - v^{(\pm)}(x)}{2v_{A_-}}\right).$$

$F_{A_\pm}$ denotes the force the motor exerts between two antiparallel microtubules that do not move relative to each other. $v_{A_\pm}$ corresponds to the motor speed of each head along the microtubule.

Finally, the mixed crosslinkers shows “mixed" behavior. For parallel microtubules they behave on average like any other crosslinker (see Fig. 3.39 for an illustration): Consider a situation where two

static (+) microtubules are crosslinked. Then, the mixed crosslinker can be bound either with the active head on microtubule 1 and with the passive one on microtubule 2 or the other way round. In the first case, the $M_\pm$ motor moves microtubule 1 in the $\pm$ direction and microtubule 2 in the $\mp$ direction. In the second case, it is just the opposite: microtubule 1 is pushed in the $\mp$ direction whereas microtubule 2 is pushed in the $\pm$ direction. Since both configurations occur with equal probability, the active contributions does cancel for parallel microtubules. For antiparallel microtubules, on the other hand, the direction of movement of the $(\pm)$ microtubule is always the same, irrespective of which heads is bound to which microtubule. The $M_\pm$ motor moves the (+) microtubule in $\pm$ direction and the (−) microtubule in the $\mp$ direction. For antiparallel microtubules, the active contributions thus do not cancel but are equivalent to the $A_\pm$ motor with two active heads. The passive contribution, steming from relative motion of the microtubules, is always the same: It acts against the direction of motion, irrespective of which head is bound where and how the relative orientation is.

Taken together, the mixed crosslinker with one active and one passive head behaves similarly to any other crosslinker in the case of parallel microtubules and similarly to an active crosslinker in the case of antiparallel microtubules:

$$F_{M_+}^{(\pm+)}(x,y) = F_{M_+}\left(\frac{v^{(\pm)}(y) - v^{(\pm)}(x)}{v_{M_+}}\right)$$
$$F_{M_+}^{(\pm-)}(x,y) = F_{M_+}\left(\pm 1 + \frac{v^{(\mp)}(y) - v^{(\pm)}(x)}{v_{M_+}}\right),$$

for the mixed motor M_+ with active head moving to the + end, and

$$F_{M_-}^{(\pm+)}(x,y) = F_{M_-}\left(\frac{v^{(\pm)}(y) - v^{(\pm)}(x)}{v_{M_-}}\right)$$
$$F_{M_-}^{(\pm-)}(x,y) = F_{M_-}\left(\mp 1 + \frac{v^{(\mp)}(y) - v^{(\pm)}(x)}{v_{M_-}}\right),$$

for the mixed motor M_- with active head moving to the − end. $F_{M_\pm}$ denotes the force a $M_\pm$ motor exerts on two static, antiparallel microtubules and $v_{M_\pm}$ is the motor speed of the active head.

Summing all the contributions from all motor types, the total force exerted on a (+) microtubule at position x by parallel (+) microtubules is given by

$$F^{(++)}(x) = \int_{x-L}^{x+L} \frac{\mathrm{d}z}{L}\, \frac{L_{\mathrm{ov}}(x,z)}{L} \varphi^{(+)}(z) C\left(v^{(+)}(z) - v^{(+)}(x)\right),$$

where $L_{\mathrm{ov}}(x,z) = \max(L - |x-z|, 0)$ denotes the overlap between two microtubules at positions x and z as defined in the main text. Furthermore, N_P, $N_{A_\pm}$ and $N_{M_\pm}$ denote the number of passive P, active $A_\pm$ and mixed crosslinkers $M_\pm$ per microtubule, respectively. Furthermore, we defined the sum of the absolute force to velocity ratios

$$C = \frac{N_P F_P}{v_P} + \frac{N_{A_+} F_{A_+}}{2 v_{A_+}} + \frac{N_{A_-} F_{A_-}}{2 v_{A_-}} + \frac{N_{M_+} F_{M_+}}{v_{M_+}} + \frac{N_{M_-} F_{M_-}}{v_{M_-}}.$$

Similarly, the total force on a (+) microtubule at position x by antiparallel (−) microtubules is given by

$$F^{(+-)}(x) = \int_{x-L}^{x+L} \frac{\mathrm{d}z}{L}\, \frac{L_{\mathrm{ov}}(x,z)}{L} \varphi^{(-)}(z) \left(C\left(v^{(-)}(z) - v^{(+)}(x)\right) + D\right),$$

where we defined D as the sum of the motor forces

$$D = N_{A_+} F_{A_+} + N_{M_+} F_{M_+} - N_{A_-} F_{A_-} - N_{M_-} F_{M_-}.$$

The forces on the (−) microtubules are determined analogously:

$$F^{(--)}(x) = \int_{x-L}^{x+L} \frac{\mathrm{d}z}{L} \frac{L_{\mathrm{ov}}(x,z)}{L} \varphi^{(-)}(z) C\left(v^{(-)}(z) - v^{(-)}(x)\right)$$
$$F^{(-+)}(x) = \int_{x-L}^{x+L} \frac{\mathrm{d}z}{L} \frac{L_{\mathrm{ov}}(x,z)}{L} \varphi^{(+)}(z) \left(C\left(v^{(+)}(z) - v^{(-)}(x)\right) - D\right).$$

Now, we proceed analogously to the case with only one motor:

$$\gamma v^{(+)}(x) = \int_{x-L}^{x+L} \frac{\mathrm{d}z}{L} \frac{L_{\mathrm{ov}}(x,z)}{L} \left(\varphi^{(+)}(z) C\left(v^{(+)}(z) - v^{(+)}(x)\right) + \varphi^{(-)}(z) C\left(v^{(-)}(z) - v^{(+)}(x)\right) + \varphi^{(-)}(z) D\right) \tag{3.155}$$

$$\gamma v^{(-)}(x) = \int_{x-L}^{x+L} \frac{\mathrm{d}z}{L} \frac{L_{\mathrm{ov}}(x,z)}{L} \left(\varphi^{(-)}(z) C\left(v^{(-)}(z) - v^{(-)}(x)\right) + \varphi^{(+)}(z) C\left(v^{(+)}(z) - v^{(-)}(x)\right) - \varphi^{(+)}(z) D\right). \tag{3.156}$$

Subtracting those two equations from one another and performing the integral $\int_{x-L}^{x+L} \frac{\mathrm{d}z}{L} \frac{L_{\mathrm{ov}}(x,z)}{L} = 1$, we find

$$\gamma\left(v^{(+)}(x) - v^{(-)}\right) = \int_{x-L}^{x+L} \frac{\mathrm{d}z}{L} \frac{L_{\mathrm{ov}}(x,z)}{L} \left(D + C\left(v^{(-)}(x) - v^{(+)}(x)\right)\right) = D + C\left(v^{(-)}(x) - v^{(+)}(x)\right).$$

As a result,

$$v^{(-)}(x) = v^{(+)}(x) - \frac{D}{\gamma + C}, \tag{3.157}$$

which is the generalization of Eq. 3.136.

As for the original case, this result can be plugged into Eq. 3.155, effectively decoupling the two equations. It follows that

$$\tilde{\epsilon} v^{(+)}(x) - \frac{D}{2C}\frac{\gamma}{\gamma + C} = \int_{x-L}^{x+L} \frac{\mathrm{d}z}{L} \frac{L_{\mathrm{ov}}(x,z)}{L} \left(v^{(+)}(z) - v^{(+)}(x)\right) - \frac{D}{2C}\frac{\gamma}{\gamma + C} \int_{x-L}^{x+L} \frac{\mathrm{d}z}{L} \frac{L_{\mathrm{ov}}(x,z)}{L} P(z),$$

where we defined $\tilde{\epsilon} = \gamma / C$ and used that we can write the densities in terms of the polarity $\varphi^{(\pm)}(z) = (1 \pm P(z))/2$. Comparing this expression with the analogous result, Eq. 3.137, we realize that

$$\epsilon = \frac{\gamma}{\frac{F_m N_m}{2V_m}} \to \tilde{\epsilon} = \frac{\gamma}{C}$$
$$V_m \alpha = V_m \frac{\gamma}{\gamma + \frac{F_m N_m}{2V_m}} \to \frac{D}{2C}\frac{\gamma}{\gamma + C}$$

Performing the same steps as above, we can thus conclude

$$v^{(+)}(x) = \frac{D}{2(\gamma + C)} \left(1 - \frac{1}{2l_c} \int_{-\infty}^{\infty} \mathrm{d}y \, P(y) e^{-|x-y|/l_c}\right) \tag{3.158}$$

$$v^{(-)}(x) = -\frac{D}{2(\gamma + C)} \left(1 + \frac{1}{2l_c} \int_{-\infty}^{\infty} \mathrm{d}y \, P(y) e^{-|x-y|/l_c}\right), \tag{3.159}$$

with the characteristic length

$$l_c = L\sqrt{\frac{C}{12\gamma}} \tag{3.160}$$

with the motor forces F_i, number of motors per filament N_i and relevant motor velocities v_i. The factors f_i are 1 for $A_\pm$ and 1/2 for $M_\pm$, corresponding to the fraction of active heads, and 0 for P due to the convention chosen. The prefactor is

$$\frac{D}{2(\gamma+C)} = \frac{N_{A_+}F_{A_+} + N_{M_+}F_{M_+} - N_{A_-}F_{A_-} - N_{M_-}F_{M_-}}{2\left(\gamma + \sum_{i=P,A_\pm,M_\pm} \frac{N_i F_i}{2 v_i f_i}\right)}. \tag{3.161}$$

Thus, the characteristic length is determined by the ratio between the friction in the fluid and the "friction" between all crosslinked microtubules. This friction is determined by the sum of the passive contribution of all motors, irrespective of their direction of motion or whether they are active or not. This passive contribution is independent of the motor properties as each motor resists relative motion of filaments compared to the favored relative velocity. In contrast, for the maximal speed of the microtubules $D/2/(\gamma+C)$ the direction of the motors is relevant, as expected: D does not correspond to an absolute sum of the different motor types but motors with opposite direction of motion enter with opposite sign, effectively competing against each other.

On a broader perspective, we conclude that systems with different types of motors behave qualitatively similarly as the original system. Their characteristic length only depends on the total passive forces exerted by all motor types and the sign and magnitude of the velocities are determined by the competition between the active motor contributions.

This result provides an insightful intuitive explanation for the characteristic length l_c. The only non-collective length scale in the system is L, the length of microtubules. Hence, by a basic scaling argument, l_c needs to be a linear function of L, multiplied by a dimensionless quantity. The only meaningful combination of the system parameters yielding a dimensionless quantity is the ratio of the different forces in the system: drag in the fluid and forces between microtubules. But, which are the relevant forces between microtubules? Is it the averaged active force on the microtubules or rather the total "friction" between microtubules induced by the motor resistance to relative motion? To obtain an intuitive answer to this question, consider a system with two types of motors whose heads move in the opposite direction. Then, for an equal proportion of both types, the average active force on all microtubules is zero, irrespective of the absolute number of motors. The force propagation through the network, however, should depend on the number of links in the network or, equivalently, the absolute number of motors. The same is true for the friction between microtubules that linearly increases with the absolute number of motors. Taken together, this suggests that l_c should depend on the total friction between microtubules rather than on the averaged active forces. Thus, l_c should be proportional to L and a function of the ratio between the drag in the fluid γV_m and the total filament friction $F_m N_m$. Note that it remains unclear from this intuitive argument why the functional dependence is given by a square root.

FOURIER REPRESENTATION OF THE AMBIENT POLARITY

The ambient polarity is given by the convolution of the local polarity with an exponentially decaying interaction kernel, Eq. 3.108b. As the Fourier transformation of a convolution of two functions is given by the product of the two Fourier transformations, it is instructive to consider the Fourier representation of the polarities. We distinguish two cases. First, we consider an infinite system where the fields are defined on the entire real axis, and, second, a periodic system with period R.

Infinite case For a polarity, $P(x)$, defined on the real axis, $x \in \mathbb{R}$, we define the Fourier transformation as

$$\hat{P}(k) = \frac{1}{2\pi}\int_{-\infty}^{\infty} \mathrm{d}y\, P(y) e^{iky}, \qquad k \in \mathbb{R},$$

with the corresponding back transformation $P(x) = \int_{-\infty}^{\infty} \mathrm{d}k\, \hat{P}(k) e^{-ikx}$. Similarly, the Fourier transformation of the ambient polarity is

$$\begin{aligned}\hat{\Pi}(k) &= \frac{1}{2\pi}\int_{-\infty}^{\infty} \mathrm{d}y\, \Pi(y) e^{iky} \\ &= \frac{1}{2\pi}\int_{-\infty}^{\infty} \mathrm{d}z P(z) \frac{1}{2l_c}\int_{-\infty}^{\infty} \mathrm{d}y\, e^{-|y-z|/l_c} e^{iky} \\ &= \hat{P}(k)\frac{1}{1+(kl_c)^2} \equiv \hat{P}(k)\hat{K}(k), \end{aligned} \tag{3.162}$$

where we exchanged the integrals and performed the Fourier transformation of the exponentially decaying interaction kernel, $\hat{K}(k) = 1/(1+(kl_c)^2)$. This result implies that the spatial modes are suppressed according to a Lorentzian. So, faster fluctuations are damped more, and the ambient polarity does not exhibit spatial variations corresponding to large wave vectors $k \gg 1/l_c$ (small wavelength). Intuitively, the lack of fast fluctuations in the ambient polarity is due to the averaging of local polarities in a range of size l_c. As we will see in the following, we get a very similar result in the periodic case.

Finite interval with periodic continuation If the system is periodic with period R, the polarity, $P(x)$, $x \in [0, R]$, is described by a Fourier series, $P(x) = \sum_{n=-\infty}^{\infty} \hat{P}_n e^{-in\frac{2\pi}{R}x}$, with Fourier coefficients

$$\hat{P}_n = \frac{1}{R}\int_0^R \mathrm{d}y\, P(y) e^{in\frac{2\pi}{R}y}, \qquad n \in \mathbb{Z}. \tag{3.163}$$

The Fourier coefficients for the ambient polarity, $\hat{\Pi}_n$, $n \in \mathbb{Z}$, are given by

$$\begin{aligned}\hat{\Pi}_n &= \frac{1}{R}\int_0^R \mathrm{d}y\, \Pi(y) e^{in\frac{2\pi}{R}y} \\ &= \frac{1}{R}\sum_{m=-\infty}^{\infty}\int_0^R \mathrm{d}w\, P(w+mR) e^{in\frac{2\pi}{R}w} \frac{1}{2l_c}\int_{-mR-w}^{-(m-1)R-w} \mathrm{d}v\, e^{-|v|/l_c} e^{in\frac{2\pi}{R}v} e^{in2\pi m} \\ &= \frac{1}{R}\int_0^R \mathrm{d}w\, P(w) e^{in\frac{2\pi}{R}w} \frac{1}{2l_c}\int_{-\infty}^{\infty} \mathrm{d}v\, e^{-|v|/l_c} e^{in\frac{2\pi}{R}v} \\ &= \hat{P}_n \frac{1}{1+(2\pi l_c n/R)^2} \equiv \hat{P}_n \hat{K}\left(\frac{2\pi n}{R}\right). \end{aligned} \tag{3.164}$$

In these steps, we exchanged the integrals and used that the infinite integral can be expressed in terms of an infinite sum of integrals over a period R each. Furthermore, we used the substitutions $w = z - mR$ and $v = y - mR - w$ and the periodicity: $P(w+mR) = P(w)$ and $e^{in2\pi m} = 1$ for $m \in \mathbb{Z}$. We could have guessed this result from the result of the infinite case, Eq. 3.162, as in the periodic case only wave vectors k which are a multiple of $2\pi/R$ are possible: $k = n2\pi/R$ for some $n \in \mathbb{Z}$. So, again, fast fluctuations are strongly suppressed in the ambient polarity.

Relevance Importantly, these results are not restricted to a specific class of polarity profiles but generally capture the relationship between the local and ambient polarity in an infinite (large) system. Hence, the ambient polarity (the velocity) is expected to vary at most on length scales larger than the characteristic length l_c. Related to this, extreme values of the local polarity are averaged out and do not show up in the distribution of velocities. This observation is illustrated by two examples in the main text, namely the pedagogical case with linear polarity profile and the *in silico* study with random polarity profile.

Linear polarity profile As a first example to illustrate the relationship between the ranges of local and ambient polarity, we consider a linear polarity profile $P(x) = a * (x - S/2)$ on a finite interval $x \in [0, S]$ (where $|a| \leq 2/S$ to ensure that the polarity does not exceed ± 1). This situation is in contrast to the main analysis in the manuscript which focuses on an infinite system. Consequently, we have to specify some boundary conditions.

Motivation of boundary conditions In order to fix the boundary conditions, we start from the premise that even at the boundary, the system is dense and the number of interaction partners of a microtubule is limited by the number of neighbors and not by the overall number of microtubules. In other words, the number of interaction partners per microtubules is the same, irrespective of whether the microtubule is located in the bulk of the system or at the boundary. This implies that microtubules at the left (right) boundary have twice as many crosslinks towards their right (left) as compared to microtubules in the bulk of the system (and none to the left (right) due to the boundary). To approximately account for this effect, we mirror the polarity profile at its boundaries $x = 0$ and $x = S$, so we have $P(-x) = P(x)$ and $P(S - x) = P(S + x)$. By repeated application of this mirroring, the polarity profile is continued to the entire real axis. The resulting continued spatial polarity profile is $2S$ periodic. Thus, we approximate our finite system by a periodically continued spatial polarity field with the same (infinite) interaction kernel $\exp(-|x - y|/l_c)$ as for the infinite system.

Fourier coefficients The local polarity is represented by a Fourier series with Fourier coefficients given in Eq.3.163 for $R = 2S$. More concretely, due to the symmetry $P(x) = P(-x)$ the Fourier coefficients are given by

$$\begin{aligned}\hat{P}_n &= \frac{1}{2S}\int_{-S}^{S} \mathrm{d}y\, P(y) e^{in\frac{\pi}{S}y} \\ &= \frac{1}{2S}\int_{0}^{S} \mathrm{d}y\, a\left(y - \frac{S}{2}\right)(e^{in\frac{\pi}{S}y} + e^{-in\frac{\pi}{S}y}) = \begin{cases} -a\frac{2S}{n^2\pi^2} & \text{n odd} \\ 0 & \text{n even.} \end{cases}\end{aligned}$$

Eq. 3.164 then implies that the Fourier coefficients of the ambient polarity are given by

$$\hat{\Pi}_n = \begin{cases} -a\frac{2S}{n^2\pi^2(1+(\pi l_c n/S)^2)} & \text{n odd} \\ 0 & \text{n even.} \end{cases}$$

Ratio between the ambient and local polarity range

From the Fourier coefficients, we can straightforwardly determine the ratio between the ranges of local and ambient polarity. Due to the monotonicity of the local polarity and the from-the-center decreasing interaction kernel, the maximum (minimum) of the ambient polarity is at the same location as the maximum (minimum) of the local polarity. In order to compute the ratio between the two ranges of values, it is thus sufficient to determine the ambient polarity at $x = S$ where it attains its maximum (due to the symmetry, the minimal value at $x = 0$ corresponds to the inverse of the maximal value):

$$\begin{aligned}\Pi_{\max} &= \Pi(x = S) \\ &= \left(1 - \frac{2l_c}{S}\tanh\left(\frac{S}{2l_c}\right)\right)\frac{aS}{2} = \left(1 - \frac{2l_c}{S}\tanh\left(\frac{S}{2l_c}\right)\right)P_{\max},\end{aligned}$$

where we used that $P_{\max} = P(x = S) = aS/2$. A more instructive expression can be obtained by using a large wavelength approximation, describing the local and ambient polarities by their lowest

modes $n = \pm 1$, $P(x) \approx 2\hat{P}_1 \cos(\frac{\pi}{S}x)$ and $\Pi(x) \approx 2\hat{\Pi}_1 \cos(\frac{\pi}{S}x)$. Thereby, the ratio of the ranges of the local and ambient polarity is approximately

$$\frac{\Pi_{\max}}{P_{\max}} \approx \frac{\hat{\Pi}_1}{\hat{P}_1} = \frac{1}{1+(\pi l_c/S)^2}.$$

As can be seen in Figure 3.23, this expression is a fairly good approximation, in particular for large enough l_c/S as expected. It predicts that the range of the ambient polarity is strongly "squeezed" for large characteristic length.

EXTENSION OF THE *in silico* STUDY TO A BROADER CLASS OF SYSTEMS

The analysis in section 3.3.2 in the main text is based on the assumption that the polarity field does not have any spatial structure. That is, the system is translationally invariant, and - on average - all positions are equivalent. However, generally, this premise will not be fulfilled. In this appendix, we thus want to extend our previous analysis to a broader class of systems.

As we have seen before in the main text the variance of the ambient polarity, $\mathrm{Var}[\Pi]$, depends on the autocorrelation of the local polarity $\langle P(x)P(y)\rangle$. Thus, in order to make any statements about the distribution of the ambient polarity, we need to make some assumptions on the correlation of the local polarities at different locations. The most obvious property of the system that leads to correlations of the local polarities at different locations is the finite extension of microtubules. As discussed before, due to the finite microtubule length $L > 0$, an excess of microtubules at one position leads to an excess of microtubules at distances maximally L apart. In the following, we will assume that this contribution to the correlation dominates, and that there are only weak correlation effects, for instance due to filament dynamics or feedback. We believe that in this case it is reasonable to assume that the covariance of the local polarity at different positions (the autocorrelation) decays linearly with distance up to $|x-y| = L$:

$$\mathrm{Cov}[P](x,y) \equiv \langle P(x)P(y)\rangle - \langle P(x)\rangle\langle P(y)\rangle \approx \mathrm{Var}[P]\left(1-\frac{|x-y|}{L}\right)\Theta\left(L-|x-y|\right). \tag{3.165}$$

Here we furthermore assumed that the magnitude of the fluctuations in the polarity is similar everywhere: $\mathrm{Var}[P]$ is approximately spatially invariant.

We will restrict our discussion to this class of system as quantitative statements for the general case are difficult to obtain.

Prediction Let us consider systems where Eq. 3.165 holds. Suppose we measure the spatial profile of the average of the local polarities and of the velocities, $\langle P(x)\rangle$ and $\langle v^{(\pm)}(x)\rangle$, where the average denotes an ensemble average at fixed position x. Moreover, we determine the average variance of the local polarity $\mathrm{Var}[P] = \langle \mathrm{Var}[P(x)]\rangle_x$, where $\mathrm{Var}[P(x)] = \langle P(x)^2\rangle - \langle P(x)\rangle^2$ is the variance of the local polarity at fixed position x and $\langle\rangle_x$ denotes an average over all locations x. Then, our theory predicts that the covariance of the velocity at different positions is

$$\begin{aligned}
\mathrm{Cov}[v^{(+)}](x,y) &\equiv \langle v^{(+)}(x)\,v^{(+)}(y)\rangle - \langle v^{(+)}(x)\rangle\langle v^{(+)}(y)\rangle = \\
&= V_m^2(1-\alpha)^2\left(\langle(1-\Pi(x))(1-\Pi(y))\rangle - \langle 1-\Pi(x)\rangle\langle 1-\Pi(y)\rangle\right) = \\
&= V_m^2(1-\alpha)^2\left(\langle\Pi(x)\Pi(y)\rangle - \langle\Pi(x)\rangle\langle\Pi(y)\rangle\right) = \\
&= V_m^2(1-\alpha)^2\frac{1}{4l_c^2}\int_{-\infty}^{\infty}\mathrm{d}z_1\int_{-\infty}^{\infty}\mathrm{d}z_2\, e^{-\frac{|x-z_1|}{l_c}}e^{-\frac{|y-z_2|}{l_c}}\left(\langle P(z_1)P(z_2)\rangle - \langle P(z_1)\rangle\langle P(z_2)\rangle\right).
\end{aligned}$$

Using assumption 3.165, this expression becomes

$$\begin{aligned}&\mathrm{Cov}[v^{(+)}](x,y) = \\ &= V_m^2(1-\alpha)^2\mathrm{Var}[P]\frac{1}{4l_c^2}\int_{-\infty}^{\infty}\mathrm{d}z_1\int_{-\infty}^{\infty}\mathrm{d}z_2 e^{-\frac{|x-z_1|}{l_c}}e^{-\frac{|y-z_2|}{l_c}}\left(1-\frac{|z_1-z_2|}{L}\right)\Theta\left(L-|z_1-z_2|\right),\end{aligned}$$

which holds for the velocities $v^{(-)}$ as well. For general distance $x-y$, the analytic expression is not very insightful and the expression is best understood graphically.

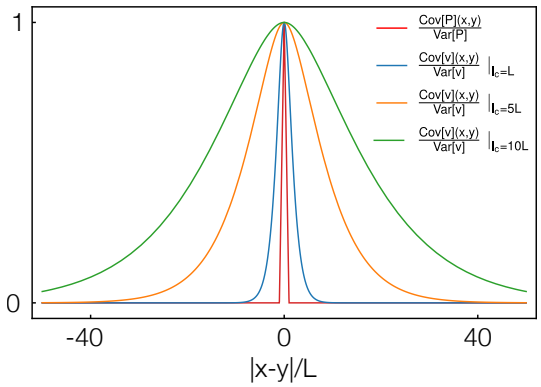

Figure 3.40: Comparison of the autocorrelation coefficient of the local polarity, $\mathrm{Cov}[P](x,y)/\mathrm{Var}[P]$, and of the velocity, $\mathrm{Cov}[v^{(\pm)}](x,y)/\mathrm{Var}[v^{(\pm)}]$, for different values of the characteristic length l_c. The velocity correlations decay much slower as compared to the correlations in the local polarity. The correlation length of the velocity scales with l_c, that is, for larger l_c, the correlations length is larger as well.

Fig. 3.40 shows a comparison between the normalized covariance of the local polarities (the autocorrelation coefficient), $\mathrm{Cov}[P](x,y)/\mathrm{Var}_P$, and of the velocity, $\mathrm{Cov}[v^{(\pm)}](x,y)/\mathrm{Var}[v^{(\pm)}]$, for different l_c. Whereas the correlation of the local polarity quickly decays to zero (after a distance $|x-y|=L$), the correlation of the velocities is much more long-ranged and its correlation length increases with l_c.

The covariance of the velocity for $x=y$, $\mathrm{Cov}[v^{(+)}](x,x)$, which corresponds to the variance of the velocity $\mathrm{Var}[v^{(\pm)}]$, is given as

$$\mathrm{Var}[v^{(+)}] = V_m^2(1-\alpha)^2\mathrm{Var}[P]\left(1-\frac{3l_c}{2L}\left(1-e^{-\frac{L}{l_c}}\right)+\frac{1}{2}e^{-\frac{L}{l_c}}\right),$$

in terms of the variance of the local polarity, $\mathrm{Var}[P]$. Similarly, the variance of the ambient polarity, $\mathrm{Var}[\Pi]$, is given by

$$\mathrm{Var}[\Pi] = \mathrm{Var}[P]\left(1-\frac{3l_c}{2L}\left(1-e^{-\frac{L}{l_c}}\right)+\frac{1}{2}e^{-\frac{L}{l_c}}\right).$$

So, for the broader class of systems considered here we recover exactly the same result as for the *in silico* study.

COMPARISON OF OUR RESULTS FOR SMALL CHARACTERISTIC LENGTH TO THE DILUTE LIMIT

One of the central results of our work is that there is an intrinsic length scale of the system that determines the velocity-polarity relation. This characteristic length l_c captures how far information

on the local forces propagates through the network. Naively, one can argue that for dilute systems l_c is small and, correspondingly, that forces only act locally. This conclusion fits well with the intuitive conception of a dilute limit where filaments are arranged in disconnected patches. Nonetheless, one has to be careful to directly compare our result to the dilute limit. With regard to this limit, there are two main assumptions in our continuum theory.

1. *Single patch:* All microtubules are directly or indirectly (via other microtubules) connected to each other and there are no disconnected patches of microtubules. This assumption corresponds to hypothesizing that the filament network works above the percolation threshold and that the average number of interaction partners N is not too small.

2. *Sufficient interaction partners:* The number of neighbors a microtubule interacts with is limited by the average number of interaction partners N and not by the number of neighbors. This assumption is based on the idea that there is always a sufficient number of neighbors (possible interaction partners) present for each microtubule. Instead of linearly depending on the microtubule densities, the force thus exhibits a dependency on the fraction $\varphi^{(\pm)}$ (Eq. 3.106).

Both assumptions do not necessarily apply to the dilute limit. We believe that the second assumption regarding a sufficient number of interaction partners can be readily relaxed also within a continuum description. For this purpose, one could, for instance, try to incorporate a phenomenological term $N\rho^{(\pm)}/(N+\rho^{+}+\rho^{-})$ for the number of interactions with $(\pm)$ microtubules. Such a term would converge to $N\varphi^{(\pm)}$ for large total density $\rho \equiv \rho^{+}+\rho^{-} \gg N$, as used in our description. Conversely, for small ρ it captures a linear dependency of the number of $(\pm)$ interactions on the respective density. Taken together, investigating how such an effective term changes the behavior should be instructive for a more quantitative understanding of the dilute limit.

The first assumption is conceptually more difficult to overcome within a continuum description. But indeed, for parameters estimated as in section "3.3.2", regions with zero density (and thus disconnected patches) occur regularly in our stochastic, agent-based simulation. These empty spaces arise due to the stochastic loss of connections between microtubules and a following drifting apart of different patches. Vice versa, such empty spaces stochastically vanish again if two patches meet. The interplay of these opposing, stochastic processes leads to patch boundaries that are not static but change randomly. We suppose that one could effectively incorporate this behavior into our continuum theory. To this end, one might first consider systems of finite sizes and then try to average their behavior with regard to exponentially distributed system sizes. Intuitively, we would expect that this procedure leads to an enhanced effective attenuation and thus to a lower effective value of the characteristic length l_c but does not change our results qualitatively: Due to the stochastic loss of connections between patches (particularly for systems close to the percolation threshold), there is not only loss of information due to drag but also abruptly at the boundaries of the patches. If these boundaries are fluctuating, the abrupt loss at the boundaries is on average smoothed and should be qualitatively comparable to a continuous loss of information by drag.

Overall, we think that - despite these assumptions of our theory - our results help bridging the gap between previous findings for dilute and heavily crosslinked filament networks.

4

CONCLUSION & OUTLOOK

In this thesis, we have studied the collective dynamics of filament-motor-mixtures. Starting from kinetic interactions of motor proteins with individual filaments, we coarse-grained the dynamics to evaluate consequences at the collective level. The guiding question in all presented projects was how interactions that happen on the scale of the protein size (nanometers) can give rise to filament structures spanning multiple filament lengths ($10-100$ micrometers). Specifically, we have studied systems composed of filaments and motors that regulate filament length and systems composed of filaments and motor cross-linkers that can generate mechanical force on the cross-linked filaments. A detailed summary is given at the end of each chapter. Let us recapitulate the main findings once again.

First, we investigated the motor-mediated length regulation in ensembles of filaments. We found that resource limitation in combination with length-dependent polymerization kinetics is sufficient to self-organize filaments in structures with aster-like orientational order that span multiple filament lengths. Those large-scale structures show emergent dynamics, including traveling wave solutions, aster coarsening, and coalescence, as well as symmetry breaking in the polar order. All those phenomena are observed even in the absence of mechanical interactions of the filaments. Their dynamics is only coupled via a shared pool of resources. This self-organization pathway is driven by a long-wavelength spatial instability that is caused by the diffusive redistribution of tubulin mass. This mass redistribution instability segregates the system into domains where filaments grow fast and slow respectively.

Second, we investigated motor-mediated mechanical interactions between filaments. Here, we asked two fundamental questions: First, which mechanisms control the propensity of a bundle of cross-linked filaments to promote contractile or extensile stress? Second, which mechanisms control the speed of filaments in a bundle of filaments that are driven by molecular motors? To answer these questions, we derive a coarse-grained filament-filament interaction based on time-scale separation arguments. Based on this filament-filament interaction, we derived a continuum description for the motor-induced filament motion in the bundle.

To evaluate the contractile or extensile nature of a motor cross-linked filament bundle, we studied a general model for motor cross-linkers and derived the collective contribution to the filament bundle tension. Thereby, we were able to identify generic requirements of motor cross-linkers to induce contractile or expansile stress in the filament bundle. First, motors that have an emergent density profile on the filament which is homogenous can neither promote extensile nor contractile tension. Second, symmetric motors like kinesin-5 can only induce extensile tension in the presence of external or internal friction in the filament bundle. In the absence of friction, filaments slide across the motor at its unloaded speed, which prevents the build-up of tension in the motor and, thereby the emergent tension in the material. Those characteristics can be quantified in terms of the motors' anisotropy factor - a measure of the inhomogeneity of the on-filament motor density.

We proceeded to apply the derived formalism to a spatially inhomogeneous filament bundle and

identified a mechanism for the collective filament motion in the bundle: Owing to the cross-linking in the bundle, locally generated forces propagate a characteristic length which is set by the competition between cross-linker forces on the filament and drag imposed on the filament by the surrounding fluid. Strikingly, we find that the filament velocity is independent of the local number of parallel and anti-parallel interaction partners, consistent with recent *in vitro* experiments [98]. Using large-scale computer simulations, we demonstrated that the presented ideas can be used to evaluate the filament sliding speed in networks.

In the living cell, motor-mediated filament length regulation and motor-mediated mechanical interactions between filaments are no isolated processes – they happen simultaneously. Having shown that both processes on their own can give rise to large-scale self-organization and complex collective dynamics the question arises: Do both processes take place simultaneously but decoupled? Or do they influence each other? Let me speculate on those questions. A decisive factor controlling a filament bundle's propensity to contract or expand is the motor anisotropy factor. For non-growing filaments plus-end directed (minus-end directed) motors will have an emergent density profile that yields a positive (negative) anisotropy factor. Which in both cases leads to neutral or extensile tension in the system. But what if growing filaments outpace the motors? This can yield an effective advective flux of motor heads opposed to its direction of motion. Thereby plus-end directed motors could have an emergent anisotropy factor smaller than zero, which in turn would cause a contractile tension in the system. Evaluating if this is indeed possible will be an interesting avenue for further research.

BIBLIOGRAPHY

[1] M. Striebel, F. Brauns, and E. Frey, "Length Regulation Drives Self-Organization in Filament-Motor Mixtures", Physical Review Letters **129**, 238102 (2022).

[2] M. Striebel, I. R. Graf, and E. Frey, "A Mechanistic View of Collective Filament Motion in Active Nematic Networks", Biophysical Journal **118**, 313–324 (2020).

[3] M. Striebel and E. Frey, "Bridging scales in filamentous active matter", Manuscript in preparation, 2023.

[4] M. Striebel, A. Sciortino, I. Maryshev, A. R. Bausch, and E. Frey, "Connectivity tunes filament velocity in filament-motor mixtures", Manuscript in preparation, 2023.

[5] A. K. Cooper G., *The cell: a molecular approach*, 5th ed. (ASM Press, Sunderland, 2009).

[6] B. Alberts, A. Johnson, J. Wilson, J. Lewis, T. Hunt, K. Roberts, M. Raff, and P. Walter, *Molecular biology of the cell* (Garland Science, 2008).

[7] T. D. Pollard, W. C. Earnshaw, and J. Lippincott-Schwartz, *Cell biology*, 3rd ed. (Philadelphia, PA, 2017).

[8] J. Howard, *Mechanics of motor proteins and the cytoskeleton* (Sinauer Associates, Publishers, 2001).

[9] D. A. Fletcher and R. D. Mullins, "Cell mechanics and the cytoskeleton", Nature **463**, 485–492 (2010).

[10] S. L. Rogers and V. I. Gelfand, "Membrane trafficking, organelle transport, and the cytoskeleton", Current Opinion in Cell Biology **12**, 57–62 (2000).

[11] T. Vignaud, L. Blanchoin, and M. Théry, "Directed cytoskeleton self-organization", Trends in Cell Biology **22**, 671–682 (2012).

[12] R. Subramanian and T. M. Kapoor, "Building Complexity: Insights into Self-Organized Assembly of Microtubule-Based Architectures", Developmental Cell **23**, 874–885 (2012).

[13] M. Dogterom and G. H. Koenderink, "Actin–microtubule crosstalk in cell biology", Nature Reviews Molecular Cell Biology **20**, 38–54 (2019).

[14] A. Akhmanova and L. C. Kapitein, "Mechanisms of microtubule organization in differentiated animal cells", Nature Reviews Molecular Cell Biology **23**, 541–558 (2022).

[15] A. B. Kolomeisky and M. E. Fisher, "Molecular Motors: A Theorist's Perspective", Annual Review of Physical Chemistry **58**, 675–695 (2007).

[16] P. I., *Non-equilibrium statistical mechanics*, 1st ed. (Dover Publications, Mineola New York, 2017).

[17] S. Petry, "Mechanisms of Mitotic Spindle Assembly", Annual Review of Biochemistry **85**, 1–25 (2016).

[18] S. L. Prosser and L. Pelletier, "Mitotic spindle assembly in animal cells: a fine balancing act", Nature Reviews Molecular Cell Biology **18**, 187–201 (2017).

[19] D. Oriola, D. J. Needleman, and J. Brugues, "The Physics of the Metaphase Spindle", Annual Review of Biophysics **47**, 655–673 (2018).

[20] S. Inoué, "Polarization optical studies of the mitotic spindle", Chromosoma **5**, 487–500 (1953).

[21] S. Inoué and H. Sato, "Cell motility by labile association of molecules. The nature of mitotic spindle fibers and their role in chromosome movement.", The Journal of general physiology **50**, Suppl:259–92 (1967).

[22] P. K. Hepler and W. T. Jackson, "Microtubules and early stages of cell-plate formation in the endosperm of Haemanthus katherinae Baker", The Journal of Cell Biology **38**, 437–446 (1968).

[23] J. R. MCINTOSH, P. K. HEPLER, and D. G. V. WIE, "Model for Mitosis", Nature **224**, 659–663 (1969).

[24] G. Goshima, R. Wollman, S. S. Goodwin, N. Zhang, J. M. Scholey, R. D. Vale, and N. Stuurman, "Genes Required for Mitotic Spindle Assembly in Drosophila S2 Cells", Science **316**, 417–421 (2007).

[25] F. Gittes, B. Mickey, J. Nettleton, and J. Howard, "Flexural rigidity of microtubules and actin filaments measured from thermal fluctuations in shape.", The Journal of cell biology **120**, 923–934 (1993).

[26] P. Venier, A. Maggs, M. Carlier, and D. Pantaloni, "Analysis of microtubule rigidity using hydrodynamic flow and thermal fluctuations.", Journal of Biological Chemistry **269**, 13353–13360 (1994).

[27] A. Kis, S. Kasas, B. Babić, A. J. Kulik, W. Benoît, G. A. D. Briggs, C. Schönenberger, S. Catsicas, and L. Forró, "Nanomechanics of Microtubules", Physical Review Letters **89**, 248101 (2002).

[28] P. J. d. Pablo, I. A. T. Schaap, F. C. MacKintosh, and C. F. Schmidt, "Deformation and Collapse of Microtubules on the Nanometer Scale", Physical Review Letters **91**, 098101 (2003).

[29] M. E. Janson and M. Dogterom, "A Bending Mode Analysis for Growing Microtubules: Evidence for a Velocity-Dependent Rigidity", Biophysical Journal **87**, 2723–2736 (2004).

[30] F. Pampaloni, G. Lattanzi, A. Jonáš, T. Surrey, E. Frey, and E.-L. Florin, "Thermal fluctuations of grafted microtubules provide evidence of a length-dependent persistence length", Proceedings of the National Academy of Sciences **103**, 10248–10253 (2006).

[31] J. Howard and A. A. Hyman, "Microtubule polymerases and depolymerases", Current Opinion in Cell Biology **19**, 31–35 (2007).

[32] A. Akhmanova and M. O. Steinmetz, "Tracking the ends: a dynamic protein network controls the fate of microtubule tips", Nature Reviews Molecular Cell Biology **9**, 309–322 (2008).

[33] A. Akhmanova and M. O. Steinmetz, "Control of microtubule organization and dynamics: two ends in the limelight", Nature Reviews Molecular Cell Biology **16**, 711–726 (2015).

[34] R. A. Cross and A. McAinsh, "Prime movers: the mechanochemistry of mitotic kinesins", Nature Reviews Molecular Cell Biology **15**, 257–271 (2014).

[35] T. D. Pollard, "Actin and Actin-Binding Proteins", Cold Spring Harbor Perspectives in Biology **8**, a018226 (2016).

[36] H. V. Goodson and E. M. Jonasson, "Microtubules and Microtubule-Associated Proteins", Cold Spring Harbor Perspectives in Biology **10**, a022608 (2018).

[37] V. Schaller, C. Weber, C. Semmrich, E. Frey, and A. R. Bausch, "Polar patterns of driven filaments", Nature **467**, 73–77 (2010).

[38] T. Sanchez, D. T. N. Chen, S. J. DeCamp, M. Heymann, and Z. Dogic, "Spontaneous motion in hierarchically assembled active matter", Nature **491**, 431–434 (2012).

[39] L. Huber, R. Suzuki, T. Krüger, E. Frey, and A. R. Bausch, "Emergence of coexisting ordered states in active matter systems", Science **361**, 255–258 (2018).

[40] B. Lemma, N. P. Mitchell, R. Subramanian, D. J. Needleman, and Z. Dogic, "Active Microphase Separation in Mixtures of Microtubules and Tip-Accumulating Molecular Motors", Physical Review X **12**, 031006 (2022).

[41] L. Brun, B. Rupp, J. J. Ward, and F. Nédélec, "A theory of microtubule catastrophes and their regulation", Proceedings of the National Academy of Sciences **106**, 21173–21178 (2009).

[42] A. Melbinger, L. Reese, and E. Frey, "Microtubule Length Regulation by Molecular Motors", Physical Review Letters **108**, 258104 (2012).

[43] H.-S. Kuan and M. D. Betterton, "Biophysics of filament length regulation by molecular motors", Physical Biology **10**, 036004 (2013).

[44] L. Reese, A. Melbinger, and E. Frey, "Molecular mechanisms for microtubule length regulation by kinesin-8 and XMAP215 proteins", Interface Focus **4**, 20140031 (2014).

[45] E. Reithmann, L. Reese, and E. Frey, "Nonequilibrium Diffusion and Capture Mechanism Ensures Tip Localization of Regulating Proteins on Dynamic Filaments", Physical Review Letters **117**, 078102 (2016).

[46] M. Lera-Ramirez and F. J. Nédélec, "Theory of antiparallel microtubule overlap stabilization by motors and diffusible crosslinkers", Cytoskeleton **76**, 600–610 (2019).

[47] S. A. Fiorenza, D. G. Steckhahn, and M. D. Betterton, "Modeling spatiotemporally varying protein–protein interactions in CyLaKS, the Cytoskeleton Lattice-based Kinetic Simulator", The European Physical Journal E **44**, 105 (2021).

[48] K. Kruse, J. F. Joanny, F. Jülicher, J. Prost, and K. Sekimoto, "Asters, Vortices, and Rotating Spirals in Active Gels of Polar Filaments", Physical Review Letters **92**, 078101 (2004).

[49] J. S. Bois, F. Jülicher, and S. W. Grill, "Pattern Formation in Active Fluids", Physical Review Letters **106**, 028103 (2011).

[50] L. Giomi, M. J. Bowick, X. Ma, and M. C. Marchetti, "Defect Annihilation and Proliferation in Active Nematics", Physical Review Letters **110**, 228101 (2013).

[51] E. Putzig, G. S. Redner, A. Baskaran, and A. Baskaran, "Instabilities, defects, and defect ordering in an overdamped active nematic", Soft Matter **12**, 3854–3859 (2016).

[52] F. Jülicher, S. W. Grill, and G. Salbreux, "Hydrodynamic theory of active matter", Reports on Progress in Physics **81**, 076601 (2018).

[53] B. Lacroix, G. Letort, L. Pitayu, J. Sallé, M. Stefanutti, G. Maton, A.-M. Ladouceur, J. C. Canman, P. S. Maddox, A. S. Maddox, N. Minc, F. Nédélec, and J. Dumont, "Microtubule Dynamics Scale with Cell Size to Set Spindle Length and Assembly Timing", Developmental Cell **45**, 496–511.e6 (2018).

[54] E. M. Rieckhoff, F. Berndt, M. Elsner, S. Golfier, F. Decker, K. Ishihara, and J. Brugués, "Spindle Scaling Is Governed by Cell Boundary Regulation of Microtubule Nucleation", Current Biology **30**, 4973–4983.e10 (2020).

[55] B. Lacroix and J. Dumont, "Spatial and Temporal Scaling of Microtubules and Mitotic Spindles", Cells **11**, 248 (2022).

[56] J. D. Wilbur and R. Heald, "Mitotic spindle scaling during Xenopus development by kif2a and importin α", eLife **2**, e00290 (2013).

[57] S. B. Reber, J. Baumgart, P. O. Widlund, A. Pozniakovsky, J. Howard, A. A. Hyman, and F. Jülicher, "XMAP215 activity sets spindle length by controlling the total mass of spindle microtubules", Nature Cell Biology **15**, 1116–1122 (2013).

[58] V. Varga, J. Helenius, K. Tanaka, A. A. Hyman, T. U. Tanaka, and J. Howard, "Yeast kinesin-8 depolymerizes microtubules in a length-dependent manner", Nature Cell Biology **8**, 957–962 (2006).

[59] J. Helenius, G. Brouhard, Y. Kalaidzidis, S. Diez, and J. Howard, "The depolymerizing kinesin MCAK uses lattice diffusion to rapidly target microtubule ends", Nature **441**, 115–119 (2006).

[60]G. J. Brouhard, J. H. Stear, T. L. Noetzel, J. Al-Bassam, K. Kinoshita, S. C. Harrison, J. Howard, and A. A. Hyman, "XMAP215 Is a Processive Microtubule Polymerase", Cell **132**, 79–88 (2008).

[61]L. Hough, A. Schwabe, M. A. Glaser, J. R. McIntosh, and M. Betterton, "Microtubule Depolymerization by the Kinesin-8 Motor Kip3p: A Mathematical Model", Biophysical Journal **96**, 3050–3064 (2009).

[62]L. Reese, A. Melbinger, and E. Frey, "Crowding of Molecular Motors Determines Microtubule Depolymerization", Biophysical Journal **101**, 2190–2200 (2011).

[63]M. Rank, A. Mitra, L. Reese, S. Diez, and E. Frey, "Limited Resources Induce Bistability in Microtubule Length Regulation", Physical Review Letters **120**, 148101 (2018).

[64]K. Doubrovinski and K. Kruse, "Self-Organization of Treadmilling Filaments", Physical Review Letters **99**, 228104 (2007).

[65]N. W. Goehring and A. A. Hyman, "Organelle Growth Control through Limiting Pools of Cytoplasmic Components", Current Biology **22**, R330–R339 (2012).

[66]L. Mohapatra, T. J. Lagny, D. Harbage, P. R. Jelenkovic, and J. Kondev, "The Limiting-Pool Mechanism Fails to Control the Size of Multiple Organelles", Cell Systems **4**, 559–567.e14 (2017).

[67]G. Arpağ, E. J. Lawrence, V. J. Farmer, S. L. Hall, and M. Zanic, "Collective effects of XMAP215, EB1, CLASP2, and MCAK lead to robust microtubule treadmilling", Proceedings of the National Academy of Sciences **117**, 12847–12855 (2020).

[68]A. Datta, D. Harbage, and J. Kondev, "Control of filament length by a depolymerizing gradient", PLoS Computational Biology **16**, e1008440 (2020).

[69]M. C. Good, M. D. Vahey, A. Skandarajah, D. A. Fletcher, and R. Heald, "Cytoplasmic Volume Modulates Spindle Size During Embryogenesis", Science **342**, 856–860 (2013).

[70]J. Hazel, K. Krutkramelis, P. Mooney, M. Tomschik, K. Gerow, J. Oakey, and J. C. Gatlin, "Changes in Cytoplasmic Volume Are Sufficient to Drive Spindle Scaling", Science **342**, 853–856 (2013).

[71]I. Gasic and T. J. Mitchison, "Autoregulation and repair in microtubule homeostasis", Current Opinion in Cell Biology **56**, 80–87 (2019).

[72]A. Milunovic´-Jevtic´, P. Jevtic´, D. L. Levy, and J. C. Gatlin, "In vivo mitotic spindle scaling can be modulated by changing the levels of a single protein: the microtubule polymerase XMAP215", Molecular Biology of the Cell **29**, 1311–1317 (2018).

[73]C. Brownlee and R. Heald, "Importin α Partitioning to the Plasma Membrane Regulates Intracellular Scaling", Cell **176**, 805–815.e8 (2019).

[74]T. Surrey, F. Nédélec, S. Leibler, and E. Karsenti, "Physical Properties Determining Self-Organization of Motors and Microtubules", Science **292**, 1167–1171 (2001).

[75]J. Roostalu, J. Rickman, C. Thomas, F. Nédélec, and T. Surrey, "Determinants of Polar versus Nematic Organization in Networks of Dynamic Microtubules and Mitotic Motors", Cell **175**, 796–808.e14 (2018).

[76]L. M. Lemma, M. M. Norton, A. M. Tayar, S. J. DeCamp, S. A. Aghvami, S. Fraden, M. F. Hagan, and Z. Dogic, "Multiscale Microtubule Dynamics in Active Nematics", Physical Review Letters **127**, 148001 (2021).

[77]L. M. Lemma, M. Varghese, T. D. Ross, M. Thomson, A. Baskaran, and Z. Dogic, "Spatio-temporal patterning of extensile active stresses in microtubule-based active fluids", PNAS Nexus **2**, pgad130 (2023).

[78]A. Senoussi, S. Kashida, R. Voituriez, J.-C. Galas, A. Maitra, and A. Estevez-Torres, "Tunable corrugated patterns in an active nematic sheet", Proceedings of the National Academy of Sciences **116**, 22464–22470 (2019).

[79] B. Najma, A. Baskaran, P. J. Foster, and G. Duclos, "Microscopic interactions control a structural transition in active mixtures of microtubules and molecular motors", bioRxiv, 2023.01.04.522797 (2023).

[80] L. Giomi, M. C. Marchetti, and T. B. Liverpool, "Complex Spontaneous Flows and Concentration Banding in Active Polar Films", Physical Review Letters **101**, 198101 (2008).

[81] L. Giomi, "Geometry and Topology of Turbulence in Active Nematics", Physical Review X **5**, 031003 (2015).

[82] S. P. Thampi, R. Golestanian, and J. M. Yeomans, "Velocity Correlations in an Active Nematic", Physical Review Letters **111**, 118101 (2013).

[83] A. Doostmohammadi, M. F. Adamer, S. P. Thampi, and J. M. Yeomans, "Stabilization of active matter by flow-vortex lattices and defect ordering", Nature Communications **7**, 10557 (2016).

[84] A. Doostmohammadi, J. Ignés-Mullol, J. M. Yeomans, and F. Sagués, "Active nematics", Nature Communications **9**, 3246 (2018).

[85] A. Doostmohammadi, T. N. Shendruk, K. Thijssen, and J. M. Yeomans, "Onset of meso-scale turbulence in active nematics", Nature Communications **8**, 15326 (2017).

[86] I. Maryshev, A. Morozov, A. B. Goryachev, and D. Marenduzzo, "Pattern formation in active model C with anchoring: bands, aster networks, and foams", Soft Matter **16**, 8775–8781 (2020).

[87] G. Henkin, S. J. DeCamp, D. T. N. Chen, T. Sanchez, and Z. Dogic, "Tunable dynamics of microtubule-based active isotropic gels", Philosophical Transactions of the Royal Society A: Mathematical, Physical and Engineering Sciences **372**, 20140142 (2014).

[88] G. Henkin, W.-X. Chew, Fran, and T. Surrey, "Cross-linker design determines microtubule network organization by opposing motors", Proceedings of the National Academy of Sciences **119**, e2206398119 (2022).

[89] L. M. Lemma, S. J. DeCamp, Z. You, L. Giomi, and Z. Dogic, "Statistical properties of autonomous flows in 2D active nematics", Soft Matter **15**, 3264–3272 (2019).

[90] B. Lemma, L. Lemma, S. C. Ems-McClung, C. E. Walczak, Z. Dogic, and D. J. Needleman, "Structure and dynamics of motor-driven microtubule bundles", arXiv, `10.48550/arxiv.2209.06637` (2022).

[91] G. Sarfati, A. Maitra, R. Voituriez, J.-C. Galas, and A. Estevez-Torres, "Crosslinking and depletion determine spatial instabilities in cytoskeletal active matter", Soft Matter **18**, 3793–3800 (2022).

[92] B. Najma, M. Varghese, L. Tsidilkovski, L. Lemma, A. Baskaran, and G. Duclos, "Competing instabilities reveal how to rationally design and control active crosslinked gels", Nature Communications **13**, 6465 (2022).

[93] W.-X. Chew, G. Henkin, F. Nédélec, and T. Surrey, "Effects of microtubule length and crowding on active microtubule network organization", iScience **26**, 106063 (2023).

[94] T. J. Mitchison, P. Nguyen, M. Coughlin, and A. C. Groen, "Self-organization of stabilized microtubules by both spindle and midzone mechanisms in Xenopus egg cytosol", Molecular Biology of the Cell **24**, 1559–1573 (2013).

[95] L. C. Kapitein, E. J. G. Peterman, B. H. Kwok, J. H. Kim, T. M. Kapoor, and C. F. Schmidt, "The bipolar mitotic kinesin Eg5 moves on both microtubules that it crosslinks", Nature **435**, 114–118 (2005).

[96] K. S. Burbank, T. J. Mitchison, and D. S. Fisher, "Slide-and-Cluster Models for Spindle Assembly", Current Biology **17**, 1373–1383 (2007).

[97] M. Uteng, C. Hentrich, K. Miura, P. Bieling, and T. Surrey, "Poleward transport of Eg5 by dynein–dynactin in Xenopus laevis egg extract spindles", The Journal of Cell Biology **182**, 715–726 (2008).

[98] B. A. Dalton, D. Oriola, F. Decker, F. Jülicher, and J. Brugués, "A gelation transition enables the self-organization of bipolar metaphase spindles", Nature Physics **18**, 323–331 (2022).

[99] S. Fürthauer, B. Lemma, P. J. Foster, S. C. Ems-McClung, C.-H. Yu, C. E. Walczak, Z. Dogic, D. J. Needleman, and M. J. Shelley, "Self-straining of actively crosslinked microtubule networks", Nature Physics **15**, 1295–1300 (2019).

[100] T. M. Svitkina, "Actin Cell Cortex: Structure and Molecular Organization", Trends in Cell Biology **30**, 556–565 (2020).

[101] A. G. Clark, K. Dierkes, and E. K. Paluch, "Monitoring Actin Cortex Thickness in Live Cells", Biophysical Journal **105**, 570–580 (2013).

[102] P. Chugh, A. G. Clark, M. B. Smith, D. A. D. Cassani, K. Dierkes, A. Ragab, P. P. Roux, G. Charras, G. Salbreux, and E. K. Paluch, "Actin cortex architecture regulates cell surface tension", Nature Cell Biology **19**, 689–697 (2017).

[103] R. Kumar, S. Saha, and B. Sinha, "Cell spread area and traction forces determine myosin-II-based cortex thickness regulation", Biochimica et Biophysica Acta (BBA) - Molecular Cell Research **1866**, 118516 (2019).

[104] T. Svitkina, "The Actin Cytoskeleton and Actin-Based Motility", Cold Spring Harbor Perspectives in Biology **10**, a018267 (2018).

[105] G. Salbreux, G. Charras, and E. Paluch, "Actin cortex mechanics and cellular morphogenesis", Trends in Cell Biology **22**, 536–545 (2012).

[106] M. S. Shutova and T. M. Svitkina, "Mammalian nonmuscle myosin II comes in three flavors", Biochemical and Biophysical Research Communications **506**, 394–402 (2018).

[107] E. Bianconi, A. Piovesan, F. Facchin, A. Beraudi, R. Casadei, F. Frabetti, L. Vitale, M. C. Pelleri, S. Tassani, F. Piva, S. Perez-Amodio, P. Strippoli, and S. Canaider, "An estimation of the number of cells in the human body", Annals of Human Biology **40**, 463–471 (2013).

[108] I. Grigoriev, S. M. Gouveia, B. v. d. Vaart, J. Demmers, J. T. Smyth, S. Honnappa, D. Splinter, M. O. Steinmetz, J. W. Putney, C. C. Hoogenraad, and A. Akhmanova, "STIM1 Is a MT-Plus-End-Tracking Protein Involved in Remodeling of the ER", Current Biology **18**, 177–182 (2008).

[109] S. Wang, F. B. Romano, C. M. Field, T. J. Mitchison, and T. A. Rapoport, "Multiple mechanisms determine ER network morphology during the cell cycle in Xenopus egg extracts", Journal of Cell Biology **203**, 801–814 (2013).

[110] S. W. Grill and A. A. Hyman, "Spindle Positioning by Cortical Pulling Forces", Developmental Cell **8**, 461–465 (2005).

[111] P. A. Nguyen, A. C. Groen, M. Loose, K. Ishihara, M. Wühr, C. M. Field, and T. J. Mitchison, "Spatial organization of cytokinesis signaling reconstituted in a cell-free system", Science **346**, 244–247 (2014).

[112] C. M. Field, A. C. Groen, P. A. Nguyen, and T. J. Mitchison, "Spindle-to-cortex communication in cleaving, polyspermic Xenopus eggs", Molecular Biology of the Cell **26**, 3628–3640 (2015).

[113] H. Tanimoto, A. Kimura, and N. Minc, "Shape–motion relationships of centering microtubule asters", The Journal of Cell Biology **212**, 777–787 (2016).

[114] K. Ishihara, P. A. Nguyen, A. C. Groen, C. M. Field, and T. J. Mitchison, "Microtubule nucleation remote from centrosomes may explain how asters span large cells", Proceedings of the National Academy of Sciences **111**, 17715–17722 (2014).

[115] K. Ishihara, P. A. Nguyen, M. Wühr, A. C. Groen, C. M. Field, and T. J. Mitchison, "Organization of early frog embryos by chemical waves emanating from centrosomes", Philosophical Transactions of the Royal Society B: Biological Sciences **369**, 20130454 (2014).

[116] K. Ishihara, K. S. Korolev, and T. J. Mitchison, "Physical basis of large microtubule aster growth", eLife **5**, e19145 (2016).

[117] T. Mitchison, M. Wühr, P. Nguyen, K. Ishihara, A. Groen, and C. M. Field, "Growth, interaction, and positioning of microtubule asters in extremely large vertebrate embryo cells", Cytoskeleton **69**, 738–750 (2012).

[118] F. C. Keber, E. Loiseau, T. Sanchez, S. J. DeCamp, L. Giomi, M. J. Bowick, M. C. Marchetti, Z. Dogic, and A. R. Bausch, "Topology and dynamics of active nematic vesicles", Science **345**, 1135–1139 (2014).

[119] K.-T. Wu, J. B. Hishamunda, D. T. N. Chen, S. J. DeCamp, Y.-W. Chang, A. Fernández-Nieves, S. Fraden, and Z. Dogic, "Transition from turbulent to coherent flows in confined three-dimensional active fluids", Science **355**, eaal1979 (2017).

[120] A. Opathalage, M. M. Norton, M. P. N. Juniper, B. Langeslay, S. A. Aghvami, S. Fraden, and Z. Dogic, "Self-organized dynamics and the transition to turbulence of confined active nematics", Proceedings of the National Academy of Sciences **116**, 4788–4797 (2019).

[121] T. E. Bate, M. E. Varney, E. H. Taylor, J. H. Dickie, C.-C. Chueh, M. M. Norton, and K.-T. Wu, "Self-mixing in microtubule-kinesin active fluid from nonuniform to uniform distribution of activity", Nature Communications **13**, 6573 (2022).

[122] A. Desai, A. Murray, T. J. Mitchison, and C. E. Walczak, "The Use of Xenopus Egg Extracts to Study Mitotic Spindle Assembly and Function in Vitro", Methods in Cell Biology **61**, 385–412 (1998).

[123] E. Hannak and R. Heald, "Investigating mitotic spindle assembly and function in vitro using Xenopus laevis egg extracts", Nature Protocols **1**, 2305–2314 (2006).

[124] A. W. Murray and M. W. Kirschner, "Cyclin synthesis drives the early embryonic cell cycle", Nature **339**, 275–280 (1989).

[125] R. Heald, R. Tournebize, T. Blank, R. Sandaltzopoulos, P. Becker, A. Hyman, and E. Karsenti, "Self-organization of microtubules into bipolar spindles around artificial chromosomes in Xenopus egg extracts", Nature **382**, 420–425 (1996).

[126] X. Cheng and J. E. FerrellJr., "Spontaneous emergence of cell-like organization in Xenopus egg extracts", Science **366**, 631–637 (2019).

[127] N. B. Gudimchuk and J. R. McIntosh, "Regulation of microtubule dynamics, mechanics and function through the growing tip", Nature Reviews Molecular Cell Biology **22**, 777–795 (2021).

[128] N. B. Gudimchuk, E. V. Ulyanov, E. O'Toole, C. L. Page, D. S. Vinogradov, G. Morgan, G. Li, J. K. Moore, E. Szczesna, A. Roll-Mecak, F. I. Ataullakhanov, and J. R. McIntosh, "Mechanisms of microtubule dynamics and force generation examined with computational modeling and electron cryotomography", Nature Communications **11**, 3765 (2020).

[129] M. Igaev and H. Grubmüller, "Microtubule instability driven by longitudinal and lateral strain propagation", PLoS Computational Biology **16**, e1008132 (2020).

[130] E. V. Ulyanov, D. S. Vinogradov, J. R. McIntosh, and N. B. Gudimchuk, "Brownian dynamics simulation of protofilament relaxation during rapid freezing", PLoS ONE **16**, e0247022 (2021).

[131] M. Igaev and H. Grubmüller, "Bending-torsional elasticity and energetics of the plus-end microtubule tip", Proceedings of the National Academy of Sciences **119**, e2115516119 (2022).

[132]V. V. Alexandrova, M. N. Anisimov, A. V. Zaitsev, V. V. Mustyatsa, V. V. Popov, F. I. Ataullakhanov, and N. B. Gudimchuk, "Theory of tip structure–dependent microtubule catastrophes and damage-induced microtubule rescues", Proceedings of the National Academy of Sciences **119**, e2208294119 (2022).

[133]M. C. Ledbetter and K. R. Porter, "Morphology of Microtubules of Plant Cell", Science **144**, 872–874 (1964).

[134]L. G. Tilney, J. Bryan, D. J. Bush, K. Fujiwara, M. S. Mooseker, D. B. Murphy, and D. H. Snyder, "MICROTUBULES: EVIDENCE FOR 13 PROTOFILAMENTS", The Journal of Cell Biology **59**, 267–275 (1973).

[135]H. Sui and K. H. Downing, "Structural Basis of Interprotofilament Interaction and Lateral Deformation of Microtubules", Structure **18**, 1022–1031 (2010).

[136]T. Mitchison and M. Kirschner, "Dynamic instability of microtubule growth", Nature **312**, 237–242 (1984).

[137]C. Janke and M. M. Magiera, "The tubulin code and its role in controlling microtubule properties and functions", Nature Reviews Molecular Cell Biology **21**, 307–326 (2020).

[138]C. Duellberg, N. I. Cade, D. Holmes, and T. Surrey, "The size of the EB cap determines instantaneous microtubule stability", eLife **5**, e13470 (2016).

[139]J. Roostalu, C. Thomas, N. I. Cade, S. Kunzelmann, I. A. Taylor, and T. Surrey, "The speed of GTP hydrolysis determines GTP cap size and controls microtubule stability", eLife **9**, e51992 (2020).

[140]E. Nogales, M. Whittaker, R. A. Milligan, and K. H. Downing, "High-Resolution Model of the Microtubule", Cell **96**, 79–88 (1999).

[141]J. M. Cleary and W. O. Hancock, "Molecular mechanisms underlying microtubule growth dynamics", Current Biology **31**, R560–R573 (2021).

[142]C. E. Coombes, A. Yamamoto, M. R. Kenzie, D. J. Odde, and M. K. Gardner, "Evolving Tip Structures Can Explain Age-Dependent Microtubule Catastrophe", Current Biology **23**, 1342–1348 (2013).

[143]M. K. Gardner, M. Zanic, C. Gell, V. Bormuth, and J. Howard, "Depolymerizing Kinesins Kip3 and MCAK Shape Cellular Microtubule Architecture by Differential Control of Catastrophe", Cell **147**, 1092–1103 (2011).

[144]D. Needleman and Z. Dogic, "Active matter at the interface between materials science and cell biology", Nature Reviews Materials **2**, 17048 (2017).

[145]E. Reithmann, L. Reese, and E. Frey, "Quantifying Protein Diffusion and Capture on Filaments", Biophysical Journal **108**, 787–790 (2015).

[146]B. Wickstead, K. Gull, and T. A. Richards, "Patterns of kinesin evolution reveal a complex ancestral eukaryote with a multifunctional cytoskeleton", BMC Evolutionary Biology **10**, 110 (2010).

[147]H. L. Sweeney and E. L. Holzbaur, "Motor Proteins", Cold Spring Harbor Perspectives in Biology **10**, a021931 (2018).

[148]A. Singh, J. A. Soler, J. Lauer, S. W. Grill, M. Jahnel, M. Zerial, and S. Thutupalli, "Two-component molecular motor driven by a GTPase cycle", Nature Physics, 1–8 (2023).

[149]C. L. Asbury, A. N. Fehr, and S. M. Block, "Kinesin Moves by an Asymmetric Hand-Over-Hand Mechanism", Science **302**, 2130–2134 (2003).

[150]K. Kaseda, H. Higuchi, and K. Hirose, "Alternate fast and slow stepping of a heterodimeric kinesin molecule", Nature Cell Biology **5**, 1079–1082 (2003).

[151] S. Verbrugge, S. M. v. d. Wildenberg, and E. J. Peterman, "Novel Ways to Determine Kinesin-1's Run Length and Randomness Using Fluorescence Microscopy", Biophysical Journal **97**, 2287–2294 (2009).

[152] S. Shrestha, M. Hazelbaker, A. L. Yount, and C. E. Walczak, "Emerging Insights into the Function of Kinesin-8 Proteins in Microtubule Length Regulation", Biomolecules **9**, 1 (2018).

[153] B. v. d. Vaart, A. Akhmanova, and A. Straube, "Regulation of microtubule dynamic instability", Biochemical Society Transactions **37**, 1007–1013 (2009).

[154] R. J. Vasquez, D. L. Gard, and L. Cassimeris, "XMAP from Xenopus eggs promotes rapid plus end assembly of microtubules and rapid microtubule polymer turnover.", The Journal of cell biology **127**, 985–993 (1994).

[155] M. Zanic, P. O. Widlund, A. A. Hyman, and J. Howard, "Synergy between XMAP215 and EB1 increases microtubule growth rates to physiological levels", Nature Cell Biology **15**, 688–693 (2013).

[156] G. Pereira and E. Schiebel, "Centrosome-microtubule nucleation", Journal of Cell Science **110**, 295–300 (1997).

[157] M. Bettencourt-Dias and D. M. Glover, "Centrosome biogenesis and function: centrosomics brings new understanding", Nature Reviews Molecular Cell Biology **8**, 451–463 (2007).

[158] S. Petry, A. C. Groen, K. Ishihara, T. J. Mitchison, and R. D. Vale, "Branching Microtubule Nucleation in Xenopus Egg Extracts Mediated by Augmin and TPX2", Cell **152**, 768–777 (2013).

[159] S. Petry and R. D. Vale, "Microtubule nucleation at the centrosome and beyond", Nature Cell Biology **17**, 1089–1093 (2015).

[160] R. Alfaro-Aco, A. Thawani, and S. Petry, "Structural analysis of the role of TPX2 in branching microtubule nucleation", Journal of Cell Biology **216**, 983–997 (2017).

[161] R. Alfaro-Aco, A. Thawani, and S. Petry, "Biochemical reconstitution of branching microtubule nucleation", eLife **9**, e49797 (2020).

[162] A. Tariq, L. Green, J. C. G. Jeynes, C. Soeller, and J. G. Wakefield, "In vitro reconstitution of branching microtubule nucleation", eLife **9**, e49769 (2020).

[163] A. C. Almeida, J. Soares-de-Oliveira, D. Drpic, L. P. Cheeseman, J. Damas, H. A. Lewin, D. M. Larkin, P. Aguiar, A. J. Pereira, and H. Maiato, "Augmin-dependent microtubule self-organization drives kinetochore fiber maturation in mammals", Cell Reports **39**, 110610 (2022).

[164] A. Thawani, R. S. Kadzik, and S. Petry, "XMAP215 is a microtubule nucleation factor that functions synergistically with the γ-tubulin ring complex", Nature Cell Biology **20**, 575–585 (2018).

[165] F. J. McNally and R. D. Vale, "Identification of katanin, an ATPase that severs and disassembles stable microtubules", Cell **75**, 419–429 (1993).

[166] C. E. Walczak and S. L. Shaw, "A MAP for Bundling Microtubules", Cell **142**, 364–367 (2010).

[167] R. E. Carazo-Salas, O. J. Gruss, I. W. Mattaj, and E. Karsenti, "Ran–GTP coordinates regulation of microtubule nucleation and dynamics during mitotic-spindle assembly", Nature Cell Biology **3**, 228–234 (2001).

[168] D. Oh, C.-H. Yu, and D. J. Needleman, "Spatial organization of the Ran pathway by microtubules in mitosis", Proceedings of the National Academy of Sciences **113**, 8729–8734 (2016).

[169] J. Lüders, U. K. Patel, and T. Stearns, "GCP-WD is a γ-tubulin targeting factor required for centrosomal and chromatin-mediated microtubule nucleation", Nature Cell Biology **8**, 137–147 (2006).

[170]J. R. A. Hutchins, Y. Toyoda, B. Hegemann, I. Poser, J.-K. Heriche, M. M. Sykora, M. Augsburg, O. Hudecz, B. A. Buschhorn, J. Bulkescher, C. Conrad, D. Comartin, A. Schleiffer, M. Sarov, A. Pozniakovsky, M. M. Slabicki, S. Schloissnig, I. Steinmacher, M. Leuschner, A. Ssykor, S. Lawo, L. Pelletier, H. Stark, K. Nasmyth, J. Ellenberg, R. Durbin, F. Buchholz, K. Mechtler, A. A. Hyman, and J.-M. Peters, "Systematic Analysis of Human Protein Complexes Identifies Chromosome Segregation Proteins", Science **328**, 593–599 (2010).

[171]M. R. King and S. Petry, "Phase separation of TPX2 enhances and spatially coordinates microtubule nucleation", Nature Communications **11**, 270 (2020).

[172]A. Roll-Mecak and F. J. McNally, "Microtubule-severing enzymes", Current Opinion in Cell Biology **22**, 96–103 (2010).

[173]R. Loughlin, J. Wilbur, F. J. McNally, F. J. Nedelec, and R. Heald, "Katanin Contributes to Interspecies Spindle Length Scaling in Xenopus", Cell **147**, 1397–1407 (2011).

[174]K. Kinoshita, I. Arnal, A. Desai, D. N. Drechsel, and A. A. Hyman, "Reconstitution of Physiological Microtubule Dynamics Using Purified Components", Science **294**, 1340–1343 (2001).

[175]V. Varga, C. Leduc, V. Bormuth, S. Diez, and J. Howard, "Kinesin-8 Motors Act Cooperatively to Mediate Length-Dependent Microtubule Depolymerization", Cell **138**, 1174–1183 (2009).

[176]J. R. Cooper, M. Wagenbach, C. L. Asbury, and L. Wordeman, "Catalysis of the microtubule on-rate is the major parameter regulating the depolymerase activity of MCAK", Nature Structural & Molecular Biology **17**, 77–82 (2010).

[177]M. J. Shelley, "The Dynamics of Microtubule/Motor-Protein Assemblies in Biology and Physics", Annual Review of Fluid Mechanics **48**, 1–20 (2015).

[178]M. Dogterom and T. Surrey, "Microtubule organization in vitro", Current Opinion in Cell Biology **25**, 23–29 (2013).

[179]A. J. Roberts, T. Kon, P. J. Knight, K. Sutoh, and S. A. Burgess, "Functions and mechanics of dynein motor proteins", Nature Reviews Molecular Cell Biology **14**, 713–726 (2013).

[180]T. U. Mayer, T. M. Kapoor, S. J. Haggarty, R. W. King, S. L. Schreiber, and T. J. Mitchison, "Small Molecule Inhibitor of Mitotic Spindle Bipolarity Identified in a Phenotype-Based Screen", Science **286**, 971–974 (1999).

[181]D. J. Sharp, K. R. Yu, J. C. Sisson, W. Sullivan, and J. M. Scholey, "Antagonistic microtubule-sliding motors position mitotic centrosomes in Drosophila early embryos", Nature Cell Biology **1**, 51–54 (1999).

[182]G. Goshima and R. D. Vale, "The roles of microtubule-based motor proteins in mitosis", The Journal of Cell Biology **162**, 1003–1016 (2003).

[183]T. J. Mitchison, P. Maddox, J. Gaetz, A. Groen, M. Shirasu, A. Desai, E. D. Salmon, and T. M. Kapoor, "Roles of Polymerization Dynamics, Opposed Motors, and a Tensile Element in Governing the Length of Xenopus Extract Meiotic Spindles", Molecular Biology of the Cell **16**, 3064–3076 (2005).

[184]J. Brugués, V. Nuzzo, E. Mazur, and D. J. Needleman, "Nucleation and Transport Organize Microtubules in Metaphase Spindles", Cell **149**, 554–564 (2012).

[185]R. R. West, T. Malmstrom, C. L. Troxell, and J. R. McIntosh, "Two Related Kinesins, klp5 + andklp6 +, Foster Microtubule Disassembly and Are Required for Meiosis in Fission Yeast", Molecular Biology of the Cell **12**, 3919–3932 (2001).

[186]M. I. Mayr, S. Hümmer, J. Bormann, T. Grüner, S. Adio, G. Woehlke, and T. U. Mayer, "The Human Kinesin Kif18A Is a Motile Microtubule Depolymerase Essential for Chromosome Congression", Current Biology **17**, 488–498 (2007).

[187] Z. R. Gergely, A. Crapo, L. E. Hough, J. R. McIntosh, and M. D. Betterton, "Kinesin-8 effects on mitotic microtubule dynamics contribute to spindle function in fission yeast", Molecular Biology of the Cell **27**, 3490–3514 (2016).

[188] A. F. Straight, J. W. Sedat, and A. W. Murray, "Time-Lapse Microscopy Reveals Unique Roles for Kinesins during Anaphase in Budding Yeast", The Journal of Cell Biology **143**, 687–694 (1998).

[189] J. Stumpff, G. v. Dassow, M. Wagenbach, C. Asbury, and L. Wordeman, "The Kinesin-8 Motor Kif18A Suppresses Kinetochore Movements to Control Mitotic Chromosome Alignment", Developmental Cell **14**, 252–262 (2008).

[190] J. Howard, "Molecular motors: structural adaptations to cellular functions", Nature **389**, 561–567 (1997).

[191] J. Howard, "Mechanical Signaling in Networks of Motor and Cytoskeletal Proteins", Annual Review of Biophysics **38**, 217–234 (2009).

[192] R. J. McKenney, W. Huynh, M. E. Tanenbaum, G. Bhabha, and R. D. Vale, "Activation of cytoplasmic dynein motility by dynactin-cargo adapter complexes", Science **345**, 337–341 (2014).

[193] R. Tan, P. J. Foster, D. J. Needleman, and R. J. McKenney, "Cooperative Accumulation of Dynein-Dynactin at Microtubule Minus-Ends Drives Microtubule Network Reorganization", Developmental Cell **44**, 233–247.e4 (2018).

[194] P. J. Foster, S. Fürthauer, M. J. Shelley, and D. J. Needleman, "Active contraction of microtubule networks", eLife **4**, e10837 (2015).

[195] P. J. Foster, W. Yan, S. Fürthauer, M. J. Shelley, and D. J. Needleman, "Connecting macroscopic dynamics with microscopic properties in active microtubule network contraction", New Journal of Physics **19**, 125011 (2017).

[196] E. Meyhöfer and J. Howard, "The force generated by a single kinesin molecule against an elastic load.", Proceedings of the National Academy of Sciences **92**, 574–578 (1995).

[197] G. Fink, L. Hajdo, K. J. Skowronek, C. Reuther, A. A. Kasprzak, and S. Diez, "The mitotic kinesin-14 Ncd drives directional microtubule–microtubule sliding", Nature Cell Biology **11**, 717–723 (2009).

[198] F. Verde, J.-C. Labbé, M. Dorée, and E. Karsenti, "Regulation of microtubule dynamics by cdc2 protein kinase in cell-free extracts of Xenopus eggs", Nature **343**, 233–238 (1990).

[199] L. Belmont, A. Hyman, K. Sawin, and T. Mitchison, "Real-time visualization of cell cycle-dependent changes in microtubule dynamics in cytoplasmic extracts", Cell **62**, 579–589 (1990).

[200] K. Ishihara, F. Decker, P. Caldas, J. F. Pelletier, M. Loose, J. Brugués, and T. J. Mitchison, "Spatial variation of microtubule depolymerization in large asters", Molecular Biology of the Cell **32**, 869–879 (2021).

[201] Z. M. Geisterfer, D. Y. Zhu, T. J. Mitchison, J. Oakey, and J. C. Gatlin, "Microtubule Growth Rates Are Sensitive to Global and Local Changes in Microtubule Plus-End Density", Current Biology **30**, 3016–3023.e3 (2020).

[202] A. Burakov, I. Vorobjev, I. Semenova, A. Cowan, J. Carson, Y. Wu, and V. Rodionov, "Persistent growth of microtubules at low density", Molecular Biology of the Cell **32**, 435–445 (2021).

[203] A. A. Hyman, S. Salser, D. N. Drechsel, N. Unwin, and T. J. Mitchison, "Role of GTP hydrolysis in microtubule dynamics: information from a slowly hydrolyzable analogue, GMPCPP.", Molecular Biology of the Cell **3**, 1155–1167 (1992).

[204] E. Nogales, "Structural insights into microtubule function", Annual Review of Biochemistry **69**, 277–302 (2000).

[205] F. J. Ndlec, T. Surrey, A. C. Maggs, and S. Leibler, "Self-organization of microtubules and motors", Nature **389**, 305–308 (1997).

[206] K. Kruse and F. Jülicher, "Actively Contracting Bundles of Polar Filaments", Physical Review Letters **85**, 1778–1781 (2000).

[207] R. Ohi, C. Strothman, and M. Zanic, "Impact of the 'tubulin economy' on the formation and function of the microtubule cytoskeleton", Current Opinion in Cell Biology **68**, 81–89 (2021).

[208] See Supplemental Material for Movies 1–5 as well as technical background information, which includes Refs. [7, 60, 63, 175, 209–211, 213, 222–233].

[209] A. Parmeggiani, T. Franosch, and E. Frey, "Phase Coexistence in Driven One-Dimensional Transport", Physical Review Letters **90**, 086601 (2003).

[210] A. Parmeggiani, T. Franosch, and E. Frey, "Totally asymmetric simple exclusion process with Langmuir kinetics", Physical Review E **70**, 046101 (2004).

[211] J. Halatek, F. Brauns, and E. Frey, "Self-organization principles of intracellular pattern formation", Philosophical Transactions of the Royal Society B: Biological Sciences **373**, 20170107 (2018).

[212] J. Halatek and E. Frey, "Rethinking pattern formation in reaction–diffusion systems", Nature Physics **14**, 507–514 (2018).

[213] F. Brauns, J. Halatek, and E. Frey, "Phase-Space Geometry of Mass-Conserving Reaction-Diffusion Dynamics", Physical Review X **10**, 041036 (2020).

[214] M. Striebel, F. Brauns, and E. Frey, "Filament bundle formation and polarity sorting through length regulation", unpublished, N.D.

[215] G. G. Borisy and E. W. Taylor, "THE MECHANISM OF ACTION OF COLCHICINE", The Journal of Cell Biology **34**, 525–533 (1967).

[216] G. G. Borisy and E. W. Taylor, "THE MECHANISM OF ACTION OF COLCHICINE", The Journal of Cell Biology **34**, 535–548 (1967).

[217] F. Decker, D. Oriola, B. Dalton, and J. Brugués, "Autocatalytic microtubule nucleation determines the size and mass of Xenopus laevis egg extract spindles", eLife **7**, e31149 (2018).

[218] J. M. Belmonte, M. Leptin, and F. Nédélec, "A theory that predicts behaviors of disordered cytoskeletal networks", Molecular Systems Biology **13**, 941 (2017).

[219] V. Wollrab, J. M. Belmonte, L. Baldauf, M. Leptin, F. Nédeléc, and G. H. Koenderink, "Polarity sorting drives remodeling of actin-myosin networks", Journal of Cell Science **132**, jcs219717 (2018).

[220] J. Rickman, F. Nédélec, and T. Surrey, "Effects of spatial dimensionality and steric interactions on microtubule-motor self-organization", Physical Biology **16**, 046004 (2019).

[221] M. Dogterom and S. Leibler, "Physical aspects of the growth and regulation of microtubule structures", Physical Review Letters **70**, 1347–1350 (1993).

[222] A. A. Hyman, D. Chrétien, I. Arnal, and R. H. Wade, "Structural changes accompanying GTP hydrolysis in microtubules: information from a slowly hydrolyzable analogue guanylyl-(alpha,beta)-methylene-diphosphonate.", The Journal of cell biology **128**, 117–125 (1995).

[223] E. D. Salmon, W. M. Saxton, R. J. Leslie, M. L. Karow, and J. R. McIntosh, "Diffusion coefficient of fluorescein-labeled tubulin in the cytoplasm of embryonic cells of a sea urchin: video image analysis of fluorescence redistribution after photobleaching.", The Journal of cell biology **99**, 2157–2164 (1984).

[224] R. Schneider, T. Korten, W. J. Walter, and S. Diez, "Kinesin-1 Motors Can Circumvent Permanent Roadblocks by Side-Shifting to Neighboring Protofilaments", Biophysical Journal **108**, 2249–2257 (2015).

[225] D. T. Gillespie, "Exact stochastic simulation of coupled chemical reactions", The Journal of Physical Chemistry **81**, 2340–2361 (1977).

[226] R. Lipowsky, S. Klumpp, and T. M. Nieuwenhuizen, "Random Walks of Cytoskeletal Motors in Open and Closed Compartments", Physical Review Letters **87**, 108101 (2001).

[227] S. Klumpp and R. Lipowsky, "Traffic of Molecular Motors Through Tube-Like Compartments", Journal of Statistical Physics **113**, 233–268 (2003).

[228] T. Chou, K. Mallick, and R. K. P. Zia, "Non-equilibrium statistical mechanics: from a paradigmatic model to biological transport", Reports on Progress in Physics **74**, 116601 (2011).

[229] P. S. Grassia, E. J. Hinch, and L. C. Nitsche, "Computer simulations of Brownian motion of complex systems", Journal of Fluid Mechanics **282**, 373–403 (1995).

[230] F. Schwabl, *Statistical mechanics*, 2nd ed. (Springer, 2006).

[231] J. Tailleur and M. E. Cates, "Statistical Mechanics of Interacting Run-and-Tumble Bacteria", Physical Review Letters **100**, 218103 (2008).

[232] M. F. Carlier, R. Melki, D. Pantaloni, T. L. Hill, and Y. Chen, "Synchronous oscillations in microtubule polymerization.", Proceedings of the National Academy of Sciences **84**, 5257–5261 (1987).

[233] R. Melki, M. F. Carlier, and D. Pantaloni, "Oscillations in microtubule polymerization: the rate of GTP regeneration on tubulin controls the period.", The EMBO Journal **7**, 2653–2659 (1988).

[234] D. T. Miyamoto, Z. E. Perlman, K. S. Burbank, A. C. Groen, and T. J. Mitchison, "The kinesin Eg5 drives poleward microtubule flux in Xenopus laevis egg extract spindles", The Journal of Cell Biology **167**, 813–818 (2004).

[235] J. O. Andreasson, B. Milic, G.-Y. Chen, N. R. Guydosh, W. O. Hancock, and S. M. Block, "Examining kinesin processivity within a general gating framework", eLife **4**, e07403 (2015).

[236] P. Chugh and E. K. Paluch, "The actin cortex at a glance", Journal of Cell Science **131**, jcs186254 (2018).

[237] P. J. Foster, S. Fürthauer, M. J. Shelley, and D. J. Needleman, "From cytoskeletal assemblies to living materials", Current Opinion in Cell Biology **56**, 109–114 (2019).

[238] T. Strübing, A. Khosravanizadeh, A. Vilfan, E. Bodenschatz, R. Golestanian, and I. Guido, "Wrinkling Instability in 3D Active Nematics", Nano Letters **20**, 6281–6288 (2020).

[239] M. C. Marchetti, J. F. Joanny, S. Ramaswamy, T. B. Liverpool, J. Prost, M. Rao, and R. A. Simha, "Hydrodynamics of soft active matter", Reviews of Modern Physics **85**, 1143–1189 (2013).

[240] T. Gao, R. Blackwell, M. A. Glaser, M. D. Betterton, and M. J. Shelley, "Multiscale Polar Theory of Microtubule and Motor-Protein Assemblies", Physical Review Letters **114**, 048101 (2015).

[241] I. Maryshev, D. Marenduzzo, A. B. Goryachev, and A. Morozov, "Kinetic theory of pattern formation in mixtures of microtubules and molecular motors", Physical Review E **97**, 022412 (2018).

[242] S. Fürthauer and M. J. Shelley, "How Cross-Link Numbers Shape the Large-Scale Physics of Cytoskeletal Materials", Annual Review of Condensed Matter Physics **13**, 365–384 (2022).

[243] T. B. Liverpool and M. C. Marchetti, "Instabilities of Isotropic Solutions of Active Polar Filaments", Physical Review Letters **90**, 138102 (2003).

[244] T. B. Liverpool and M. C. Marchetti, "Bridging the microscopic and the hydrodynamic in active filament solutions", EPL (Europhysics Letters) **69**, 846–852 (2005).

[245] I. S. Aranson and L. S. Tsimring, "Pattern formation of microtubules and motors: Inelastic interaction of polar rods", Physical Review E **71**, 050901 (2005).

[246]D. Saintillan and M. J. Shelley, "Instabilities and Pattern Formation in Active Particle Suspensions: Kinetic Theory and Continuum Simulations", Physical Review Letters **100**, 178103 (2008).

[247]I. Maryshev, A. B. Goryachev, D. Marenduzzo, and A. Morozov, "Dry active turbulence in a model for microtubule–motor mixtures", Soft Matter **15**, 6038–6043 (2019).

[248]J. Denk and E. Frey, "Pattern-induced local symmetry breaking in active-matter systems", Proceedings of the National Academy of Sciences **117**, 31623–31630 (2020).

[249]F. Nedelec and D. Foethke, "Collective Langevin dynamics of flexible cytoskeletal fibers", New Journal of Physics **9**, 427–427 (2007).

[250]T. Gao, R. Blackwell, M. A. Glaser, M. D. Betterton, and M. J. Shelley, "Multiscale modeling and simulation of microtubule–motor-protein assemblies", Physical Review E **92**, 062709 (2015).

[251]L. Huber, T. Krüger, and E. Frey, "Microphase separation in active filament systems maintained by cyclic dynamics of cluster size and order", Physical Review Research **3**, 013280 (2021).

[252]W. Yan, S. Ansari, A. Lamson, M. A. Glaser, R. Blackwell, M. D. Betterton, and M. Shelley, "Toward the cellular-scale simulation of motor-driven cytoskeletal assemblies", eLife **11**, e74160 (2022).

[253]H. Nakazawa and K. Sekimoto, "Polarity Sorting in a Bundle of Actin Filaments by Two-Headed Myosins", Journal of the Physical Society of Japan **65**, 2404–2407 (1996).

[254]M. Lenz, "Reversal of contractility as a signature of self-organization in cytoskeletal bundles", eLife **9**, e51751 (2020).

[255]F. D. Luca, I. Maryshev, and E. Frey, "Micelle instabilities and active foams in microtubule-motor mixtures with asymmetric interactions", Manuscript in preparation, N.D.

[256]M. Braun, D. R. Drummond, R. A. Cross, and A. D. McAinsh, "The kinesin-14 Klp2 organizes microtubules into parallel bundles by an ATP-dependent sorting mechanism", Nature Cell Biology **11**, 724–730 (2009).

[257]A. Ravichandran, G. A. Vliegenthart, G. Saggiorato, T. Auth, and G. Gompper, "Enhanced Dynamics of Confined Cytoskeletal Filaments Driven by Asymmetric Motors", Biophysical Journal **113**, 1121–1132 (2017).

[258]F. Hilitski, A. R. Ward, L. Cajamarca, M. F. Hagan, G. M. Grason, and Z. Dogic, "Measuring Cohesion between Macromolecular Filaments One Pair at a Time: Depletion-Induced Microtubule Bundling", Physical Review Letters **114**, 138102 (2015).

[259]L. Onsager, "THE EFFECTS OF SHAPE ON THE INTERACTION OF COLLOIDAL PARTICLES", Annals of the New York Academy of Sciences **51**, 627–659 (1949).

[260]G. Vliegenthart, A. Ravichandran, M. Ripoll, T. Auth, and G. Gompper, "Filamentous Active Matter: Band Formation, Bending, Buckling, and Defects", Science Advances, 10.1126/sciadv.aaw9975 (2020).

[261]P. Chandrakar, J. Berezney, B. Lemma, B. Hishamunda, A. Berry, K.-T. Wu, R. Subramanian, J. Chung, D. Needleman, J. Gelles, and Z. Dogic, "Engineering stability, longevity, and miscibility of microtubule-based active fluids", Soft Matter **18**, 1825–1835 (2022).

[262]I. Brust-Mascher, G. Civelekoglu-Scholey, M. Kwon, A. Mogilner, and J. M. Scholey, "Model for anaphase B: Role of three mitotic motors in a switch from poleward flux to spindle elongation", Proceedings of the National Academy of Sciences **101**, 15938–15943 (2004).

[263]G. Fink, I. Schuchardt, J. Colombelli, E. Stelzer, and G. Steinberg, "Dynein-mediated pulling forces drive rapid mitotic spindle elongation in Ustilago maydis", The EMBO Journal **25**, 4897–4908 (2006).

[264] G. Goshima, F. Nédélec, and R. D. Vale, "Mechanisms for focusing mitotic spindle poles by minus end–directed motor proteins", The Journal of Cell Biology **171**, 229–240 (2005).

[265] M. W. Elting, C. L. Hueschen, D. B. Udy, and S. Dumont, "Force on spindle microtubule minus ends moves chromosomes", Journal of Cell Biology **206**, 245–256 (2014).

[266] G. Popkin, "The physics of life", Nature **529**, 16–18 (2016).

[267] T. Krüger, I. Maryshev, and E. Frey, "Hierarchical defect-induced condensation in active nematics", arXiv, 10.48550/arxiv.2307.05716 (2023).

[268] C. Joshi, S. Ray, L. M. Lemma, M. Varghese, G. Sharp, Z. Dogic, A. Baskaran, and M. F. Hagan, "Data-Driven Discovery of Active Nematic Hydrodynamics", Physical Review Letters **129**, 258001 (2022).

[269] M. Golden, R. O. Grigoriev, J. Nambisan, and A. Fernandez-Nieves, "Physically informed data-driven modeling of active nematics", Science Advances **9**, eabq6120 (2023).

[270] N. P. Ferenz, A. Gable, and P. Wadsworth, "Mitotic functions of kinesin-5", Seminars in Cell & Developmental Biology **21**, 255–259 (2010).

[271] G. Yang, L. A. Cameron, P. S. Maddox, E. D. Salmon, and G. Danuser, "Regional variation of microtubule flux reveals microtubule organization in the metaphase meiotic spindle", The Journal of Cell Biology **182**, 631–639 (2008).

[272] T. Gao, R. Blackwell, M. A. Glaser, M. D. Betterton, and M. J. Shelley, "Multiscale Polar Theory of Microtubule and Motor-Protein Assemblies", Physical Review Letters **114**, 048101 (2015).

[273] A. Zemel and A. Mogilner, "Motor-induced sliding of microtubule and actin bundles", Physical Chemistry Chemical Physics **11**, 4821–4833 (2009).

[274] A. Hunt, F. Gittes, and J. Howard, "The force exerted by a single kinesin molecule against a viscous load", Biophysical Journal **67**, 766–781 (1994).

[275] K. Svoboda and S. M. Block, "Force and velocity measured for single kinesin molecules", Cell **77**, 773–784 (1994).

[276] K. Visscher, M. J. Schnitzer, and S. M. Block, "Single kinesin molecules studied with a molecular force clamp", Nature **400**, 184–189 (1999).

[277] M. T. Valentine, P. M. Fordyce, T. C. Krzysiak, S. P. Gilbert, and S. M. Block, "Individual dimers of the mitotic kinesin motor Eg5 step processively and support substantial loads in vitro", Nature Cell Biology **8**, 470–476 (2006).

[278] K. Tawada and K. Sekimoto, "Protein friction exerted by motor enzymes through a weak-binding interaction", Journal of Theoretical Biology **150**, 193–200 (1991).

[279] R. Loughlin, R. Heald, and F. Nédélec, "A computational model predicts Xenopus meiotic spindle organization", Journal of Cell Biology **191**, 1239–1249 (2010).

[280] G. Letort, A. Z. Politi, H. Ennomani, M. Théry, F. Nedelec, and L. Blanchoin, "Geometrical and Mechanical Properties Control Actin Filament Organization", PLoS Computational Biology **11**, e1004245 (2015).

[281] T. Mitchison and L. Cramer, "Actin-Based Cell Motility and Cell Locomotion", Cell **84**, 371–379 (1996).

[282] J. Brugués and D. Needleman, "Physical basis of spindle self-organization", Proceedings of the National Academy of Sciences **111**, 18496–18500 (2014).

[283] R. Suzuki, C. A. Weber, E. Frey, and A. R. Bausch, "Polar pattern formation in driven filament systems requires non-binary particle collisions", Nature Physics **11**, 839–843 (2015).

[284]V. Bratanov, F. Jenko, and E. Frey, "New class of turbulence in active fluids", Proceedings of the National Academy of Sciences **112**, 15048–15053 (2015).

[285]A. J. Tan, E. Roberts, S. A. Smith, U. A. Olvera, J. Arteaga, S. Fortini, K. A. Mitchell, and L. S. Hirst, "Topological chaos in active nematics", Nature Physics **15**, 1033–1039 (2019).

[286]R. Alert, J. Casademunt, and J.-F. Joanny, "Active Turbulence", Annual Review of Condensed Matter Physics **13**, 1–28 (2021).

[287]J. Alvarado, M. Sheinman, A. Sharma, F. C. MacKintosh, and G. H. Koenderink, "Molecular motors robustly drive active gels to a critically connected state", Nature Physics **9**, 591–597 (2013).

[288]T. Torisawa, D. Taniguchi, S. Ishihara, and K. Oiwa, "Spontaneous Formation of a Globally Connected Contractile Network in a Microtubule-Motor System", Biophysical Journal **111**, 373–385 (2016).

[289]Y. Eliaz, F. Nedelec, G. Morrison, H. Levine, and M. S. Cheung, "Insights from graph theory on the morphologies of actomyosin networks with multilinkers", Physical Review E **102**, 062420 (2020).

[290]S. Fürthauer, D. J. Needleman, and M. J. Shelley, "A design framework for actively crosslinked filament networks", New Journal of Physics **23**, 013012 (2021).

[291]J. F. Pelletier, C. M. Field, S. Fürthauer, M. Sonnett, and T. J. Mitchison, "Co-movement of astral microtubules, organelles and F-actin by dynein and actomyosin forces in frog egg cytoplasm", eLife **9**, e60047 (2020).

[292]G. R. X. Hickson and P. H. O'Farrell, "Anillin: a pivotal organizer of the cytokinetic machinery", Biochemical Society Transactions **36**, 439–441 (2008).

[293]K. L. Weirich, S. Banerjee, K. Dasbiswas, T. A. Witten, S. Vaikuntanathan, and M. L. Gardel, "Liquid behavior of cross-linked actin bundles", Proceedings of the National Academy of Sciences **114**, 2131–2136 (2017).

[294]S. Banerjee, M. L. Gardel, and U. S. Schwarz, "The Actin Cytoskeleton as an Active Adaptive Material", Annual Review of Condensed Matter Physics **11**, 1–19 (2020).

[295]M. P. Murrell and M. L. Gardel, "F-actin buckling coordinates contractility and severing in a biomimetic actomyosin cortex", Proceedings of the National Academy of Sciences **109**, 20820–20825 (2012).

[296]M. Lenz, M. L. Gardel, and A. R. Dinner, "Requirements for contractility in disordered cytoskeletal bundles", New Journal of Physics **14**, 033037 (2012).

[297]M. Murrell, P. W. Oakes, M. Lenz, and M. L. Gardel, "Forcing cells into shape: the mechanics of actomyosin contractility", Nature Reviews Molecular Cell Biology **16**, 486–498 (2015).

[298]S. Stam, S. L. Freedman, S. Banerjee, K. L. Weirich, A. R. Dinner, and M. L. Gardel, "Filament rigidity and connectivity tune the deformation modes of active biopolymer networks", Proceedings of the National Academy of Sciences **114**, E10037–E10045 (2017).

ACKNOWLEDGEMENTS

Doing a Ph.D. is a journey, a journey with ups and downs and a journey alongside which one meets many smart and inspiring people. During my journey, I had the pleasure of meeting, discussing, and working with many talented and supportive scientists whom I want to thank.

First, I would like to thank my Ph.D. supervisor, Erwin Frey. I would like to thank you for the freedom you gave me in finding, choosing, and exploring my own projects and my own scientific ideas. Thank you for the time you invested in our projects, your support in teaching me to formulate and communicate scientific ideas, and your guidance in political tactics in the scientific publishing process. Besides scientific guidance, I would like to thank you as a person. Doing a Ph.D. in times of Corona, facing ongoing lockdown, home office, and kita closure while having a young child at home, was not always easy to handle. If I had to leave early, couldn't finish work that should have been done, needed additional time, or if a one-year-old boy interrupted our Zoom meeting, I never heard anything but: "It's complicated times. I understand, take your time." Thank you!

During my research projects, I had the luck to work with two extremely talented scientists: Isabella Graf and Fridjof Brauns. Isabella, collaborating with you on a research project was a pleasure. Your enthusiasm and optimism, even at times when research becomes frustrating, are contagious. Your eye for mathematical detail and your ability to perform pen-and-paper calculations error-free within seconds are impressive. I definitely profited from our collaboration.

Fridjof, you influenced my way of scientific thinking. In a good way! Your eye for the bigger picture, your talent for asking the right questions, and your structured way of scientific arguing cannot be overstated. I did not only profit from our discussions during our collaboration but even beyond. I wish you all the best for your further scientific career. Besides that, I am not sure if I should thank or curse you for teaching me how to design figures, have an eye for color schemes, and have an eye for fonts. It definitely cost me hours, if not days, when I wrote this thesis.

Moreover, I would like to thank Ivan Maryshev for many stimulating discussions and helpful insights into the world of active matter field theories.

Among my colleagues, I would like to thank Alexander Ziepke, Tom Burkart, and Laeschkir Würthner for being admins and taking care of all our IT problems and needs. Timo Krüger for being a great office mate who was always up for scientific, coding and sometimes random discussions. Aida Hashtroud for being a tolerant office colleague and accepting the chaos that always emerges on my desk without my involvement.

I would like to thank all my colleagues in the group for creating a supportive, collaborative, and fun working atmosphere. George Dadunashvili, the social life at the chair (and the Munich breweries) differently profit from you being back in the group.

For proofreading parts of my thesis and giving helpful feedback, I would like to thank: Tom Burkart, George Dadunashvili, David Muramatsu, Henrik Weyer, Laeschkir Würthner, and Alexander Ziepke.

It is surprisingly difficult to write "science German". I thank Nicole Biolik for proofreading and correcting the most embarrassing mistakes in my German "Zusammenfassung".

In the beginning, I said a Ph.D. is a journey with ups and downs - if there are downs, it is good to have support. In my case, this support comes from my family. My mother and my uncle Peti, who always have an open ear and a supporting hand, no matter what. And finally, my wife Pia: Your support, your backing, that I can always rely on you, and your ability together with Joshua to put a smile on my lips have made this work possible. I love you.